

UCLA

UCLA Electronic Theses and Dissertations

Title

The Prevalence of Distant Giant Planets in the Presence of Close-In Small Planets

Permalink

<https://escholarship.org/uc/item/2hh9c090>

Author

Van Zandt, Judah

Publication Date

2025

Peer reviewed|Thesis/dissertation

UNIVERSITY OF CALIFORNIA
Los Angeles

The Prevalence of Distant Giant Planets in the
Presence of Close-In Small Planets

A dissertation submitted in partial satisfaction
of the requirements for the degree of
Doctor of Philosophy
in Astronomy and Astrophysics

by

Judah Emmanuel Van Zandt

2025

© Copyright by
Judah Emmanuel Van Zandt
2025

ABSTRACT OF THE DISSERTATION

The Prevalence of Distant Giant Planets in the Presence of Close-In Small Planets

by

Judah Emmanuel Van Zandt

Doctor of Philosophy in Astronomy and Astrophysics

University of California, Los Angeles, 2025

Professor Erik A. Petigura, Chair

One of the Solar System’s most prominent characteristics is the division of its planets into two distinct groups. The terrestrial planets have short periods, low masses, and negligible atmospheres, while the gas and ice giants have wider separations and masses 1–2 orders of magnitude larger than their inner neighbors, the majority of which is stored in prodigious atmospheres surrounding small solid cores. This feature raises the question of whether our system’s architecture is the result of chance, or if Nature has a tendency to produce planetary systems like ours. Until recently, an answer to this question was beyond reach, owing to the lack of available systems hosting both planet types. In this thesis, I investigate the occurrence rate of long-period giant planets in systems known to host an inner small planet. I used the *TESS* target pool to compile a high-purity sample of 47 Sun-like stars hosting transiting planets, which I then observed for three years to search for long-period giants. Along the way, I discovered three giant planets and developed a novel computational tool for analyzing partial orbits. I found that the occurrence rate of giant planets increases from 16% for typical Sun-like stars to 30% in systems with a close-in small planet, an enhancement factor of ~ 2 . This enhancement demonstrates that Solar System analogs are not rare, and that the processes which produced Earth may obtain elsewhere in the Universe.

The dissertation of Judah Emmanuel Van Zandt is approved.

Tuan H. Do

Bradley M. Hansen

Smadar Naoz

Erik A. Petigura, Committee Chair

University of California, Los Angeles

2025

DEDICATION

For my Dad, who paved my way, and for Jenna, who walked it with me.

TABLE OF CONTENTS

	Page
LIST OF FIGURES	x
LIST OF TABLES	xxx
ACKNOWLEDGMENTS	xxxi
VITA	xxxiv
ABSTRACT OF THE DISSERTATION	1
1 Introduction	1
1.1 Exoplanet Discovery	2
1.2 Exoplanet Demographics	6
2 TESS-Keck Survey XIV: Two giant exoplanets from the Distant Giants	
Survey	10
2.1 Introduction	11
2.2 Distant Giants Survey Design	14
2.2.1 Target Selection	14
2.2.2 Observing Strategy	19
2.2.3 RV Observations	22
2.2.4 <i>TESS</i> Detections of TOI-1669.01 and TOI-1694 b	22

2.3	A Jovian companion to TOI-1669	24
2.3.1	RV Model	24
2.3.2	False Alarm Probability	26
2.3.3	Companion Properties	27
2.4	A Jovian companion to TOI-1694	28
2.4.1	RV Model	28
2.4.2	Companion Properties	29
2.5	Discussion	30
2.6	Conclusions and Future Work	31
2.7	Acknowledgments	33
3	ethraid: A simple method for characterizing long-period companions using Doppler, astrometric, and imaging constraints	41
3.1	Introduction	42
3.2	ethraid’s Fitting Algorithm	44
3.2.1	Parameter Sampling from Priors	46
3.2.2	Forward Modeling and Likelihood Calculation	49
3.2.3	Marginalization	49
3.3	Forward model	49
3.3.1	RV Constraints	50
3.3.2	Astrometry Constraints	52
3.3.3	Direct Imaging Constraints	59
3.4	Performance	61
3.5	Usage, fitting, saving, and plotting	63
3.5.1	Command Line Interface	65
3.6	Validation	67
3.6.1	Case Study: HD 117207’s 7.5-year super-Jupiter is identified using 1.8-year baselines	68

3.6.2	Case Study: TOI-1694’s companion mass is bounded by direct imaging	69
3.6.3	Case Study: HD 114729’s two companions conspire to produce misleading parameter estimates	71
3.6.4	Case Study: HD 12661’s two planets are misinterpreted as a single companion	73
3.7	Future Improvements	75
3.8	Conclusions	77
3.9	Acknowledgments	78
3.10	Appendix 3A: Posterior Shapes	79
3.10.1	RV Posterior	79
3.10.2	Astrometry Posterior	81
3.11	Appendix 3B: Approximate Angular Separation Calculation	85
3.12	Appendix 3C: Rotation Matrix	89
4	No evidence for a metallicity-dependent enhancement of distant giant companions to close-in small planets in the California Legacy Survey	91
4.1	Introduction	92
4.2	Bryan & Lee (2024)	94
4.3	The California Legacy Survey	95
4.4	Binomial Occurrence Model	96
4.5	No Evidence of Enhanced Occurrence of Distant Giants in Metal-rich Stars	98
4.5.1	P(DG)	98
4.5.2	P(DG CS)	99
4.6	Broader Planet Definitions Increase P(DG CS)	102
4.7	Excluding evolved stars has little effect on occurrence	104
4.8	Discussion	105
4.9	Acknowledgments	107

5	The TESS-Keck Survey XXIV: Outer Giants may be More Prevalent in the Presence of Inner Small Planets	108
5.1	Introduction	109
5.2	Survey Review	111
5.3	Planet Detection Algorithm	116
5.4	Planet Catalog	119
5.4.1	Six companions with resolved orbits	119
5.4.2	Six companions with partial orbits	120
5.4.3	Treatment of pre-survey data	122
5.5	Trend Analysis	124
5.5.1	ethraid	124
5.5.2	Mass-Separation prior	125
5.6	Survey Sensitivity	128
5.6.1	Distant Giants Survey	128
5.6.2	California Legacy Survey	130
5.7	Computing Planet Occurrence	131
5.7.1	Definitions	131
5.7.2	Occurrence Model	131
5.7.3	Occurrence Computation	133
5.8	Results	133
5.8.1	Distant giants may be enhanced in the presence of close-in small planets	133
5.8.2	No strong evidence that high-metallicity systems exhibit a greater enhancement of distant giants	135
5.8.3	Inner companions to resolved giants may be preferentially closer-in	137
5.8.4	Outer companions may have preferentially low eccentricities	138
5.8.5	Systems with multiple transiting planets may be more likely to host an outer companion	139

5.8.6	Outer companion occurrence does not correlate with stellar parameters	141
5.9	Discussion	142
5.9.1	Distant giant occurrence	142
5.9.2	Distant giants and metallicity	143
5.9.3	Distant giants and inner planet properties	144
5.9.4	Brown dwarf occurrence	146
5.10	Conclusion	147
5.11	Acknowledgments	148
5.12	Appendix 5A: Companions Detected as Trends	149
5.12.1	TOI-1174	149
5.12.2	HD 191939	151
5.12.3	TOI-1438	151
5.12.4	HD 219134	154
5.12.5	HD 12572	154
5.12.6	HD 156141	157
5.12.7	HD 75732	157
5.12.8	HD 93963	157
5.12.9	TIC 142381532	158
	Bibliography	164

LIST OF FIGURES

	Page
1.1 Exoplanets discovered by the four most popular detection techniques as of March 2025. Method-specific biases are evident: the transit technique (red circles) excels at detecting short-period planets due to their higher transit probability; RVs (blue squares) are sensitive to close-in planets, but are well-suited to detecting giant planets at wide separations; gravitational microlensing (green diamonds) can detect a wide range of planet masses, but is limited to a relatively narrow range of periods by the requirement of favorable lensing geometry; and direct imaging (purple x's) enables the detection of high-mass planets at very wide separations around young stars. The legend gives the number of planet detections using each technique. We estimated the masses of transiting planets for which the mass was unknown using the mass-radius relationship of Weiss and Marcy (2014) . The parameters of Venus, Earth, Jupiter, Saturn, Uranus, and Neptune are shown with their initials, demonstrating our low sensitivity to most Solar System planets across all methods.	9

2.1	Stellar and transiting planet parameters of the TKS survey. Filled points show targets selected for the Distant Giants sample. Panels a) through c) show stellar parameters. TOI-1775 and TOI-2088 are not shown in panel b) because they lacked measured $\log R'_{\text{HK}}$ values when we finalized our sample. Panel d) shows parameters of the transiting planets. For multi-transiting Distant Giants systems, we checked planet radii in order of ascending TOI number, and show the first planet to pass our survey filters.	35
2.2	Observations of the Distant Giants sample between its official start in August 2020 and late 2022. Red squares are HIRES RVs and gray circles are APF RVs. Targets are ordered by right ascension, shown in the right margin. The typical target in our sample is inaccessible from Keck Observatory for about three months out of the year, which is reflected in the bands of decreased observation density which run diagonally through the plot. During their observing seasons, all targets generally meet or exceed the prescribed monthly cadence.	36

2.3	The RV time series and orbit models for TOI-1669’s AIC-preferred circular model (left) and our preferred model including eccentricity (right). Although the circular model has a lower AIC, we adopt the more general model including eccentricity, and emphasize that our limited RV sample contributes to model selection uncertainty. In both figures, a) shows our full Keck/HIRES RV time series (black points) with the fitted model in blue. The residuals to the fit are given in b) . Each subsequent panel shows the time series phase-folded to a particular model planet period. Both models recover consistent periods and masses for the giant TOI-1669 b, as well as a long-term linear trend, suggesting that these parameters are not highly sensitive to our choice of model. By contrast, our eccentric model shows that TOI-1669 b’s orbit may deviate from circular. Future observations will resolve this disagreement. The existence of TOI-1669.01 is known from TESS photometry, so we include it in our model despite its low RV amplitude.	37
2.4	The RV time series of TOI-1694, together with orbit models assuming a circular (left) or eccentric (right) outer planet. In both figures, a) shows our full Keck/HIRES RV time series (black points) with the fitted model in green. The residuals to the preferred fit are shown in b) . Each subsequent panel shows the time series phase-folded to a particular model planet period. For consistency with our treatment of TOI-1669, we include two models that differ only in the eccentricity of the outer planet. However, in contrast to TOI-1669, the eccentric model we adopted for TOI-1694 is also formally preferred by the AIC. TOI-1694 b’s mass and orbital separation identify it as a hot Neptune.	38

2.5	Masses and periods of known exoplanets discovered by RVs (blue circles) and transits (red circles). Transiting planet masses are estimated from their radii using the mass-radius relation of Weiss and Marcy (2014). Transiting/resolved Distant Giants companions are overlaid as red/blue squares. Inner and outer companions in the resolved systems, HD 219134, HD 75732, TOI-1669 and TOI-1694, are connected with black lines. We also plot estimated parameters of HD 191939 f, though our analysis of this planet’s RV signal is still preliminary. TOI-1669 b and TOI-1694 c have masses and periods typical of cold Jupiters. The red arrows indicate planetary periods shorter and longer than the current ~ 2 -year survey baseline. HD 75732 d and HD 219134 g have orbits well beyond three years, and are only resolved due to their extensive observing histories.	39
2.6	Distribution of eccentricity versus orbital separation for confirmed exoplanets between 0.01 and 30 AU with $\sigma_e \lesssim 0.1$ (blue points). The four resolved giants in our sample are shown in orange. TOI-1669 b and HD 219134 g have eccentricities consistent with zero, and each is represented by an arrow, the base of which shows the 84% upper eccentricity limit. It is not obvious that the distribution from which these planets’ eccentricities are drawn is distinct from that of the underlying population.	40

3.1	<p>ethraid’s fitting algorithm. The steps are the same for RVs (left), astrometry (center), and direct imaging (right): ethraid samples a set of model orbital parameters, forward models the data-specific parameters, evaluates the model likelihood, and finally marginalizes many such likelihoods to derive the posterior PDF. Arrows represent inputs used in a given step: blue arrows show inputs from the previous step, red arrows show inputs provided by the user, and purple arrows show inputs that are fixed in the code. The bottom row shows three of the plots available to the user through the <code>plot</code> command.</p> <p>Left: The 2D m_c-a posteriors for each of the RV (green), astrometry (blue), and imaging (gray line) data sets, plus the combined posterior (red) conditioned on all three. The dark/light regions of each posterior show 68/95% confidence intervals. For imaging, the gray contour marks the 95% confidence boundary, with models below/above the contour ruled in/out by the data.</p> <p>Right: CDFs of the marginalized a and m_c posteriors. The vertical red lines indicate 95% confidence intervals. ethraid also produces corresponding PDFs by default.</p>	45
3.2	<p>Our model of astrometric proper motion anomaly. Red ellipses show the stellar orbit associated with a non-luminous bound companion (not shown). Green arrows show the average proper motion vectors fitted to the data from <i>Hipparcos</i> (left) and <i>Gaia</i> (right). Gold stars show the average positions during <i>Gaia</i> and <i>Hipparcos</i>, and the blue arrow shows $\vec{\mu}_{HG}$, the average proper motion <i>between</i> them, calculated as the difference in average positions divided by the difference between the mission midpoints. The proper motion anomaly $\Delta\mu$, shown in red, quantifies the difference between the average <i>Gaia</i> proper motion and the position-derived proper motion. Figure adapted from Kervella et al. (2019).</p>	54

- 3.3 `ethraid`'s likelihood calculation for direct imaging. Beginning with a set of sampled parameters (left), `ethraid` models angular separation (either **exactly** or **approximately**) using the orbital elements, and contrast using the companion mass, together with a linear interpolation function derived from Table 5 of [Pecaut and Mamajek \(2013a\)](#) and Table 4 of [Baraffe et al. \(2003\)](#), denoted by 'PM13' and 'B03,' respectively. `ethraid` then determines whether the model companion's brightness would have exceeded the minimum detectability threshold at the model separation in the real imaging data (gold line) and assigns a likelihood of 0 for detectable companions and 1 for non-detectable companions. The example model in the diagram (red star) falls above the threshold, indicating a companion that would have been detected if it were truly in the system, so we assign it a likelihood of 0. 62
- 3.4 The top panel shows a 7.5-year subset of HD 117207's RV time series, divided into four slices based on the epoch in which the RVs were measured. Panels **a)-d)** show the RVs from each slice, along with the linear/quadratic trend fit to those RVs using `radvel`. We show the measurement error of each RV with horizontal black lines. We used `ethraid` to model each trend/curvature pair, along with HGCA astrometry, in panels **e)-h)**, respectively. The gold star in each panel shows HD 117207 b's semi-major axis and $m_c \sin i$ values measured by long-baseline RV surveys: $a = 3.744$ AU, $m_c \sin i = 1.87 M_J$, where we have approximated a conversion from $m_c \sin i$ to m_c by dividing by the median $\sin i$ value of 0.866. The overlap between `ethraid`'s predicted parameters and the true values in all four panels demonstrates `ethraid`'s reliability in estimating companion parameters over a range of orbital phases. 70

- 3.5 Same as Figure 3.4 for TOI-1694’s two year baseline. The gray lines in panels **d)**-**f)** show posteriors derived from direct imaging. The gold stars show TOI-1694 b’s median semi-major axis and adjusted $m_c \sin i$ values measured by [Van Zandt et al. \(2023\)](#): $a = 0.98$ AU, $m_c \sin i = 1.05 M_J$. Without astrometry, the trend and imaging data provide too little information to constrain the planet’s mass and separation. However, they are able to rule out massive stars as well as the (a, m_c) pairs in the white regions. Note also that the posteriors in panels **e)** and **f)** favor shorter-period models due to the higher RV curvature associated with their trends. 72
- 3.6 Same as Figure 3.4 for HD 114729. The gold star at the lower left of each panel shows the semi-major axis and adjusted $m_c \sin i$ of HD 114729 Ab measured by long-baseline RV surveys: 2.094 AU, $m_c \sin i = 0.892 M_J$. The upper right star shows the same for HD 114729 B, with a projected separation and mass of 282 AU and $M = 0.253 M_\odot$. We estimated HD 114729 B’s true separation by dividing the projected separation of 282 AU by 0.79, as described in Section 3.3.3. Agreement between the planet parameters and the RV posteriors indicates that `ethraid` is correctly recovering HD 114729 Ab’s RV signature. Meanwhile, the consistency between HD 114729 B’s parameters and the astrometric posterior suggests that HD 114729 B produced the astrometric trend. Note that in panels **a)** and **d)**, the fitted trend/curve values had precisions $< 2\sigma$, leading to broad RV posteriors in panels **e)** and **h)**. 74

- 3.7 Same as Figure 3.4 for HD 12661. For this system, we include RVs from both the Keck/HIRES and APF/Levy instruments. The gold stars show the a and adjusted $m_c \sin i$ values of HD 12661 b (left) and c (right). Planet b dominates the RV signature due to its short period, as shown by its consistency with the green RV posteriors in each slice. Meanwhile, planet c is responsible for the majority of the astrometric signal. The inconsistency between these planets' measured parameters and the combined posterior (red) shows that `ethraid` misinterpreted these separate contributions as originating from a single object of higher mass. 76
- 3.8 **Left:** An RV posterior calculated using both $\dot{\gamma}$ and $\ddot{\gamma}$. The blue line follows the relationship $m_c \propto a^2$, while the red line follows $m_c \propto a^{7/2}$. **Right:** An RV posterior calculated using $\ddot{\gamma}$ only, with a host star of $1 M_\odot$. In the low-mass regime, the posterior follows $m_c \propto a^{7/2}$. However, the slope shifts to $m_c \propto a^{7/3}$ near $1 M_\odot$ 81

3.9 **Left:** A diagram of the circular, face-on orbit we use to understand the behavior of the astrometry posterior. The black circle shows the orbit of the host star about the system barycenter due to a companion at wide separation ($\gtrsim 20$ AU). Solid and dotted arrows show the average stellar position and proper motion vectors, respectively, in each of the *Hipparcos*, *HG*, and *Gaia* EDR3 epochs. θ_{HG} gives the position angle at the *HG* epoch relative to the position angle during the *Hipparcos* epoch. In the long-period regime, using the small angle approximation for θ_{HG} is appropriate. **Right:** A similar diagram for short periods ($\lesssim 2$ AU). Arrows t_1 and t_2 show the position of the host star at the beginning and end of the *Gaia* EDR3 data collection window. We chose t_2 's position arbitrarily to illustrate that for short periods, the angle between the two position vectors is not small, but rather can take any value on $[0, 2\pi]$. We do not show the analogous vectors for $\vec{\mu}_{HG}$ because T_{HG} is nearly nine times the duration of T_G ; this larger denominator drives $\vec{\mu}_{HG}$ to nearly zero for short-period orbits. 82

3.10 **Left:** The posterior surface calculated from astrometric data. The red line follows the relationship $m_c \propto a^{-1}$, while the green line follows $m_c \propto a^2$. **Right:** The short-period regime of the surface at left. Iso-period lines are shown in red: the right-most line traces $P = T_G \sim 2.83$ yr, the next follows $P = \frac{T_G}{2}$, then $P = \frac{T_G}{3}$, and so on. High-likelihood models near these periods must have large companion masses to counter the small net displacement of the star. The same effect can be seen at harmonics of the ~ 25 -yr *Hipparcos-Gaia* baseline ($\sim 4-16$ AU), though it is less pronounced because $\vec{\mu}_G$ remains nonzero in this regime even when $\vec{\mu}_{HG}$ vanishes. 86

3.11	<p>Left: Panel d) from Figure 3.5, showing the companion models consistent with a subset of the RVs of TOI-1694, as well as the imaging data. Note that despite falling above the gray 95% contour, some high-mass models are consistent with the imaging data because their orbital geometries result in small projected angular separations from the host star. Right: Parameter constraints for the same RV and imaging data, but using the approximate imaging calculation. In the approximate case, the imaging contour represents a hard bound, above which companions are ruled out with certainty. This causes the 1σ upper bound on mass (dark red) to be underestimated by $\sim 30\%$ at 16 AU, while being roughly unaffected at 8 AU.</p>	88
4.1	<p>The companions in the sample of Bryan and Lee (2024) (yellow) and the FGK subsample of Rosenthal et al. (2021) (blue). BL24 has companions between $\sim 1 M_{\oplus}$ and $20 M_{J}$, and R21 includes companions from a few M_{\oplus} up to $80 M_{J}$. The legend gives the number of companions in each sample in parentheses. We show BL24’s definitions of close-in small (CS) and distant giant (DG) planets with black dashed boxes. We use blue diamonds to highlight HD 75732, the only system in the metal-rich R21 sample with planets satisfying both of these definitions. We use filled black circles to show six planets in the BL24 sample without measured masses. We estimate their masses using the mass-radius relationship of Weiss and Marcy (2014). The distributions of giant plants are similar among the two samples. They also have comparable inner planet distributions, though BL24 contains many more such planets due to its selection function. This latter similarity makes it unlikely that a dependence of giant occurrence on inner planet properties, if such a dependence exists, affected our comparison.</p>	97

4.2 Measurements of field (blue) and conditional (orange) occurrence of distant giants in metal-rich subsets of the Bryan and Lee (2024) and Rosenthal et al. (2021) samples. BL24 found that distant giants are about twice as prevalent in the presence of close-in small planets as the field rate they measured from the R21 sample (far left). We measured both the conditional and field rates using the R21 sample and four different sets of definitions for close-in small planets and distant giants. The "Default" definition matches BL24: the inner planets satisfy $1 \leq M \sin i \leq 20 M_{\oplus}$ and the distant giants satisfy $0.5 \leq M \sin i \leq 20 M_J$ and $1 \leq a \leq 10$ AU. The "Small DG" definition used a $90 M_{\oplus}$ floor for distant giants. The "Big CS, Small DG" definition used a $30 M_{\oplus}$ ceiling for inner planets and a $90 M_{\oplus}$ floor for distant giants. Finally, our "Small CS, Small DG" definition used a $10 M_{\oplus}$ ceiling for inner planets and a $90 M_{\oplus}$ floor for distant giants. We annotate each distribution with the planet sample used to calculate it, and include the CS and DG definitions on the x -axis. Horizontal dotted lines denote distribution quartiles. We use black solid lines to indicate the 95% confidence interval of a 2x enhancement over each field occurrence rate, and label the upper line with the percentage of each conditional occurrence distribution that falls within it. BL24's conditional occurrence distribution is fully consistent with a 2x enhancement, whereas only 8% of our Default distribution overlaps this interval. Expanding our definitions of inner planets and distant giants increases the conditional rate, because a significant fraction of the giant planets in the R21 sample have masses below $0.5 M_J$ 101

5.1	Stellar and transiting planet parameters of the Distant Giants Survey. Panel (a): metallicity and V -band magnitude of stars with companions detected as resolved orbits (blue squares), companions detected as accelerations (red diamonds), and with no detected companions (black circles). Unfilled circles show other systems in the larger <i>TESS</i> -Keck Survey. Other panels are same as (a) but for $V \sin i$ and $\log R'_{HK}$ (panel b), stellar radius and temperature (panel c), and transiting planet radius and orbital period (panel d). For multi-transiting systems we show the first planet to pass our survey filter (lowest TOI number).	112
5.2	Radial velocity observations of the Distant Giants Survey. In total we collected 1990 RVs from Keck/HIRES (red squares) and 2036 observations from APF/Levy (gray circles) between 1 August 2020 and 31 January 2024. Note a few targets had prior RVs which are not shown. TOI identifiers are shown in the left margin, ordered by right ascension. Each year label on the x -axis marks February 1, the first day of the “A” observing semester. The typical target in our survey is not accessible from Keck for about three months per year, resulting in the diagonal cadence gaps. The eruption of Mauna Loa in November 2022, as well as unrelated damage to the lower shutter of the Keck I dome between November 2022 and May 2023, resulted in a substantial decrease in observation cadence for targets between RA ~ 16 –22 hr, which did not reach elevations $>40^\circ$ during this period.	113

5.3 Flow diagram of our planet detection algorithm. We used the same algorithm for detecting planets (Section 5.4) and for computing completeness (Section 5.6). We began by initializing an orbital model with the RV data and the ephemerides of any known transiting planets. We then determined whether the data supported the inclusion of a trend, that is, if a trend model was favored over a flat model by $\Delta\text{BIC} > 5$, after which we added a new planet to the model. We computed ΔBIC between the starting model and a model with a trial planet over a dense grid of trial periods. If the maximum ΔBIC exceeded 30, we performed a final model comparison test to select a model with a planet, a trend, or both. We iteratively added planets to the model in this way until no more were found. For the injection/recovery experiments described in Section 5.6, we began with the final model from Section 5.4 to retain any planets found during the initial search. We then injected a synthetic planetary signal into the data and began the recovery at the trend test step (outlined in red). When the search terminated, we checked whether the injected signal was recovered, either as a planet or as a trend, and recorded the result. 117

5.4	Close-in small planets and their distant giant companions. Masses and periods of exoplanets from our survey (bold squares) and the NASA Exoplanet Archive (faded circles) for context . Red/blue points indicate planets discovered using the transit/RV method. Red squares show true masses of transiting planets in the Distant Giants Survey measured by RVs (Polanski et al., 2024), while blue squares show minimum mass measurements ($M \sin i$). For systems with multiple transiting planets, we show the parameters of the transiting planet with the lowest TOI designation that passed our filters. Red squares with yellow borders indicate systems in which we detected a linear/quadratic trend. Giant planets in our sample are connected to the inner planet in their system by a black line. The box corresponds to our nominal definition of a Distant Giant.	121
5.5	Masses and orbital spacings of the planets in each system in our survey. Systems are ordered according to the semi-major axis of the innermost transiting planet. Transiting planets are shown with black markers and non-transiting planets are colored according to their eccentricity. Marker sizes are proportional to the square root of the planet true mass (for transiting planets) or minimum mass (for non-transiting planets). We use red borders to indicate planets which meet our definition of a distant giant. For systems with RV trends, we place a red triangle at a separation corresponding to six years, the approximate maximum period for which we could resolve a Keplerian orbit. Based on Figure 4 of Weiss et al. (2024).	123

5.6 **Mass/separation prior informed by the Rosenthal et al. (2021) and Raghavan et al. (2010) surveys.** **Left:** Minimum masses and orbital separations of the CLS (Rosenthal et al., 2021) sample of planets (blue points) and brown dwarfs (orange points). We also show the survey-averaged completeness map (red contours) emphasizing the 50% contour with a black line. We compute companion occurrence in the cells defined by the red dashed lines. Hatch marks show cells containing fewer than three objects, giving rise to highly uncertain occurrence rates. However, inspection of the RV constraints in Appendix 5.12 shows negligible overlap with these regions, so they do not affect our overall results. **Right:** The domain of M and a we explore in our companion search. Each M - a sub-domain is colored with the number of objects per star and serves as our joint M - a prior described in Section 5.5.2. The highest mass bins are based on the Raghavan et al. (2010) rates. 126

- 5.7 Side-by-side comparison of injection/recovery results and calculated completeness to resolved orbits (left) and trends (right). We tracked whether our automated search algorithm recovered injected RV signals successfully (blue/green points for resolved orbits/trends), or unsuccessfully (red points). From this collection of recoveries, we calculated a sensitivity map, with contour lines marking completeness deciles, and the black contour denoting the 50% completeness boundary. We injected 2000 signals for each system. **Top row:** Completeness for a typical system in our survey (TOI-1173: 3.9-year baseline, 27 observations). **Bottom row:** Average completeness of the 47 targets in our survey, with blue boxes indicating our nominal definition of a distant giant. Our average sensitivity in this interval is 30% for resolved orbits and 35% for trends. Orange and purple dashed boxes indicate the giant planet definitions used by Rosenthal et al. (2022) and Bryan et al. (2019), respectively. Our survey had 32% (27%) sensitivity to resolved orbits (trends) using the Rosenthal et al. (2022) definition, and 30% (43%) sensitivity using that of Bryan et al. (2019). Note that we treated resolved orbits and trends as distinct detection classes, meaning that an orbit recovered as a trend was considered an unsuccessful recovery in the resolved recovery map, and vice versa. 127
- 5.8 Average sensitivity to companions as a function of minimum mass and separation for the California Legacy Survey. Shaded regions show domains of constant detection probability, and the solid black contour shows the 50% detection probability boundary. We recalculated this map after adjusting for inclination effects to determine the CLS sensitivity to true mass (see Section 5.6.2). We show the 50% boundary of the adjusted map as a dashed black line. We use a blue rectangle to show our nominal definition of a distant giant ($a = 1 - 10$, $M = 70 - 4000 M_{\oplus}$). The average CLS sensitivity to minimum/true masses within this domain is 59%/52%. 129

5.9	Measurements of the field (blue) and conditional (orange) occurrence of distant giants under different planet definitions. Black lines show distribution quartiles. The left set of distributions show occurrence rates for our nominal definitions: $a = 1\text{--}10$ AU, $M_p \sin i = 70\text{--}4000 M_\oplus$ for DGs and $a > 1$ AU, $R_p = 1\text{--}4 R_\oplus$ for CS planets. The distributions in the center and right show occurrence rates for planet definitions matching those of Rosenthal et al. (2022) and Bryan et al. (2019), respectively. We annotate each distribution with the probability that the conditional rate is enhanced over the field rate.	136
5.10	Distribution of eccentricity versus orbital separation for confirmed exoplanets in the NEA with $\sigma_e \leq 0.13$. Confirmed planets are shown as unfilled circles and confirmed distant giants (1–10 AU and 70–4000 M_\oplus) as blue circles. For confirmed giants, marker size is proportional to our survey-averaged completeness at the planet’s mass and separation. We show giants in our survey in orange and indicate measurements with less than 3σ eccentricity precision with an arrow, placing the bottom of the arrow at the 1σ upper limit. The giant companions in our survey may have lower eccentricities than the average distant giant, but a larger sample is needed to draw a strong conclusion. . . .	140

5.11 **Left:** Our orbital fit to the TOI-1174 system using `radvel`. Panel a) shows the full RV time series and errors with black circles, with our preferred model as a blue line. Panel b) shows the residuals to the planetary model, isolating the fitted trend/curvature. Panel c) shows the RV time series phase-folded to the period of the inner planet in this system. Red points give binned RV values. We did not recover the inner transiting planet signal in the RVs. **Right:** Our `ethraid` posterior surface derived using the measured trend. Green regions show models consistent with the RV trend, and red regions show models consistent with both the RVs and the direct imaging for this system, which revealed no luminous companions. Dark (light) regions indicate 68% (95%) confidence intervals. The gray line approximates the contrast limits imposed by imaging for a circular, face-on companion. Gray panels at low mass and short separations show companion parameters incompatible with the observed trend due to our observing baseline. 150

5.12 Same as Figure 5.11 for HD 191939. We included the three transiting planets in our model, and our blind search algorithm detected the known 100-day super-Saturn as well as a spurious long-period planet. The blue posterior surface shows constraints imposed by the astrometric acceleration measured in this system. The trend and curvature in our truncated RV time series along with the astrometric acceleration, yield a high planetary odds ratio. 152

5.13 Same as Figure 5.11 for TOI-1438. We were unable to detect the transiting planets in this system, but we measured strong trend and curvature, consistent with planetary, brown dwarf, or stellar companion models. 153

5.14	Same as Figure 5.11 for HD 219134. We chose RV measurements from an arbitrary four-year span of this system’s full data set. We recovered one of the non-transiting planets using a blind search, but missed two others. We analyzed the measured trend and HGCA astrometry to calculate a probability near 1 of this signal originating from a planet. We also tested other four-year spans and verified that our choice did not strongly influence our final odds ratio.	155
5.15	Same as Figure 5.11 for HD 12572. We measured the mass of the 20-day sub-Neptune in this system and also found a strong linear trend with no significant curvature. We also measured a marginal astrometric acceleration, which imposed added constraints (blue contours). Note that the gray line marks orbital models which are ruled out by direct imaging under the assumption of a circular, face-on orbit. Companions with non-zero inclinations and eccentricities may lie beyond the line without being ruled out.	156
5.16	Same as Figure 5.11 for HD 156141. We obtained a marginally significant measurement of the inner transiting planet’s mass, and high-significance trend and curvature measurements. The long-term signals in this system are consistent with planets and brown dwarfs, whereas stellar models are nearly ruled out with the aid of direct imaging.	159
5.17	Same as Figure 5.11 for HD 75732. We detected only one of the four non-transiting planets in this system using our blind search algorithm. The residual trend, together with a low-significance astrometric acceleration, constrains the mass-separation posterior primarily to the planetary regime.	160
5.18	Same as Figure 5.11 for HD 93963. We did not recover either of this system’s two transiting planets at high significance. We measured a significant trend and marginal curvature in this system. Our analysis showed that the source of this RV variability is most likely a planet.	161

- 5.19 Our second analysis of the trend in the HD 93963 system. We expanded the semi-major axis range over which we tested companion models and therefore did not use the informative mass/separation prior described in Section 5.5.2, which is defined for separations ≤ 64 AU. We indicate the position of the stellar companion, HD 93963 B, with a yellow star. Our analysis suggests that an M5 dwarf at a separation of 484 AU is too small/too distant to have caused the observed trend. 162
- 5.20 Same as Figure 5.11 for TIC 142381532. The inner transiting planet in this system is a sub-Saturn, which we characterized at high significance. Although this planet passed our $R_p < 10 R_\oplus$, it is likely a gas giant, so we exclude this system from our occurrence calculations. Our trend measurement is marginal, and evinces planetary and brown dwarf models with roughly equal probability. 163

LIST OF TABLES

	Page
2.1 Survey Criteria	17
2.2 Distant Giants Sample	17
2.3 Resolved Distant Giants planet properties	23
2.4 Resolved Distant Giants stellar properties	23
2.5 Radial Velocities	26
3.1 Configuration file parameters	64
3.2 Command line interface parameters	66
4.1 Occurrence Rates	100
4.2 Sample Sizes and Completeness	102
5.1 Distant Giants Sample	114
5.2 Distant Giants Radial Velocities	116
5.3 Resolved Distant Giants planet properties	119
5.3 (continued)	120
5.4 Distant Giants trend data	121
5.5 Distant Giants occurrence rates	134

ACKNOWLEDGMENTS

A lot has changed since I began graduate school six years ago, both in my own life and beyond. Reflecting on these changes has helped me realize the enormous number of people who have supported me in achieving my dream of becoming an astronomer. I could not have even begun this journey, let alone finished it, without all of you.

First and foremost, I am thankful to my PhD advisor, Erik Petigura. Erik, from our first night observing together, when you walked me through the the HIRES optical path, even to my last days as your student, I leave every one of our interactions having learned something valuable. Your enthusiasm for Astronomy is infectious, and your incisiveness is inspiring. Many times over the last six years, I faced obstacles that seemed overwhelming, but you have a way of cutting away the extraneous parts of a problem, laying it out so clearly that I wonder how I didn't see the answer in the first place. Thank you for embodying such a high standard, and for helping me build the confidence to do the same. I hope that as I take the next step in my career, I'll maintain the curiosity and determination that you exemplify.

Before coming to graduate school, I worked in a variety of disciplines that ignited my interest in scientific research. I'm grateful to my first two Astronomy mentors, Dimitri Mawet and Kent Wallace. Kent, your guidance through my first exoplanet research project opened the door to my pursuit of Astronomy, and your lighthearted demeanor made every meeting fun and engaging. I would like to thank George Helou and my father-in-law, Mazen Wahbeh, for connecting me with Dimitri and encouraging me to apply to a summer research fellowship in his lab at Caltech. Thanks also to my undergraduate research mentors at Notre Dame: Graham Peaslee, Morten Eskildsen, and Justin Crepp. In their labs I researched nuclear physics, magnetic vortices in superconductors, and exoplanet imaging. These early research experiences were major precursors to my journey through graduate school, and I'm grateful to all of you for helping me get started.

At UCLA I was fortunate to be surrounded by a strong community of fellow students. Graduate school can feel isolating, but the effort that each grad invests into our department has created a culture capable of supporting students through strikes, comprehensive exams, and a global pandemic. Thanks especially to Rory Bentley and Nick Ferraro, my fellow graduate representatives, as well as our predecessors, Ronald Lopez and Veronica Dike, for embodying the values of selflessness and guardianship that preserve our grad community. Thanks also to all the Grampers, the Groffee drinkers, and the Dewar-ites who made that community worth preserving. I'm grateful to have been accepted into this environment when I came to UCLA, and I feel confident, though wistful, to leave it in the hands of the next generation.

It was a joy to work alongside the talented and dedicated astronomers in the Petigura group: Mason MacDougall, Isabel Angelo, Dakotah Tyler, Greg Gilbert, and Jack Lubin. Whether on observing trips to the Big Island, or group meetings on the PABio, each of you brought a unique perspective that helped me view my research, and Astronomy in general, in new ways. Greg deserves particular recognition; from the moment you joined our group, you never hesitated to read over a proposal draft, debug some code, or give your two cents on any problem I had. You went beyond the call of a postdoc's duty, and helped me advance immensely as a scientist.

I had the additional privilege of working with a thriving research team outside UCLA. My time in graduate school coincided fortuitously with the *TESS*-Keck Survey (TKS), a collaboration between multiple UCs as well as other universities across the country, to measure the masses of planets found by NASA's *TESS* mission. TKS comprised dozens of professors, postdocs, and graduate students, and was an ideal environment to learn the ropes of exoplanet observation. It was an honor to learn with and from so many brilliant scientists. Thank you to everyone who participated in this effort to produce incredible scientific insights and many lasting friendships.

It's difficult to express my gratitude to my family for their unwavering support in my academic endeavors. To Dad in particular, thank you for encouraging me at every stage, and for working so hard to give me the opportunities I had. You taught me the value of honesty, persistence, and dedication, and to make the most of every chance I get. These lessons have made me who I am, and gave me the good sense to recognize the greatest blessing I ever received. Jenna, you are my sunshine and my best friend. It would have been enough if you had just been my emotional support, my most consistent motivation, and my biggest fan, but you were all of those while braving a PhD of your own. You are my inspiration, and I can't imagine doing this without you.

I would like to acknowledge support I've received from the Future Investigators in NASA Earth and Space Sciences and Technology program, as well as the University of California, Los Angeles. Additionally, my doctoral research relied on data from Keck Observatory and *TESS*, both of which receive public funding. I am fortunate to have benefited from these institutions, and I hope that the scientific results they and others like them have produced will be recognized as evidence of their value in promoting curiosity, engagement, and the pursuit of knowledge.

I want to recognize the important cultural role that the summit of Maunakea has within the Native Hawaiian community. I have been very fortunate during my graduate school career to conduct observations from Keck Observatory, which sits atop this mountain.

The following chapters have been reproduced from the corresponding Astronomical Journal articles with permission from the Institute of Physics (© IOP Publishing, all rights reserved): Chapter 2 (Van Zandt et al., 2023), Chapter 3 (Van Zandt and Petigura, 2024a), Chapter 4 (Van Zandt and Petigura, 2024b), Chapter 5 (Van Zandt et al., 2025).

VITA

Judah Emmanuel Van Zandt

EDUCATION

M.S. – Astronomy and Astrophysics	2022
UCLA	<i>Los Angeles, CA</i>
B.S. – Physics and Mathematics	2019
University of Notre Dame	<i>South Bend, IN</i>

RESEARCH EXPERIENCE

Graduate Research Assistant	2019–2025
University of California, Los Angeles	<i>Los Angeles, CA</i>
Summer Undergraduate Research Fellow	2018
California Institute of Technology	<i>Pasadena, CA</i>
Undergraduate Research Assistant	2017–2019
University of Notre Dame	<i>South Bend, IN</i>

TEACHING EXPERIENCE

Teaching Assistant	2019–2025
University of California, Los Angeles	<i>Los Angeles, CA</i>
Teaching Assistant	2018–2019
University of Notre Dame	<i>South Bend, IN</i>

REFEREED JOURNAL PUBLICATIONS

Judah Van Zandt and 42 colleagues (2025). The TESS-Keck Distant Giants Survey XXIV: Outer Giants May be More Prevalent in the Presence of Inner Small Planets. *The Astronomical Journal*, 169(5):235

Lubin, J., Petigura, E. A., **Judah Van Zandt**, and 25 colleagues (2024a). The HD 191939 Exoplanet System is Well Aligned and Flat. *The Astronomical Journal*, 168(5):196

Judah Van Zandt and Petigura, E. A. (2024b). No Evidence for a Metallicity-dependent Enhancement of Distant Giant Companions to Close-in Small Planets in the California Legacy Survey. *The Astronomical Journal*, 168(6):268

Judah Van Zandt and Petigura, E. A. (2024a). ethraid: A Simple Method for Characterizing Long-period Companions Using Doppler, Astrometric, and Imaging Constraints. *The Astronomical Journal*, 167(6):250

Judah Van Zandt and 44 colleagues (2023). TESS-Keck Survey. XIV. Two Giant Exoplanets from the Distant Giants Survey. *The Astronomical Journal*, 165(2):60

Lubin, J., **Judah Van Zandt**, and 34 colleagues (2022a). TESS-Keck Survey. IX. Masses of Three Sub-Neptunes Orbiting HD 191939 and the Discovery of a Warm Jovian plus a Distant Substellar Companion. *The Astronomical Journal*, 163(2):101. [\[ADS\]](#)

Chontos, A., Akana Murphy, J. M., MacDougall, M. G., Fetherolf, T., **Judah Van Zandt**, and 26 colleagues (2022a). The TESS-Keck Survey: Science Goals and Target Selection. *The Astronomical Journal*, 163(6):297. [\[ADS\]](#)

Polanski, A. S. and 72 colleagues, including **Judah Van Zandt** (2024). The TESS-Keck Survey. XX. 15 New TESS Planets and a Uniform RV Analysis of All Survey Targets. , 272(2):32

Chapter 1

Introduction

The unexamined life is not worth living.

— Socrates, Plato's *Apology*

For thousands of years, humans have looked to the sky to understand the mechanisms governing the Universe. The Ancients developed speculative models of the Solar System that persisted for centuries; natural philosophers of the Renaissance hypothesized that stars in the night sky were themselves "suns" hosting planets of their own; and just 30 years ago, two Swiss astronomers discovered the first extrasolar planet orbiting a Sun-like star (Mayor and Queloz, 1995). This monumental detection not only ushered in a new era of exoplanet discovery, it also demonstrated that the fundamental processes that created the Solar System — and perhaps those that gave rise to life on Earth — obtain elsewhere in the Universe.

Since 1995, nearly 6000 exoplanets have been discovered,¹ spanning a vast range of masses, orbital separations, and compositions. This expansive pool has facilitated the study of whole planetary subgroups, a field known as exoplanet demographics. My thesis centers on the relationship between two of these subgroups: small planets with short orbital periods,

¹<https://exoplanetarchive.ipac.caltech.edu/>

and giant planets at wider separations. Both of these archetypes are represented in the Solar System, and their preference for (or aversion to) forming in the same environment could indicate whether our system’s configuration is a typical one. In the remainder of this chapter, I review the study of exoplanets and contextualize my thesis work. The bulk of my thesis consisted of a three-year observational search for giant planets in a sample of 47 Sun-like stars hosting close-in small planets. This survey resulted in the discovery of three new giant exoplanets, as well as numerous partial orbit signals whose causes are uncertain. I introduce the survey and the two planet discoveries in Chapter 2, and I present an original computational tool, `ethraid`, designed to fit the partial orbits in Chapter 3. I independently tested another study’s claim that the relationship between long-period giants and inner small planets is heavily dependent on host star properties. Repeating their analysis, I found this claim to be unreliable (Chapter 4). Finally, I synthesize the results of my survey in Chapter 5, incorporating both full and partial orbit detections into a statistical measurement of the prevalence of Solar System analogs.

1.1 Exoplanet Discovery

Mankind’s understanding that stars are alike to our own Sun, and therefore might have planets orbiting them, was hindered by a combination of philosophical and religious views that held sway from the Hellenistic period of Ancient Greece (c. 323–146 B.C.) well into the Renaissance. Under the geocentric view of Aristotle (384–322 B.C.), the Sun was of secondary importance to the Earth, both metaphysically and dynamically. The idea that other stars possessed earths of their own contravened Earth’s privileged position in the Cosmos. The philosophical arguments for Aristotelianism were eventually challenged by Nicolaus Copernicus (1473–1543), who posited a heliocentric model to more accurately predict the motions of the Solar System bodies. Expanding on these ideas, Giordano Bruno (1548–1600) made

bold assertions about the nature of the Universe, chiefly that it is infinite, and that the stars which suffuse it are indeed like the Sun, are orbited by planets like Earth, and that those planets are teeming with complex lifeforms. Whereas Copernicus had been careful to couch his claims in theoretical terms, Bruno's unapologetic contradiction of Catholic scriptural interpretation drew the ire of the Roman Inquisition, and he was burned at the stake as a heretic.

The existence of exoplanets remained speculative for the next few centuries due to limitations in observational precision. In 1938, David Belorizky suggested that the shadows cast by Jupiter-size planets passing in front of their host stars could be detected by state-of-the-art photoelectric cells, but remarked that such planets were too dim to be imaged directly, and caused too minuscule a change in their host stars' motion for spectrographs to detect (Belorizky, 1938). Over a decade later, Otto Struve reaffirmed Belorizky's proposed photometric approach, adding that massive planets with short orbital periods "might be just detectable" with the most powerful spectrographs available (Struve, 1952).

The photometric and spectroscopic detection methods described by Belorizky and Struve are known as the transit and radial velocity (RV) techniques, respectively. The transit technique measures the periodic dimming of a star as a passing planet blocks a portion of its emitted light. The fraction of blocked light is roughly equal to the ratio of the areas of the planetary and stellar disks:

$$\Delta F = F \left(\frac{R_p}{R_\star} \right)^2,$$

where R_p and R_\star are the radii of the planet and star, respectively, F is the stellar flux received by the unobstructed stellar disk, and ΔF is the "dip" in brightness during transit.

Jupiter, with a radius one tenth that of the Sun, would produce a 1% brightness dip for a distant observer, while Earth would block only 0.01% of the Sun's light.

The RV technique measures the periodic Doppler shift of a stellar spectrum toward bluer or redder wavelengths induced by the gravitational pull of an unseen orbiting planet. The magnitude of this shift is dependent on the planetary and stellar masses, as well as the planetary orbital separation, a :

$$RV \propto \frac{M_p \cdot \sin i}{\sqrt{a \cdot M_\star}}.$$

Unlike the transit method, RVs are sensitive to the planet-star separation. Thus, while Jupiter produces RV fluctuations in the Sun of ~ 13 m/s, a "hot Jupiter" of the same mass but at much closer separation might produce fluctuations of over 100 m/s. Meanwhile, Earth's tug on the Sun yields a diminutive 9 cm/s RV. Note that the strength of the RV signal depends also on the planet's orbital inclination i , where $i = 90^\circ$ indicates an "edge-on" orbit from the perspective of a terrestrial observer. The transit signal depends on inclination as well — a planet with i significantly different from 90° will not transit at all. Broadly, planets that create larger flux dips in photometric data, or that induce larger RV shifts in spectroscopic data, are easier to detect. Today, these two methods are responsible for over 90% of all exoplanet discoveries.

Throughout the 1980s, astronomers used RV observations to probe ever-smaller oscillations in stellar motion, beginning with searches for binary star systems (e.g. [Mayor et al. 1984](#); [Latham et al. 1984](#)), and achieving sensitivity to objects intermediate between stellar and planetary mass, known as brown dwarfs ([Latham et al., 1989](#)).² By the end of the decade,

²HD 114762 b, discovered by [Latham et al. \(1989\)](#), had a minimum mass of $M \sin i \sim 11 M_{\text{Jup}}$, but three-dimensional constraints from the Gaia mission showed that this object is in fact a highly inclined stellar companion ([Kiefer, 2019](#)).

multiple teams had come tantalizingly close to discovering a true exoplanet. In 1988, a Canadian team presented six years of RV data for 12 Sun-like stars with a precision of 13 m/s, but found no dispositive evidence for planetary companions (Campbell et al., 1988).

The next decade saw multiple revolutionary discoveries. The first exoplanets ever detected were found around a millisecond pulsar through the perturbations they introduced in the pulsar’s highly regular emission pattern (Wolszczan and Frail, 1992). A few years later, Mayor and Queloz (1995) announced their RV discovery of 51 Pegasi b, a hot Jupiter with $M_p = 0.4 M_J$ and a four-day orbital period, and the first exoplanet found around a main sequence star. Over the next five years, two dozen more giant exoplanets were discovered using RVs (e.g. Marcy and Butler 1996; Cochran et al. 1997; Butler et al. 1997, 1999), although doubt remained as to the planetary nature of these objects, owing to the RV method’s vulnerability to highly inclined orbits. Yet another breakthrough came with the first confirmation of an RV-detected planet using the transiting method, HD 209458 b (Henry et al., 2000; Charbonneau et al., 2000). Transiting planets have edge-on orbits, ruling out the possibility of an inclined star or brown dwarf. Further, transit observations provide a measurement of planet radius which, together with measured mass from RVs, can constrain the planetary bulk composition.

Both the transit and RV methods enjoyed massive success in the first decade of the 21st century, with the number of transit discoveries exploding after the launch of the spaceborne *Kepler* satellite in 2009. *Kepler* discovered about 4000 exoplanets, and its successor, NASA’s *TESS* mission, has contributed over 600 exoplanet discoveries of its own since launching in 2018. In the meantime, ground-based observatories have amassed over 1000 RV detections, with current spectrographs nearly sensitive enough to detect Earth analogs. The development of other techniques led to hundreds of further discoveries. For example, gravitational microlensing — the transient brightening of a background source due to the bending of light around a foreground system in accordance with general relativity — and direct imag-

ing — the detection of self-luminous planets without recourse to the influence they exert on their host stars — each announced their first planetary detections in 2004 (Bond et al., 2004; Chauvin et al., 2004), and have together produced over 300 more exoplanet discoveries since. The current census of exoplanets, shown in Figure 1.1, exhibits a rich diversity of properties, and has grown large enough to allow for the identification and comparison of different exoplanet classes.

1.2 Exoplanet Demographics

The discovery of thousands of exoplanets over the last 30 years has enabled nuanced investigation of planets not only as individuals, but as populations. Among the most striking results from the *Kepler* mission are that planets between the size of Earth and Neptune ($R_p \sim 1 - 4 R_{\text{Earth}}$) and with orbital periods less than one year occur around most stars in our galaxy (Petigura et al., 2013, 2018); that these planets exhibit a bimodal radius distribution, with relatively few planets having $R_p = 1.5 - 2 R_{\text{Earth}}$ (Fulton et al., 2017); and that planets in the same system tend to have uniform sizes and orbital spacings (Weiss et al., 2018; Millholland and Winn, 2021).

Meanwhile, RV surveys have constrained the occurrence rate of Jupiter analogs as a function of orbital period and host star properties. Gas giants are more common around more massive stars (e.g. Johnson et al. 2010, 2012) and stars with high abundances of heavy elements (Fischer and Valenti, 2005a). The hot Jupiters seen in the upper left corner of Figure 1.1 are intrinsically rare ($\sim 1\%$ occurrence rate; Marcy et al. 2005a; Wittenmyer et al. 2020), but overrepresented in our detections due to the large signals they produce.³ By comparison, cold Jupiters are fairly common around Sun-like stars ($\sim 10\text{--}20\%$; Cumming et al. 2008;

³It is worth noting that the scarcity of hot Jupiters was a key factor in the non-detection of planets by Campbell et al. (1988), who otherwise had ample RV precision and baseline to make such a detection. Had they chanced to include a hot Jupiter-hosting star in their sample, they would likely have discovered the first exoplanet.

Wittenmyer et al. 2016; Rosenthal et al. 2022).

My thesis focuses on the relationship between two well-studied classes of planets: the small planets with short periods found in abundance by *Kepler*, and the long-period Jupiter analogs found primarily by RV surveys. Although the Solar System’s terrestrial planets and gas giants do not fit neatly into these categories, generally having longer periods and smaller masses (see Figure 1.1), the close-in small planets and distant giants nevertheless serve as useful analogs to understand the Solar System’s formation and development.

Owing to the distinct observing strategies employed to discover these planets (*Kepler* continuously observed both nearby and distant stars in a single patch of the sky for four years, while RV surveys targeted nearby bright stars over the full sky), the stars searched for transiting planets by *Kepler* and those searched for outer giants are essentially disjoint. As a result, these two populations cannot help us determine whether outer giants are more, less, or equally common in systems with an inner planet as they are around a typical FGK star. The prevalence of these giants in systems with a known inner planet, called the conditional occurrence rate, quantifies the correlation between these two classes, and could potentially hint at causal links that govern their joint formation. Multiple early studies of conditional occurrence returned similar results: giant planets are more prevalent in systems with a close-in small planet Zhu and Wu (2018); Bryan et al. (2019); Rosenthal et al. (2022). However, these studies lacked the benefit of a uniform target pool with high sensitivity to small planets. This limitation variously affected sample size, purity, or both.

NASA’s *TESS* mission provided the missing link between inner small planets and outer giants by searching for transiting planets around the same bright, nearby stars that can be observed with RVs. The thousands of transiting planet candidates delivered by *TESS* served as an ideal pool from which to construct a homogeneous survey. I compiled a sample of stars with inner planets detected by *TESS* and used it to carry out a three-year RV search for outer giants, ultimately finding that giant planets are indeed more common in systems with

a close-in small planet than around a random Sun-like star by a factor of ~ 2 (Van Zandt et al., 2025). This result agrees with theoretical models predicting that exoplanets form in place out of the metal-rich material in the protoplanetary disk (Hansen and Murray, 2012; Chiang and Laughlin, 2013), and the dynamical relationships I observed further hint that giant planets may interact with their diminutive siblings after they have formed.

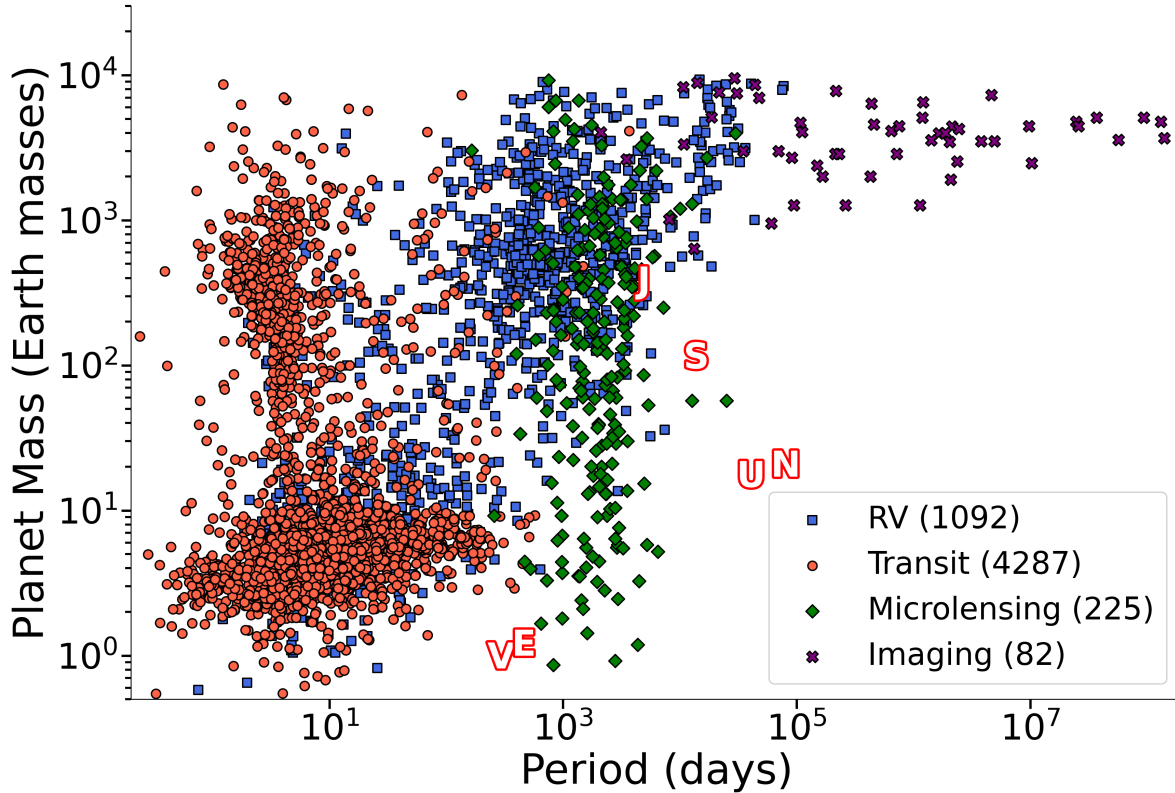


Figure 1.1: Exoplanets discovered by the four most popular detection techniques as of March 2025. Method-specific biases are evident: the transit technique (red circles) excels at detecting short-period planets due to their higher transit probability; RVs (blue squares) are sensitive to close-in planets, but are well-suited to detecting giant planets at wide separations; gravitational microlensing (green diamonds) can detect a wide range of planet masses, but is limited to a relatively narrow range of periods by the requirement of favorable lensing geometry; and direct imaging (purple x's) enables the detection of high-mass planets at very wide separations around young stars. The legend gives the number of planet detections using each technique. We estimated the masses of transiting planets for which the mass was unknown using the mass-radius relationship of [Weiss and Marcy \(2014\)](#). The parameters of Venus, Earth, Jupiter, Saturn, Uranus, and Neptune are shown with their initials, demonstrating our low sensitivity to most Solar System planets across all methods.

Chapter 2

TESS-Keck Survey XIV: Two giant exoplanets from the Distant Giants Survey

A version of this chapter was previously published in *The Astronomical Journal* (Judah Van Zandt et al., 2023, AJ 165, 2, 60).

Abstract

We present the Distant Giants Survey, a three-year radial velocity (RV) campaign to measure $P(\text{DG}|\text{CS})$, the conditional occurrence of distant giant planets (DG; $M_p \sim 0.3 - 13 M_J$, $P > 1$ year) in systems hosting a close-in small planet (CS; $R_p < 10 R_\oplus$). For the past two years, we have monitored 47 Sun-like stars hosting small transiting planets detected by TESS. We present the selection criteria used to assemble our sample and report the discovery of two distant giant planets, TOI-1669 b and TOI-1694 c. For TOI-1669 b we find

that $M \sin i = 0.573 \pm 0.074 M_J$, $P = 502 \pm 16$ days, and $e < 0.27$, while for TOI-1694 c, $M \sin i = 1.05 \pm 0.05 M_J$, $P = 389.2 \pm 3.9$ days, and $e = 0.18 \pm 0.05$. We also confirmed the 3.8-day transiting planet TOI-1694 b by measuring a true mass of $M = 26.1 \pm 2.2 M_\oplus$. At the end of the Distant Giants Survey, we will incorporate TOI-1669 b and TOI-1694 c into our calculation of $P(\text{DG}|\text{CS})$, a crucial statistic for understanding the relationship between outer giants and small inner companions.

2.1 Introduction

The past 30 years of exoplanet discovery have revealed a variety of distinct planet classes. The most abundant of these discovered to date around Sun-like stars are between the size of Earth and Neptune with orbital periods of a year or less. Statistical analyses of Kepler data (Borucki et al., 2010) have shown that such planets occur at a rate of ~ 1 per star (see, e.g., Petigura et al. (2018)). Meanwhile, ground-based radial velocity (RV) surveys (e.g., Rosenthal et al. 2022; Cumming et al. 2008; Fischer et al. 2014; Wittenmyer et al. 2016) report that long-period ($P \gtrsim 1$ year) giant planets are somewhat rare, orbiting $\sim 5\text{-}20\%$ of Sun-like stars. However, the distinct observing strategies employed by Kepler versus RV surveys produced stellar samples with little overlap. On the one hand, Kepler continuously monitored $> 10^5$ stars along a fixed line of sight; the typical planet host in this sample is 600 parsecs from Earth with a brightness of $V = 14$. By contrast, ground-based RV surveys have targeted bright, nearby stars that are distributed roughly evenly on the sky; the typical planet host in this sample is 40 parsecs from Earth with a brightness of $V = 8$. Because the inner transiting planets mostly discovered by Kepler and the outer giants mostly discovered by RVs are drawn from nearly disjoint stellar samples, the connection between them is unclear.

Current planet formation models differ on whether the processes that produce long-period

gas giants and close-in small planets are positively or negatively correlated. Strict in-situ models (e.g., [Chiang and Laughlin 2013](#)) predict that the metal-rich protoplanetary disks known to facilitate gas giant formation ([Fischer and Valenti, 2005b](#); [Mordasini et al., 2009](#)) also promote the growth of sub-Jovian cores at close separations. On the other hand, models involving significant planetary migration predict an *anti*-correlation, where nascent planetary cores either 1) develop beyond the ice line and are blocked from inward migration by newly-formed giants at a few AU ([Izidoro et al., 2015](#); [Izidoro and Raymond, 2018](#)), or 2) develop close in and are driven into their host star by inward giant planet migration ([Batygin and Laughlin, 2015](#)).

Recent observational works have directly estimated the conditional occurrence of distant giant companions to close-in small planets, $P(\text{DG}|\text{CS})$. [Zhu and Wu \(2018\)](#) and [Bryan et al. \(2019\)](#), hereafter Z18 and B19, respectively, each analyzed archival RV data for systems with super-Earths. Z18 estimated $P(\text{DG}|\text{CS}) \approx 30\%$ using the following procedure: first, they counted the known systems with a Sun-like host, at least one inner super-Earth ($R_p < 4 R_\oplus$, $P < 400$ days) and an RV baseline > 1 year; then they divided the number of these systems reported to host a distant giant by the total. B19 estimated $P(\text{DG}|\text{CS}) = 39 \pm 7\%$ using a similar procedure. They selected systems with at least one confirmed super-Earth and at least 10 RVs over 100 days. Unlike Z18, they re-fit those RVs using `radvel` ([Fulton et al., 2018](#)) to search for unknown companions, considering both full and partial orbits. Both analyses indicate a factor of ~ 3 – 4 enhancement over the field occurrence rate, but are vulnerable to systematic biases due to their loosely-defined target selection functions and heterogeneity of RV time series (quality, sampling strategy, and baseline). In particular, Z18 and B19 selected targets where significant RV baselines had already been collected by other surveys. However, earlier studies may have chosen their RV targets based on a variety of criteria, including an increased probability of hosting planets. The aggregation of RV targets from separate studies may bias the associated planet populations, and because Z18 and B19 did not address these factors on a target-by-target basis, the extent to which this bias may

have influenced their final results is unclear.

A more uniform analysis was carried out as part of the California Legacy Survey (CLS; Rosenthal et al. 2022). The CLS sample consists of 719 Sun-like stars with similar RV baselines and precisions, and chosen without bias toward stars with a higher or lower probability of hosting planets. Furthermore, Rosenthal et al. (2022) performed a uniform iterative search for periodic signals in each RV time series using the `rvsearch` package (Rosenthal et al., 2021), recovering populations of both inner small planets (0.023 – 1 AU, 2 – 30 M_{\oplus}) and outer giants (0.23 – 10 AU, 30 – 6000 M_{\oplus}). The authors measured a conditional occurrence of $P(\text{DG}|\text{CS})=41\pm 15\%$. Although this value is consistent with the findings of both Z18 and B19, Rosenthal et al. (2022) also found a prior distant giant occurrence of $P(\text{DG})=17.6\pm 2.2\%$, meaning that their conditional occurrence is $\sim 1.6\sigma$ separated from a null result.

We present the Distant Giants Survey, a three-year RV survey to determine $P(\text{DG}|\text{CS})$ in a sample of Sun-like transiting planet hosts from the TESS mission (Ricker et al., 2015).¹ In designing our survey, we took care to construct a uniform stellar sample to avoid bias against or in favor of stars that host outer giant planets. We also applied a single observing strategy to achieve uniform planet sensitivity across our sample. Since beginning the survey in mid 2020, we have found evidence for 11 outer companions, both as resolved (i.e., complete) orbits and long-term trends. Distant Giants is part of the larger TESS-Keck Survey (TKS; Chontos et al. 2022b), a multi-institutional collaboration to explore exoplanet compositions, occurrence, and system architectures (see, e.g., Dalba et al. 2020, Weiss et al. 2021, Rubenzahl et al. 2021).

¹Because our survey requires that all systems host a transiting inner planet, we are actually constraining the conditional occurrence of distant giant companions to *transiting* close-in small ones. However, we expect the population of stars with transiting inner small planets to host outer giants at the same rate as stars hosting inner planets irrespective of a transiting geometry. On the other hand, if systems hosting both planet types tend to be coplanar, we will have greater RV sensitivity to giants in transiting systems. We will account for the resulting bias in detail in our statistical analysis.

In this paper, we introduce the Distant Giants Survey and highlight two new giant planets, TOI-1669 b and TOI-1694 c, detected in our sample. In Section 2.2, we describe the Distant Giants Survey as a whole, including our target selection process, observing strategy, and procedure for obtaining precise RVs from Keck-HIRES. Sections 2.3 and 2.4 detail our analysis of TOI-1669 and TOI-1694, including our RV model and the properties of the planets in each system. In Section 2.5, we discuss our findings. In Section 2.6, we summarize our results and outline future work.

2.2 Distant Giants Survey Design

2.2.1 Target Selection

Our ability to draw robust statistical conclusions from the Distant Giants Survey relies critically on the assembly of a well-defined stellar sample. We designed our target selection criteria to yield a sample of Sun-like stars hosting at least one small transiting planet found by TESS. We also required that all targets be amenable to precise RV follow-up from the northern hemisphere. To impose these criteria, we began with the master target list produced by Chontos et al. (2022b), which contains 2136 individual TESS Objects of Interest (TOIs) among 2045 planetary systems. We then applied the following sets of filters:

1. *Photometric and astrometric measurements.* To allow for efficient observation from the Northern Hemisphere, we required that all stars have $\delta > 0^\circ$ and $V < 12.5$, where δ is the declination and V is the V-band magnitude. We excluded stars with a *Gaia* Renormalized Unit Weight Error (RUWE; Lindegren et al. 2018, Lindegren et al. 2021) greater than 1.3 to ensure precise fits to *Gaia*'s 5-parameter astrometric model. $\text{RUWE} < 1.2$ is a conservative limit to exclude binary systems mis-classified as single sources (Bryson et al. 2020, A. Kraus et al. in preparation). All but one target in

the Distant Giants sample satisfy $\text{RUWE} < 1.2$, implying a low probability that we included any unwanted binary systems. We chose an upper bound of $10 R_{\oplus}$ on the transiting planet radius. In the event that a star hosted multiple transiting planets, we required that at least one meet our planet size requirement. These cuts reduced the target pool from 2045 to 147 systems.

2. *Data Quality.* We evaluated transit quality using TESS data validation (DV) reports retrieved from the TOI Catalog in July 2020. To ensure high-significance transits, we only included TOIs with at least one light curve produced by the TESS Science Processing Operations Center pipeline (SPOC, [Jenkins et al. 2016](#)). Furthermore, we used the Multiple Event Statistic (MES, [Jenkins 2002](#)), a proxy for the signal-to-noise ratio (SNR), to evaluate transit quality. After visual inspection of a subset of SPOC transit fits, we found that $\text{MES} = 12$ was a suitable lower limit for identifying compelling detections. We also excluded targets with close visual companions, which we defined as companions within $4''$ and 5 V-band magnitudes. These filters further reduced the pool from 147 to 67 systems.
3. *Inactive and slowly-rotating stars.* We used `SpecMatch` ([Petigura et al., 2017](#)) to analyze each target's "template" spectrum (§2.2.3). `SpecMatch` interpolates over a grid of synthetic stellar spectra to estimate stellar parameters such as effective temperature T_{eff} , projected rotational velocity $v \sin(i)$, surface gravity $\log g$, and metallicity $[\text{Fe}/\text{H}]$. For stars cooler than 4700 K, we used `SpecMatch-Emp` ([Yee et al., 2017](#)) to interpolate over real spectra of K and M dwarfs, which are more reliable than model spectra at low temperatures. We excluded rapidly rotating stars ($v \sin(i) > 5$ km/s), as well as those with T_{eff} above the Kraft break (~ 6250 K); such stars offer limited RV precision due to Doppler broadening ([Kraft, 1967](#)). We also derived stellar mass according to the methods of [Fulton and Petigura \(2018\)](#), and selected only main sequence stars between 0.5 and $1.5 M_{\odot}$, consistent with our solar analog requirement.

We measured each star’s chromospheric activity through its $\log R'_{\text{HK}}$ index (Isaacson and Fischer, 2010; Noyes et al., 1984). This value quantifies the emission in the cores of the Calcium II H and K lines relative to the total bolometric emission of the star, with higher core emission corresponding to enhanced activity and therefore greater RV variability in the epoch that the activity is measured. We required that $\log R'_{\text{HK}} < -4.7$. This limit, adopted from Howard et al. (2010b), restricts our sample to ‘inactive’ and ‘very inactive’ stars, as defined by Henry et al. (1996). We note that restricting $\log R'_{\text{HK}}$ and $v \sin(i)$ introduces a bias toward older stars due to the correlations between age and both Calcium H and K line emission and rotation speed (e.g., Soderblom et al. 1991; Noyes et al. 1984). We retained these filters to ensure RV quality, and will account for the associated bias in our final results.

We applied this $\log R'_{\text{HK}}$ filter using available activity values in mid-2020, but because stellar activity is variable, some of our targets fluctuate above the $\log R'_{\text{HK}} = -4.7$ limit. Furthermore, two targets, TOI-1775 and TOI-2088, did not have available activity values at the time we applied this filter. They were thus not excluded based on activity, and we retained them in the sample. Since then, we have found $\log R'_{\text{HK}} = -4.72$ for TOI-2088 and -4.28 for TOI-1775. Knowing that TOI-1775 fails our $\log R'_{\text{HK}}$ cut, we will carefully monitor its activity against any signals that develop in the RVs. Of the remaining 67 systems, 48 passed these filters. Due to time constraints, 47 of these were selected for TKS by the target prioritization algorithm detailed in Chontos et al. (2022b). The filters of both Distant Giants and TKS are given in Table 2.1.

From the original set of 2045 TOI-hosting systems, 86 were ultimately selected for TKS and 47 were selected for Distant Giants. The final Distant Giants sample is given in Table 2.2, and we summarize key stellar and planetary parameters of both Distant Giants and TKS in Figure 2.1.

Table 2.1: Survey Criteria

Parameter	TKS	Distant Giants Survey		
		Photometric	Manual	Spectroscopic
Declination	$> -30^\circ$	$> 0^\circ$	—	—
V	< 13.0	< 12.5	—	—
Evolutionary State	MS or SG	MS	—	—
RUWE	< 2	< 1.3	—	—
R_p	$< 22 R_\oplus$	$< 10 R_\oplus$	—	—
Transit Pipeline	—	—	SPOC	—
Detection Significance	SNR > 10	—	MES > 12	—
Close Companion	$\Delta V > 5$ or sep $> 2''$	—	$\Delta V > 5$ or sep $> 4''$	—
M_\star	—	—	—	$0.5 M_\odot < M_\star < 1.5 M_\odot$
T_{eff}	< 6500 K	—	—	< 6250 K
$v \sin i$	—	—	—	< 5.0 km/s
$\log R'_{\text{HK}}$	—	—	—	< -4.7

Note: Filters applied to 2045 TESS systems to produce the Distant Giants sample. TKS filters are taken from [Chontos et al. \(2022b\)](#). Although other filters were applied to produce the TKS sample, we show only those used in our survey’s target selection process. MS and SG refer to main sequence and subgiant stars, respectively.

Table 2.2: Distant Giants Sample

TOI	CPS Name	V	RA (deg)	Dec (deg)	$R_p (R_\oplus)$	P (days)
465	WASP156	11.6	32.8	2.4	5.6	3.8
509	63935	8.6	117.9	9.4	3.1	9.1
1173	T001173	11.0	197.7	70.8	9.2	7.1
1174	T001174	11.0	209.2	68.6	2.3	9.0
1180	T001180	11.0	214.6	82.2	2.9	9.7
1194	T001194	11.3	167.8	70.0	8.9	2.3
1244	T001244	11.4	256.3	69.5	2.4	6.4
1246	T001246	11.6	251.1	70.4	3.3	18.7
1247	135694	9.1	227.9	71.8	2.8	15.9
1248	T001248	11.8	259.0	63.1	6.6	4.4
1249	T001249	11.1	200.6	66.3	3.1	13.1
1255	HIP97166	9.9	296.2	74.1	2.7	10.3
1269	T001269	11.6	249.7	64.6	2.4	4.3

(Continued on next page)

(Continued from previous page)

TOI	CPS Name	V	RA (deg)	Dec (deg)	$R_p (R_{\oplus})$	P (days)
1272	T001272	11.9	199.2	49.9	4.3	3.3
1279	T001279	10.7	185.1	56.2	2.6	9.6
1288	T001288	10.4	313.2	65.6	4.7	2.7
1339	191939	9.0	302.0	66.9	3.2	8.9
1410	T001410	11.1	334.9	42.6	2.9	1.2
1411	GJ9522A	10.5	232.9	47.1	1.4	1.5
1422	T001422	10.6	354.2	39.6	3.1	13.0
1437	154840	9.2	256.1	56.8	2.4	18.8
1438	T001438	11.0	280.9	74.9	2.8	5.1
1443	T001443	10.7	297.4	76.1	2.1	23.5
1444	T001444	10.9	305.5	70.9	1.3	0.5
1451	T001451	9.6	186.5	61.3	2.5	16.5
1469	219134	5.6	348.3	57.2	1.2	3.1
1471	12572	9.2	30.9	21.3	4.3	20.8
1472	T001472	11.3	14.1	48.6	4.3	6.4
1611	207897	8.4	325.2	84.3	2.7	16.2
1669	T001669	10.2	46.0	83.6	2.2	2.7
1691	T001691	10.1	272.4	86.9	3.8	16.7
1694	T001694	11.4	97.7	66.4	5.5	3.8
1710	T001710	9.5	94.3	76.2	5.4	24.3
1716	237566	9.4	105.1	56.8	2.7	8.1
1723	T001723	9.7	116.8	68.5	3.2	13.7
1742	156141	8.9	257.3	71.9	2.2	21.3
1751	146757	9.3	243.5	63.5	2.8	37.5
1753	T001753	11.8	252.5	61.2	3.0	5.4
1758	T001758	10.8	354.7	75.7	3.8	20.7
1759	T001759	11.9	326.9	62.8	3.2	37.7
1773	75732	6.0	133.1	28.3	1.8	0.7
1775	T001775	11.6	150.1	39.5	8.1	10.2
1794	T001794	10.3	203.4	49.1	3.0	8.8
1797	93963	9.2	162.8	25.6	3.2	3.6
1823	TIC142381532	10.7	196.2	63.8	8.1	38.8
1824	T001824	9.7	197.7	61.7	2.4	22.8

Note: Properties of the 47 stars in the Distant Giants sample, plus the periods and radii of their inner companions. For multi-transiting systems, we checked planets in the order that TESS detected them, and show the properties of the first one that passed the filters in Table 2.1. Period precisions are truncated for readability. Median uncertainties are as follows: R_p —9.6%; P—60 ppm. Values retrieved from Chontos et al. (2022b).

2.2.2 Observing Strategy

We tailored the Distant Giants observing strategy to planets with periods $\gtrsim 1$ year and masses above $\sim 100 M_\oplus$. Such planets require neither high observing cadence nor high SNR to detect; however, they do require a longer observing baseline than shorter-period planets. In order to maximize Distant Giants’s sensitivity to long-period planets within a fixed telescope award, we traded observational cadence and precision for a greater survey duration and target pool. We adopted the following observing strategy: we obtain one observation per target per month. We use the HIRES exposure meter to obtain a minimum SNR of 110 per reduced pixel on blaze at 5500 Å. The procedure we use to derive radial velocities and uncertainties from raw spectra is described in Butler et al. (1996). The ~ 800 spectra we have collected for Distant Giants targets at this SNR have a median statistical uncertainty of 1.7 m/s. Adding our statistical uncertainties in quadrature with the ~ 2 m/s instrumental noise floor of HIRES (Fulton, 2017a), we estimate a typical RV uncertainty of 3 m/s. We are conducting monthly observations of each target until we have attained 30 observations over 3 years; the six-month surplus compensates for weather losses and target observability seasons. This baseline will allow us to resolve the full orbits of planets with orbital periods $\lesssim 3$ years and sense partial orbits of longer-period companions. Although our sample includes a few legacy RV targets with multi-decade baselines (Fischer et al. 2014, Rosenthal et al. 2021), uniform observation of the Distant Giants sample began near mid-

2020. The observing baselines of our full sample over a 200-day period are shown in Figure 2.2.

For targets brighter than $V = 10$, we also obtain observations with the Levy spectrograph on the 2.4-meter Automated Planet Finder telescope (APF, Vogt et al. 2014). However, because most of our targets are too dim to benefit from APF observations, we maintain monthly cadence with Keck/HIRES for all targets. This will allow us to analyze our final time series both with and without APF RVs to avoid biasing our planet sensitivity toward brighter stars.

2.2.2.1 Existing Observations

Our target selection process was agnostic to observations collected before the beginning of the survey, which many of our targets possess. After assembling our sample, we examined each target’s observing history to determine whether any prior observations could be applied to our survey. We identified three types of systems in our sample:

1. *No existing baseline.* 28 targets did not have any useful RV baseline before the beginning of the survey. For our purposes, a useful baseline consisted of observations meeting or exceeding our requirements of monthly cadence and SNR=110, leading up to \sim July 2020. We have maintained at least monthly cadence for these targets since Distant Giants began. One of these targets, HD 207897, has RVs as early as 2003, but monthly monitoring only began with our survey.
2. *Partial existing baseline.* 17 targets already possessed a useful RV baseline before the beginning of the survey. These targets will reach their observation quota before those in the subset above.
3. *Finished prior to the survey.* 2 targets, HD 219134 and HD 75732, passed all the cuts in

Section 2.2.1 and had already received 30+ observations over 3+ years at the beginning of the survey. We therefore include them in our sample and statistical analysis, but do not obtain further observations. We emphasize that although both HD 219134 and HD 75732 are known to host outer companions, this had no influence on their inclusion in our sample. Had any legacy RV targets exhibiting *non*-detections passed our cuts, they would have been selected as well.

2.2.2.2 Surplus Observations and/or Baseline

Because our survey is carried out under the broader umbrella of TKS, a subset of our targets are observed according to other science objectives with higher cadence requirements. We found that 25 of our selected targets receive more than one observation per month on average, and thus have a greater sensitivity to planets than the remainder of our sample. These systems will require special consideration in our final statistical analysis to correct for their higher planet sensitivity.

In addition to surplus cadence, HD 219134 and HD 75732 have useful RV baselines of nearly 30 years. Their long-period giants, HD 219134 g and HD 75732 d (5.7 years and 14.4 years, respectively), might not have been detectable using the Distant Giants observing strategy. Our prior knowledge of these planets highlights the importance of completeness corrections to account for long-period companions missed due to insufficient observing baseline and/or cadence. Moreover, our detections of HD 219134 g and HD 75732 d will help to characterize completeness in the rest of our systems.

2.2.3 RV Observations

We take RV observations according to the standard procedure of the California Planet Search (CPS; Howard et al. 2010a). We use the HIRES spectrometer (Vogt et al., 1994) coupled to the Keck I Telescope to observe all Distant Giants targets. We place a cell of gaseous iodine in the light path to project a series of fiducial absorption lines onto the stellar spectrum. These references allow us to track the instrumental profile and precisely wavelength-calibrate the observed spectra. For each star, we collected a high SNR iodine-free "template" spectrum. The template, together with the instrumental point-spread function (PSF) and iodine transmission function, is a component of the forward model employed by the CPS Doppler analysis pipeline (Howard et al. 2010a; Butler et al. 1996).

In the first two years of our survey, we resolved the full orbits of giant planets in two of our 47 systems: TOI-1669 and TOI-1694. Although two more systems, HD 219134 and HD 75732, host resolved companions, these planets were detected using hundreds of RVs over multi-decade baselines; further analysis is needed to determine whether they would have been detectable using our observing strategy alone. Finally, seven systems show non-periodic RV trends. We discuss these trends briefly in the conclusion to this paper (§2.6) and will treat them fully in future work. The parameters of the companions in the four resolved systems are given in Table 2.3, and their stellar parameters are given in Table 2.4.

2.2.4 *TESS* Detections of TOI-1669.01 and TOI-1694 b

The SPOC conducted a transit search of Sector 19 on 17 January 2020 with an adaptive, noise-compensating matched filter (Jenkins, 2002; Jenkins et al., 2010, 2020), detecting a transit crossing event (TCE) for TOI-1669. An initial limb-darkened transit model was fitted to this signal (Li et al., 2019) and a suite of diagnostic tests were conducted to evaluate whether it was planetary in nature (Twicken et al., 2018). The transit signature was also

detected in a search of Full Frame Image (FFI) data by the Quick Look Pipeline (QLP) at MIT (Huang et al., 2020a,b). The TESS Science Office (TSO) reviewed the vetting information and issued an alert on 29 January 2020 (Guerrero et al., 2021). The signal was repeatedly recovered as additional observations were made in sectors 20, 25, 26, 52, and 53, and the transit signature of TOI-1669.01 passed all the diagnostic tests presented in the DV reports. The source of the transit signal was localized within 4.925 ± 4.5 arcseconds of the host star.

The transit signature of TOI-1694 b was identified in a SPOC transit search of Sectors 19 on 17 January 2020. It passed all the DV diagnostic tests and was alerted by the TESS Science Office on 29 January 2020. It was redetected in a SPOC multisector transit search of Sectors 19 and 20 conducted on 5 May 2020, and the difference image centroiding test located the source of the transits to within 0.8 ± 3.0 arcsec of the host star.

Table 2.3: Resolved Distant Giants planet properties

TOI	CPS Name	Period (days)	Radius (R_{\oplus})	Mass (M_{\oplus})	Period (days)	Mass (M_J)	Reference
1469	219134	3.09307 ± 0.00024	1.29 ± 0.55	—	2100.6 ± 2.9	0.308 ± 0.014	1, 2
1669	T001669	2.68005 ± 0.00003	2.40 ± 0.18	5.2 ± 3.1	502 ± 16	0.573 ± 0.074	3
1694	T001694	3.77015 ± 0.00010	5.44 ± 0.18	26.1 ± 2.2	389.2 ± 3.9	1.05 ± 0.05	3
1773	75732	0.73649 ± 0.00002	2.02 ± 0.26	—	5285 ± 5	3.84 ± 0.08	2

References — (1) Vogt et al. (2015), (2) Rosenthal et al. (2021), (3) This work.

Note: TOI-1669 and TOI-1694 host newly-discovered distant giant planets. HD 219134 and HD 75732 also host outer giants, which were discovered over a much longer baseline. We quote the transiting planet parameters from the TESS DV reports.

Table 2.4: Resolved Distant Giants stellar properties

TOI	CPS Name	V	B-V	$M_{\star} (M_{\odot})$	$T_{\text{eff}} (K)$	$\log g$	[Fe/H]	$v \sin i$ (km/s)
1469	219134	5.57	1.02	0.79 ± 0.03	4839.5 ± 100.0	4.48 ± 0.10	0.11 ± 0.06	0.6 ± 1.0
1669	T001669	10.22	0.76	1.00 ± 0.05	5542.3 ± 100.0	4.28 ± 0.10	0.26 ± 0.06	0.6 ± 1.0
1694	T001694	11.45	0.76	0.84 ± 0.03	5066.4 ± 100.0	4.53 ± 0.10	0.12 ± 0.06	1.2 ± 1.0

1773	75732	5.95	0.86	0.97 ± 0.05	5363.3 ± 100.0	4.31 ± 0.10	0.42 ± 0.06	0.2 ± 1.0
------	-------	------	------	-----------------	--------------------	-----------------	-----------------	---------------

Note: Stellar parameters for the four stars in our survey hosting fully resolved companions. The effective temperatures, surface gravities, metallicities, and rotational velocities we list here were calculated using `SpecMatch`, which assigns a fixed uncertainty to each derived parameter. Stellar masses incorporate isochrone constraints, as described in [Fulton and Petigura \(2018\)](#).

2.3 A Jovian companion to TOI-1669

2.3.1 RV Model

We visually inspected the time series of the targets in our sample, and found that TOI-1669 exhibited RV variability beyond the noise background. TOI-1669 is a bright ($V = 10.2$) mid-G type solar analog exhibiting low chromospheric activity ($\log R'_{\text{HK}} = -5.2$) and low rotational velocity ($v \sin i = 0.3$ km/s), as required by our survey filters. Because it is not shared by any other TKS science cases, TOI-1669 was observed according to the Distant Giants observing strategy: we collected 20 HIRES spectra between July 2020 and July 2022 at monthly cadence, except during periods when the target was not observable. A subset of TOI-1669’s time series is given in Table 2.5.

We used `radvel` ([Fulton et al., 2018](#)) to fit a preliminary model to this system’s time series. The model consisted of the inner transiting planet, TOI-1669.01, and the newly-identified outer planet, TOI-1669 b, as well as parameters for linear and quadratic trends and a term characterizing astrophysical and instrumental jitter. We fixed the orbital period (P) and time of conjunction (T_c) of TOI-1669.01 to the values listed in the TESS DV reports. We fit for the three remaining orbital parameters: eccentricity (e), argument of periastron (ω), and semi-amplitude (K).

For TOI-1669 b, we fit for all five orbital parameters with initial values based on visual estimates from the RV time series. We imposed wide priors on free orbital parameters to minimize the bias incurred by our estimates. We used Powell’s method (Powell, 1964) to optimize our likelihood function, and derived parameter uncertainties using Markov chain Monte Carlo (MCMC) simulations, as implemented in Foreman-Mackey et al. (2013).

We generated a set of alternative models by excluding different combinations of 1) RV trend/curvature, 2) eccentricity of both planets, and 3) the outer planet itself. We performed a model comparison using the Akaike Information Criterion (AIC; Akaike 1974) to find which of these combinations was preferred. The consideration of only one- and two-planet models leaves open the possibility that one or more planets were missed by our analysis. However, the aim of this procedure was not to find every planet in this system, but rather to determine whether it satisfied the basic detection criterion of our survey: hosting at least one outer giant planet in the presence of a close-in small one.

We found that all viable models included both TOI-1669 b and a linear trend. We ruled out models that excluded TOI-1669.01 because this planet was independently confirmed by transit photometry. Eccentricity of either planet improved the model likelihood, but not enough to outweigh the penalty imposed by the AIC for higher model complexity. Quadratic curvature was similarly disfavored. The model preferred by the AIC consists of two planets with circular orbits, as well as a linear trend.

We also considered a variation of the AIC-preferred model, with the outer giant eccentricity allowed to vary. Although this model is formally disfavored ($\Delta\text{AIC} = 8.6$), it represents a more realistic scenario than the forced circular case. Moreover, this eccentric model subsumes the circular one, meaning that it could naturally fit a circular orbit for TOI-1669 b if it were favored by the data. The fact that this model instead fits a moderate eccentricity to the outer planet suggests that the AIC-preferred circular fit may not be physical, but rather a result of the AIC’s penalization of models with more parameters, which is intended to

prevent the over-fitting of small data sets. We adopt the eccentric model and quote its fitted parameters, though we present the circular model alongside it to emphasize the uncertainty in our model selection process. In subsequent sections, we refer to the model with free outer giant eccentricity as "preferred." We show both models together with the full and phase-folded time series in Figure 2.3.

Table 2.5: Radial Velocities

TOI	CPS Name	BJD	RV (m/s)	RV err (m/s)	S-value	S-value err
1669	T001669	2459537.902	-13.598	1.874	0.145	0.001
1669	T001669	2459565.861	-11.912	1.919	0.146	0.001
1669	T001669	2459591.838	-5.688	1.884	0.151	0.001
1669	T001669	2459632.799	-2.411	1.669	0.143	0.001
1669	T001669	2459781.120	-6.998	1.671	0.136	0.001
1694	T001694	2459591.833	-13.204	1.873	0.196	0.001
1694	T001694	2459626.823	-9.860	1.888	0.190	0.001
1694	T001694	2459654.763	-40.566	1.861	0.186	0.001
1694	T001694	2459681.789	-39.828	1.663	0.201	0.001
1694	T001694	2459711.753	-36.029	1.843	0.200	0.001

Note: We provide subsets of our time series for TOI-1669 and TOI-1694 here for reference. We obtained all RVs for these systems using Keck/HIRES. The full machine-readable versions are available online.

2.3.2 False Alarm Probability

To evaluate the significance of our giant planet detection, we calculated the false alarm probability (FAP) by adapting the procedure of Howard et al. (2010a). The FAP estimates the probability that a recovered signal arose from random statistical fluctuations rather than an actual planet. We created 1000 "scrambled" versions of TOI-1669's time series by randomly drawing RV values from the original data, with replacement. For each of these data sets, we compared the preferred 2-planet model to the null hypothesis: a model with the inner planet only, with P and T_c fixed and e , ω , and K allowed to vary, and no linear

trend. For a given data set, the improvement of the preferred model fit to the data over the single-planet fit to the data is quantified by the difference in χ^2 statistic, $\Delta\chi^2 = \chi_{\text{inner}}^2 - \chi_{\text{pref}}^2$, where χ_{inner}^2 and χ_{pref}^2 are the minimized χ^2 values of the single-planet and preferred fits to the data, respectively. A more positive $\Delta\chi^2$ value indicates greater performance of the preferred model over the single-planet model. The FAP is simply the fraction of scrambled time series with a greater $\Delta\chi^2$ value than the original time series. Put another way, the FAP gives the fraction of scrambled time series for which the statistical improvement granted by the preferred model over a single-planet model is greater than the improvement granted by the preferred model over a single-planet model for the actual RVs. We found that no scrambled data sets had $\Delta\chi^2$ greater than TOI-1669’s original time series, implying an FAP value of less than 0.1%. We emphasize that this technique quantifies only the probability of false detections as the result of statistical noise, not the probability that one or more planetary signatures were missed in the fitting procedure. However, as we note above, the latter is irrelevant to our search for *at least* one outer giant in each system.

2.3.3 Companion Properties

We recovered a cold sub-Jupiter orbiting TOI-1669 with a period and minimum mass of 502 ± 16 days and $M \sin i = 0.573 \pm 0.074 M_J$. We found that $e_c = 0.14 \pm 0.13$, corresponding to a 1σ upper limit of 0.27. Our data set for this system is small, consisting of only 20 RVs, so we defer precise claims about TOI-1669 b’s eccentricity until we have collected more data. Nevertheless, our data is sufficient to indicate that this planet exists and is a distant giant by the standards of our survey.

TOI-1669 also hosts a 2.7-day candidate sub-Neptune detected by TESS. Assuming TOI-1669.01 is a planet, its fitted radius of $R = 2.40 \pm 0.18 R_{\oplus}$ suggests that it resides on the edge of the Radius Valley, an interval between 1.5 and 2.0 R_{\oplus} which exhibits a distinct

reduction in planet occurrence (Fulton et al., 2017; Van Eylen et al., 2018). We derived a mass of $5.2 \pm 3.1 M_{\oplus}$ for TOI-1669.01 and used it to calculate a bulk density of 2.06 ± 1.13 g/cc, corresponding to a 1σ upper bound of 3.19 g/cc. Due to the uncertainty of our mass measurement, we have not independently confirmed TOI-1669.01 as a planet. Nevertheless, TOI-1669 meets our transit quality requirements (§2.2.1), so we treat TOI-1669.01 as a transiting planet for the purposes of our survey.

Finally, TOI-1669 exhibits a linear trend in the RV residuals. The trends found by our preferred model (-0.0261 ± 0.0058 m/s/day) and the circular model (-0.0286 ± 0.0047 m/s/day) are each significant at $> 4\sigma$, and agree with each other to within 1σ . The trend is likely physical, as evidenced by its persistence in both models, and may be caused by an additional long-period companion with a period $\gtrsim 2200$ days. To test this hypothesis, we examined direct imaging of TOI-1669 obtained in the I-band (832 nm) with the 'Alopeke speckle imager (Scott et al., 2021) coupled to the 8-meter Gemini-North telescope. The imaging reached a roughly constant contrast of $\Delta\text{mag} \approx 4$ from 0.1"–1.0" and showed no evidence of a luminous companion. This rules out stellar companions $\gtrsim 250 M_J$ within 100 AU, but leaves open the possibility that a substellar companion orbits TOI-1669 at close separation. If this is the case, extending TOI-1669's observational baseline over the next year will give us greater sensitivity to the companion's orbit.

2.4 A Jovian companion to TOI-1694

2.4.1 RV Model

We also observed significant RV variation in the time series of TOI-1694. TOI-1694 is an early K dwarf with $V = 11.4$, $\log R'_{\text{HK}} = -5.0$, and $v \sin i = 0.4$ km/s. Like TOI-1669, TOI-1694 was observed at the low cadence prescribed by Distant Giants: we obtained 20

HIRES spectra of this target between August 2020 and September 2022. We show a subset of TOI-1694’s RV time series in Table 2.5.

We used the procedure described in Section 2.3.1 to fit an RV model to TOI-1694’s time series. We found that a two-planet model with an eccentric outer planet and no trend was preferred over the same model with both orbits forced to circular ($\Delta\text{AIC} = 8.41$). We also tested the preferred model with an added linear trend, and found that the fitted value was consistent with 0 m/s/day, which we interpret as evidence that our model selection process was not heavily influenced by our limited data set. We therefore adopt the AIC-preferred model: an inner planet with a circular orbit, an eccentric outer giant, and no linear trend. Under this model, we calculated $\text{FAP} < 0.1\%$ for TOI-1694 c. For consistency with our treatment of TOI-1669, we also present a modified version of the preferred model, with the outer planet’s orbit fixed to circular. This model fits similar values to the giant planet’s mass and period, suggesting that model uncertainty does not greatly contribute to our overall uncertainty in these parameters. Figure 2.4 shows the preferred RV model for TOI-1694, along with the alternative circular model.

2.4.2 Companion Properties

TOI-1694 hosts an RV-resolved distant giant as well as a TESS-detected inner transiting planet. The outer companion, TOI-1694 c, is a Jupiter analog ($M \sin i = 1.05 \pm 0.05 M_J$) with a period of 389.2 ± 3.9 days and a modest eccentricity of $e = 0.18 \pm 0.05$.

The inner companion in this system, TOI-1694 b, is a hot super-Neptune with a radius of $5.44 \pm 0.18 R_\oplus$ and a period of ~ 3.8 days. This planet is recovered at high significance by our RV model and has a true mass of $26.1 \pm 2.2 M_\oplus$. With our mass and radius measurements, we calculate a bulk density of 0.89 ± 0.12 g/cc. TOI-1694 b’s low density and large radius suggest that it comprises a rocky core surrounded by a substantial gaseous envelope (Weiss

and Marcy, 2014; Rogers, 2015; Fulton et al., 2017). TOI-1694 b is noteworthy because it lies in the Hot Neptune Desert, which refers to the low occurrence of short-period ($P \lesssim 10$ days) planets with masses of $\sim 10\text{--}100 M_{\oplus}$ (Mazeh et al., 2016).

2.5 Discussion

TOI-1669 b and TOI-1694 c are among the first fully resolved outer companions in the Distant Giants sample, along with HD 219134 g (Vogt et al., 2015) and HD 75732 d (Fischer et al., 2008), which were known prior to the start of the survey. In a recent analysis of the multi-transiting system HD 191939 (Lubin et al., 2022b), we measured a linear trend consistent with a super-Jupiter at a few AU. This detection has become clearer with our extended RV baseline, and we will constrain its parameters more precisely in future work. With our two new giants, two known giants, and a forthcoming characterization of HD 191939’s outer giant, we estimate a lower bound of $P(\text{DG}|\text{CS}) \gtrsim 5/47$, or roughly 11%, which is comparable to the underlying occurrence rate of $\approx 10\%$ for distant giants out to six-year periods (Cumming et al., 2008). If the six remaining trend systems host distant giant planets and not brown dwarfs or stars, the rate would be $11/47 \approx 23\%$. Because these companions likely have periods much longer than six years, it is more appropriate to compare our 23% estimate to the $P(\text{DG})=17.6^{+2.4}_{-1.9}\%$ value found by Rosenthal et al. (2022) for giant planets out to 30-year periods. Using either period limit for distant giants, our preliminary conditional occurrence is similar to the underlying rate. After completing our survey, we will revise our estimate with a full statistical treatment.

In addition to $P(\text{DG}|\text{CS})$, the results of our survey will shed light on the period and eccentricity distributions of outer companions to inner small planets. Figure 2.5 shows the resolved companions in our sample in the mass-period plane. Figure 2.6 compares the resolved companion eccentricities and orbital separations to the underlying population of giant planets.

Although we cannot infer population-level traits in either parameter space from these four planets alone, they will serve as a reference in future studies, when we have constrained the properties of more of the companions in our sample.

2.6 Conclusions and Future Work

We presented the Distant Giants Survey, an RV study designed to search for long-period giant companions to inner transiting planets detected by TESS. The objective of Distant Giants is to unify our understanding of two planet classes: the inner small planets discovered in abundance by Kepler, and the Jupiter analogs found by ground-based RV surveys, which are drawn from nearly disjoint stellar samples. In particular, we aim to directly measure $P(\text{DG}|\text{CS})$, the conditional occurrence of distant giants in systems hosting a close-in small planet. Our sample consists of 47 inactive Sun-like stars, and our once-per-month observing strategy targets long-period companions. We have completed two years of the three-year survey, allowing us to fully resolve orbits shorter than this baseline.

We reported the discovery of two outer giant planets, TOI-1669 b and TOI-1694 c, identified using Keck-HIRES RVs. We also constrained the masses of each system’s inner planet, TOI-1669.01 and TOI-1694 b. TOI-1669 b has a minimum mass consistent with a sub-Jupiter ($M \sin i = 0.573 \pm 0.074 M_J$) with a period of 502 ± 16 days. Though our data set is currently too limited to precisely constrain the planet’s eccentricity, it is unlikely to be highly eccentric. The inner planet, TOI-1669.01, was recovered at low significance by our RV model, and is probably less than $\sim 10 M_\oplus$. TOI-1694 c is a Jupiter analog ($M \sin i = 1.05 \pm 0.05 M_J$) with a slightly eccentric orbit ($e = 0.18 \pm 0.05$) and a period of 389.2 ± 3.9 days. We recovered the inner planet, TOI-1694 b, at high significance and used the derived true mass of $26.1 \pm 2.2 M_\oplus$ to calculate a bulk density of 0.89 ± 0.12 g/cc. TOI-1694 b’s mass and 3.8-day period place it in the Hot Neptune Desert. Aside from making inroads for dynamical investigation, the

coexistence of an inner small planet and an outer giant in these two systems admits them to the subset of unambiguous detections among our sample, which sets the lower bound on our estimate of $P(\text{DG}|\text{CS})$.

In addition to TOI-1669 and TOI-1694, long-period giants were already known to orbit HD 219134 and HD 75732 at the beginning of the survey, and we have observed a partial orbit of the outer planet HD 191939 f. We also see linear trends in six RV time series, which we associate with unresolved long-period companions. Combining these groups, we see evidence for distant giants in $\sim 23\%$ of our sample. We caution that neither the current number of resolved planets nor the resolved planets plus linear trends should be used for precise calculations of $P(\text{DG}|\text{CS})$. There is still a year remaining in the survey, during which new long-period planetary signals could develop and existing trends could be found to be non-planetary. In our final analysis, we will refine the approximation above by computing completeness maps for each target and deriving planet occurrence rates using Poisson point process statistics.

This paper is the first in a series tracking the progress of the Distant Giants Survey. In future work, we will characterize companions discovered during the remaining year of the survey, including HD 191939 f, a trend system which we first predicted to be a 6–20-year super-Jupiter through partial orbit analysis (Lubin et al., 2022b). The increased phase coverage we have since achieved will let us test our prediction by fitting this object’s orbit directly. We will also use this partial orbit analysis to treat the RV trends in six more systems. We will incorporate astrometry and direct imaging to constrain the properties of the objects inducing these accelerations, helping to identify them as planets, brown dwarfs, or stellar companions. Finally, we will refine the relationship between small inner planets and outer giants by using our results to calculate $P(\text{DG}|\text{CS})$.

Facilities: Automated Planet Finder (Levy), Keck I (HIRES), Gemini-North (’Alopeke), TESS

Software: `radvel` (Fulton et al., 2018), `emcee` (Foreman-Mackey et al., 2013), `SpecMatch` (Petigura et al., 2017).

2.7 Acknowledgments

J.V.Z. acknowledges support from the Future Investigators in NASA Earth and Space Science and Technology (FINESST) grant 80NSSC22K1606. J.M.A.M. is supported by the National Science Foundation Graduate Research Fellowship Program under Grant No. DGE-1842400. J.M.A.M. acknowledges the LSSTC Data Science Fellowship Program, which is funded by LSSTC, NSF Cybertraining Grant No. 1829740, the Brinson Foundation, and the Moore Foundation; his participation in the program has benefited this work. T.F. acknowledges support from the University of California President’s Postdoctoral Fellowship Program.

We thank the time assignment committees of the University of California, the California Institute of Technology, NASA, and the University of Hawaii for supporting the TESS-Keck Survey with observing time at Keck Observatory and on the Automated Planet Finder. We thank NASA for funding associated with our Key Strategic Mission Support project. We gratefully acknowledge the efforts and dedication of the Keck Observatory staff for support of HIRES and remote observing. We recognize and acknowledge the cultural role and reverence that the summit of Maunakea has within the indigenous Hawaiian community. We are deeply grateful to have the opportunity to conduct observations from this mountain. We thank Ken and Gloria Levy, who supported the construction of the Levy Spectrometer on the Automated Planet Finder. We thank the University of California for supporting Lick Observatory and the UCO staff for their dedicated work scheduling and operating the telescopes of Lick Observatory.

Funding for the TESS mission is provided by NASA's Science Mission Directorate. We acknowledge the use of public TESS data from pipelines at the TESS Science Office and at the TESS Science Processing Operations Center at NASA Ames Research Center. This research has made use of the Exoplanet Follow-up Observation Program website, which is operated by the California Institute of Technology, under contract with the National Aeronautics and Space Administration under the Exoplanet Exploration Program.

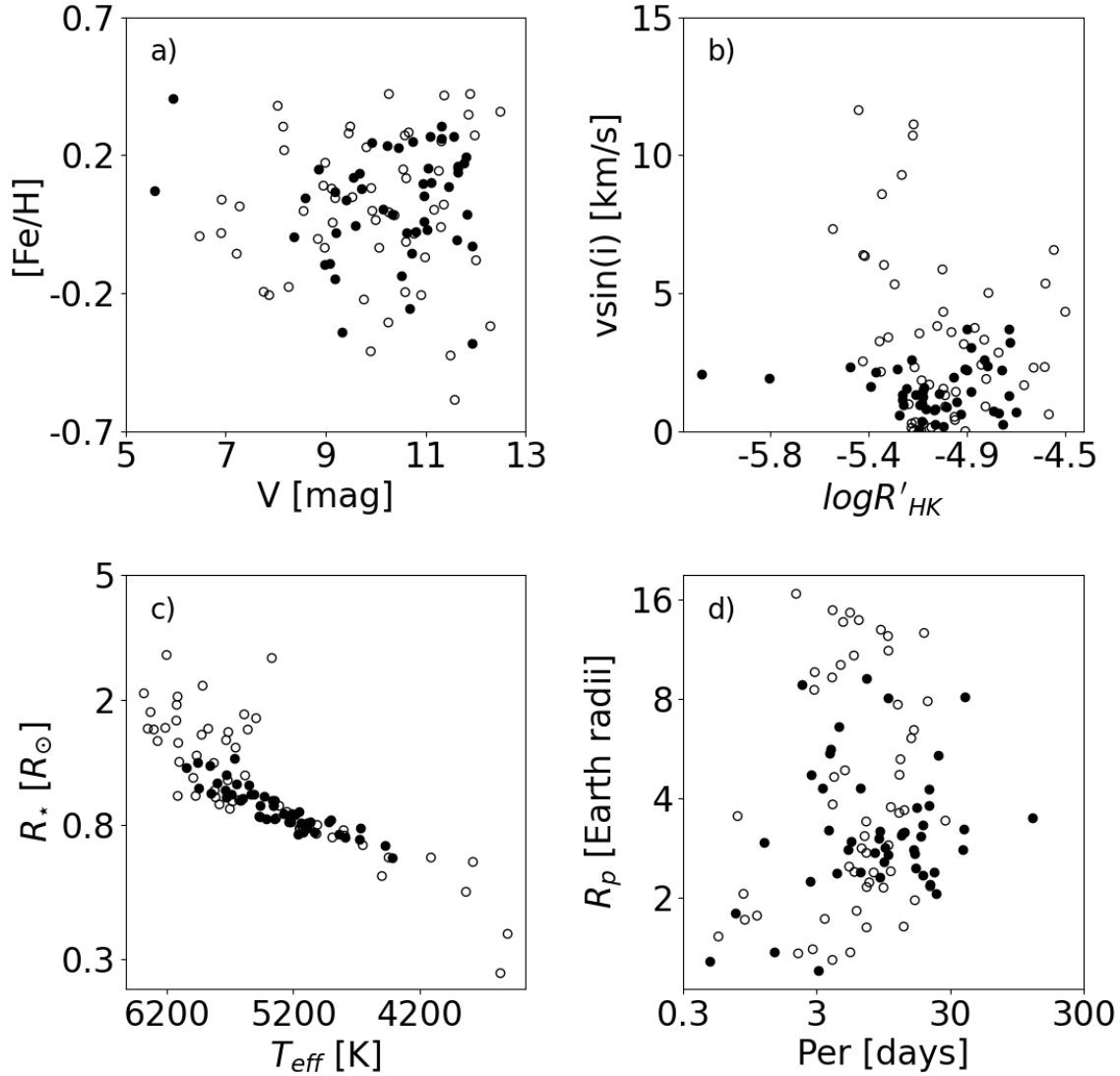


Figure 2.1: Stellar and transiting planet parameters of the TKS survey. Filled points show targets selected for the Distant Giants sample. Panels a) through c) show stellar parameters. TOI-1775 and TOI-2088 are not shown in panel b) because they lacked measured $\log R'_{\text{HK}}$ values when we finalized our sample. Panel d) shows parameters of the transiting planets. For multi-transiting Distant Giants systems, we checked planet radii in order of ascending TOI number, and show the first planet to pass our survey filters.

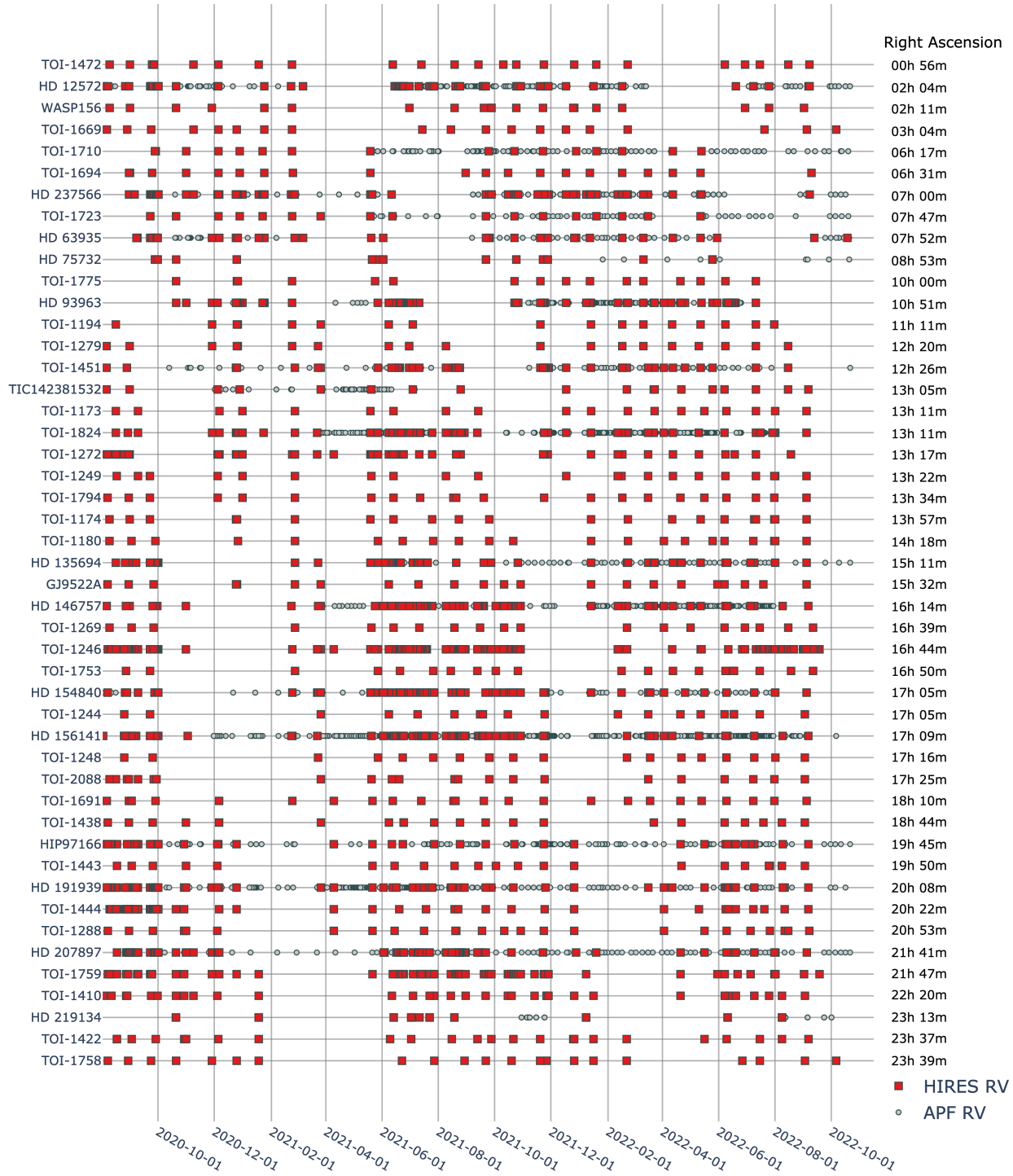


Figure 2.2: Observations of the Distant Giants sample between its official start in August 2020 and late 2022. Red squares are HIRES RVs and gray circles are APF RVs. Targets are ordered by right ascension, shown in the right margin. The typical target in our sample is inaccessible from Keck Observatory for about three months out of the year, which is reflected in the bands of decreased observation density which run diagonally through the plot. During their observing seasons, all targets generally meet or exceed the prescribed monthly cadence.

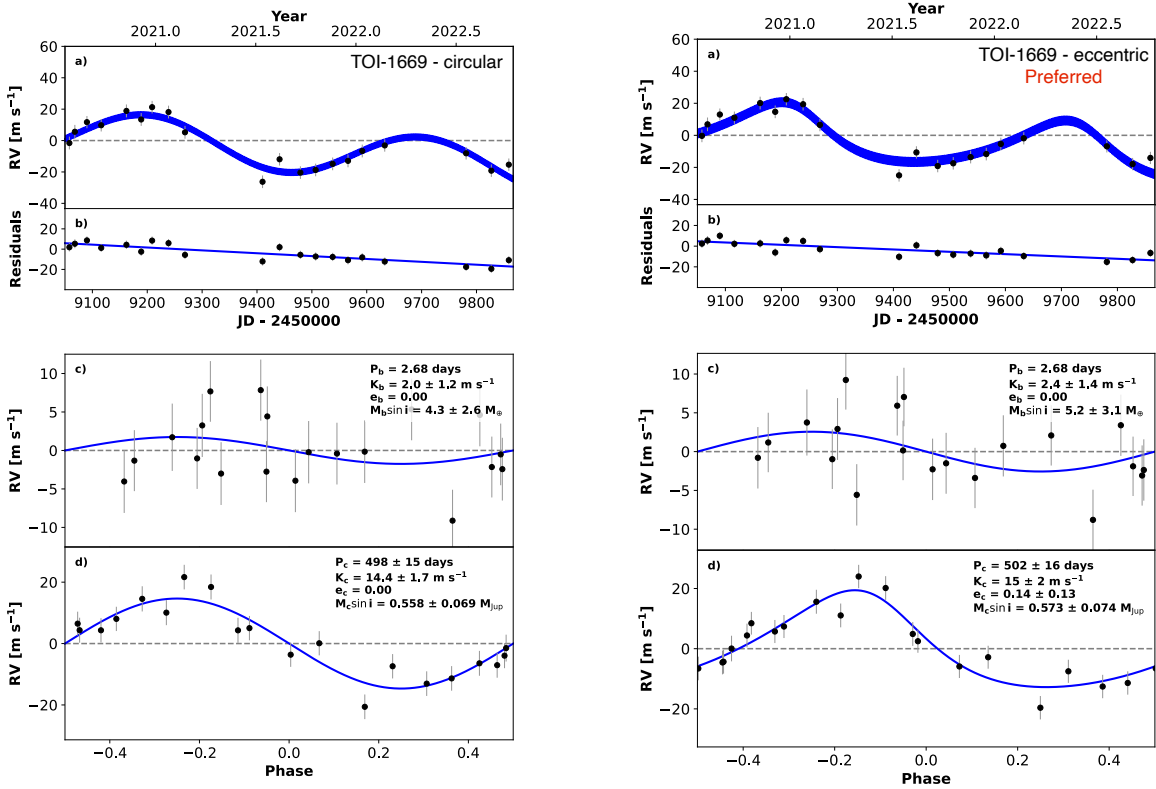


Figure 2.3: The RV time series and orbit models for TOI-1669’s AIC-preferred circular model (left) and our preferred model including eccentricity (right). Although the circular model has a lower AIC, we adopt the more general model including eccentricity, and emphasize that our limited RV sample contributes to model selection uncertainty. In both figures, **a)** shows our full Keck/HIRES RV time series (black points) with the fitted model in blue. The residuals to the fit are given in **b)**. Each subsequent panel shows the time series phase-folded to a particular model planet period. Both models recover consistent periods and masses for the giant TOI-1669 b, as well as a long-term linear trend, suggesting that these parameters are not highly sensitive to our choice of model. By contrast, our eccentric model shows that TOI-1669 b’s orbit may deviate from circular. Future observations will resolve this disagreement. The existence of TOI-1669.01 is known from TESS photometry, so we include it in our model despite its low RV amplitude.

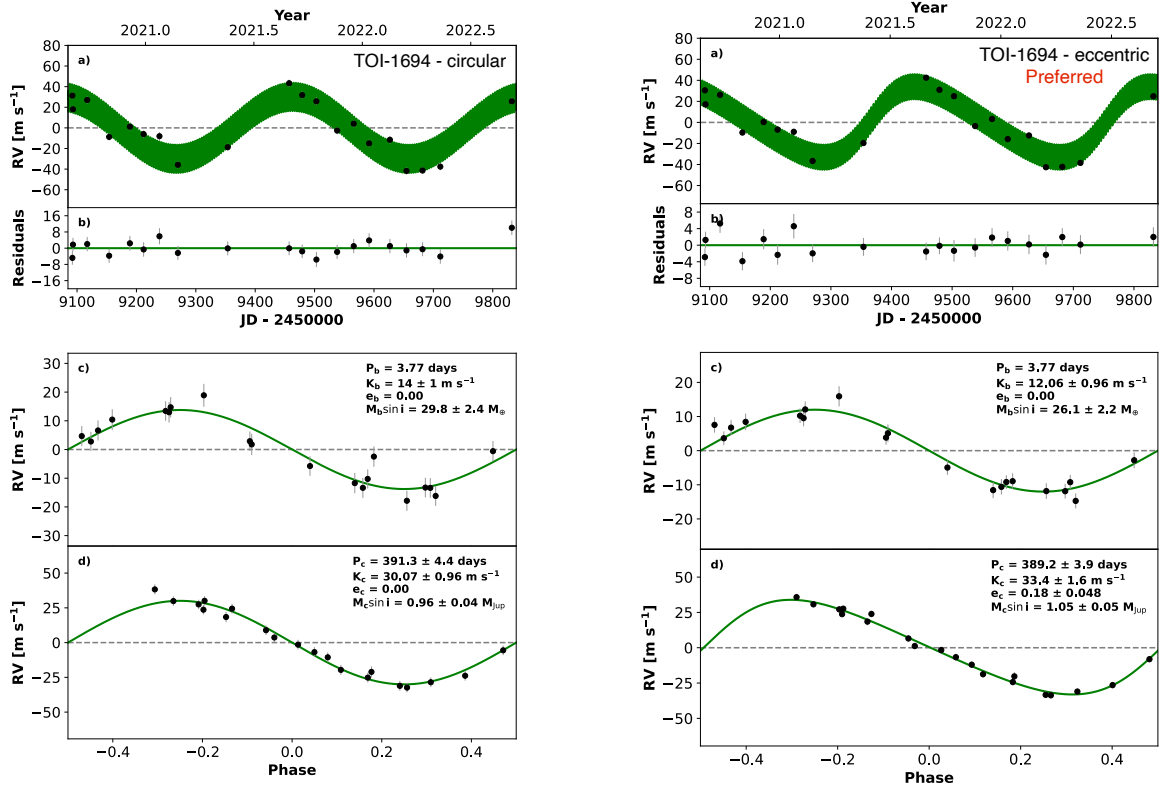


Figure 2.4: The RV time series of TOI-1694, together with orbit models assuming a circular (left) or eccentric (right) outer planet. In both figures, **a)** shows our full Keck/HIRES RV time series (black points) with the fitted model in green. The residuals to the preferred fit are shown in **b)**. Each subsequent panel shows the time series phase-folded to a particular model planet period. For consistency with our treatment of TOI-1669, we include two models that differ only in the eccentricity of the outer planet. However, in contrast to TOI-1669, the eccentric model we adopted for TOI-1694 is also formally preferred by the AIC. TOI-1694 b’s mass and orbital separation identify it as a hot Neptune.

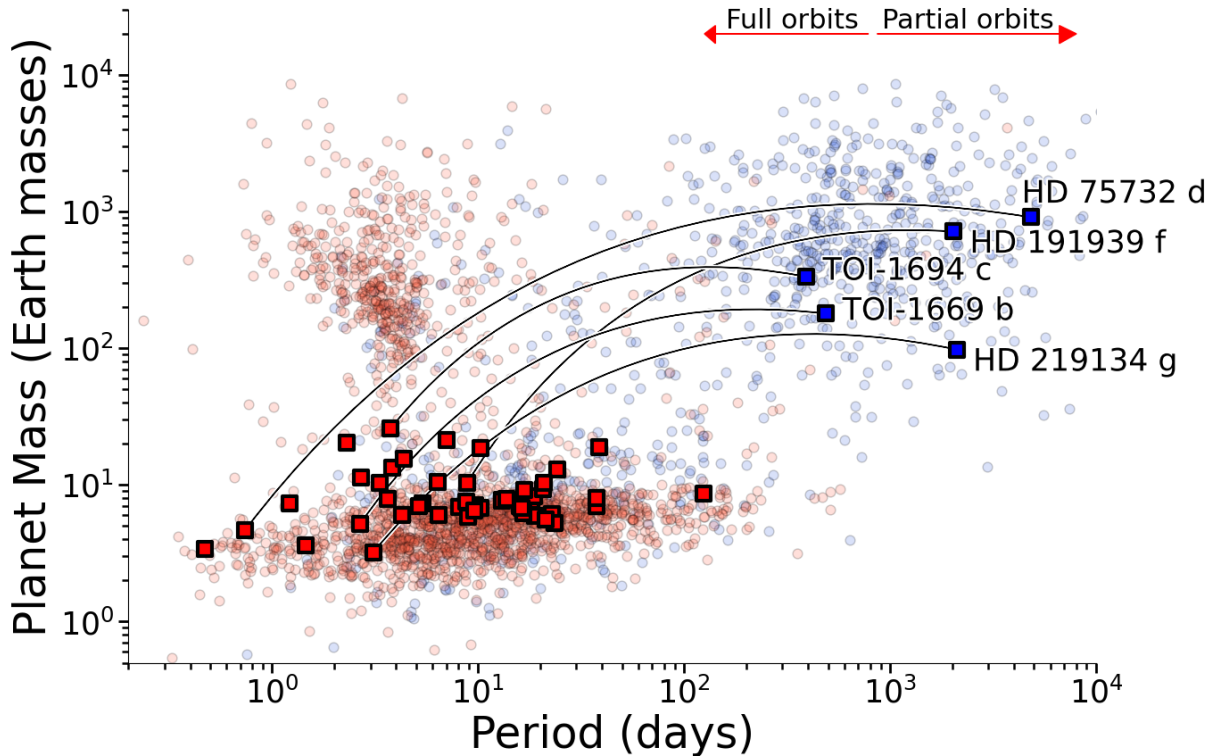


Figure 2.5: Masses and periods of known exoplanets discovered by RVs (blue circles) and transits (red circles). Transiting planet masses are estimated from their radii using the mass-radius relation of [Weiss and Marcy \(2014\)](#). Transiting/resolved Distant Giants companions are overlaid as red/blue squares. Inner and outer companions in the resolved systems, HD 219134, HD 75732, TOI-1669 and TOI-1694, are connected with black lines. We also plot estimated parameters of HD 191939 f, though our analysis of this planet’s RV signal is still preliminary. TOI-1669 b and TOI-1694 c have masses and periods typical of cold Jupiters. The red arrows indicate planetary periods shorter and longer than the current ~ 2 -year survey baseline. HD 75732 d and HD 219134 g have orbits well beyond three years, and are only resolved due to their extensive observing histories.

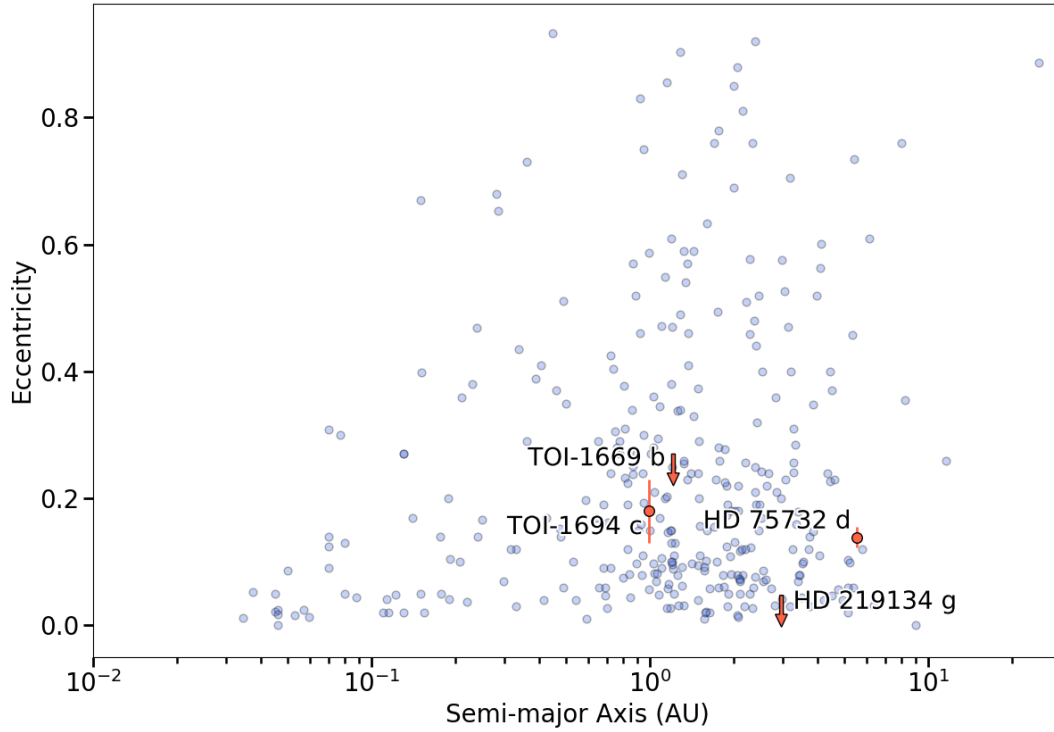


Figure 2.6: Distribution of eccentricity versus orbital separation for confirmed exoplanets between 0.01 and 30 AU with $\sigma_e \lesssim 0.1$ (blue points). The four resolved giants in our sample are shown in orange. TOI-1669 b and HD 219134 g have eccentricities consistent with zero, and each is represented by an arrow, the base of which shows the 84% upper eccentricity limit. It is not obvious that the distribution from which these planets' eccentricities are drawn is distinct from that of the underlying population.

Chapter 3

ethraid: A simple method for characterizing long-period companions using Doppler, astrometric, and imaging constraints

A version of this chapter was previously published in *The Astronomical Journal* (Judah Van Zandt & Erik A. Petigura, 2024a, AJ 167, 6, 250).

Abstract

We present **ethraid**,¹ an open source Python package designed to measure the mass (m_c) and separation (a) of a bound companion from measurements covering a fraction of the orbital period. **ethraid** constrains m_c and a by jointly modeling radial velocity (RV), astrometric,

¹Van Zandt and Petigura (2024c)

and/or direct imaging data in a Bayesian framework. Partial orbit data sets, especially those with highly limited phase coverage, are well-represented by a few method-specific summary statistics. By modeling these statistics rather than the original data, `ethraid` optimizes computational efficiency with minimal reduction in accuracy. `ethraid` uses importance sampling to efficiently explore the often broad posteriors that arise from partial orbits. The core computations of `ethraid` are implemented in Cython for speed. We validate `ethraid`'s performance by using it to constrain the masses and separations of the planetary companions to HD 117207 and TOI-1694. We designed `ethraid` to be both fast and simple, and to give broad, "quick look" constraints on companion parameters using minimal data. `ethraid` is pip installable and available on Github².

3.1 Introduction

Fitting the orbits of exoplanets is one of the best tools for uncovering their origins, evolutionary history, and relationship to neighboring planets. Keplerian fits to RV observations produced the first detections of hot Jupiters orbiting Sun-like stars (Mayor and Queloz, 1995; Butler et al., 1997; Cochran et al., 1997), and higher-precision measurements have facilitated mass determinations of smaller planets (Pinamonti et al., 2018; Luque et al., 2019).

Planets with long periods, from years to decades, present multiple observational challenges. In particular, their orbits require consistent and prolonged monitoring to characterize. Long-term RV surveys (see, e.g., Rosenthal et al. 2021) confront this problem directly by compiling observational baselines over multiple decades. Though fruitful, these efforts are costly in terms of both human time and telescope time.

Furthermore, these surveys are observationally inefficient in two ways. First, the precise mass and orbital parameters of each companion are often not of immediate interest. For example,

²<https://github.com/jvanzand/ethraid>

studies of giant planet occurrence rates (Fulton et al., 2021) or the correlation between giants and other planet classes (Bryan et al., 2019; Rosenthal et al., 2022) are principally concerned with differentiating between giant planets, brown dwarfs, and stars, which may be accomplished with less than a full orbit. Although precise constraints may be useful, some science cases benefit from greater statistical breadth over precision measurements of specific orbital parameters.

Second, once legacy surveys end, their final catalogs may still include targets with too little phase coverage to characterize (Rosenthal et al., 2021). Without further observation, these time series represent significant investments of telescope time with minimal scientific return. Both of these limitations motivate tools for extracting planetary information from partial orbits.

Many existing Bayesian orbit fitters are well-suited to performing precise fits using RVs (radvel, Fulton et al. 2018; *The Joker*, Price-Whelan et al. 2017), astrometry (orbitize!, Blunt et al. 2020; OFTI, Blunt et al. 2017), or both (orvara, Brandt et al. 2021). Some of these codes are designed to be robust against specific orbit fitting challenges (e.g., non-Gaussian posteriors, low phase coverage, and high-dimensional parameter spaces). However, their performance tends to suffer as these limitations are taken to the extreme.

In this work, we present **ethraid**, an open source Python package designed specifically to constrain companion mass and separation given partial phase coverage. **ethraid** can simultaneously model summary statistics of up to three independent data types: linear/quadratic RV trends, astrometric trends from the *Hipparcos-Gaia* Catalog of Accelerations (Brandt, 2018, 2021), and direct imaging contrast curves. In the remainder of this paper, we refer to these summary statistics as the "data."

This paper takes the following structure. In Section 3.2 we describe **ethraid**'s fitting algorithm, including parameter sampling, forward modeling and likelihood calculation, and

marginalization to derive posteriors. Section 3.3 gives the mathematical details of our forward model for each of RVs, astrometry, and direct imaging data. We discuss `ethraid`'s performance in Section 3.4 and basic usage in Section 3.5. We test the strengths and weaknesses of this code in Section 3.6. Finally, we give a brief list of future improvements planned for `ethraid` in Section 3.7 before concluding in Section 3.8.

3.2 `ethraid`'s Fitting Algorithm

Given some RV, astrometric, or imaging data, `ethraid` samples a space of orbital models, assesses each model's probability of having produced the signal based on both its *a priori* probability and the likelihood of the measured signal in light of the model, and uses the resulting posterior surface to calculate confidence intervals for the inferred companion's mass and semi-major axis. `ethraid`'s approach to this problem consists of three steps:

1. Random sampling of orbital parameters from prior distributions
2. Forward modeling and likelihood calculation
3. Marginalization over orbital parameters

These steps are summarized in Figure 3.1. Before detailing them below, we note an important assumption that `ethraid` makes, namely, that any measured signals were produced by a single bound companion. Consequently, RV and astrometric trends produced by multiple companions, stellar activity, or instrumental systematics will not be properly interpreted and may produce misleading results (see Section 3.6).

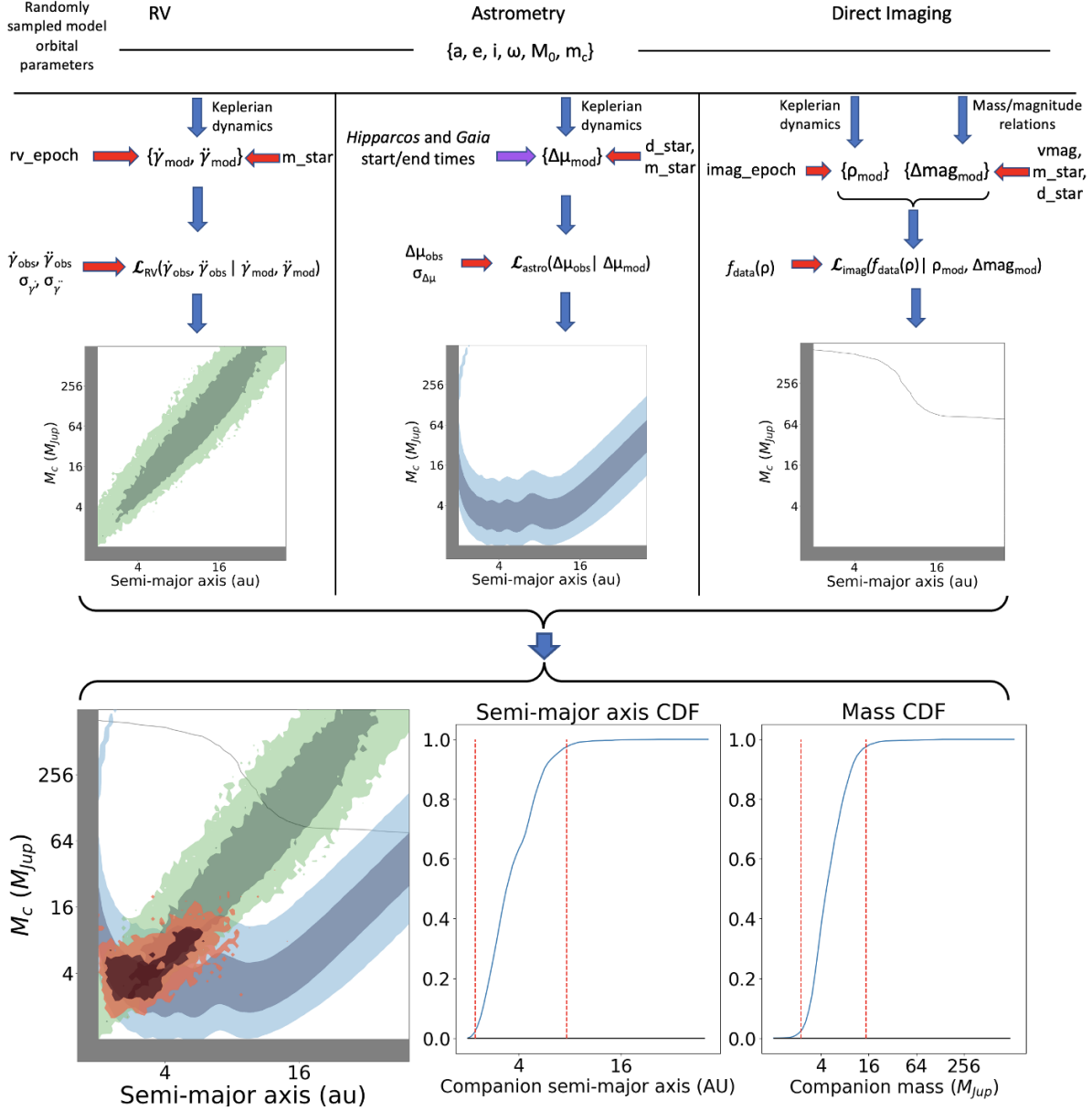


Figure 3.1: `ethraid`'s fitting algorithm. The steps are the same for RVs (left), astrometry (center), and direct imaging (right): `ethraid` samples a set of model orbital parameters, forward models the data-specific parameters, evaluates the model likelihood, and finally marginalizes many such likelihoods to derive the posterior PDF. Arrows represent inputs used in a given step: blue arrows show inputs from the previous step, red arrows show inputs provided by the user, and purple arrows show inputs that are fixed in the code. The bottom row shows three of the plots available to the user through the `plot` command. **Left:** The 2D m_c - a posteriors for each of the RV (green), astrometry (blue), and imaging (gray line) data sets, plus the combined posterior (red) conditioned on all three. The dark/light regions of each posterior show 68/95% confidence intervals. For imaging, the gray contour marks the 95% confidence boundary, with models below/above the contour ruled in/out by the data. **Right:** CDFs of the marginalized a and m_c posteriors. The vertical red lines indicate 95% confidence intervals. `ethraid` also produces corresponding PDFs by default.

3.2.1 Parameter Sampling from Priors

The algorithm used to sample observations (in our case, model parameters) from a distribution is a key component of any Monte Carlo method. `ethraid` uses importance sampling (Kloek et al., 1978), an approach in which observations $\boldsymbol{\theta}$ are sampled according to an importance function $q(\boldsymbol{\theta})$. The result is that the histogram of a set of N samples, $\{\boldsymbol{\theta}_n\}_{n=1}^N$, converges to q in the limit of large N :

$$\{\boldsymbol{\theta}_n\}_{n=1}^N \sim q(\boldsymbol{\theta}), \quad (3.1)$$

where " \sim " denotes "has the distribution of." However, because our goal is to calculate the posterior probability $p(\boldsymbol{\theta})$, we must weight each observation:

$$\{\boldsymbol{\theta}_n \cdot w_n\}_{n=1}^N \sim p(\boldsymbol{\theta}), \quad (3.2)$$

where the weights w_n are given by

$$w_n = \frac{p(\boldsymbol{\theta}_n)}{q(\boldsymbol{\theta}_n)}. \quad (3.3)$$

Following the earlier partial orbit fitters `OFTI` and *The Joker*, we sample orbital elements directly from their respective priors, $\pi(\boldsymbol{\theta})$. This choice is motivated by the fact that partial orbit data is generally uninformative, resulting in prior-dominated posteriors. Conveniently,

choosing $q = \pi(\boldsymbol{\theta})$ simplifies the weight of each model to the model likelihood:

$$w_n = \frac{\mathcal{L}(\boldsymbol{\theta}_n)\pi(\boldsymbol{\theta}_n)}{\pi(\boldsymbol{\theta}_n)} = \mathcal{L}(\boldsymbol{\theta}_n). \quad (3.4)$$

Thus, `ethraid` approximates the posterior surface $p(\boldsymbol{\theta})$ by creating a histogram of orbital models, each sampled from the appropriate prior distributions and weighted by its likelihood.

The first step of this procedure is to sample six orbital parameters according to their respective priors: semi-major axis a , eccentricity e , inclination i , argument of periastron of the companion (not the host star, as is sometimes the case in RV codes; see [Householder and Weiss 2022](#)) ω , the mean anomaly at a reference epoch M_0 , and companion mass m_c . As all data products we model are insensitive to the longitude of the ascending node (Ω), we fix it to 0 arbitrarily. The prior PDFs for these parameters are:

$$\log\left(\frac{a}{1 \text{ AU}}\right) \sim \mathcal{U}(a_{\min}, a_{\max})$$

$$\log\left(\frac{m_c}{1 M_J}\right) \sim \mathcal{U}(m_{c,\min}, m_{c,\max})$$

$$\cos(i) \sim \mathcal{U}(0, 1)$$

$$\omega \sim \mathcal{U}(0, 2\pi)$$

$$M_0 \sim \mathcal{U}(0, 2\pi)$$

$$e \sim \mathcal{E}(a, m_c)$$

where \mathcal{U} denotes a uniform distribution and \mathcal{E} is a user-selected eccentricity distribution.

Options for the latter include

- ‘**zero**’: a constant distribution of $e = 0$

- ‘uniform’: a uniform distribution between 0 and 0.99
- ‘kipping’: the piecewise beta distribution for short- and long-period exoplanets presented by [Kipping \(2013\)](#)
- ‘piecewise’: a combination of the [Kipping \(2013\)](#) distribution for planets ($\frac{m_c}{M_J} \leq 13$), the beta distribution derived by [Bowler et al. \(2020\)](#) for brown dwarfs ($13 < \frac{m_c}{M_J} \leq 80$), and a uniform distribution between 0.1 and 0.8 for stars ($80 < \frac{m_c}{M_J}$) found by [Raghavan et al. \(2010\)](#).

While the last of these is the most physically motivated in general, the others give users the option to include prior knowledge about a given system. For example, a dynamically cool system with multiple known planets on circular orbits may be unlikely to host an eccentric outer giant. In this case, a user might opt for the ‘kipping’ distribution to favor lower-eccentricity models.

Our importance sampling strategy differs from MCMC sampling (e.g. `radvel`), where each model draw in a chain is dependent on the previous step. Drawing samples independently is advantageous for characterizing highly non-gaussian or multi-modal posterior surfaces, which arise often in partial orbit analysis. Our method is similar to the rejection sampling technique used by `OFTI` and *The Joker*, which also draws models independently from a proposal distribution. However, rather than accepting or rejecting models based on their posterior probability, `ethraid` assigns each model a weight according to its likelihood. In practice, models with a high chance of rejection under rejection sampling are assigned vanishingly small weights under importance sampling, yielding similar performance.

3.2.2 Forward Modeling and Likelihood Calculation

After sampling a set of parameters, `ethraid` evaluates the model likelihood, that is, the probability of observing the measured data given the model under consideration. `ethraid` accomplishes this by generating synthetic RV, astrometric, and/or imaging data sets, and comparing them to the observed data. This procedure is repeated for a number of model orbits specified by the user (typically 10^6 – 10^8). The likelihood calculations for each data type are detailed in Section 3.3.

In the case that multiple data sets are provided, `ethraid` records the likelihood of each data set conditioned on each model. Because the RVs, astrometry, and imaging are independent, `ethraid` calculates the combined likelihood of all provided data sets as the product of the likelihoods of each individual data set.

3.2.3 Marginalization

`ethraid` can generate visualizations of the 1D and 2D marginalized posteriors for a and m_c . The marginalization step displays the desired posterior by summing the likelihoods of all models in the same interval of parameter space. For a 1D posterior, these are intervals in the desired parameter, for example, $\Delta m_{c,i}$. For a 2D posterior, they are interval pairs $(\Delta a_i, \Delta m_{c,i})$.

3.3 Forward model

In this section we detail `ethraid`'s likelihood calculations for RV, astrometry, and imaging data, including the forward modeling procedure which produces an analytic counterpart to each measured quantity.

3.3.1 RV Constraints

If a body on a long-period orbit is left unmodeled, it will present as a gradual increase or decrease in the RV residuals. For an orbital period much longer than the observing baseline, the variation is almost purely linear; for a period only a few times the baseline, there may also be significant quadratic curvature. The RV data therefore comprises the linear and quadratic coefficients to a second order polynomial fit to the RVs, denoted $\dot{\gamma}$ (m/s/day) and $\ddot{\gamma}$ (m/s/day²), respectively.

For each set of sampled parameters, our goal is to forward model $\dot{\gamma}$ and $\ddot{\gamma}$, whose analytic forms are given by differentiating the stellar radial velocity γ :

$$\begin{aligned}\gamma &= K [e \cos \omega + \cos(\nu + \omega)] \\ \dot{\gamma} &= -K [\dot{\nu} \sin(\nu + \omega)] \\ \ddot{\gamma} &= -K [\dot{\nu}^2 \cos(\nu + \omega) + \ddot{\nu} \sin(\nu + \omega)],\end{aligned}\tag{3.5}$$

where K is the RV semi-amplitude:

$$K = \sqrt{\frac{G}{1 - e^2}} \frac{m_c \sin i}{\sqrt{a(m_c + m_\star)}}\tag{3.6}$$

and ν is the true anomaly, related to the eccentric anomaly E by (Murray and Dermott, 2010)

$$\nu = 2 \operatorname{atan} \left[\sqrt{\frac{1+e}{1-e}} \tan \frac{E}{2} \right]. \quad (3.7)$$

The derivatives of ν are

$$\dot{\nu} = \frac{2\pi\sqrt{1-e^2}}{P(1-e\cos E)^2} \quad (3.8)$$

$$\ddot{\nu} = -\dot{\nu}^2 \frac{2e \sin E}{\sqrt{1-e^2}}.$$

We obtain E by numerically solving Kepler's equation:

$$M = E - e \sin E, \quad (3.9)$$

where M is the mean anomaly, calculated by advancing the sampled initial mean anomaly M_0 some duration t past a reference epoch via

$$M(t) = M_0 + \frac{2\pi}{P}t, \quad (3.10)$$

where P is the orbital period calculated from Kepler's third law. We choose our reference epoch to be 1989.5 (see Section 3.3.2).

We evaluate the model log-likelihood by calculating $\dot{\gamma}$ and $\ddot{\gamma}$ at the epoch of the RV observations and comparing them to their measured counterparts via

$$\begin{aligned} \ln(\mathcal{L}_{RV}(\boldsymbol{\theta})) &= -\frac{1}{2}\chi_{RV}^2 + C_{RV} \\ &= -\frac{1}{2}\left(\frac{(\dot{\gamma}_{data} - \dot{\gamma})^2}{\sigma_{\dot{\gamma}_{data}}^2} + \frac{(\ddot{\gamma}_{data} - \ddot{\gamma})^2}{\sigma_{\ddot{\gamma}_{data}}^2}\right) + C_{RV}, \end{aligned} \quad (3.11)$$

where $\dot{\gamma}_{data}$ and $\ddot{\gamma}_{data}$ are the measured slope and curvature of the RV time series, $\sigma_{\dot{\gamma}_{data}}$ and $\sigma_{\ddot{\gamma}_{data}}$ are their respective uncertainties, and C_{RV} is a constant.

From Equations 3.5 one may derive (see Appendix 3.10) that for small companion masses, surfaces of constant $\dot{\gamma}$ and $\ddot{\gamma}$ follow $m_c \propto a^2$ and $m_c \propto a^{7/2}$, respectively. Thus, for any sampled companion mass, there is a physical separation at which such a companion would produce the observed RV trend and curvature. In other words, RV constraints are generally consistent with a large range of (a, m_c) pairs. We seek to break this degeneracy by incorporating an independent data set: astrometry.

3.3.2 Astrometry Constraints

A star with no orbiting companions will have a constant proper motion. Meanwhile, a massive companion will induce a change in its host star’s proper motion vector over some time interval, called the proper motion anomaly (PM_a ; Kervella et al. 2019). Our goal is to model the magnitude of the PM_a vector.

Our forward modeling procedure for astrometry is similar to the RV case, but is tailored to the data provided by the *Hipparcos-Gaia* Catalog of Accelerations (HGCA; Brandt 2021). This catalog aligned the reference frames of *Hipparcos* (1989.85–1993.21, Hip 1997) and *Gaia*

EDR3 (25 July 2014–28 May 2017; [Lindegren et al. 2021](#)) to measure the accelerations of over 115,000 stars. We choose 1989.5 as the reference epoch t_0 for our RV, astrometric, and direct imaging models.

The HGCA reports three proper motions for each target: the epoch proper motions of *Hipparcos* ($\vec{\mu}_H$) and *Gaia* ($\vec{\mu}_G$) near 1991.25 and 2016.0, respectively, and the average proper motion given by the difference in position between these epochs divided by their ~ 25 -year baseline, $\vec{\mu}_{HG}$. The position-derived proper motion is generally the most precise proper motion measurement owing to the long baseline between the two missions, while $\vec{\mu}_G$ is usually the next-most precise. We therefore quantify PM_a as $\Delta\vec{\mu}$, the difference between $\vec{\mu}_G$ and $\vec{\mu}_{HG}$, and model its norm:

$$\Delta\mu = |\Delta\vec{\mu}| = |\vec{\mu}_G - \vec{\mu}_{HG}|. \quad (3.12)$$

We likewise obtain $\sigma_{\Delta\mu}$ by propagating the measurement uncertainties provided in the HGCA. The astrometric picture is summarized in [Figure 3.2](#).

Our derivations of $\vec{\mu}_G$ and $\vec{\mu}_{HG}$ differ in one key respect from the procedure used to construct the HGCA. [Brandt \(2021\)](#) obtained the best-fit positions and proper motions by recalibrating astrometric fits to the full *Hipparcos* or *Gaia* time series. Because simulating and fitting a model to a full time series would be computationally expensive, we instead calculate the analytic average of position and proper motion during each mission by integrating over the host star’s orbit. We take these average quantities to approximate the stellar position and proper motion at the mission midpoints. To minimize positional uncertainty, Brandt evaluated the fitted positions at target-specific “characteristic epochs” rather than the mission midpoints. This disparity introduces an error on the order of 0.01 mas/yr to our model, which we con-

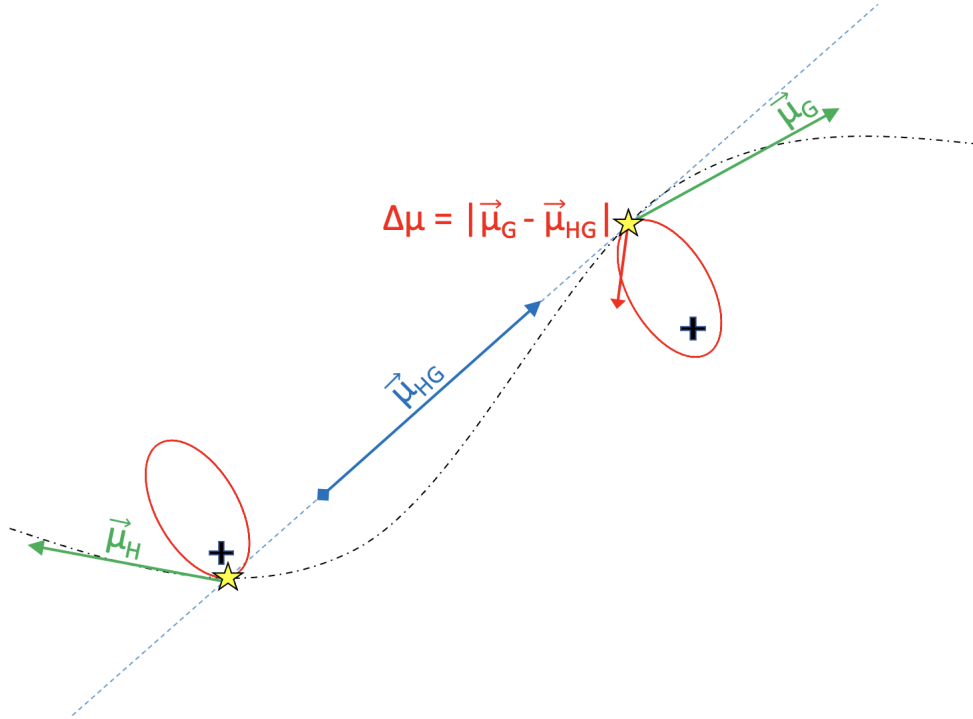


Figure 3.2: Our model of astrometric proper motion anomaly. Red ellipses show the stellar orbit associated with a non-luminous bound companion (not shown). Green arrows show the average proper motion vectors fitted to the data from *Hipparcos* (left) and *Gaia* (right). Gold stars show the average positions during *Gaia* and *Hipparcos*, and the blue arrow shows $\vec{\mu}_{HG}$, the average proper motion *between* them, calculated as the difference in average positions divided by the difference between the mission midpoints. The proper motion anomaly $\Delta\mu$, shown in red, quantifies the difference between the average *Gaia* proper motion and the position-derived proper motion. Figure adapted from [Kervella et al. \(2019\)](#).

sider negligible because it is below both the median (0.047 mas/yr) and minimum (0.016 mas/yr) $\Delta\mu$ uncertainty in the HGCA.

Below we derive expressions for the stellar position and velocity due to a companion, and use them to model $\Delta\mu$. Calculating $\vec{\mu}_{HG}$ requires the average stellar position over each mission, while $\vec{\mu}_G$ requires the average stellar proper motion over only the *Gaia* mission.

In a two-body system composed of a host star and a bound companion, the star's position in the orbital plane relative to the system barycenter is ([Murray and Dermott 2010](#), eq. 2.41)

$$\begin{aligned}
X &= -a_\star(\cos E - e) \\
Y &= -a_\star\sqrt{1 - e^2} \sin E,
\end{aligned}
\tag{3.13}$$

where $a_\star = a \frac{m_c}{m_\star + m_c}$ is the semi-major axis of the star's orbit and the positive X -axis is in the direction of the companion's periastron. We use uppercase letters to refer to coordinates in the orbital plane, and lowercase letters for the sky plane. The average position over a time interval $[t_1, t_2]$ can be calculated analytically in the usual way: for the X -component, it is

$$\langle X \rangle = \frac{1}{t_2 - t_1} \int_{t_1}^{t_2} X(t) dt,
\tag{3.14}$$

with a similar formula for $\langle Y \rangle$. We may reformulate this integral as:

$$\langle X \rangle = \frac{1}{t_2 - t_1} \int_{E(t_1)}^{E(t_2)} X(E) \frac{dt}{dE} dE.
\tag{3.15}$$

We have $X(E)$ from Equations 3.13 and $\frac{dt}{dE} = \frac{P(1 - e \cos E)}{2\pi}$ can be obtained from Equation 3.9. Carrying out the above integral and the corresponding one for Y yields

$$\begin{aligned}
\langle X \rangle &= \frac{-a_\star P}{2\pi(t_2 - t_1)} \left[(1 + e^2) \sin E - \frac{e}{4}(6E + \sin(2E)) \right]_{E(t_1)}^{E(t_2)} \\
\langle Y \rangle &= \frac{a_\star P \sqrt{1 - e^2}}{2\pi(t_2 - t_1)} \left[\cos E - \frac{e}{2} \cos^2(E) \right]_{E(t_1)}^{E(t_2)}.
\end{aligned}
\tag{3.16}$$

To calculate average proper motion over the same time interval $[t_1, t_2]$, we simply evaluate Equations 3.13 at the interval boundaries and divide their difference by the elapsed time:

$$\langle \dot{X} \rangle = \frac{-1}{t_2 - t_1} \left[a_* (\cos E - e) \right]_{E(t_1)}^{E(t_2)} \quad (3.17)$$

$$\langle \dot{Y} \rangle = \frac{-1}{t_2 - t_1} \left[a_* \sqrt{1 - e^2} \sin E \right]_{E(t_1)}^{E(t_2)}.$$

Equations 3.16 and 3.17 allow us to define the average stellar position and proper motion relative to the system barycenter in the orbital plane:

$$\vec{r}_{orb} = \begin{bmatrix} \langle X \rangle \\ \langle Y \rangle \\ 0 \end{bmatrix}, \quad \vec{v}_{orb} = \begin{bmatrix} \langle \dot{X} \rangle \\ \langle \dot{Y} \rangle \\ 0 \end{bmatrix}. \quad (3.18)$$

To express these vectors in the observer frame, that is, with the x - and y -axes in the sky plane and the z -axis toward the observer, we apply the rotation matrix \mathbf{R} (Murray and Dermott, 2010), which is given in its full form in Appendix 3.12.

$$\vec{r}_{obs} = \mathbf{R} \vec{r}_{orb} \quad (3.19)$$

$$\vec{v}_{obs} = \mathbf{R} \vec{v}_{orb}$$

We project these three-dimensional vectors onto the sky by ignoring the z -component, and convert to angular coordinates using the system's distance from Earth. The anomalous position $\vec{\rho}_{anom}$ and proper motion $\vec{\mu}_{anom}$ over either *Hipparcos* or *Gaia* are given by

$$\begin{aligned}
\vec{\rho}_{anom} &= \begin{bmatrix} \alpha_{anom}^* \\ \delta_{anom} \end{bmatrix} = \frac{1}{d} \begin{bmatrix} r_{obs,x} \\ r_{obs,y} \end{bmatrix} \\
\vec{\mu}_{anom} &= \begin{bmatrix} \mu_{\alpha^*} \\ \mu_{\delta} \end{bmatrix} = \frac{1}{d} \begin{bmatrix} v_{obs,x} \\ v_{obs,y} \end{bmatrix},
\end{aligned} \tag{3.20}$$

and the absolute position and proper motion at the mission midpoint t_{mid} are

$$\begin{aligned}
\vec{\rho}_{abs} &= \begin{bmatrix} \alpha_{abs}^* \\ \delta_{abs} \end{bmatrix} \\
&= \begin{bmatrix} \alpha_0^* + \mu_{0,\alpha^*} \cdot (t_{mid} - t_0) + \alpha_{anom}^* \\ \delta_0 + \mu_{0,\delta} \cdot (t_{mid} - t_0) + \delta_{anom} \end{bmatrix} \\
\vec{\mu}_{abs} &= \vec{\mu}_0 + \vec{\mu}_{anom},
\end{aligned} \tag{3.21}$$

where the subscript ‘0’ refers to the barycentric position and proper motion at the reference epoch t_0 and $\alpha^* \equiv \alpha \cos \delta$, where δ is the Dec at the epoch at which α is evaluated.³

We use the above results to estimate 1) $\{\alpha_{H,abs}^*, \delta_{H,abs}\}$, the stellar RA/Dec at the *Hipparcos* midpoint $t_{H,mid}$; 2) $\{\alpha_{G,abs}^*, \delta_{G,abs}\}$, the stellar RA/Dec at the *Gaia* midpoint $t_{G,mid}$; and 3) $\{\mu_{\alpha,G,abs}^*, \mu_{\delta,G,abs}\}$, the stellar proper motions in the RA/Dec directions at $t_{G,mid}$. We provide here the procedure for calculating the RA component of the position-derived proper motion $\mu_{HG,abs}$. The calculation for the Dec component is analogous.

³For concision, we misuse the α^* notation in the case of α_{abs}^* , as it is composed of multiple terms evaluated at different epochs.

$$\begin{aligned}
\mu_{HG,\alpha,abs*} &= \frac{\alpha_{G,abs*} - \alpha_{H,abs*}}{t_{G,mid} - t_{H,mid}} \\
&= \frac{1}{t_{G,mid} - t_{H,mid}} \\
&\quad \left[[\alpha_0 * + \alpha_{G,anom*} + \mu_{0,\alpha*} \cdot (t_{G,mid} - t_0)] \right. \\
&\quad \left. - [(\alpha_0 * + \alpha_{H,anom*}) + \mu_{0,\alpha*} \cdot (t_{H,mid} - t_0)] \right] \\
&= \frac{\alpha_{G,anom*} - \alpha_{H,anom*} + \mu_{0,\alpha*} \cdot (t_{G,mid} - t_{H,mid})}{t_{G,mid} - t_{H,mid}} \\
&= \frac{\alpha_{G,anom*} - \alpha_{H,anom*}}{t_{G,mid} - t_{H,mid}} + \mu_{0,\alpha*} \\
&= \mu_{HG,\alpha,anom*} + \mu_{0,\alpha*}.
\end{aligned} \tag{3.22}$$

Combining $\vec{\mu}_{HG,abs}$ with $\vec{\mu}_{G,abs}$ from Equations 3.21, we have our final result:

$$\Delta\mu = |\vec{\mu}_{G,abs} - \vec{\mu}_{HG,abs}| = |\vec{\mu}_{G,anom} - \vec{\mu}_{HG,anom}|. \tag{3.23}$$

The modeled $\Delta\mu$ is thus a function only of the anomalous proper motions, i.e., those induced by the companion. As in Section 3.3.1, we calculate the model log-likelihood as

$$\begin{aligned}
\ln(\mathcal{L}_{astro}(\boldsymbol{\theta})) &= -\frac{1}{2}\chi_{astro}^2 + C_{astro} \\
&= -\frac{1}{2} \left(\frac{(\Delta\mu_{data} - \Delta\mu)^2}{\sigma_{\Delta\mu_{data}}^2} \right) + C_{astro}
\end{aligned} \tag{3.24}$$

3.3.3 Direct Imaging Constraints

RV and astrometric trends are often insufficient to constrain a companion’s properties, either because one data set is not available (e.g., any star that is not in the original *Hipparcos* catalog does not have an HGCA acceleration) or because the constraints they do provide rule out the same regions of parameter space, leaving the same $a-m_c$ degeneracy described in Section 3.3.2. In these cases, we turn to direct imaging to place an upper limit on the companion mass.

Our data is the measured contrast curve, a table of angular separations and corresponding magnitude differences indicating the dimmest detectable companion at a given projected separation from the host star. For simplicity, we treat the contrast curve as a step function with no associated uncertainties. That is, at a given angular separation, any companion dimmer than the listed limit is completely undetectable, whereas any companion brighter than the limit would be detected in all cases. Our goal is to calculate a model companion’s angular separation and magnitude difference to compare to the contrast curve. We begin with the angular separation.

3.3.3.1 Angular Separation Calculation

Similar to Equations 3.13, we calculate the host-companion separation via

$$\begin{aligned} x &= a(\cos E - e) \\ y &= a\sqrt{1 - e^2} \sin E, \end{aligned} \tag{3.25}$$

where we now use the full semi-major axis a instead of a_* . Rotating the separation vector into the sky plane with the rotation matrix \mathbf{R} and dividing by the distance to the system d , we obtain the projected angular separation ρ :

$$\vec{\rho} = \frac{\mathbf{R}}{d} \begin{bmatrix} x \\ y \\ 0 \end{bmatrix}. \quad (3.26)$$

This approach is fully consistent with Sections 3.3.1 and 3.3.2 in that it incorporates all orbital parameters into the modeled quantity.

The angular separation calculation above accounts for the fact that each model companion’s projected separation is a function not only of a , but also of e , i , ω , and E . However, this detailed procedure is expensive, requiring nearly 300% and 70% the time of the RV and astrometry calculations, respectively. We detail an approximate calculation of ρ in Appendix 3.11 which significantly decreases run time at the cost of a slight reduction in accuracy.

3.3.3.2 Contrast Calculation

After modeling a companion’s angular separation, we seek to convert its mass m_c to a Δmag contrast in the appropriate band. We model contrast as dependent on m_c and the stellar V_{mag} only. We linearly interpolated magnitude-mass relations for both stellar (Pecaut and Mamajek 2013a, Table 5) and brown dwarf (Baraffe et al. 2003, Table 4) companions in multiple bandpasses to define a function $F(m_c)$ which converts a model companion mass to Δmag in whichever of the following bands most closely matches the band of the given contrast curve: $\{V, R, I, J, H, K, L'\}$. Pecaut and Mamajek (2013a) do not include magnitude relations for the K or L' bands, though they do for K_s and $W1$. We approximated that $K_s \approx K$ ($2.15 \mu m \approx 2.2 \mu m$) and $W1 \approx L'$ ($3.37 \mu m \approx 3.78 \mu m$) to concatenate the two tables. The brown dwarf mass-magnitude relations of Baraffe et al. (2003) correspond to mature systems (5 Gyr).

We also performed a linear interpolation of the measured contrast curve, yielding another

function $f_{data}(\rho)$ which converts measured angular separation to measured Δmag contrast. The imaging ‘data’ is then the function f_{data} , together with the assumption that at any separation ρ' , no companion with $\Delta\text{mag} < f_{data}(\rho')$ was detected.

We therefore have that for a given model separation ρ and contrast $\Delta\text{mag} = F(m_c)$, both derived from the initial model parameters $\boldsymbol{\theta}$, the log-likelihood that no companions were detected with $\Delta\text{mag} < f_{data}(\rho)$ is given by

$$\ln(\mathcal{L}_{imag}(\boldsymbol{\theta})) = \begin{cases} -\infty & \Delta\text{mag} < f_{data}(\rho) \\ 0 & \Delta\text{mag} \geq f_{data}(\rho) \end{cases} + C_{imag} . \quad (3.27)$$

We visualize `ethraid`’s imaging likelihood calculation in Figure 3.3.

The independence of the RV, astrometric, and imaging measurements allows us to find the log-likelihood of all three data sets in light of a model orbit by simply summing Equations 3.11, 3.24, and 3.27.

3.4 Performance

Four processes contribute meaningfully to the computational cost of an orbital fit. These include sampling orbital parameters from their prior PDFs and, for each sampled orbit, calculating the likelihood of each of the RV, astrometry, and/or direct imaging data sets. Therefore, the total time required to run an orbital fit is predetermined by the number of orbital models sampled (a value input by the user) and the number of data sets provided.

The time required to sample one model orbit and calculate the likelihood of all three data sets conditioned on that model is $\sim 5.75 \mu\text{s}$ using a single core of a 2.6 GHz Intel Core i7

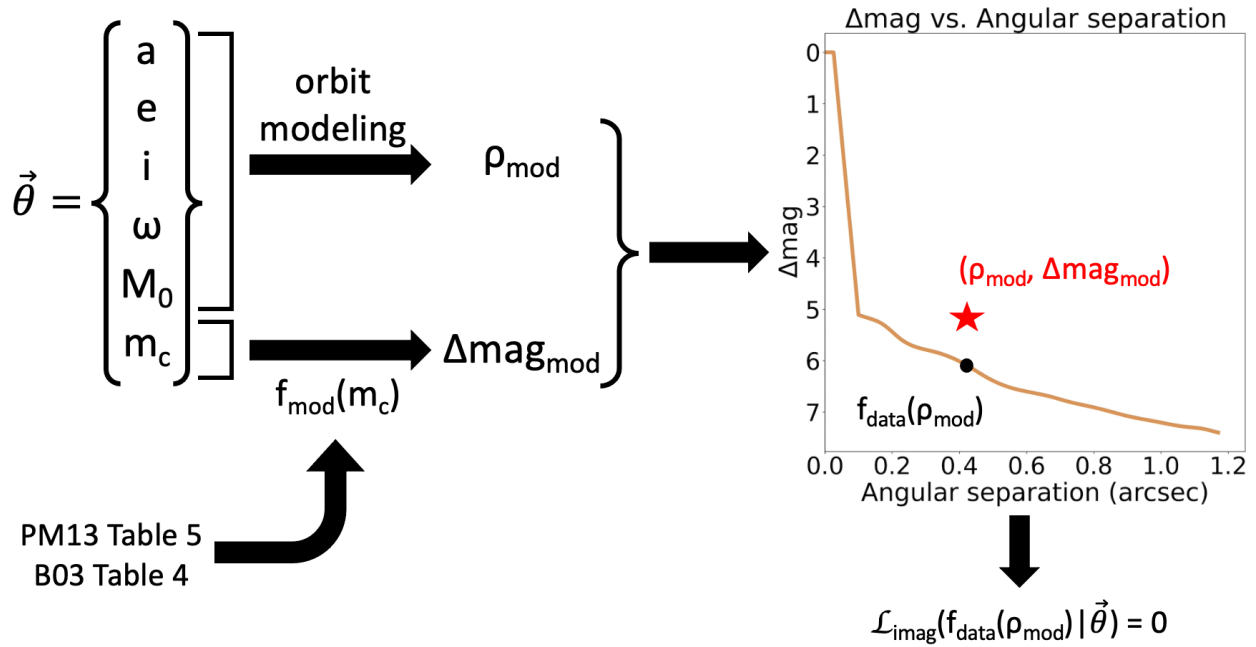


Figure 3.3: `ethraid`'s likelihood calculation for direct imaging. Beginning with a set of sampled parameters (left), `ethraid` models angular separation (either *exactly* or *approximately*) using the orbital elements, and contrast using the companion mass, together with a linear interpolation function derived from Table 5 of [Pecaut and Mamajek \(2013a\)](#) and Table 4 of [Baraffe et al. \(2003\)](#), denoted by 'PM13' and 'B03,' respectively. `ethraid` then determines whether the model companion's brightness would have exceeded the minimum detectability threshold at the model separation in the real imaging data (gold line) and assigns a likelihood of 0 for detectable companions and 1 for non-detectable companions. The example model in the diagram (red star) falls above the threshold, indicating a companion that would have been detected if it were truly in the system, so we assign it a likelihood of 0.

processor. `ethraid` takes another $0.25 \mu\text{s}$ to multiply the three likelihoods to produce the combined likelihood, for a total of $6 \mu\text{s}$ per model. The average fraction of total run time required for each of these steps is: sampling - 6.8%, RVs - 11.0%, astrometry - 46.3%, imaging - 31.8%, combined likelihood - 4.1%. If the approximate angular separation calculation is used for the imaging posterior instead of the detailed calculation (see Section 3.3.3), the share of time required by the imaging calculations drops to $< 1\%$, reducing the overall run time by $\sim 30\%$.

`ethraid` implements the core calculations of Section 3.3 in Cython, which provides a $\sim 5\text{x}$ speedup over the standard Python equivalent functions, allowing users to produce informative posterior plots with $10^6 - 10^7$ sampled models on one core in 6 – 60 seconds.

Two potential improvements to the current approach would substantially increase `ethraid`'s performance. First, the likelihood calculations are trivially parallelizable. Calculating the likelihoods for all data sets concurrently could decrease the total run time by 50%, and further parallelizing within data sets would give greater speedups. Second, the likelihood and sampled parameter lists tend to overload the working memory when the number of model orbits is large ($\gtrsim 10^8$), causing significant slowdowns. An alternative would be to store these arrays in temporary cached files, or to perform all necessary calculations associated with a given model or likelihood and then overwrite it immediately.

3.5 Usage, fitting, saving, and plotting

`ethraid` is installable through pip, and basic usage instructions are available on GitHub.

The typical use case of `ethraid` is for a system with an unexplained RV trend, though it may be run on systems with any combination of constraints from RVs, astrometry, or imaging.

The majority of parameters required to run an `ethraid` fit are stored in the corresponding system’s `.py` configuration file. An `ethraid` configuration file contains all of the RV, astrometry, and direct imaging data needed to carry out the forward modeling algorithm laid out in Sections 3.2 and 3.3 (with the exception of the optional contrast curve for direct imaging constraints), as well as parameters for saving and plotting the calculated posteriors. We provide descriptions of these inputs in Table 3.1.

Table 3.1: Configuration file parameters

Parameter Name	Data Type	Default Value	Description
General			Parameters unrelated to any one data set, but necessary to perform fits
<code>num_points</code>	Integer	10^6	Number of model orbits to sample
<code>grid_num</code>	Integer	[required]	Number of bins to divide parameter space into
<code>min_a</code>	Float	1	Lower bound of semi-major axis sampling range (AU)
<code>max_a</code>	Float	100	Upper bound of semi-major axis sampling range (AU)
<code>min_m</code>	Float	1	Lower bound of companion mass sampling range (M_J)
<code>max_m</code>	Float	1000	Upper bound of companion mass sampling range (M_J)
<code>e_dist</code>	String	‘piecewise’	Prior distribution from which model eccentricity values are sampled; options: {‘zero’, ‘uniform’, ‘kipping’, ‘piecewise’}
Stellar			Parameters of the host star or whole system
<code>star_name</code>	String	[required]	Host star name to label files; need not match any catalog
<code>m_star</code>	Float	[required]	Host star mass (M_J)
<code>d_star</code>	Float	[required]	Earth-system distance (AU)
RVs			
<code>run_rv</code>	Bool	[required]	Whether to use RV data; if False, all other RV arguments are optional
<code>gammadot</code>	Float	—	Linear RV trend (m/s/day)
<code>gammadot_err</code>	Float	—	Error on <code>gammadot</code> (m/s/day)
<code>gammaddot</code>	Float	—	Quadratic RV curvature (m/s/day ²); setting to <code>None</code> excludes curvature
<code>gammaddot_err</code>	Float	—	Error on <code>gammaddot</code> (m/s/day ²); setting to <code>None</code> excludes curvature
<code>rv_epoch</code>	Float	—	Epoch approximating the midpoint of the RV baseline (BJD)
Astrometry			
<code>run_astro</code>	Bool	[required]	Whether to use astrometry data; if False, all other astrometry arguments are optional
<code>delta_mu</code>	Float	—	Magnitude of proper motion change (mas/yr)
<code>delta_mu_err</code>	Float	—	Error on <code>delta_mu</code> (mas/yr)

(Continued on next page)

(Continued from previous page)

Parameter Name	Data Type	Default Value	Description
<code>hip_id</code>	String	—	Hipparcos identifier of host star; alternative to providing <code>delta_mu</code> directly
<code>gaia_id</code>	String	—	Gaia DR3 identifier of host star; alternative to providing <code>delta_mu</code> directly
Direct Imaging			
<code>run_imag</code>	Bool	[required]	Whether to use imaging data; if False, all other imaging arguments are optional
<code>imag_calc</code>	String	‘exact’	‘exact’ or ‘approx’: calculate imaging posterior exactly or approximately
<code>vmag</code>	Float	—	Host star V magnitude
<code>imag_wavelength</code>	Float	—	Wavelength of imaging data (μm)
<code>contrast_str</code>	String	—	Path to .csv file containing contrast curve
<code>imag_epoch</code>	Float	—	Epoch at which imaging data was taken (BJD)
Save			
<code>save</code>	List	[‘proc’]	Save processed arrays (‘proc’; binned 2D posteriors) and/or raw arrays (‘raw’; unbinned 1D likelihoods)
<code>out_dir</code>	String	‘’	Path to save directory
Plot			
<code>scatter_plot</code>	List	—	List of (a, m_c) pairs to plot 1 or more known companion positions on 2D posterior
<code>num_points</code>	Integer	10^6	Number of model orbits to sample
<code>grid_num</code>	Integer	[required]	Number of bins to divide parameter space into

Note: `ethraid`’s configuration files are analogous to those used by `orvara`, and we model this table after Table 2 in [Brandt et al. \(2021\)](#).

3.5.1 Command Line Interface

`ethraid` supports three different commands from the command line: `run`, `plot`, and `lims`. `run` samples the six-dimensional parameter space and calculates a posterior for each data set provided, plus an additional combined posterior conditioned on all provided data sets. Using the `save` parameter in the configuration file, the user has the option to save the ‘raw’ unbinned posteriors, which they may reshape as desired, or the ‘processed’ posteriors, which

are smaller and load more quickly but cannot be reshaped. All arrays are saved as `hdf5`⁴ files in the specified output directory.

After running a fit, the user may access and plot the saved arrays using the `plot` command. `plot` loads a set of posterior arrays from the specified file path and optionally produces and saves three figures. The first includes two one-dimensional marginalized posterior PDFs side by side, one for a and the other for m_c . The second is analogous to the first, but shows CDFs instead of PDFs. The third is a two-dimensional plot in m_c - a space displaying the posteriors conditioned on each data set individually as well as the combined posterior. We show examples of the one-dimensional CDFs and two dimensional PDFs in in Figure 3.1.

The `lims` command simply prints the 2σ confidence intervals (i.e., 2.5th and 97.5th percentiles) of both the m_c and a posterior PDFs to the terminal. It is intended to give a quick quantitative summary of the orbit fit. Users may load the raw or processed posterior arrays directly if they wish to calculate more detailed statistics. We caution that the bare numerical results returned by `lims` will not necessarily give an accurate summary of the posterior distribution, particularly in cases where the posterior is under-sampled. We encourage users to use both the one- and two-dimensional posterior plots to guide their interpretation of the confidence intervals returned by this command.

Finally, the `all` command runs `run`, `plot`, and `lims` sequentially. We give more information on the command line interface in Table 3.2.

Table 3.2: Command line interface parameters

Argument Name	Data Type	Default Value	Description
General			
<code>-version</code>	—	—	Version number of current <code>ethraid</code> installation
All			
Arguments common to all commands			
<code>-od/-outdir</code>	String	‘ ’	Directory to which probability arrays and posterior plots will be saved

Continued on next page

⁴<https://www.h5py.org/>

(Continued from previous page)

Argument Name	Data Type	Default Value	Description
<code>-v/-verbose</code>	—	False	Whether to print verbose output; no arguments needed.
<code>run</code>			Command to perform orbital fit
<code>-cf/-config</code>	String	[required]	Relative path of configuration file
<code>plot</code>			Command to plot fit results
<code>-cf/-config</code>	String	[required]	Path to configuration file
<code>-rfp/-read_file_path</code>	String	[required]	Path to saved <code>.h5</code> results file
<code>-t/-type</code>	List	[required]	‘1d’ and/or ‘2d’; Whether to save 1d or 2d posterior plots. No brackets or quotation marks needed; separate multiple arguments by a space
<code>lims</code>			Command to display 95% a and M_p confidence intervals
<code>-rfp/-read_file_path</code>	String	[required]	Path to saved <code>.h5</code> results file
<code>all</code>			Command to run the <code>run</code> , <code>plot</code> , and <code>lims</code> commands sequentially
<code>-cf/-config</code>	String	[required]	Path to configuration file
<code>-rfp/-read_file_path</code>	String	[required]	Path to saved <code>.h5</code> results file
<code>-t/-type</code>	List	[required]	‘1d’ and/or ‘2d’; whether to save 1d or 2d posterior plots. No brackets or quotation marks needed; separate multiple arguments by a space

3.6 Validation

We tested `ethraid` on four systems to judge its strengths and weaknesses in estimating companion parameters. We chose the first two systems, HD 117207 and TOI-1694, to illustrate `ethraid`’s capacity to characterize single companions with fractional orbital coverage. Both systems host RV-characterized giant planets with well-constrained orbital parameters. We find that `ethraid`’s parameter estimates are consistent with these ‘ground truth’ values, regardless of the planet’s phase during the interval of RV observation. We chose the other two systems, HD 114729 and HD 12661, to demonstrate `ethraid`’s failure modes. Both of these systems host two long-period giant companions, violating one of `ethraid`’s key assumptions that RV/astrometric signatures originate from a single companion. `ethraid`’s failure to accurately characterize the companions in either system illustrates the perils of applying this

code blindly.

We designed our validation algorithm to mimic real applications of `ethraid`. For systems exhibiting periodic RV variability, we identified and isolated a subset of the RVs which we then subdivided into ‘slices’ of equal duration. We chose the number of slices so that the RV variability was approximately linear/quadratic over each slice, emulating a real data set with limited coverage of the companion’s phase. We used `radvel` to fit a second order polynomial to each slice and recorded the fitted trend and curvature terms. We then applied `ethraid` to each fitted trend/curvature pair and determined whether the results were consistent with the known companion parameters. For all fits, we used the ‘`piecewise`’ eccentricity prior and simulated 10^8 model orbits. We included astrometric trends from the *Hipparcos-Gaia* Catalog of Accelerations (HGCA; Brandt 2021) in our analysis when available.

3.6.1 Case Study: HD 117207’s 7.5-year super-Jupiter is identified using 1.8-year baselines

HD 117207 is a chromospherically quiet ($\log R'_{HK} = -5.06$) G8 dwarf hosting a super-Jupiter companion, HD 117207 b, with minimum mass and separation initially reported as $2.06 M_J$ and 3.78 AU (Marcy et al., 2005b). Rosenthal et al. (2021), using RVs spanning over 20 years, refined these values to $m_c \sin i = 1.87 \pm 0.075 M_J$ and $a = 3.744^{+0.059}_{-0.060}$ AU.

We identified a roughly 7.5-year section of the full time series and divided it into four slices. We used `radvel` (Fulton et al., 2018) to fit linear and quadratic trend terms to these slices. The results of this fitting procedure are shown in the top five panels of Figure 3.4.

We supplied the linear and quadratic trends from each slice as inputs to a partial orbit fit using `ethraid`. We also retrieved this star’s astrometric trend of 0.13 ± 0.03 mas/yr from the HGCA and included it in our model. `ethraid` performed each joint RV/astrometric fit

in about six minutes. We provide the posteriors of our partial orbit analysis of each slice in Figure 3.4 and compare these results to the known parameters of HD 117207 b, shown in each panel as a gold star. In all four cases, the 68% confidence interval derived by `ethraid` encompasses the true planet parameters.

We also validated our results for this system against `orvara`. We used the same HGCA astrometry and the raw RVs for each slice to emulate our `ethraid` fits. We ran 10 temperatures and 20 walkers over 10^5 steps, which took about seven minutes (comparable to our `ethraid` runs). However, these fits did not converge and gave substantially broader mass and separation estimates than we obtained with `ethraid`. After increasing to 10^6 steps, we obtained parameter estimates comparable to those from `ethraid` in about 80 minutes. We conclude that `ethraid`'s data compression approach allows it to match the performance of other robust fitters with minimal loss of information in the regime of highly limited orbital coverage and with only RVs and absolute astrometry.

3.6.2 Case Study: TOI-1694's companion mass is bounded by direct imaging

TOI-1694 is an early K-dwarf with low chromospheric activity ($\log R'_{HK} = -5.0$) hosting a Jupiter analog with a minimum mass of $1.05 \pm 0.05 M_J$ at a separation of 0.98 ± 0.01 AU (Van Zandt et al., 2023).

We divided the full two-year time series into three slices and fit linear and quadratic trend terms to them using `radvel` (Fulton et al., 2018). The results of this fitting procedure are shown in the top four panels of Figure 3.5.

We supplied the linear and quadratic trends from each slice as inputs to a partial orbit fit using `ethraid`. This star is not listed in the HGCA, and therefore has no available

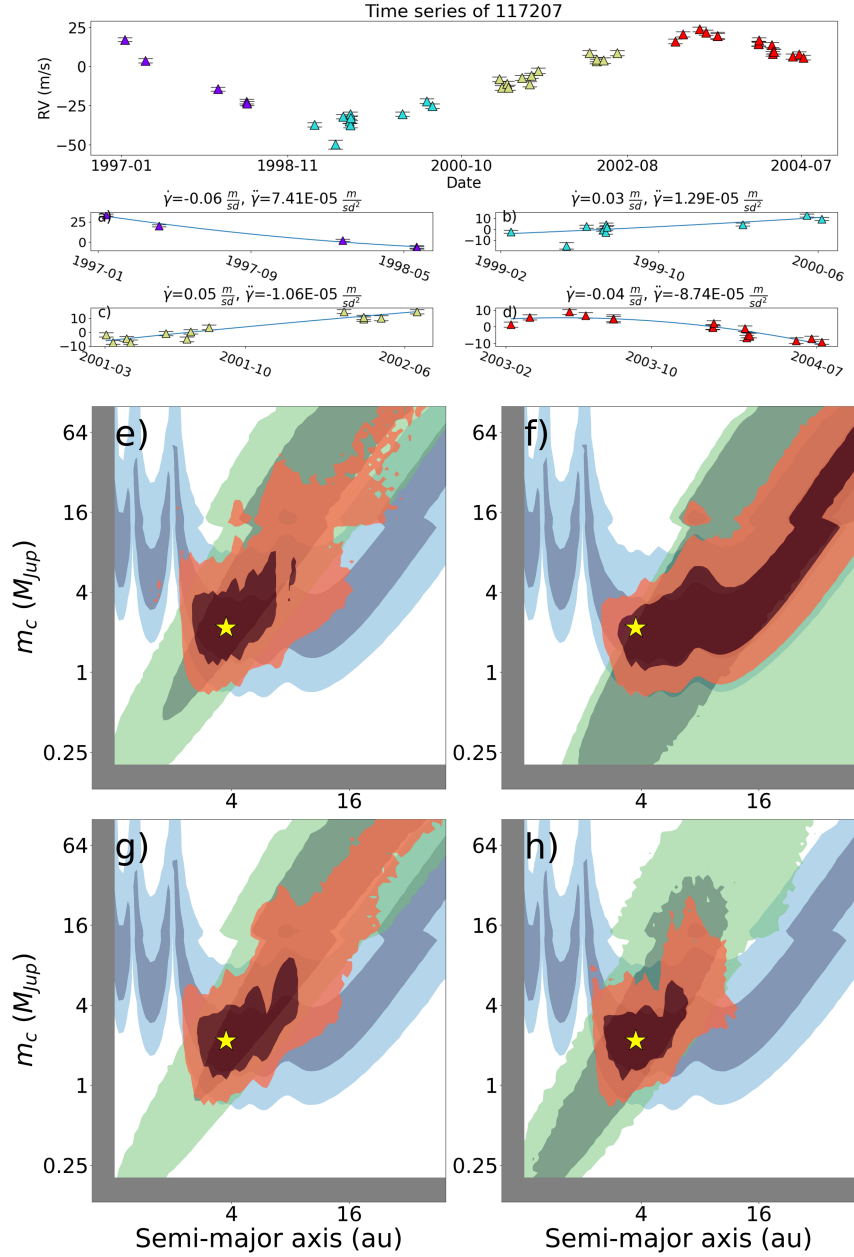


Figure 3.4: The top panel shows a 7.5-year subset of HD 117207’s RV time series, divided into four slices based on the epoch in which the RVs were measured. Panels a)-d) show the RVs from each slice, along with the linear/quadratic trend fit to those RVs using `radvel`. We show the measurement error of each RV with horizontal black lines. We used `ethraid` to model each trend/curvature pair, along with HGCA astrometry, in panels e)-h), respectively. The gold star in each panel shows HD 117207 b’s semi-major axis and $m_c \sin i$ values measured by long-baseline RV surveys: $a = 3.744$ AU, $m_c \sin i = 1.87 M_J$, where we have approximated a conversion from $m_c \sin i$ to m_c by dividing by the median $\sin i$ value of 0.866. The overlap between `ethraid`’s predicted parameters and the true values in all four panels demonstrates `ethraid`’s reliability in estimating companion parameters over a range of orbital phases.

astrometric trend. However, we included direct imaging of this system (Mistry et al., 2023) obtained in the *I*-band (832 nm) with the 'Alopeke speckle imager (Scott et al., 2021) in our analysis. We provide the posteriors from our partial orbit analysis of each slice in Figure 3.5. Although in this case the RV trend and imaging cannot disambiguate between planets, brown dwarfs, and low-mass stars, they are sufficient to rule out high-mass stars as well as planetary and brown dwarf companions beyond ~ 10 AU. Additionally, detection of curvature in some slices strongly favors models with shorter periods. The RV posteriors are consistent with TOI-1694 b's true parameters in all cases.

3.6.3 Case Study: HD 114729's two companions conspire to produce misleading parameter estimates

HD 114729 is an inactive ($\log R'_{HK} = -5.02$), metal-poor ($[Fe/H] = -0.22$) solar analog (G0 V) hosting a sub-Jupiter companion with a minimum mass and semi-major axis of $m_c \sin i = 0.892 \pm 0.053 M_J$ and $a = 2.094 \pm 0.022$ AU (Rosenthal et al., 2021). We refer to this planet as HD 114729 Ab. This system also hosts an M dwarf companion: Mugrauer et al. (2005) directly imaged HD 114729 and found a bound companion at a projected separation of 282 AU. Using the stellar cooling models of Baraffe et al. (1998), as well as Butler et al. (2003)'s chromospherically derived age of 6 Gyr, Mugrauer et al. (2005) estimated HD 114729 B's mass to be $0.253 M_\odot$.

We isolated a subset of the RV baseline covering approximately four years, divided it into four equal slices, and fit a second order polynomial to the RVs in each slice. The time series slices and polynomial fits are shown in the top of Figure 3.6.

We used `ethraid` to derive m_c - a posteriors for each slice, incorporating both the fitted trend and curvature as well as HGCA astrometry (0.11 ± 0.03 mas/yr), which is the same for all slices. In all cases, `ethraid`'s derived posterior distributions are discrepant with the true

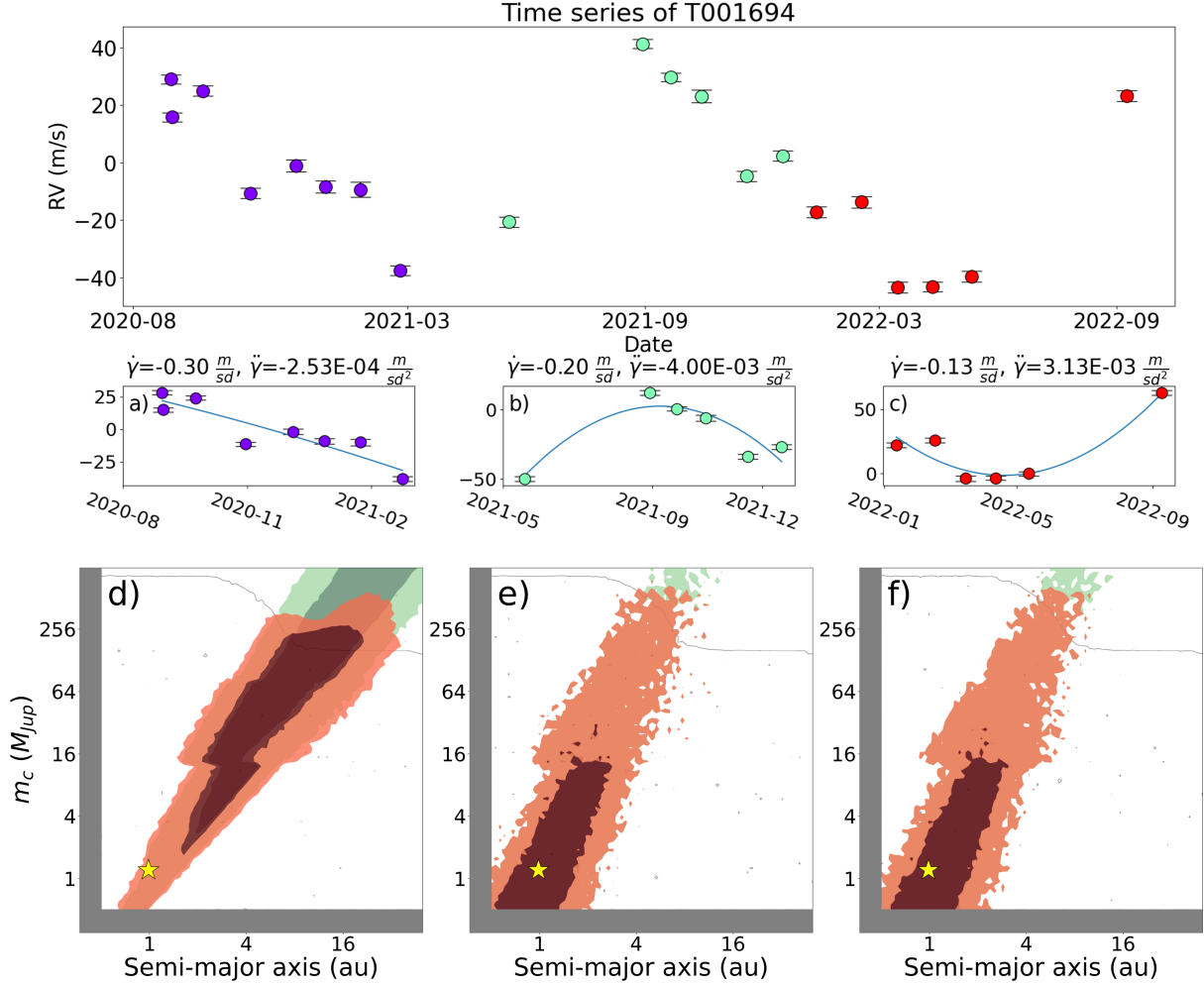


Figure 3.5: Same as Figure 3.4 for TOI-1694’s two year baseline. The gray lines in panels d)-f) show posteriors derived from direct imaging. The gold stars show TOI-1694 b’s median semi-major axis and adjusted $m_c \sin i$ values measured by [Van Zandt et al. \(2023\)](#): $a = 0.98$ AU, $m_c \sin i = 1.05 M_J$. Without astrometry, the trend and imaging data provide too little information to constrain the planet’s mass and separation. However, they are able to rule out massive stars as well as the (a, m_c) pairs in the white regions. Note also that the posteriors in panels e) and f) favor shorter-period models due to the higher RV curvature associated with their trends.

mass and semi-major axis of HD 114729 Ab at $> 2\sigma$ (Figure 3.6, bottom). This disagreement is driven by the astrometric data. The RV variability in the one-year slices is dominated by HD 114729 Ab because of its relatively short ~ 3 -year orbital period, and indeed the RV-only posteriors agree more closely with that planet’s true parameters. Meanwhile, the astrometric variability reported in the HGCA is measured over 25 years, and thus includes a strong contribution from HD 114729 B’s 4400-year orbit. We also plot this companion’s parameters in Figure 3.6 to demonstrate its consistency with the astrometry data.

Our analysis of HD 114729 illustrates how `ethraid`’s fits may be misleading in the case of multiple companions. It is very valuable to provide direct imaging constraints whenever available to mitigate this failure mode.

3.6.4 Case Study: HD 12661’s two planets are misinterpreted as a single companion

HD 12661 is an inactive ($\log R'_{HK} = -5.06$), metal-rich ($[Fe/H] = 0.293$) G6 V star with two gas giant companions (Fischer et al., 2001, 2003). HD 12661 b has a minimum mass of $m_c \sin i = 2.283^{+0.062}_{-0.063} M_J$ and a separation of $a = 0.824 \pm 0.011$ AU, while HD 12661 c has $m_c \sin i = 1.855 \pm 0.054 M_J$ and $a = 2.86^{+0.038}_{-0.039}$ AU (Rosenthal et al., 2021).

We chose a ~ 2.5 -year subset of the RVs and divided it into three slices, each covering the same time interval. We fit linear and quadratic terms to each slice. The RV subset and slices are shown in the upper panels of Figure 3.7.

We used the trend and curvature derived for each slice in an `ethraid` partial orbit fit. We also included the astrometric trend of 0.23 ± 0.05 mas/yr. The orbit posteriors are shown in the lower panels of Figure 3.7, along with the the orbital parameters of HD 12661 b and c. `ethraid`’s RV posteriors are consistent with planet b’s parameters, which is expected

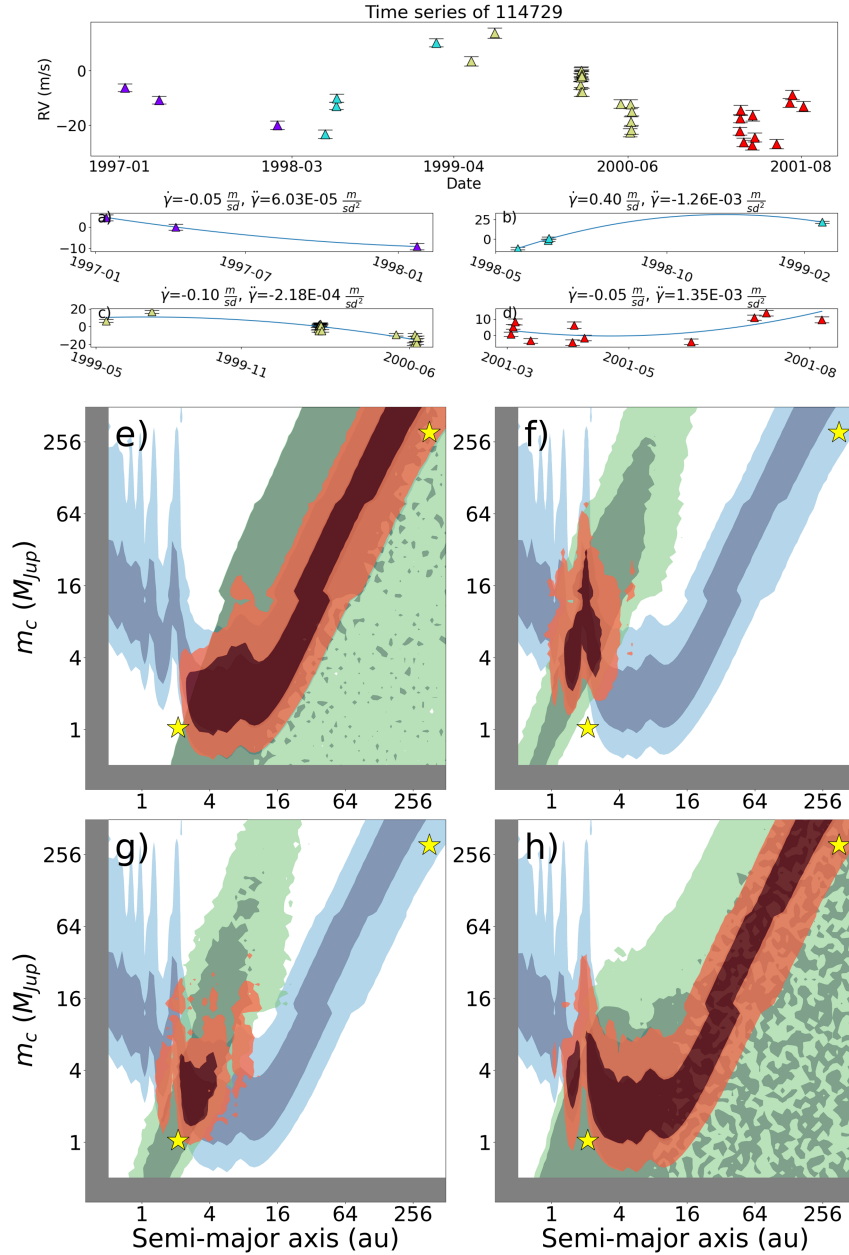


Figure 3.6: Same as Figure 3.4 for HD 114729. The gold star at the lower left of each panel shows the semi-major axis and adjusted $m_c \sin i$ of HD 114729 Ab measured by long-baseline RV surveys: 2.094 AU, $m_c \sin i = 0.892 M_J$. The upper right star shows the same for HD 114729 B, with a projected separation and mass of 282 AU and $M = 0.253 M_\odot$. We estimated HD 114729 B’s true separation by dividing the projected separation of 282 AU by 0.79, as described in Section 3.3.3. Agreement between the planet parameters and the RV posteriors indicates that **ethraid** is correctly recovering HD 114729 Ab’s RV signature. Meanwhile, the consistency between HD 114729 B’s parameters and the astrometric posterior suggests that HD 114729 B produced the astrometric trend. Note that in panels **a)** and **d)**, the fitted trend/curve values had precisions $< 2\sigma$, leading to broad RV posteriors in panels **e)** and **h)**.

because with a larger mass than planet c and a period of 264 days, this planet dominates the RV variability over the 200-day slices. Furthermore, this consistency is not sensitive to the phase or curvature of the RV slices. The slices in Figure 3.7 exhibit linear, quadratic, and higher order curvature, but are all nevertheless consistent with HD 12661 b's parameters in the lower panels.

The astrometry posterior, on the other hand, is consistent with neither planet's parameters. We modeled the combined astrometric signature of both planets and found that planet c dominates this signal due to its wider separation. Furthermore, we found that if planet c's inclination is within 25 degrees of 0 (i.e., a "face-on" orbit), then the resulting underestimate of planet c's mass (a factor of $\gtrsim 2.4$) may account for the disparity between this system's measured and expected astrometric signatures. A third, more distant companion could also explain this signal, though we did not explore this possibility in detail.

Like HD 114729, HD 12661 shows the limitations of `ethraid`'s approach to treating RV/astrometric trends. While planet b dominated the RV trend/curvature because of its short period, planet c had a much greater influence on the astrometric signal. `ethraid`'s assumption that both signals were due to one companion produced constraints inconsistent with either planet. We caution that unless the presence of multiple giant planets can be ruled out, `ethraid`'s single companion assumption may produce false parameter estimates.

3.7 Future Improvements

Development of `ethraid` is ongoing, and we plan to implement a number of improvements in future versions, including:

1. Parallelization of likelihood calculations.

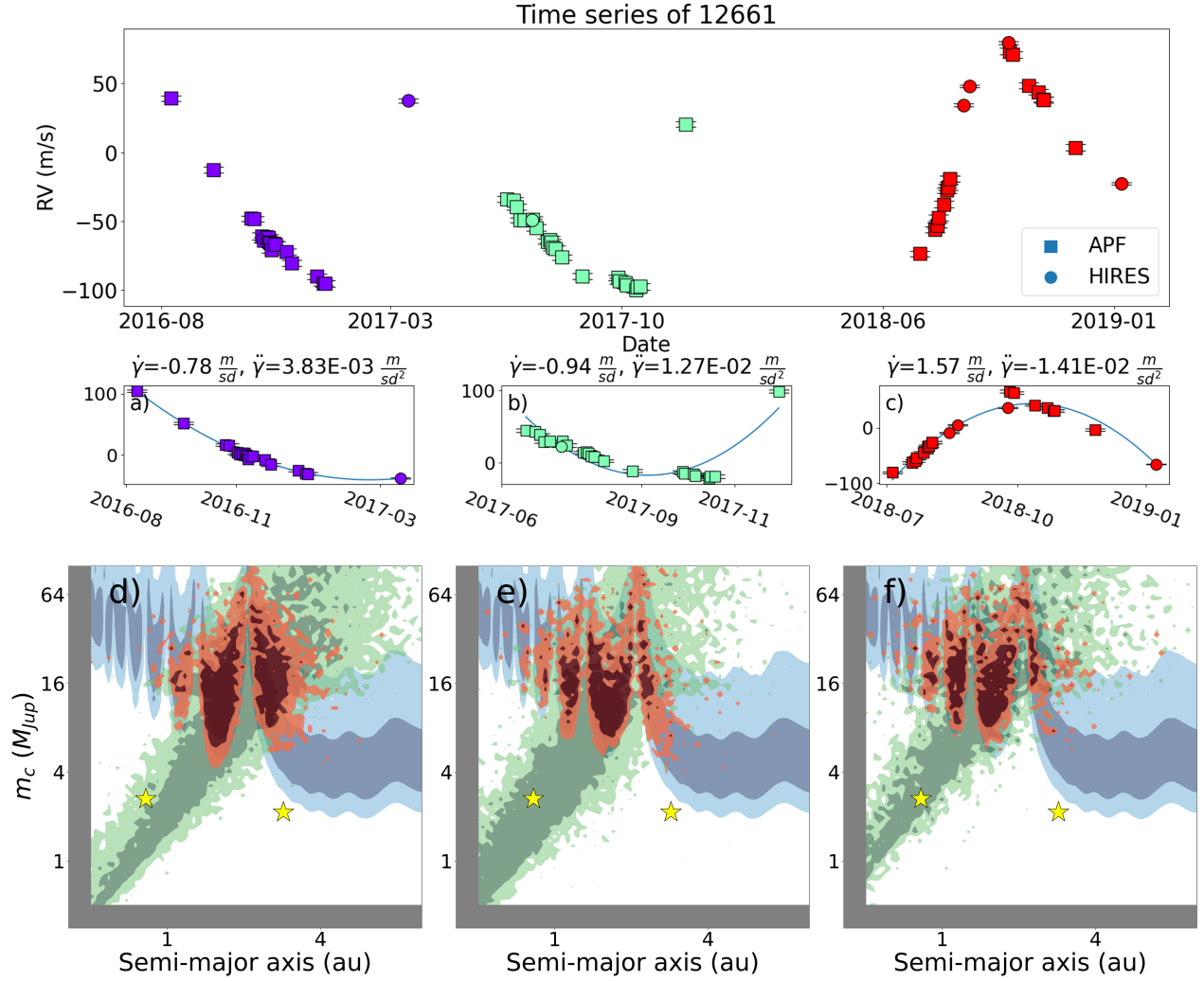


Figure 3.7: Same as Figure 3.4 for HD 12661. For this system, we include RVs from both the Keck/HIRES and APF/Levy instruments. The gold stars show the a and adjusted $m_c \sin i$ values of HD 12661 b (left) and c (right). Planet b dominates the RV signature due to its short period, as shown by its consistency with the green RV posteriors in each slice. Meanwhile, planet c is responsible for the majority of the astrometric signal. The inconsistency between these planets’ measured parameters and the combined posterior (red) shows that **ethraid** misinterpreted these separate contributions as originating from a single object of higher mass.

2. Dynamic likelihood storage to mitigate RAM overload.
3. Analytical removal of the RV and astrometric signatures of known stellar companions, improving `ethraid`'s predictive power in systems like HD 114729 (Section 3.6.3).
4. Improved companion mass prior to reflect the relative prevalences of planets, brown dwarfs, and low-mass stellar companions.
5. Inclusion of brown dwarf cooling models for systems of ages other than 5 Gyr.

We compiled the above improvements based primarily on our own use of `ethraid`, but we welcome contributions from the exoplanet community to make `ethraid` a useful and accessible tool.

3.8 Conclusions

In this work we presented `ethraid`, an open-source Python package for constraining the masses and separations of long-period companions using RVs, astrometry, and direct imaging. `ethraid` uses simple data inputs to calculate RV and astrometric posteriors, requiring only two values and their errors for the first and one value and its error for the second. Due to the limited information content of this data, `ethraid` is designed to broadly constrain companion parameters rather than to produce tight orbital fits, giving a ‘first look’ at the nature of a companion and helping to disambiguate between multiple competing hypotheses (e.g., a close-in planet vs. a distant M dwarf). `ethraid` is pip-installable and may be downloaded from GitHub.

We demonstrated `ethraid`'s strengths and weaknesses by testing it on four systems hosting one or more known companions. HD 114729 (Butler et al., 2003) hosts a giant planet and a stellar companion, and HD 12661 (Fischer et al., 2001, 2003) hosts two gas giant

planets. In both cases, `ethraid`'s assumption of a single companion led to spurious parameter predictions. HD 117207 and TOI-1694 each host only one distant giant planet. `ethraid` consistently recovered HD 117207 b's parameters, and although a lack of astrometric data prevented a recovery of TOI-1694 b, our combined RV-direct imaging analysis ruled out high-mass stellar companions and high-separation ($\gtrsim 10$ AU) planets and brown dwarfs.

`ethraid` leverages up to three exoplanet detection techniques to constrain companion properties given minimal observational data. It is intended to help users evaluate the merit of potential companion models, as opposed to giving precise parameter constraints. We caution that due to `ethraid`'s implicit assumption that any input signals are caused by a single companion, applying it to multi-companion systems may give nonphysical results. Users may run `ethraid` on a system using one configuration file. We plan to maintain and improve `ethraid` so that it may be of use to the community.

Software: `radvel` (Fulton et al., 2018)

3.9 Acknowledgments

J.V.Z. acknowledges support from NASA FINESST Fellowship 80NSSC22K1606. J.V.Z. and E.A.P. acknowledge support from NASA XRP award 80NSSC21K0598. We thank the anonymous reviewer for constructive input on our methodology, which significantly improved this manuscript. We also thank Tim Brandt for useful discussions regarding orbital fitting from limited data.

3.10 Appendix 3A: Posterior Shapes

The RV and astrometry posteriors derived in Section 3.3 take on specific shapes, i.e., m_c - a dependencies. Moreover, these dependencies vary as functions of a and m_c because different approximations hold in different regimes. We describe these dependencies here. Note that `ethraid` does not employ the following analytic descriptions during orbital fits; we provide them to aid the user in interpreting their results.

3.10.1 RV Posterior

We first reproduce Equations 3.5–3.8:

$$\begin{aligned}
 \gamma &= K [e \cos \omega + \cos(\nu + \omega)] \\
 \dot{\gamma} &= -K [\dot{\nu} \sin(\nu + \omega)] \\
 \ddot{\gamma} &= -K [\dot{\nu}^2 \cos(\nu + \omega) + \ddot{\nu} \sin(\nu + \omega)]
 \end{aligned} \tag{3.28}$$

$$K = \sqrt{\frac{G}{1 - e^2}} \frac{m_c \sin i}{\sqrt{a(m_c + m_\star)}} \tag{3.29}$$

$$\dot{\nu} = \frac{2\pi\sqrt{1 - e^2}}{P(1 - e \cos E)^2} \tag{3.30}$$

$$\ddot{\nu} = -\dot{\nu}^2 \frac{2e \sin E}{\sqrt{1 - e^2}}$$

along with Kepler’s third law,

$$P^2 = \frac{4\pi^2 a^3}{G(m_\star + m_c)}. \quad (3.31)$$

From Equation 3.29, we see that $K \propto \frac{m_c}{\sqrt{a(m_c+m_\star)}}$, while Equations 3.30–3.31 tell us that $\dot{\nu} \propto \sqrt{\frac{(m_c+m_\star)}{a^3}}$ and $\ddot{\nu} \propto \frac{(m_c+m_\star)}{a^3}$. Using these proportionalities in Equations 3.28, we obtain

$$\dot{\gamma} \propto \frac{m_c}{a^2}, \quad \ddot{\gamma} \propto \frac{m_c \sqrt{(m_c + m_\star)}}{a^{7/2}}. \quad (3.32)$$

`ethraid` explores different (a, m_c) combinations given fixed values of RV trend and curvature, so the posterior shapes are more clearly expressed by taking $\dot{\gamma}$ and $\ddot{\gamma}$ to be constant. In that case, we have

$$m_c \propto a^2, \quad m_c \sqrt{(m_c + m_\star)} \propto a^{7/2}. \quad (3.33)$$

Because of $\ddot{\gamma}$ ’s dependence on $\sqrt{(m_c + m_\star)}$, the corresponding m_c - a relation varies from $m_c \propto a^{7/2}$ to $m_c \propto a^{7/3}$ for $m_c \ll m_\star$ and $m_c \gtrsim m_\star$, respectively. In practice, most sampled companions have masses well below that of the host star, so $m_c \propto a^{7/2}$ prevails. Meanwhile, when both $\dot{\gamma}$ and $\ddot{\gamma}$ are provided, the RV posterior exhibits character of both relations in Equation 3.33. Figure 3.8 illustrates the interplay between $\dot{\gamma}$ and $\ddot{\gamma}$ in the RV posterior as well as $\ddot{\gamma}$ posterior’s behavior at the transition between high and low companion masses.

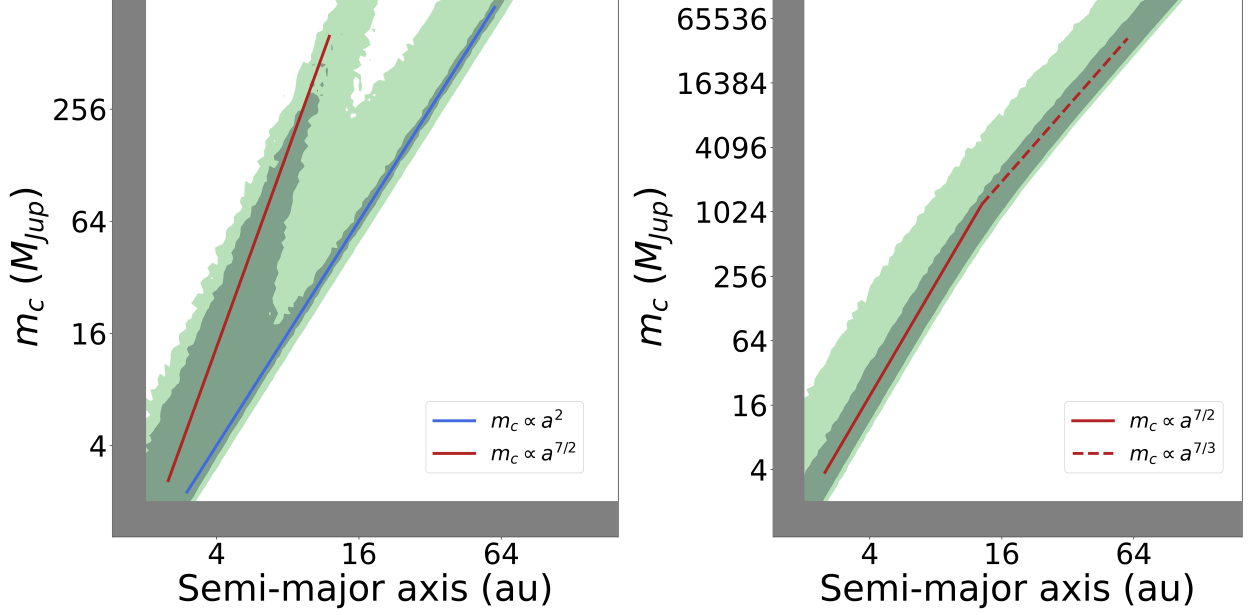


Figure 3.8: **Left:** An RV posterior calculated using both $\dot{\gamma}$ and $\tilde{\gamma}$. The blue line follows the relationship $m_c \propto a^2$, while the red line follows $m_c \propto a^{7/2}$. **Right:** An RV posterior calculated using $\tilde{\gamma}$ only, with a host star of $1 M_\odot$. In the low-mass regime, the posterior follows $m_c \propto a^{7/2}$. However, the slope shifts to $m_c \propto a^{7/3}$ near $1 M_\odot$.

3.10.2 Astrometry Posterior

Finding a general relationship between a , m_c , and $\Delta\mu$ is challenging because of the averaging procedure we carried out in Section 3.3.2. However, the simplifying assumptions that $e \sim i \sim 0$ allow us to reach analytical expressions that still capture the shape of the astrometry posterior. Figure 3.9 shows a diagram of this scenario. We reproduce Equations 3.17 and 3.23 below.

$$\langle \dot{X} \rangle = \frac{-1}{t_2 - t_1} \left[a_\star (\cos E - e) \right]_{E(t_1)}^{E(t_2)} \quad (3.34)$$

$$\langle \dot{Y} \rangle = \frac{-1}{t_2 - t_1} \left[a_\star \sqrt{1 - e^2} \sin E \right]_{E(t_1)}^{E(t_2)}$$

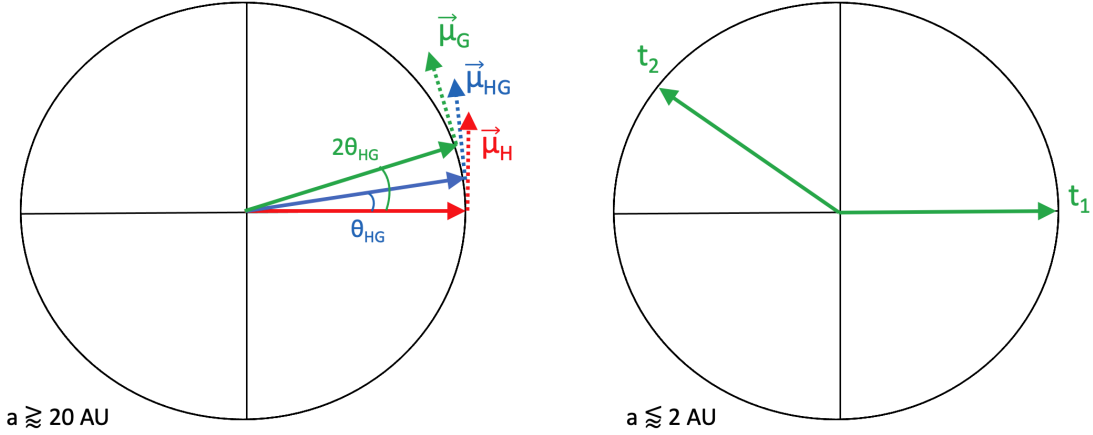


Figure 3.9: **Left:** A diagram of the circular, face-on orbit we use to understand the behavior of the astrometry posterior. The black circle shows the orbit of the host star about the system barycenter due to a companion at wide separation ($\gtrsim 20$ AU). Solid and dotted arrows show the average stellar position and proper motion vectors, respectively, in each of the *Hipparcos*, *HG*, and *Gaia* EDR3 epochs. θ_{HG} gives the position angle at the *HG* epoch relative to the position angle during the *Hipparcos* epoch. In the long-period regime, using the small angle approximation for θ_{HG} is appropriate. **Right:** A similar diagram for short periods ($\lesssim 2$ AU). Arrows t_1 and t_2 show the position of the host star at the beginning and end of the *Gaia* EDR3 data collection window. We chose t_2 's position arbitrarily to illustrate that for short periods, the angle between the two position vectors is not small, but rather can take any value on $[0, 2\pi]$. We do not show the analogous vectors for $\vec{\mu}_{HG}$ because T_{HG} is nearly nine times the duration of T_G ; this larger denominator drives $\vec{\mu}_{HG}$ to nearly zero for short-period orbits.

$$\Delta\mu = |\vec{\mu}_{G,abs} - \vec{\mu}_{HG,abs}| = |\vec{\mu}_{G,anom} - \vec{\mu}_{HG,anom}| \quad (3.35)$$

We begin with the long-period regime, that is, separations corresponding to orbital periods much longer than T_{HG} , the 24.75-year interval between the *Hipparcos* and *Gaia* characteristic epochs. From Equation 3.35 we see that $\Delta\mu$ depends only on the anomalous proper motions, so we may neglect center-of-mass proper motion in this derivation.

Because the companion orbit is circular and face-on, the proper motion vector has the same magnitude at all epochs, that is, $|\vec{\mu}_H| = |\vec{\mu}_G| = \frac{2\pi a_*}{d_* P}$. Furthermore, in the long-period regime,

the average proper motion approximates the instantaneous value: $|\vec{\mu}_{HG}| \sim |\vec{\mu}_G|$. The proper motion components at the *Gaia* and *HG* epochs are thus

$$\begin{aligned}\mu_{G_x} &= -|\vec{\mu}_G| \sin(2\theta_{HG}) \\ \mu_{G_y} &= |\vec{\mu}_G| \cos(2\theta_{HG})\end{aligned}\tag{3.36}$$

$$\begin{aligned}\mu_{HG_x} &= -|\vec{\mu}_{HG}| \sin(\theta_{HG}) \\ \mu_{HG_y} &= |\vec{\mu}_{HG}| \cos(\theta_{HG}),\end{aligned}$$

where θ_{HG} is the position angle of the host star at the *HG* epoch (see Figure 3.9, left panel), given by

$$\theta_{HG} = 2\pi \frac{T_{HG}}{2P} = \frac{T_{HG}}{2} \sqrt{\frac{G(m_\star + m_c)}{a^3}}.\tag{3.37}$$

From these proper motions, we may compute $\Delta\mu$:

$$\begin{aligned}\Delta\mu_x &= \mu_{HG} [\sin(\theta_{HG}) - \sin(2\theta_{HG})] \approx \mu_{HG} [-\theta_{HG}] \\ \Delta\mu_y &= \mu_{HG} [\cos(2\theta_{HG}) - \cos(\theta_{HG})] \approx \mu_{HG} \left[-\frac{3}{2}\theta_{HG}^2 \right] \\ \Delta\vec{\mu} &= -\mu_{HG} \left[\theta_{HG}, \frac{3}{2}\theta_{HG}^2 \right],\end{aligned}\tag{3.38}$$

where we approximated that $\sin \theta_{HG} \sim \theta_{HG}$ and $\cos \theta_{HG} \sim 1 - \frac{\theta_{HG}^2}{2}$. We further approximate that the x-component of $\Delta\vec{\mu}$ dominates in the long-period regime, yielding:

$$\begin{aligned}
|\Delta\vec{\mu}| &\approx \mu_{HG} \cdot \theta_{HG} = \frac{2\pi a_\star}{d_\star P} \cdot \frac{T_{HG}}{2} \sqrt{\frac{G(m_\star + m_c)}{a^3}} \\
&= \frac{T_{HG}}{2d_\star} a_\star \frac{G(m_\star + m_c)}{a^3} = \frac{G \cdot T_{HG}}{2d_\star} \frac{m_c}{a^2} \propto \frac{m_c}{a^2}.
\end{aligned} \tag{3.39}$$

Thus, $m_c \propto a^2$ in the long-period regime. This behavior is shown for large a values ($a \gtrsim 20$ AU) in the left panel of Figure 3.10.

The short-period portion of the astrometry posterior surface displays two distinct features: an overall negative slope and a series of spike-like formations extending to high mass. We derive the general linear character of the astrometry posterior in the short-period regime using the same picture we used to understand the long-period behavior. First examining $\vec{\mu}_G$, we have from Equation 3.34:

$$|\vec{\mu}_G| = \frac{1}{d_\star} \left| \begin{array}{c} \left[\begin{array}{c} \frac{-a_\star}{t_2-t_1} \cos M \\ \frac{-a_\star}{t_2-t_1} \sin M \end{array} \right]_{M(t_1)}^{M(t_2)} \\ \end{array} \right|, \tag{3.40}$$

where we have applied our assumptions of a face-on circular orbit and converted velocity to proper motion. Unlike in the long-period regime, T_G is comparable to or multiple times the duration of orbits in the short-period regime. As a result, $M(t_1)$ and $M(t_2)$ may differ by any angle from 0 to 2π . To continue, we set $M(t_1) = 0$ without loss of generality, and average over the possible values of $M(t_2)$:

$$|\vec{\mu}_G| d_\star \approx \left| \begin{array}{c} \left[\begin{array}{c} \frac{-a_\star}{t_2-t_1} \langle \cos M - 1 \rangle \\ \frac{-a_\star}{t_2-t_1} \langle \sin M - 0 \rangle \end{array} \right] \\ \end{array} \right| = \frac{a_\star}{t_2 - t_1}, \tag{3.41}$$

where $\langle \ \rangle$ denotes the average over the interval $[0, 2\pi]$. We may apply this same procedure

to $\vec{\mu}_{HG}$, but note that in this case, the denominator of the right-hand side of Equation 3.41 is ~ 25 years, as opposed to $\lesssim 3$ years for $\vec{\mu}_G$. Thus, $\vec{\mu}_G$ dominates in the short-period regime, and we neglect $\vec{\mu}_{HG}$. See the right panel of Figure 3.9 for a pictorial representation of this scenario. Finally, we use the relation between a and a_* to find that $m_c \propto a^{-1}$ for short periods:

$$|\vec{\mu}_G|_{d_*} \approx \frac{a_*}{t_2 - t_1} = \frac{a}{t_2 - t_1} \frac{m_c}{m_* + m_c} \propto a \cdot m_c. \quad (3.42)$$

We show this relation in Figure 3.10.

The spikes represent harmonics of T_G , the 34-month *Gaia* EDR3 mission baseline. For periods shorter than the ~ 25 -year *Hipparcos-Gaia* baseline, averaging the orbital position over that interval produces a cancellation effect, reducing the magnitude of $\vec{\mu}_{HG}$ so that $\vec{\mu}_G$ dominates $\Delta\mu$ in the short-period regime. For orbital periods which divide T_G , i.e. T_G itself, $\frac{T_G}{2}$, etc., $\vec{\mu}_G \rightarrow 0$ as well because the host star returns to its original position over the course of the *Gaia* mission, resulting in an average measured velocity of zero. The spikes in the right panel of Figure 3.10 demonstrate that model orbits must have higher companion mass near the harmonics to produce a constant value of $\Delta\mu$. We observe a similar effect at harmonics of T_{HG} (left panel of Figure 3.10), though these spikes are less pronounced because both $\vec{\mu}_{HG}$ and $\vec{\mu}_G$ contribute to $\Delta\mu$ in that regime.

3.11 Appendix 3B: Approximate Angular Separation Calculation

In this appendix we present an alternative method to the one described in Section 3.3.3 which makes use of two simplifying approximations to reduce computation time. First, for

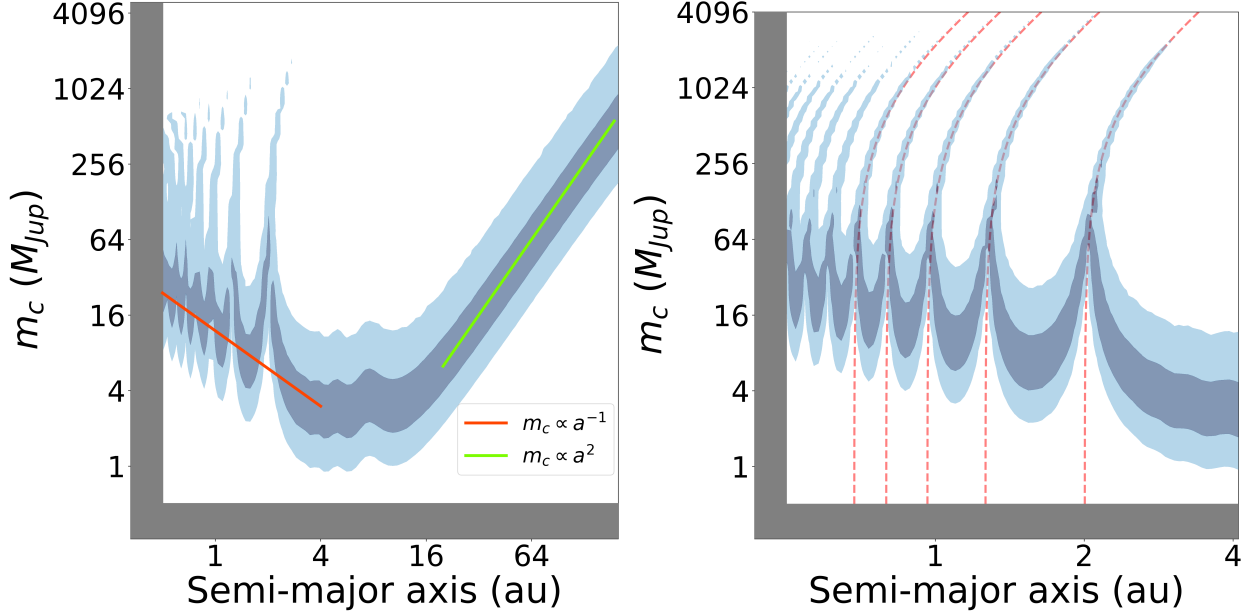


Figure 3.10: **Left:** The posterior surface calculated from astrometric data. The red line follows the relationship $m_c \propto a^{-1}$, while the green line follows $m_c \propto a^2$. **Right:** The short-period regime of the surface at left. Iso-period lines are shown in red: the right-most line traces $P = T_G \sim 2.83$ yr, the next follows $P = \frac{T_G}{2}$, then $P = \frac{T_G}{3}$, and so on. High-likelihood models near these periods must have large companion masses to counter the small net displacement of the star. The same effect can be seen at harmonics of the ~ 25 -yr *Hipparcos-Gaia* baseline ($\sim 4 - 16$ AU), though it is less pronounced because $\vec{\mu}_G$ remains nonzero in this regime even when $\vec{\mu}_{HG}$ vanishes.

the imaging likelihood only, `ethraid` approximates that all models that fall into the same a - m_c bin have the same value of a and m_c , namely, the geometric mean of the lower and upper bin limits. This simplification allows `ethraid` to evaluate the imaging model likelihood once per two-dimensional *bin* rather than once per *model*, reducing the number of likelihood evaluations from $\sim 10^6$ – 10^8 to N^2 , where N is the number of bins in both a and m_c space ($N = 100$ by default).

Second, `ethraid` models angular separation as dependent only on a . In particular, it makes the following approximation:

$$\rho \approx \frac{\langle p \rangle}{d} = \frac{Ca}{d}, \quad (3.43)$$

where $\langle p \rangle$ is the projected physical separation p averaged over a companion's possible inclinations and orbital positions, and C is a constant. If C equals 1, Equation 3.43 gives the angular separation for a circular, face-on orbit. We calculate the true value of C by averaging p , which itself is given by

$$\vec{p} \approx \mathbf{R} \begin{bmatrix} a \cos M \\ a \sin M \\ 0 \end{bmatrix} = a \begin{bmatrix} \cos M \\ \sin M \cos i \\ \sin M \sin i \end{bmatrix} \quad (3.44)$$

where the approximate equality comes from fixing $e = 0$ (and $\omega = 0$ arbitrarily) for simplicity, so that true anomaly is equivalent to mean anomaly. Noting that the probability density function of i on $[0, \pi/2]$ is $P(i) = \sin i$ and $P(M) = 1/2\pi$ on $[0, 2\pi]$, the average value of p is

$$\langle p \rangle = \frac{a}{2\pi} \int_0^{2\pi} \int_0^{\pi/2} \sqrt{\cos^2 M + \sin^2 M \cos^2 i} \sin i \, di \, dM. \quad (3.45)$$

Note that the vector norm (i.e., the square root term) includes only the components of \vec{p} that are in the sky plane. Evaluating this integral numerically, we find $\langle p \rangle/a = C = \pi/4$, meaning that the sky-projected separation is approximately 0.79 times the true separation on average.

For systems where the RV and astrometric data rule out high-mass models, using the approximation described here may have a negligible effect. The disparity in parameter constraints

is more pronounced when astrometry is not available, and imaging plays a more central role in ruling out stellar models. Figure 3.11 illustrates the effect of using this approximation for TOI-1694: some high-mass models that might in reality have gone undetected by the imaging data due to their orbital geometries are incorrectly ruled out. Using this approach to calculating angular separation is a suitable option for users who are comfortable incurring an error in their imaging constraints in exchange for cutting run time by a factor of $\sim 1/3$.

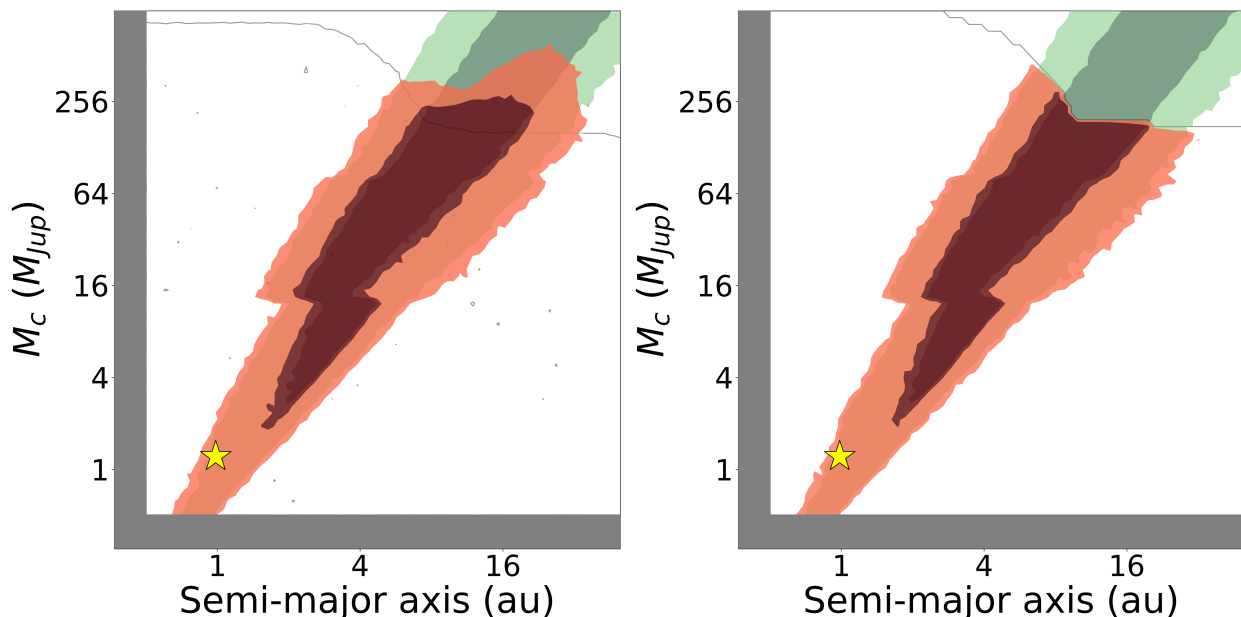


Figure 3.11: **Left:** Panel d) from Figure 3.5, showing the companion models consistent with a subset of the RVs of TOI-1694, as well as the imaging data. Note that despite falling above the gray 95% contour, some high-mass models are consistent with the imaging data because their orbital geometries result in small projected angular separations from the host star. **Right:** Parameter constraints for the same RV and imaging data, but using the approximate imaging calculation. In the approximate case, the imaging contour represents a hard bound, above which companions are ruled out with certainty. This causes the 1σ upper bound on mass (dark red) to be underestimated by $\sim 30\%$ at 16 AU, while being roughly unaffected at 8 AU.

3.12 Appendix 3C: Rotation Matrix

\mathbf{R} is the rotation matrix $\mathbf{P}_3\mathbf{P}_2\mathbf{P}_1$, described in Equations 2.119-2.121 of [Murray and Dermott \(2010\)](#). It is not given explicitly in that text.

$$\mathbf{R} = \begin{pmatrix} \cos \Omega \cos \omega - \cos i \sin \Omega \sin \omega & -\cos \Omega \sin \omega - \cos i \sin \Omega \cos \omega & \sin i \sin \Omega \\ \sin \Omega \cos \omega + \cos i \cos \Omega \sin \omega & \cos i \cos \Omega \cos \omega - \sin \Omega \sin \omega & -\sin i \cos \Omega \\ \sin i \sin \omega & \sin i \cos \omega & \cos i \end{pmatrix} \quad (3.46)$$

We exploit a symmetry in Sections 3.3.2 and 3.3.3 which warrants explanation here. In those sections, we apply \mathbf{R} to the *stellar* position and velocity vectors, despite the fact that i , ω , and Ω correspond to the *companion* orbit. Ω and i are the same for the star and the companion, but the stellar argument of periapsis is offset from that of the companion by π radians: $\omega_\star = \omega_c + \pi$. This means that rotating the stellar position and velocity vectors using ω_c is not correct in general. We demonstrate below that for our calculations, this asymmetry vanishes.

First, we relabel the matrix \mathbf{R} above as \mathbf{R}_c to denote its use of the sampled ω_c . We also define the matrix \mathbf{R}_\star , which results from the substitution $\omega_c \rightarrow \omega_\star$:

$$\mathbf{R}_c = \begin{pmatrix} R_{0,0} & R_{0,1} & R_{0,2} \\ R_{1,0} & R_{1,1} & R_{1,2} \\ R_{2,0} & R_{2,1} & R_{2,2} \end{pmatrix}, \quad \mathbf{R}_\star = \begin{pmatrix} -R_{0,0} & -R_{0,1} & R_{0,2} \\ -R_{1,0} & -R_{1,1} & R_{1,2} \\ -R_{2,0} & -R_{2,1} & R_{2,2} \end{pmatrix}. \quad (3.47)$$

where we have abbreviated the matrix elements for clarity.

We summarize the rotation steps of Section 3.3.2 as

$$\vec{r}_{obs} = \mathbf{R}_c \vec{r}_{orb} = \mathbf{R}_c \begin{bmatrix} \langle X \rangle \\ \langle Y \rangle \\ 0 \end{bmatrix} = \begin{bmatrix} R_{0,0}\langle X \rangle + R_{1,0}\langle Y \rangle \\ R_{1,0}\langle X \rangle + R_{1,1}\langle Y \rangle \\ 0 \end{bmatrix} = - \begin{bmatrix} -R_{0,0}\langle X \rangle + (-R_{1,0}\langle Y \rangle) \\ -R_{1,0}\langle X \rangle + (-R_{1,1}\langle Y \rangle) \\ 0 \end{bmatrix} = -\mathbf{R}_\star \begin{bmatrix} \langle X \rangle \\ \langle Y \rangle \\ 0 \end{bmatrix}. \quad (3.48)$$

The situation is analogous for \vec{v}_{obs} , as well as for $\vec{\rho}$ in Section 3.3.3. Thus, the use of \mathbf{R}_c instead of \mathbf{R}_\star introduces a single negative sign to each rotated vector. Because all vectors are equally affected, and in all cases we ultimately work with the vector moduli, this negative sign has no effect on our likelihood calculation.

Chapter 4

No evidence for a metallicity-dependent enhancement of distant giant companions to close-in small planets in the California Legacy Survey

A version of this chapter was previously published in *The Astronomical Journal* (Judah Van Zandt & Erik A. Petigura, 2024b, AJ 168, 6, 268).

Abstract

Understanding the relationship between close-in small planets (CS) and distant giants (DG) is central to understanding the formation of planetary systems like our own. Most studies of this connection have found evidence for a positive correlation, though significant statistical and systematic uncertainties remain due to differences in sample size, target selection

bias, and even the definitions of ‘close-in small’ and ‘distant giant’ planets. Recently, [Bryan and Lee \(2024\)](#) conducted a study of 184 stars hosting super-Earths ($M \sin i = 1 - 20 M_{\oplus}$ or $R = 1 - 4 R_{\oplus}$) to determine the effect of stellar metallicity on the prevalence of distant giant companions ($M \sin i = 0.5 - 20 M_J$, $a = 1 - 10$ AU). They found that such giants are twice as common in the presence of inner planets, but *only* in metal-rich systems: $P(\text{DG}|\text{CS}, [\text{Fe}/\text{H}]>0) = 28.0^{+4.9}_{-4.6}\%$ vs. $P(\text{DG}|[\text{Fe}/\text{H}]>0) = 14.3^{+2.0}_{-1.8}\%$. Further, they found that this correlation disappears for metal-poor stars: $P(\text{DG}|\text{CS}, [\text{Fe}/\text{H}]\leq 0) = 4.5^{+2.6}_{-1.9}\%$ vs. $P(\text{DG}|[\text{Fe}/\text{H}]\leq 0) = 5.0^{+1.6}_{-1.3}\%$. We conducted an analogous study to test whether this effect was present in the California Legacy Survey sample. Using the same planet definitions, we did not find evidence for an enhancement in metal-rich systems: $P(\text{DG}|\text{CS}, [\text{Fe}/\text{H}]>0) = 14^{+12}_{-8}\%$ vs. $P(\text{DG}|[\text{Fe}/\text{H}]>0) = 16.4^{+2.5}_{-2.4}\%$. We also found a 2σ tension between our conditional rate and a 2x enhancement. We brought our results into closer agreement with [Bryan and Lee \(2024\)](#) by repeating our analysis with different planet definitions. For example, considering only CS planets with $1 \leq M \sin i \leq 10 M_{\oplus}$ and DG planets with $0.5 \leq M \sin i \leq 20 M_J$ gives $P(\text{DG}|\text{CS}, [\text{Fe}/\text{H}]>0) = 47^{+17}_{-17}\%$ and $P(\text{DG}|[\text{Fe}/\text{H}]>0) = 20.2^{+2.9}_{-2.7}\%$, consistent with a 2x enhancement. However, we find that this 2x enhancement is also present when we apply the same planet definitions to the overall sample, challenging the idea that metallicity is responsible. Our sample, though only $\sim 1/6$ the size of [Bryan and Lee \(2024\)](#)’s, was assembled and analyzed self-consistently. The discrepancy between our findings and theirs may arise from a variety of sources, underscoring the need for large exoplanet surveys to overcome both small number statistics and sample inhomogeneities.

4.1 Introduction

Planets between the size of Earth and Neptune with orbits less than 1 AU are ubiquitous ([Petigura et al., 2018](#)). In contrast, radial velocity (RV) surveys have uncovered a separate

population of giant planets at wider separations ($a \approx 1 - 10$ AU), which orbit 10 – 20% of stars, depending on the definition used (Rosenthal et al. 2021; Wittenmyer et al. 2020; Fischer et al. 2014; Cumming et al. 2008). Although rarer than the super-Earths and sub-Neptunes, these giants are believed to have a significant impact on the development of close-in planets (Batygin and Laughlin 2015; Izidoro et al. 2015).

The relationship between close-in small planets (CS) and outer distant giants (DG) has garnered significant attention in recent years. Zhu and Wu (2018) and Bryan et al. (2019) assembled samples of stars with archival RVs to calculate the occurrence of distant giants in systems hosting close-in small planets. Both studies found that distant giant occurrence is enhanced in the presence of inner small planets ($P(\text{DG}|\text{CS}) = 32 \pm 8\%$ and $39 \pm 7\%$, respectively). Rosenthal et al. (2022) leveraged the California Legacy Survey (CLS), a large sample of FGKM RV targets with multi-decade baselines, to answer the same question, and also found an enhancement: $P(\text{DG}|\text{CS}) = 41^{+15}_{-13}\%$.

The emerging picture of a positive correlation was challenged by Bonomo et al. (2023), who found evidence for an anti-correlation ($P(\text{DG}|\text{CS}) = 9.3^{+7.7}_{-2.9}\%$) in a sample of 38 *Kepler* and *K2* systems. RV surveys tailored to the detection of outer giants are currently being carried out on samples with transiting inner planets discovered by *Kepler* (Weiss et al., 2024) and *TESS* (Van Zandt et al., 2023).

Zhu (2024) added another dimension to the DG-CS relation by proposing that the enhancement of giants found by earlier studies is driven by host star metallicity. In particular, they suggested that giants are strongly enhanced in the presence of inner companions *only* in systems with metal-rich ($[\text{Fe}/\text{H}] > 0$) host stars. They demonstrated that analyzing only the metal-rich stars in the Bonomo et al. (2023) sample produces a positive correlation.

To test the claim put forward by Zhu (2024), Bryan and Lee (2024) compiled a sample of 184 Sun-like stars with archival RV observations, as well as transit- and RV-discovered

CS planets. They found that distant giants are twice as prevalent in the presence of inner small planets versus the field rate for metal-rich systems, reinforcing the hypothesis that metallicity plays a key role in this connection.

The enhancement in giant planet occurrence around metal-rich stars is well known (e.g., Santos et al. 2004; Fischer and Valenti 2005b; Johnson et al. 2010). Thus, one would expect that in metal-rich systems, the prevalence of DG companions in CS systems would increase, but so would the prevalence of DG planets overall, nullifying any relative increase. The conclusions of Zhu (2024) and Bryan and Lee (2024) imply that the conditional occurrence rate of DGs is a more steeply rising function of metallicity than the field occurrence rate.

In this paper we emulate the study carried out by Bryan and Lee (2024) using the California Legacy Survey (CLS) sample, a catalog of 719 FGKM stars and 178 planets discovered through RV monitoring over 30 years. Our objective is to test the claim that there exists a strong positive correlation between CS and DG planets specifically for metal-rich host stars in this sample. We review the methods and results of Bryan and Lee (2024) in Section 4.2. In Section 4.3 we give an overview of the CLS sample. We describe our binomial occurrence model in Section 4.4, and use it to calculate giant planet occurrence rates in Section 4.5. We explore the effects of expanding our planet definitions and excluding evolved stars in Sections 4.6 and 4.7, respectively, and discuss our results in Section 4.8.

4.2 Bryan & Lee (2024)

This paper examines the key finding of Bryan and Lee (2024), hereafter BL24, namely, that in metal-rich systems, DG planets are twice as prevalent in the presence of CS planets as the field DG rate for metal-rich systems in the CLS sample. Therefore, we begin by describing the BL24 sample, including its construction and planet class definitions.

BL24 selected 184 FGK stars with >20 publicly available RVs and hosting at least one CS planet, which they defined as having either $M \sin i = 1 - 20 M_{\oplus}$ or $R = 1 - 4 R_{\oplus}$. Figure 4.1 shows the minimum masses and separations of the planets in their sample.¹

They calculated the conditional occurrence rate of DG planets, which they defined by $M \sin i = 0.5 - 20 M_J$ and $a = 1 - 10$ AU, in the metal-rich and metal-poor subsamples, finding that $P(\text{DG}|\text{SE}, [\text{Fe}/\text{H}]>0) = 28.0^{+4.9}_{-4.6}\%$ and $P(\text{DG}|\text{SE}, [\text{Fe}/\text{H}]<0) = 4.5^{+2.6}_{-1.9}\%$.

They then calculated the distant giant field occurrence rates using the CLS sample of [Rosenthal et al. \(2021\)](#), hereafter R21. They first removed 121 M dwarfs ($M_{\star} < 0.6 M_{\odot}$) and four targets with fewer than 20 RV observations, and found $P(\text{DG}||[\text{Fe}/\text{H}]>0) = 14.3^{+2.0}_{-1.8}\%$ and $P(\text{DG}||[\text{Fe}/\text{H}]<0) = 5.0^{+1.6}_{-1.3}\%$ among the remaining 594 stars. We refer to this filtered subset as the R21 sample in the remainder of this paper, and we show the planets orbiting these stars in Figure 4.1. Whereas the conditional and field occurrence rates for metal-poor systems are comparable, the metal-rich conditional rate is larger than its field counterpart by a factor of two. The sharp divide between the metal-rich and metal-poor samples supports the claim of [Zhu \(2024\)](#).

4.3 The California Legacy Survey

In this work, we derive all conditional and field occurrence rates using the same 594-star subset of the California Legacy Survey sample used by BL24. Using a single stellar and planetary sample naturally controls for selection biases when comparing different statistics.

This sample consists of FGK stars with RV baselines spanning up to 30 years. The R21

¹We cross-referenced the system names provided in Table A.1 of BL24 with the Exoplanet Archive (<https://exoplanetarchive.ipac.caltech.edu/>; Accessed 9 June 2024) to reconstruct their sample. We found only one meaningful discrepancy: the putative super-Earth HD 26965 b was initially reported by [Ma et al. \(2018\)](#), but recently found to be spurious ([Lalot et al., 2023](#)). The removal of this planet would also exclude HD 26965 from the BL24 sample. We anticipate that this change would have a negligible effect on the statistical findings of BL24, and conduct our comparison against their original results.

sample has a median metallicity of 0.0 dex and a median stellar mass of $0.94 M_{\odot}$. The R21 catalog comprises 171 substellar and planetary companions ($M \sin i < 80 M_J$), 154 of which have $M \sin i < 13 M_J$, and 33 of which have $M \sin i < 30 M_{\oplus}$. All companions in the sample were detected using a uniform search algorithm (RVSearch, Rosenthal et al. 2021). Fulton et al. (2021) measured the sensitivity of this algorithm in the R21 data set through a suite of injection/recovery experiments published as part of that study.

The CLS sample may not be free of bias, as Zhu (2022) showed that it hosts hot Jupiters at about three times the canonical occurrence rate of 1% (Wright et al., 2012). Nevertheless, our goal is not to measure the absolute conditional occurrence of DG planets. Rather, it is to test BL24’s finding that metal-rich stars exhibit an increased relative enhancement of $P(\text{DG}|\text{CS})$ over $P(\text{DG})$. To do this, we calculated $P(\text{DG})$ and $P(\text{DG}|\text{CS})$ from a single sample, allowing us to rule out sample differences as a source of disparity. We chose the R21 sample to match BL24 as closely as possible. We show in Figure 4.1 that the distributions of small inner planets and outer giants are comparable in the BL24 and R21 samples.

4.4 Binomial Occurrence Model

In this work, we define occurrence as the fraction of systems hosting at least one planet, rather than the number of planets per star. Following BL24, we calculated occurrence using binomial statistics, assuming that planet occurrence was log-uniform over the parameter space we considered ($M \sin i = 0.5 - 20 M_J$, $a = 1 - 10 \text{ AU}$). We calculated the average completeness Q of the R21 survey and used that to calculate $n_{\star, \text{eff}} = Q \cdot n_{\star}$, where n_{\star} is the total number of stars in the sample and $n_{\star, \text{eff}}$ is the effective number of stars after correcting for completeness. The binomial likelihood function for the fraction f_{cell} of stars hosting planets in a given domain is

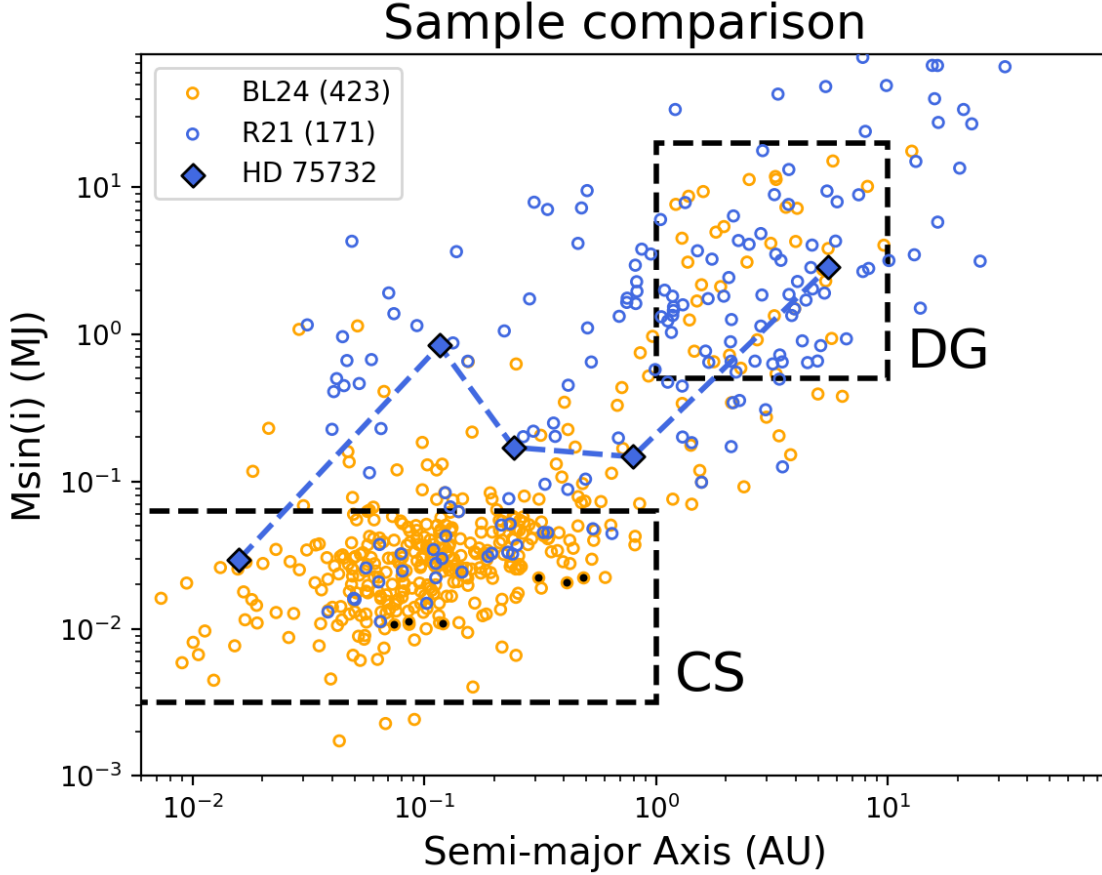


Figure 4.1: The companions in the sample of [Bryan and Lee \(2024\)](#) (yellow) and the FGK subsample of [Rosenthal et al. \(2021\)](#) (blue). BL24 has companions between $\sim 1 M_{\oplus}$ and $20 M_J$, and R21 includes companions from a few M_{\oplus} up to $80 M_J$. The legend gives the number of companions in each sample in parentheses. We show BL24’s definitions of close-in small (CS) and distant giant (DG) planets with black dashed boxes. We use blue diamonds to highlight HD 75732, the only system in the metal-rich R21 sample with planets satisfying both of these definitions. We use filled black circles to show six planets in the BL24 sample without measured masses. We estimate their masses using the mass-radius relationship of [Weiss and Marcy \(2014\)](#). The distributions of giant plants are similar among the two samples. They also have comparable inner planet distributions, though BL24 contains many more such planets due to its selection function. This latter similarity makes it unlikely that a dependence of giant occurrence on inner planet properties, if such a dependence exists, affected our comparison.

$$P(f_{\text{cell}}|n_{\text{det}}, n_{\star, \text{eff}}) = C f_{\text{cell}}^{n_{\text{det}}} (1 - f_{\text{cell}})^{n_{\text{nd}}}, \quad (4.1)$$

where n_{det} is the number of systems hosting a detected planet, $n_{\text{nd}} = n_{\star, \text{eff}} - n_{\text{det}}$ is the number of systems in which no planet was detected, and C is a normalization constant: ²

$$C = \frac{(n_{\star, \text{eff}} + 1) \cdot \Gamma(n_{\star, \text{eff}} + 1)}{\Gamma(n_{\text{det}} + 1) \Gamma(n_{\text{nd}} + 1)}. \quad (4.2)$$

We set a uniform prior between zero and one on the planet occurrence rate and numerically optimized our likelihood function.

4.5 No Evidence of Enhanced Occurrence of Distant Giants in Metal-rich Stars

4.5.1 P(DG)

We first calculated the field occurrence of distant giants in the R21 sample to establish a point of comparison for conditional occurrence. Of the 594 stars in the R21 sample, 52 host one or more distant giants, and 43 of those hosts are metal-rich. We calculated metal-rich and metal-poor distant giant field occurrence rates of $P(\text{DG} | [\text{Fe}/\text{H}] > 0) = 16.4^{+2.5}_{-2.4}\%$ and $P(\text{DG} | [\text{Fe}/\text{H}] \leq 0) = 5.8^{+2.0}_{-1.7}\%$.

Our metal-rich field rate differs from that obtained by BL24 ($14.3^{+2.0}_{-1.8}\%$) by $> 1\sigma$. For two unrelated studies of the same phenomenon, such a disparity could reasonably be attributed to statistical variation. However, we used the same sample, planet definitions, and occurrence

²We use Γ to represent the extension of the factorial function to real numbers: $\Gamma(x + 1) = x!$.

model as BL24. We therefore attribute this disagreement to our different completeness correction methodologies. In brief, both our and BL24’s completeness corrections involved injecting and recovering planetary signals in the measured RVs. However, BL24 considered a signal “recovered” if a one-planet model offered a significantly improved fit over the flat line model ($\Delta\text{BIC} > 10$). By contrast, R21 required that a planetary model be preferred and that the recovered parameters agree with the injected ones to within 25%. This stricter criterion would lead to lower completeness, and therefore a higher measured occurrence, as we observe.

In principle, there is no problem with using a more or less strict completeness correction. It is only necessary that the same criteria be applied during the initial planet search and the completeness correction. Thus, a strict planet search will find fewer planets and correct more, while a less strict search will find more planets and correct less. Because the R21 sample was compiled using RVSearch, we expect that the RVSearch completeness framework we used provides a more accurate correction.

4.5.2 P(DG|CS)

We next calculated the conditional occurrence of distant giants in the presence of close-in small planets (CS). We adopted the mass limits used by BL24 for these planets, $M \sin i = 1 - 20 M_{\oplus}$. We also used a separation limit of $a < 1$ AU, though this filter did not remove any targets from our subsample. Under this definition, 18 R21 systems host a close-in small planet, and only one hosts both a close-in small planet and a distant giant. Of this sub-sample, 13 systems, including the distant giant host, are metal-rich. We calculated a metal-rich distant giant conditional occurrence rate of $P(\text{DG}|\text{CS}, [\text{Fe}/\text{H}] > 0) = 14^{+12}_{-8}\%$. This value is *lower* than our metal-rich field occurrence rate calculated above, in tension with most previous studies of this relationship using various CS and DG definitions (e.g. [Bryan](#)

et al. 2019; Rosenthal et al. 2022; Zhu 2024). Moreover, our measured rate is inconsistent with a 2x enhancement at the 2σ level, in contrast to BL24’s finding of a 2x enhancement at 3σ confidence. We compare these measurements and their uncertainties in Figure 4.2.

Table 4.1: Occurrence Rates

Test	Metallicity			% within 2σ (2x Enhancement)
	Criterion	P(DG CS)	P(DG)	
BL24	[Fe/H]>0	$28.0^{+4.9}_{-4.6}\%$	$14.3^{+2.0}_{-1.8}\%$	—
	[Fe/H] ≤ 0	$4.5^{+2.6}_{-1.9}\%$	$3.8^{+1.4}_{-1.1}\%$	—
Default	[Fe/H]>0	$14^{+12}_{-8}\%$	$16.4^{+2.5}_{-2.4}\%$	8%
	[Fe/H] ≤ 0	<45%	$5.8^{+2.0}_{-1.7}\%$	22%
	—	$10^{+9}_{-6}\%$	$12.0^{+1.7}_{-1.6}\%$	9%
Small DG	[Fe/H]>0	$31^{+14}_{-12}\%$	$20.2^{+2.8}_{-2.7}\%$	23%
	[Fe/H] ≤ 0	<46%	$6.3^{+2.3}_{-1.8}\%$	23%
	—	$23^{+11}_{-9}\%$	$14.6^{+2.0}_{-1.9}\%$	22%
Big CS, Small DG	[Fe/H]>0	$34^{+13}_{-12}\%$	$20.2^{+2.9}_{-2.6}\%$	28%
	[Fe/H] ≤ 0	<38%	$6.3^{+2.2}_{-1.9}\%$	24%
	—	$25^{+11}_{-9}\%$	$14.5^{+1.9}_{-1.8}\%$	25%
Small CS, Small DG	[Fe/H]>0	$47^{+17}_{-17}\%$	$20.2^{+2.9}_{-2.7}\%$	23%
	[Fe/H] ≤ 0	<72%	$6.2^{+2.2}_{-1.8}\%$	16%
	—	$40^{+16}_{-15}\%$	$14.5^{+2.0}_{-1.8}\%$	16%

Note: (1) BL24: CS = 1–20 M_{\oplus} ; DG = 1–10 AU, 0.5–20 M_J ; (2) Default: Same as BL24 definition; (3) Small DG: Same as BL24 but with DG mass limits of 90 M_{\oplus} –20 M_J ; (4) Big CS, Small DG: CS = 1–30 M_{\oplus} ; DG = 90 M_{\oplus} –20 M_J ; (5) Small CS, Small DG: CS = 1–10 M_{\oplus} ; DG = 90 M_{\oplus} –20 M_J . We provide the median occurrence rates, with uncertainties representing 16th and 84th percentiles. For occurrence rates consistent with zero, we quote 90% upper limits. The right-most column indicates the fraction of each of our conditional posterior distributions that falls within the 95% confidence interval of a 2x-enhancement over the corresponding field distribution.

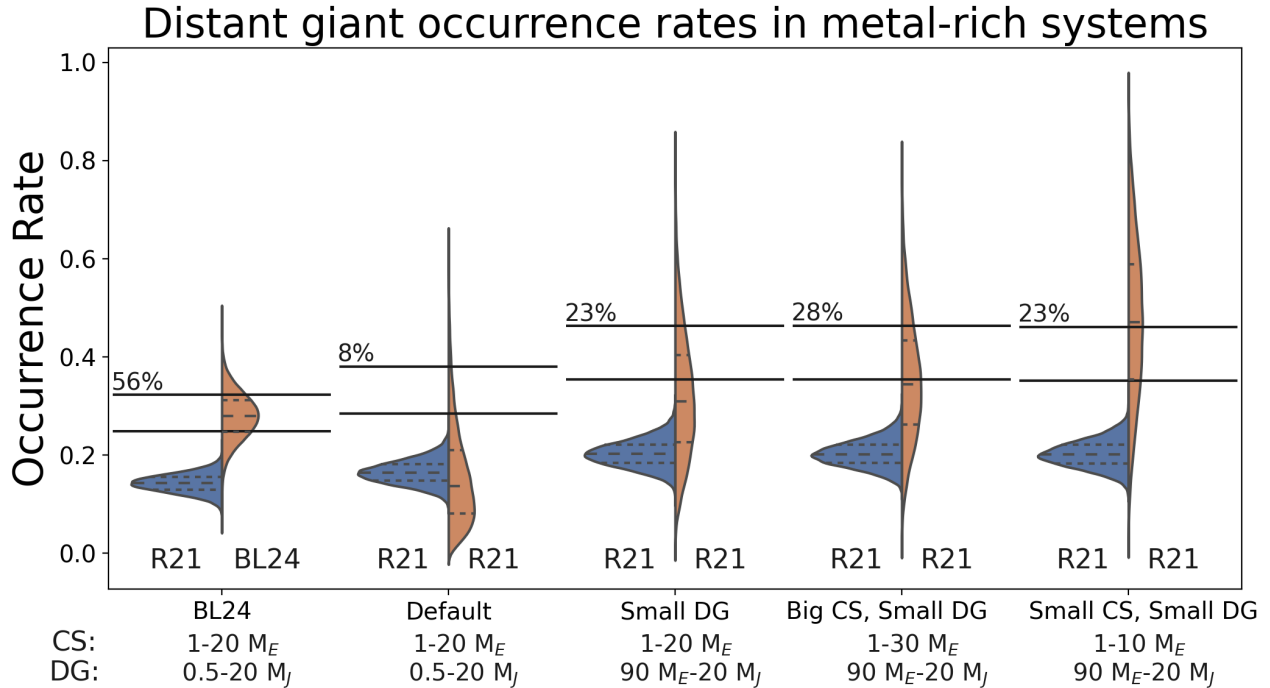


Figure 4.2: Measurements of field (blue) and conditional (orange) occurrence of distant giants in metal-rich subsets of the [Bryan and Lee \(2024\)](#) and [Rosenthal et al. \(2021\)](#) samples. BL24 found that distant giants are about twice as prevalent in the presence of close-in small planets as the field rate they measured from the R21 sample (far left). We measured both the conditional and field rates using the R21 sample and four different sets of definitions for close-in small planets and distant giants. The "Default" definition matches BL24: the inner planets satisfy $1 \leq M \sin i \leq 20 M_\oplus$ and the distant giants satisfy $0.5 \leq M \sin i \leq 20 M_J$ and $1 \leq a \leq 10$ AU. The "Small DG" definition used a $90 M_\oplus$ floor for distant giants. The "Big CS, Small DG" definition used a $30 M_\oplus$ ceiling for inner planets and a $90 M_\oplus$ floor for distant giants. Finally, our "Small CS, Small DG" definition used a $10 M_\oplus$ ceiling for inner planets and a $90 M_\oplus$ floor for distant giants. We annotate each distribution with the planet sample used to calculate it, and include the CS and DG definitions on the x -axis. Horizontal dotted lines denote distribution quartiles. We use black solid lines to indicate the 95% confidence interval of a 2x enhancement over each field occurrence rate, and label the upper line with the percentage of each conditional occurrence distribution that falls within it. BL24's conditional occurrence distribution is fully consistent with a 2x enhancement, whereas only 8% of our Default distribution overlaps this interval. Expanding our definitions of inner planets and distant giants increases the conditional rate, because a significant fraction of the giant planets in the R21 sample have masses below $0.5 M_J$.

4.6 Broader Planet Definitions Increase P(DG|CS)

We performed our analysis in the previous sections in exact analogy to BL24, including using the same definitions of close-in small planets and distant giants. Under these definitions, there were 43 DG hosts, 13 CS hosts, and 1 system hosting both. Here we examine the effect of broadening these criteria to admit a wider range of planets. The values we quote in this section are specifically for the metal-rich sample unless otherwise indicated. We show the metal-rich occurrence rate distributions in Figure 4.2, and we list the corresponding results for the full and metal-poor samples in Tables 4.1 and 4.2.

Table 4.2: Sample Sizes and Completeness

Test		Metallicity Criterion	Average Completeness	N_{\star}	$N_{\star, \text{eff}}$	N_{hosts}
Default	P(DG)	$[\text{Fe}/\text{H}] > 0$	0.70	351	244.0	43
	P(DG CS)	$[\text{Fe}/\text{H}] > 0$	0.83	13	10.7	1
	P(DG)	$[\text{Fe}/\text{H}] \leq 0$	0.70	243	170.8	9
	P(DG CS)	$[\text{Fe}/\text{H}] \leq 0$	0.81	5	4.1	0
	P(DG)	—	0.70	594	413.8	52
	P(DG CS)	—	0.82	18	14.8	1
Small DG	P(DG)	$[\text{Fe}/\text{H}] > 0$	0.63	351	222.6	48
	P(DG CS)	$[\text{Fe}/\text{H}] > 0$	0.81	13	10.6	3
	P(DG)	$[\text{Fe}/\text{H}] \leq 0$	0.64	243	156.5	9
	P(DG CS)	$[\text{Fe}/\text{H}] \leq 0$	0.80	5	4.0	0
	P(DG)	—	0.64	594	377.9	57
	P(DG CS)	—	0.81	18	14.6	3
Big CS, Small DG	P(DG)	$[\text{Fe}/\text{H}] > 0$	0.63	351	222.6	48
	P(DG CS)	$[\text{Fe}/\text{H}] > 0$	0.81	16	13.0	5
	P(DG)	$[\text{Fe}/\text{H}] \leq 0$	0.64	243	156.5	9
	P(DG CS)	$[\text{Fe}/\text{H}] \leq 0$	0.83	6	5.0	0
	P(DG)	—	0.64	594	377.9	57
	P(DG CS)	—	0.82	22	18.0	5
Small CS, Small DG	P(DG)	$[\text{Fe}/\text{H}] > 0$	0.63	351	222.6	48
	P(DG CS)	$[\text{Fe}/\text{H}] > 0$	0.81	8	6.5	3
	P(DG)	$[\text{Fe}/\text{H}] \leq 0$	0.64	243	156.5	9
	P(DG CS)	$[\text{Fe}/\text{H}] \leq 0$	0.70	2	1.4	0
	P(DG)	—	0.64	594	377.9	57

Continued on next page

Table 4.2 – Continued from previous page

Test	Metallicity Criterion	Average Completeness	N_*	$N_{*,\text{eff}}$	N_{hosts}
P(DG CS)	—	0.79	10	7.9	3

Note: N_* gives the number of stellar hosts satisfying the associated metallicity criterion (and the CS criterion, for P(DG|CS) measurements). $N_{*,\text{eff}}$ gives the product of N_* and the completeness to distant giants among this stellar subsample. N_{hosts} denotes the number of systems hosting at least one DG planet under the given criteria.

First, we decreased the lower bound on DG mass to $90 M_{\oplus}$ to include Saturn-mass planets, giving 48 DG hosts, 13 CS hosts, and 3 hosts of both. The decreased mass limit added more DGs to our sample and also extended the parameter space to regions of lower sensitivity, resulting in a larger completeness correction. As a result, we found enhancements in both the field rate and the conditional rate, $P(\text{DG}|\text{[Fe/H]}) = 20.2^{+2.8\%}_{-2.7\%}$ and $P(\text{DG}|\text{CS}, \text{[Fe/H]}) = 31^{+14\%}_{-12\%}$, this time finding consistency with a 2x enhancement within 1σ .

Next, we retained the lower DG mass bound increased the upper bound on CS planets to $30 M_{\oplus}$. We recovered the same 48 DG hosts, this time with 16 CS hosts among them, and 5 systems hosting both. Our results under this change, $P(\text{DG}|\text{[Fe/H]}) = 20.2^{+2.9\%}_{-2.6\%}$ and $P(\text{DG}|\text{CS}, \text{[Fe/H]}) = 34^{+13\%}_{-12\%}$, were consistent with a 2x enhancement. However, the overall sample exhibited a comparable relative enhancement under these same definitions, suggesting that metallicity is not responsible (see Table 4.1).

Finally, we lowered the CS mass ceiling to $10 M_{\oplus}$ to test giant occurrence around typical super-Earths. This definition gave 48 DG hosts, 8 CS hosts, and 3 hosts of both. The only difference between this definition and the first definition in this section is the smaller CS mass ceiling ($10 M_{\oplus}$ versus $20 M_{\oplus}$). Although this change cut out five CS hosts, we retained all three of the systems hosting both a CS and a DG, meaning that no giants in our sample orbit inner planets with mass $10 - 20 M_{\oplus}$. We found $P(\text{DG}|\text{[Fe/H]}) = 20.2^{+2.9\%}_{-2.7\%}$ and $P(\text{DG}|\text{CS},$

$[\text{Fe}/\text{H}] = 47_{-17}^{+17}\%$. In this case, our results were fully consistent with a 2x enhancement, with our median conditional rate greater than the field rate by a factor of 2.2. Again, we saw a comparable relative enhancement (2.6x) when we applied these definitions to the overall sample.

4.7 Excluding evolved stars has little effect on occurrence

Stars hosting close-in planets are expected to engulf these companions as they evolve off the main sequence (Villaver et al., 2014). Although the number of known exceptions to this picture is growing (e.g., Grunblatt et al. 2024; Wittenmyer et al. 2022; Wang et al. 2019), evolved stars as a population may host CS planets at a reduced rate, and would therefore tend to increase $P(\text{DG})$ in relation to $P(\text{DG}|\text{CS})$.

We removed evolved hosts and repeated our analysis to examine conditional occurrence among only main sequence stars. To exclude evolved hosts from our sample, we removed all stars with $\log(g) < 4$, which reduced our sample from 598 to 531 stars, 324 of which were metal-rich and 207 of which were metal-poor. The 67 evolved stars we removed host 12 of the 52 giant planets in the CLS, including HD 11964 A, which hosts both a transiting super-Neptune ($M \sin i \sim 24 M_{\oplus}$) and an outer sub-Jupiter ($M \sin i \sim 0.6 M_J$).

We then recomputed the statistics of Sections 4.5 and 4.6. Our average completeness did not change by more than 2% for any of our experiments. We found that removing evolved stars decreased our field distant giant rates, though not enough to reach statistical significance. Finally, because only a single CS system was removed in our "Big CS, Small DG" experiment, and none were removed in the other experiments, our conditional occurrence rates were essentially unaffected.

4.8 Discussion

We used the R21 sample to reproduce the measurement of distant giant occurrence in metal-rich systems conducted by [Bryan and Lee \(2024\)](#). We focused on the primary result of that study: that the conditional occurrence of distant giants is significantly enhanced over the field rate specifically for metal-rich host stars. We used BL24’s finding of a factor of 2 enhancement as a benchmark to test against.

Adopting the same planet definitions and statistical methods as BL24, we did not find evidence for a strong enhancement of DGs in the presence of CS planets in metal-rich systems. Instead, our measurements are in tension with a factor of 2 enhancement at the 2σ level.

We tested the effect of changing our DG and CS definitions on our inferred occurrence rates. Broadening these definitions to admit more CS or DG planets increased the measured conditional occurrence by a greater factor than it did the field occurrence (see [Table 4.1](#)), leading to larger relative enhancements for broader planet definitions. However, we saw similar increases in relative enhancement for the overall sample, suggesting that the enhancement of $P(\text{DG}|\text{CS})$ over $P(\text{DG})$ is not dependent on metallicity.

As a final test, we checked whether removing evolved stars from our sample caused an appreciable change in our calculated occurrence rates. We found that although our basic prediction that this would decrease $P(\text{DG})$ in relation to $P(\text{DG}|\text{CS})$ was borne out, the effect was not statistically significant.

The design of our study differs from BL24 in both the sizes of our respective samples and the homogeneity of our analyses. BL24 assembled a sample of 184 small-planet-hosting stars, a number of which also hosted distant giants. Their large sample size allowed them to compute $P(\text{DG}|\text{CS})$ with a 5% fractional uncertainty. However, because their sample only included systems with inner planets, they could not use it to establish $P(\text{DG})$. They therefore

compared their conditional occurrence rate to the field rate from the R21 sample with the assumption that the two samples were drawn from the same underlying distribution of stars with the same $P(\text{DG})$. This assumption may not be correct, and the increased measurement precision from using a larger sample may have come at the cost of decreased accuracy.

We used the R21 sample to compute $P(\text{DG})$ and $P(\text{DG}|\text{CS})$ self-consistently, so we did not contend with biases arising from different samples. However, the R21 sample contains far fewer CS planets than BL24, resulting in large fractional uncertainties on our measurements of $P(\text{DG}|\text{CS})$.

A third difference is the use of different completeness correction algorithms. In particular, we used stricter criteria for injected planet recoveries, resulting in lower average completeness and therefore higher inferred occurrence rates. Because these criteria resemble the actual detection pipeline used to compile the R21 sample more closely than BL24's, we expect that our completeness correction is more accurate.

Despite the rapid growth of the census of exoplanets over the last few decades, samples large enough to support homogeneous, multi-dimensional analyses, such as conditional occurrence rate estimates, are not yet available. The largest blind RV surveys, with sample sizes of ~ 1000 , were compiled over decades and are unlikely to grow by an order of magnitude in the near future. However, improvements in RV precision will provide increased sensitivity to small planets over time. This will directly enable more precise measurements of $P(\text{CS})$, but it will also reveal CS planets in DG-hosting systems. Therefore, we expect improved precision on $P(\text{DG}|\text{CS})$ even in the absence of larger samples.

Leveraging other detection methods is another promising avenue for improving occurrence rate statistics. For example, using uniform transit missions to identify close-in small planets can efficiently establish a sample of CS-hosting stars, and using RVs to follow up such a sample homogeneously (i.e., without regard to metallicity, probability of a distant giant,

etc.) can provide $P(\text{DG}|\text{CS})$ even with modest RV precision. Furthermore, searching for distant giant signatures in astrometric data from *Gaia* could be used to make a robust measurement of $P(\text{DG})$ for comparison. The risk of inter-sample biases from cross-method comparisons remains a concern, but will diminish as large surveys approach statistically identical target samples.

4.9 Acknowledgments

We thank the reviewer for helpful comments which improved this manuscript.

J.V.Z. acknowledges support from NASA FINESST Fellowship 80NSSC22K1606. J.V.Z. and E.A.P. acknowledge support from NASA XRP award 80NSSC21K0598.

Chapter 5

The TESS-Keck Survey XXIV: Outer Giants may be More Prevalent in the Presence of Inner Small Planets

A version of this chapter was accepted to be published in *The Astronomical Journal* (Judah Van Zandt et al., 2025, Accepted to AJ).

abstract

We present the results of the Distant Giants Survey, a three-year radial velocity (RV) campaign to search for wide-separation giant planets orbiting Sun-like stars known to host an inner transiting planet. We defined a distant giant to have $a = 1\text{--}10$ AU and $M_p \sin i = 70\text{--}4000 M_\oplus = 0.2\text{--}12.5 M_J$, and required transiting planets to have $a < 1$ AU and $R_p = 1\text{--}4 R_\oplus$. We assembled our sample of 47 stars using a single selection function, and observed each star at monthly intervals to obtain ≈ 30 RV observations per target. The final catalog includes

a total of twelve distant companions: four giant planets detected during our survey, two previously known giant planets, and six objects of uncertain disposition identified through RV/astrometric accelerations. Statistically, half of the uncertain objects are planets and the remainder are stars/brown dwarfs. We calculated target-by-target completeness maps to account for missed planets. We found evidence for a moderate enhancement of distant giants (DG) in the presence of close-in small planets (CS), $P(\text{DG}|\text{CS}) = 31_{-11}^{+12}\%$, over the field rate of $P(\text{DG}) = 16_{-2}^{+2}\%$. No enhancement is disfavored ($p \sim 8\%$). In contrast to a previous study, we found no evidence that stellar metallicity raises the enhancement of $P(\text{DG}|\text{CS})$ over $P(\text{DG})$. We found evidence that distant giant companions are preferentially found in systems with multiple transiting planets and have lower eccentricities than randomly selected giant planets. This points toward dynamically cool formation pathways for the giants that do not disturb the inner systems.

5.1 Introduction

Planets between the size of Earth and Neptune with orbital periods less than one year occur around the majority of Sun-like stars (Petigura et al., 2018). Meanwhile, giant planets with orbital periods longer than one year occur around 10–20% of stars (Rosenthal et al., 2022; Wittenmyer et al., 2020; Fischer et al., 2014; Cumming et al., 2008). The spread in values arises from different stellar samples along with different definitions of what constitutes a “distant giant planet.” The close-in small planet (CS) population was compiled primarily using the transit method (*Kepler*/*K2*/*TESS*), while most distant giants (DG) were discovered with the radial velocity (RV) technique. Historically, transit and RV surveys have targeted nearly disjoint stellar populations (Wright et al., 2012; Winn and Fabrycky, 2015), resulting in few systems thoroughly searched for both planet types.

Different planet formation theories disagree on whether the occurrence rates of CS and

DG planets should be positively or negatively correlated. *In-situ* models predict solid-rich protoplanetary disks will facilitate the growth of planetary cores both interior and exterior to the ice line, suggesting a positive correlation (e.g., Hansen and Murray 2012; Chiang and Laughlin 2013). By contrast, models that involve significant migration predict that distant giants could dynamically perturb the cores of nascent small planets, either barring them from inward migration (Izidoro et al., 2015; Izidoro and Raymond, 2018) or driving them into their host star (Batygin and Laughlin, 2015; Naoz, 2016).

Multiple studies have sought to clarify this picture in recent years by measuring the conditional occurrence of distant giants, $P(\text{DG}|\text{CS})$, the probability of a system hosting a giant planet given the presence of a close-in small planet. Using samples compiled from literature systems with archival RVs, Zhu and Wu (2018) and Bryan et al. (2019) found enhancements of giants in CS-hosting systems over the field rate: $P(\text{DG}|\text{CS}) \approx 30\%$ and $P(\text{DG}|\text{CS}) = 39 \pm 7\%$, respectively. Rosenthal et al. (2022) also found an enhancement of $P(\text{DG}|\text{CS}) = 41 \pm 15\%$ using a uniform sample of legacy RV targets from the California Legacy Survey (CLS; Rosenthal et al. 2021). In contrast, Bonomo et al. (2023) found no evidence for a correlation among a sample of 38 Kepler/K2 systems: $P(\text{DG}|\text{CS}) = 9.3^{+7.7}_{-2.9}\%$. However, Zhu (2024) noted that the average metallicity of the Bonomo et al. (2023) sample was sub-solar, and that correcting for this raised the conditional rate to $39^{+12}_{-11}\%$. The variation among these results highlights the importance of uniform sample selection in statistical analyses. For example, Hot Jupiter occurrence rates measured from transit surveys ($\sim 0.6\%$) differ at the 3σ level from those measured from RV surveys ($\sim 0.8\text{-}1.2\%$), which is likely attributable to the suppression of binary star systems in RV surveys (see Winn and Petigura 2024 and references therein).

The Distant Giants Survey aims to measure $P(\text{DG}|\text{CS})$ in a homogeneously compiled sample of Sun-like stars hosting transiting CS planets detected by *TESS* (Ricker et al., 2015). We introduced the survey and presented the confirmed giant plants in our sample in Van Zandt

et al. (2023). In this work, we present the completed Distant Giants Survey, including a uniform analysis of the partial orbits in our catalog, as well as our measurement of $P(\text{DG}|\text{CS})$. In Section 5.2, we review our survey’s target selection function and observing strategy. We describe our planet detection algorithm in Section 5.3. We summarize our catalog of full and partial orbit detections in Section 5.4, and describe the partial orbits in detail in Section 5.5. We characterize our survey sensitivity in Section 5.6, and measure conditional occurrence framework in Section 5.7. We present our results in Section 5.8 and discuss them in Section 5.9.

5.2 Survey Review

The Distant Giants Survey targeted 47 Sun-like ($M_\star = 0.5 - 1.5 M_\odot$, $T_{\text{eff}} < 6250$ K) *TESS* targets, each hosting at least one transiting planet candidate (Guerrero et al., 2021), compiled to determine the conditional occurrence rate of long-period gas giants in the presence of inner small planets (Van Zandt et al., 2023). We carried out our survey as part of the larger *TESS*-Keck Survey (TKS), a multi-institutional RV survey of over 100 *TESS* objects of interest (Chontos et al., 2022b). We prioritized RV amenability in our sample, selecting stars with low activity ($\log R'_{\text{HK}} < -4.7$), low rotational velocity ($v \sin i < 5.0$ km/s), and high declination ($\delta > 0^\circ$) to facilitate observations from Keck and Lick Observatories. We did not require our targets to have prior RV observations, nor did we exclude targets with extant RVs. We required that the transiting companion have $R_p < 10 R_\oplus$ to include a few sub-Jovian size planets, but we apply further restrictions on inner planet radius in our occurrence calculations (see Section 5.7). Our final sample exhibits a metallicity consistent with solar (median $[\text{Fe}/\text{H}] = 0.10$, $\sigma_{[\text{Fe}/\text{H}]} = 0.17$ dex). For stars with $T_{\text{eff}} > 4800$ K, we report metallicity values calculated using *SpecMatch-Synthetic* (Petigura, 2015), while for stars with $T_{\text{eff}} \leq 4800$ K, we report metallicities from *SpecMatch-Empirical* (Yee et al., 2017).

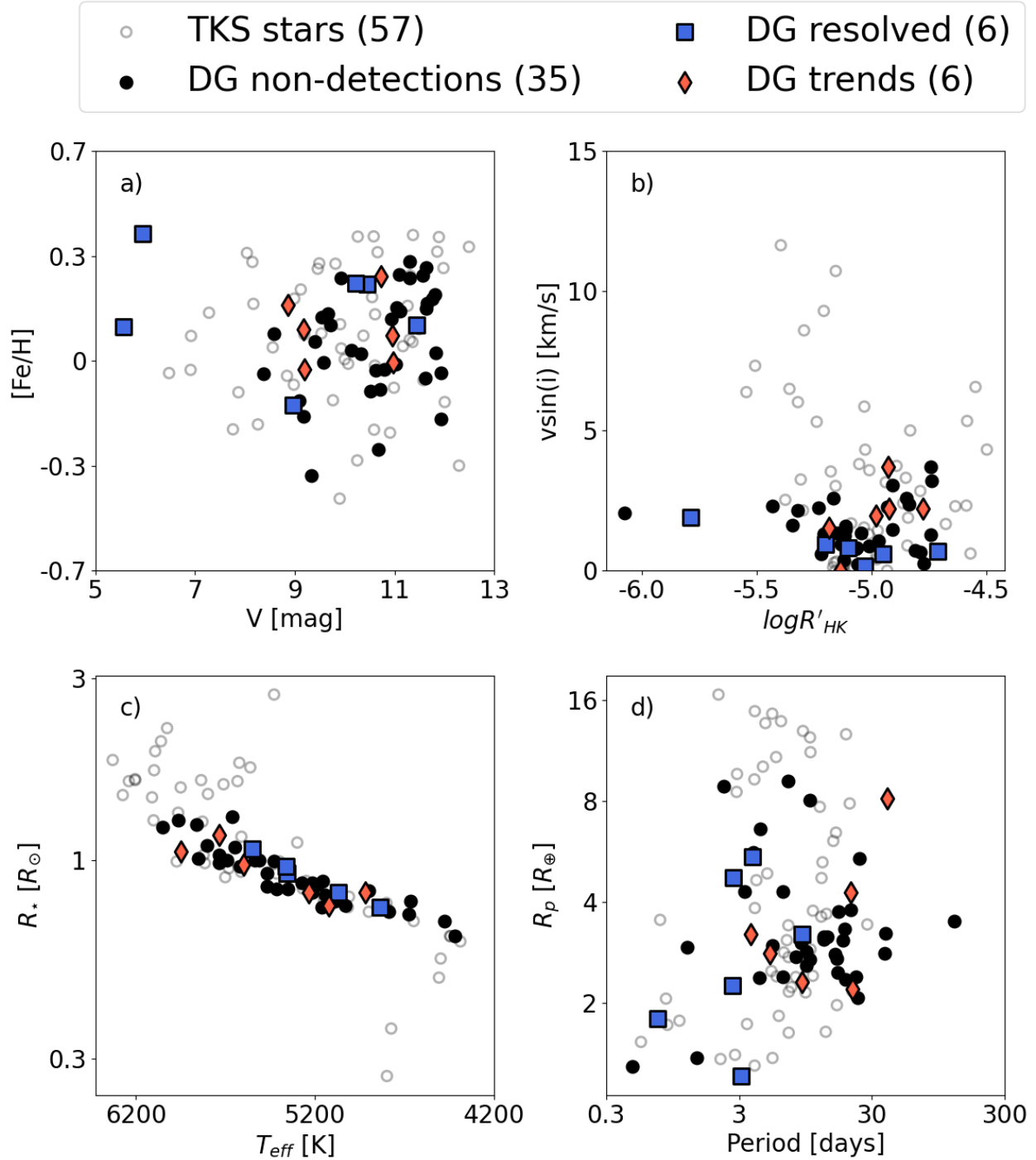


Figure 5.1: **Stellar and transiting planet parameters of the Distant Giants Survey.** Panel (a): metallicity and V -band magnitude of stars with companions detected as resolved orbits (blue squares), companions detected as accelerations (red diamonds), and with no detected companions (black circles). Unfilled circles show other systems in the larger *TESS*-Keck Survey. Other panels are same as (a) but for for $V \sin i$ and $\log R'_{HK}$ (panel b), stellar radius and temperature (panel c), and transiting planet radius and orbital period (panel d). For multi-transiting systems we show the first planet to pass our survey filter (lowest TOI number).

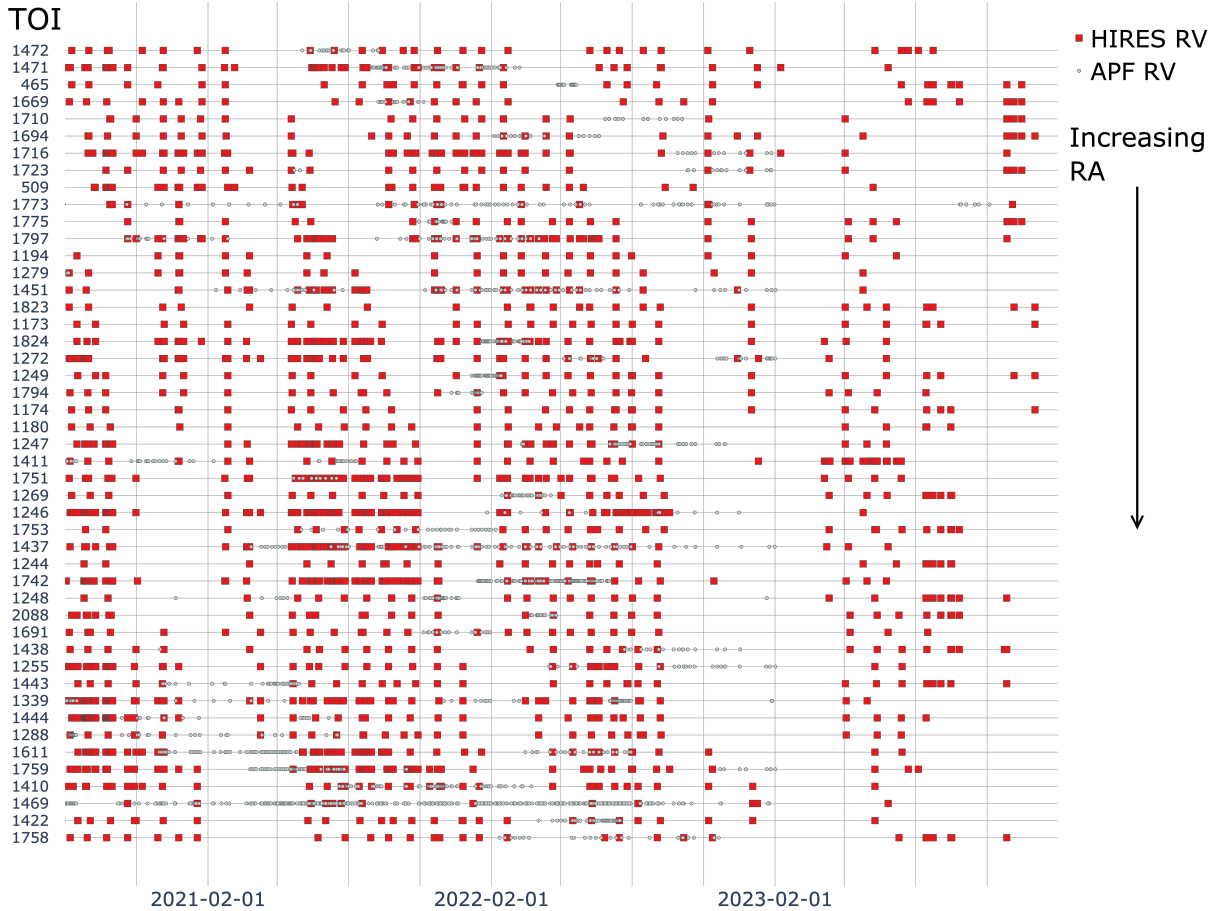


Figure 5.2: **Radial velocity observations of the Distant Giants Survey.** In total we collected 1990 RVs from Keck/HIRES (red squares) and 2036 observations from APF/Levy (gray circles) between 1 August 2020 and 31 January 2024. Note a few targets had prior RVs which are not shown. TOI identifiers are shown in the left margin, ordered by right ascension. Each year label on the x -axis marks February 1, the first day of the “A” observing semester. The typical target in our survey is not accessible from Keck for about three months per year, resulting in the diagonal cadence gaps. The eruption of Mauna Loa in November 2022, as well as unrelated damage to the lower shutter of the Keck I dome between November 2022 and May 2023, resulted in a substantial decrease in observation cadence for targets between RA \sim 16–22 hr, which did not reach elevations $>40^\circ$ during this period.

We summarize the stellar properties of the targets in the TKS and our sample in Figure 5.1, and we provide stellar and transiting planet properties in Table 5.1.

Table 5.1: Distant Giants Sample

TOI	TKS Name	RA (deg)	Dec (deg)	V	T_{eff}	[Fe/H]	$R_p (R_{\oplus})$	P (days)	Distant Giant?	Trend?
465	WASP156	32.8	2.4	11.6	5032	0.29	5.6	3.8	X	X
509	63935	117.9	9.4	8.6	5534	0.09	3.1	18.1	X	X
1173	T001173	197.7	70.8	11.0	5352	0.18	9.2	7.1	X	X
1174	T001174	209.2	68.6	11.0	5124	0.00	2.3	9.0	X	✓
1180	T001180	214.6	82.2	11.0	4790	-0.01	2.8	9.7	X	X
1194	T001194	167.8	70.0	11.3	5428	0.33	8.9	2.3	X	X
1244	T001244	256.3	69.5	11.9	4675	-0.04	2.4	6.4	X	X
1246	T001246	251.1	70.4	11.6	5158	0.17	3.3	18.7	X	X
1247	135694	227.9	71.8	9.1	5648	-0.13	2.8	15.9	X	X
1248	T001248	259.0	63.1	11.8	5272	0.22	6.6	4.4	X	X
1249	T001249	200.6	66.3	11.1	5514	0.29	3.2	13.1	X	X
1255	HIP97166	296.2	74.1	9.9	5214	0.28	2.7	10.3	X	X
1269	T001269	249.7	64.6	11.6	5466	-0.06	2.4	4.3	X	X
1272	T001272	199.2	49.9	11.8	5091	0.21	4.3	3.3	X	X
1279	T001279	185.1	56.2	10.7	5414	-0.10	2.6	9.6	X	X
1288	T001288	313.2	65.6	10.4	5357	0.26	4.7	2.7	✓	X
1339	191939	302.0	66.9	9.0	5355	-0.15	3.2	8.9	✓	X
1410	T001410	334.9	42.6	11.1	4666	0.16	2.9	1.2	X	X
1411	GJ9522A	232.9	47.1	10.5	4478	-0.10	1.4	1.5	X	X
1422	T001422	354.2	39.6	10.6	5852	-0.03	3.1	13.0	X	X
1437	154840	256.1	56.8	9.2	6049	-0.19	2.4	18.8	X	X
1438	T001438	280.9	74.9	11.0	5234	0.08	2.8	5.1	X	✓
1443	T001443	297.4	76.1	10.7	5160	-0.30	2.1	23.5	X	X
1444	T001444	305.5	70.9	10.9	5466	0.14	1.3	0.5	X	X
1451	T001451	186.5	61.3	9.6	5735	-0.01	2.5	16.5	X	X
1469	219134	348.3	57.2	5.6	4839	0.11	1.2	3.1	✓	X
1471	12572	30.9	21.3	9.2	5599	-0.03	4.3	20.8	X	✓
1472	T001472	14.1	48.6	11.3	5186	0.28	4.3	6.4	X	X
1611	207897	325.2	84.3	8.4	5091	-0.04	2.7	16.2	X	X
1669	T001669	46.0	83.6	10.2	5551	0.26	2.2	2.7	✓	X
1691	T001691	272.4	86.9	10.1	5689	0.03	3.8	16.7	X	X
1694	T001694	97.7	66.4	11.4	5069	0.12	5.5	3.8	✓	X
1710	T001710	94.3	76.2	9.5	5734	0.15	5.4	24.3	X	X
1716	237566	105.1	56.8	9.4	5861	0.06	2.7	8.1	X	X
1723	T001723	116.8	68.5	9.7	5800	0.16	3.2	13.7	X	X

Continued on next page

Table 5.1 – Continued from previous page

TOI	TKS Name	RA (deg)	Dec (deg)	V	T_{eff}	[Fe/H]	$R_p (R_{\oplus})$	P (days)	Distant Giant?	Trend?
1742	156141	257.3	71.9	8.9	5733	0.18	2.2	21.3	X	✓
1751	146757	243.5	63.5	9.3	5961	-0.38	2.8	37.5	X	X
1753	T001753	252.5	61.2	11.8	5620	0.03	3.0	5.4	X	X
1758	T001758	354.7	75.7	10.8	5142	-0.03	3.8	20.7	X	X
1759	T001759	326.9	62.8	11.9	4420	-0.20	3.2	37.7	X	X
1773	75732	133.1	28.3	6.0	5363	0.42	1.8	0.7	✓	X
1775	T001775	150.1	39.5	11.6	5349	0.19	8.1	10.2	X	X
1794	T001794	203.4	49.1	10.3	5663	0.02	3.0	8.8	X	X
1797	93963	162.8	25.6	9.2	5948	0.10	3.2	3.6	X	✓
1823	TIC142381532	196.2	63.8	10.7	4917	0.28	8.1	38.8	X	✓
1824	T001824	197.7	61.7	9.7	5216	0.12	2.4	22.8	X	X
2088	T002088	261.4	75.9	11.6	4902	0.31	3.5	124.7	X	X

Note: Properties of the 47 stars in the Distant Giants sample, plus the periods and radii of their inner companions. For multi-transiting systems, we checked planets in the order that TESS detected them, and show the properties of the first one that passed our filters. We truncated period precisions for readability. Median uncertainties are as follows: [Fe/H]—0.06-0.09 dex; R_p —9.6%; P—60 ppm. We calculated metallicity values using the `SpecMatch-Synthetic` code (Petigura, 2015) for host stars with $T_{\text{eff}} > 4800$ K ($\sigma_{[\text{Fe}/\text{H}]} = 0.06$ dex). We used `SpecMatch-Empirical` (Yee et al., 2017) for host stars below this limit ($\sigma_{[\text{Fe}/\text{H}]} = 0.09$ dex). We retrieved all other values from Chontos et al. (2022b). We also indicate in the two right-most columns which systems exhibit either a fully resolved giant planet signal or a long-term RV trend.

We tailored our observing strategy to detect planets with long periods and large K -amplitudes: we observed each target once per month, primarily using the HIRES spectrograph coupled to the Keck I telescope (Vogt et al., 1994), with supplementary observations for bright targets ($V < 10$) from the APF/Levy spectrograph at Lick Observatory (Vogt et al., 2014). We used the HIRES exposure meter to integrate to a minimum SNR of 110 per pixel. We set a goal of 30 total HIRES observations per target over the nominal three-year duration of the survey. We obtained median values of 37 RV observations, an 1109-day (3.0-year) observing

baseline, and 1.7 m/s photon-limited RV uncertainty per target. We add HIRES’s 2 m/s instrumental noise floor (Fulton, 2017b) to this last value in quadrature to obtain 2.6 m/s total RV uncertainty. We collected a total of 4026 RVs, 1990 of which were taken using Keck/HIRES. We reached at least 25 RVs and at least 1096-day (3.0-year) baselines for all of our 47 systems. We show our target cadence over the survey duration in Figure 5.2, and provide a subset of the full RV data set in Table 5.2.

Table 5.2: Distant Giants Radial Velocities

TOI	TKS Name	BJD	RV (m/s)	RV Error (m/s)	Instrument
TOI-465	WASP156	2.459071e+06	-18.054364	1.564020	hires_j
TOI-465	WASP156	2.459093e+06	1.107389	1.559804	hires_j
TOI-465	WASP156	2.459143e+06	-0.437076	1.581019	hires_j
TOI-465	WASP156	2.459182e+06	-12.919443	1.729959	hires_j
TOI-465	WASP156	2.459239e+06	5.979829	2.182647	hires_j
TOI-465	WASP156	2.459269e+06	18.029111	1.558576	hires_j
TOI-465	WASP156	2.459396e+06	11.567155	1.714726	hires_j
TOI-465	WASP156	2.459445e+06	21.068103	1.478714	hires_j
TOI-465	WASP156	2.459477e+06	1.831015	1.563436	hires_j

Note: A subset of the radial velocity measurements used in our analysis. All measurements were collected between 1 August 2020 and 31 January 2024 using the Keck/HIRES and APF/Levy spectrometers. We provide the full set of 4026 RVs in the online publication of this chapter.

5.3 Planet Detection Algorithm

We detected planets using an automated algorithm that we applied uniformly to all RV timeseries. In broad strokes, our approach follows that of the Rosenthal et al. (2021) analysis of the California Legacy Survey (CLS). We used the `RVSearch` blind search algorithm to select an RV model by iteratively adding planet signals, then we fit the preferred model to the RV data using `radvel`. However, there are some key differences between our survey and CLS:

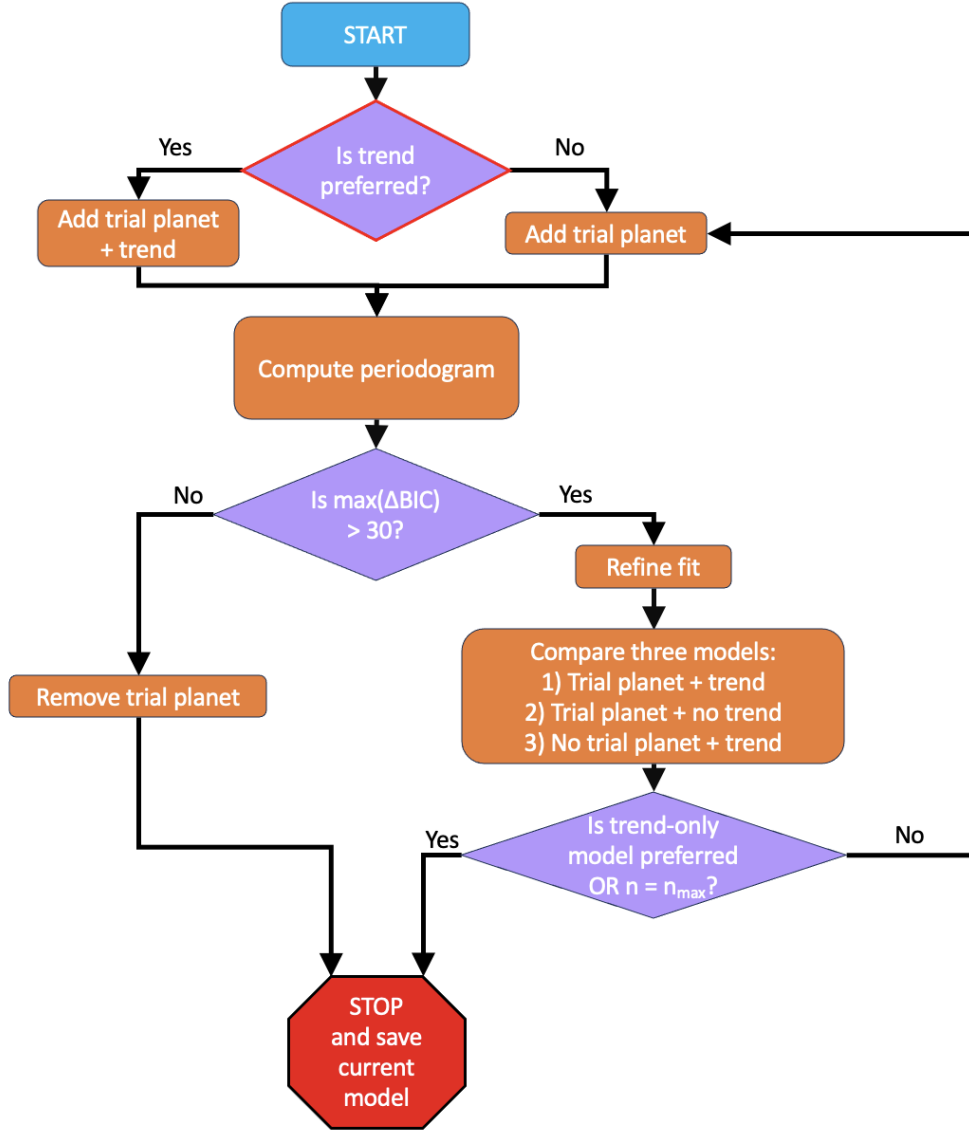


Figure 5.3: **Flow diagram of our planet detection algorithm.** We used the same algorithm for detecting planets (Section 5.4) and for computing completeness (Section 5.6). We began by initializing an orbital model with the RV data and the ephemerides of any known transiting planets. We then determined whether the data supported the inclusion of a trend, that is, if a trend model was favored over a flat model by $\Delta\text{BIC} > 5$, after which we added a new planet to the model. We computed ΔBIC between the starting model and a model with a trial planet over a dense grid of trial periods. If the maximum ΔBIC exceeded 30, we performed a final model comparison test to select a model with a planet, a trend, or both. We iteratively added planets to the model in this way until no more were found. For the injection/recovery experiments described in Section 5.6, we began with the final model from Section 5.4 to retain any planets found during the initial search. We then injected a synthetic planetary signal into the data and began the recovery at the trend test step (outlined in red). When the search terminated, we checked whether the injected signal was recovered, either as a planet or as a trend, and recorded the result.

in the CLS, the targets had more RVs ($N \sim 70$) recorded over longer observing baselines ($t \sim 20$ yr). We therefore tuned the search algorithm to the characteristics of our dataset. We summarize our procedure schematically in Figure 5.3 and provide further details below.

We first established an initial model which included the transiting planet(s) along with their periods P and times of conjunction t_c , which we retrieved from the *TESS* data validation reports. We optionally included a linear and/or quadratic term in our model to account for any long-term non-periodic variability.

Next, we constructed a grid of trial periods. The spacing is such that there is at most a phase slip of 1 radian between the trial periods to ensure significant peaks are not missed. For each candidate period, we introduced an additional planet to the model, which we will refer to as the ‘trial planet.’ With the trial planet’s period fixed, we fit the remaining orbital parameters — time of periastron t_p , eccentricity e , argument of periastron ω , and RV semi-amplitude K . If a trend was included based on the prior step, we allowed its parameters to vary as well. During the fitting, we held parameters of all other planets fixed. We calculated the change in Bayesian Information Criterion (ΔBIC ; Schwarz 1978) between each model and a model without the added planet. We repeated this step for all trial periods to produce a ΔBIC periodogram.

In principle, we may adopt any significance threshold to accept or reject periodic signals, provided that it is used in both the initial search and the completeness correction (described in Section 5.6). We identified $\Delta\text{BIC} > 30$ as a threshold that produced relatively few false positive and false negative detections across our sample. If the maximum ΔBIC value did not exceed 30, we removed the trial planet from the model, designated the current model as preferred, and terminated the search. If the maximum ΔBIC exceeded 30, we refined the fit using a finer period search, and performed a final comparison to select a trend or a planetary model. To do this, we generated three copies of the orbit model: (1) trial planet and no trend, (2) no trial planet and a trend, and (3) both trial planet and trend. From these, we

selected the model with the highest ΔBIC .

If our three-way model comparison favored a trend only, we designated the current model as preferred. Otherwise, we added another planet to our model and repeated the search until one of the termination conditions was met. As an additional termination condition, we set a maximum of eight planets on each system’s model, though in practice never found evidence for more than two. After determining our final preferred model, we derived credible orbital solutions by sampling our posterior probability with `emcee` (Foreman-Mackey et al., 2013).

5.4 Planet Catalog

5.4.1 Six companions with resolved orbits

We identified six giant planets with $P \lesssim t_{\text{base}}$ where we could fully resolve the orbits and measure planetary parameters with small fractional uncertainties. Two such planets, HD 219134 g (Vogt et al., 2015) and HD 75732 d (Fischer et al., 2008), were known prior to the start of our survey. We announced the discovery of two more, TOI-1669 b and TOI-1694 c, in Van Zandt et al. (2023), and confirmed the mass of HD 191939 f in Lubin et al. (2024b). Knudstrup et al. (2023) independently resolved TOI-1288 c for a total of six giants. We display the masses and periods of these giants and their inner companions in Figure 5.4 and Table 5.3.

Table 5.3: Resolved Distant Giants planet properties

TOI	TKS Name	Transiting Planet			Giant Planet			Ref
		Period (days)	Radius (R_{\oplus})	Mass (M_{\oplus})	Period (days)	Separation (AU)	$M \sin i$ (M_J)	
1288	T001288	2.7	5.24 ± 0.09	42 ± 3	443^{+11}_{-13}	1.1 ± 0.4	0.26 ± 0.02	1
1339	191939	8.9	3.39 ± 0.07	10.4 ± 0.9	8.5 ± 0.9	3.6 ± 0.2	3.2 ± 0.5	2
1469	219134	3.1	1.3 ± 0.6	4.5 ± 0.5	2101 ± 3	3.06 ± 0.04	0.31 ± 0.01	3, 4
1669	T001669	2.7	2.4 ± 0.2	5.2 ± 3.1	502 ± 16	1.13 ± 0.03	0.57 ± 0.07	5

Table 5.3: (continued)

TOI	TKS Name	Transiting Planet			Giant Planet			Ref
		Period (days)	Radius (R_{\oplus})	Mass (M_{\oplus})	Period (days)	Separation (AU)	$M \sin i$ (M_J)	
1694	T001694	3.8	5.4 ± 0.2	26 ± 2	389 ± 4	0.98 ± 0.02	1.05 ± 0.05	5
1773	75732	0.7	2.0 ± 0.3	8.3 ± 0.3	5285 ± 5	5.61 ± 0.09	3.84 ± 0.08	4, 6

References — (1) [Knudstrup et al. \(2023\)](#), (2) [Lubin et al. \(2024b\)](#), (3) [Vogt et al. \(2015\)](#), (4) [Rosenthal et al. \(2021\)](#), (5) [Van Zandt et al. \(2023\)](#), (6) [Dawson and Fabrycky \(2010\)](#)

Note: Columns 3–5 refer to properties of the transiting companion, and columns 6–8 refer to the distant giant. The right-most column gives the reference(s) for giant planet mass and period, as well as the transiting planet mass, if available. We list our own fitted giant planet separations. For TOI-1288, the reference is for all parameters of both planets. We cite transiting planet parameters for HD 191939 from [Lubin et al. \(2022b\)](#). We cite transiting planet parameters for the remaining systems from the *TESS* Data Validation Reports. Typical transiting planet period uncertainties are of order $10^{-4} - 10^{-5}$ days. We include HD 191939, HD 219134, and HD 75732 in this table because we detected them in our full RV data sets. However, we treat these signals as trends in our homogeneous statistical analysis.

5.4.2 Six companions with partial orbits

We detected six massive companions as long-term linear and/or quadratic RV trends and list them in Table 5.4. We noted that multiple trends with 3σ significance manifested in our sample, only to be ruled out by subsequent RV measurements. We therefore adopted a trend threshold of 4σ to exclude these signals while retaining as many true trends as possible. The masses and orbital period of such objects have large uncertainties; often the RVs alone are insufficient to determine whether the object is a planet, brown dwarf, or star. We compute

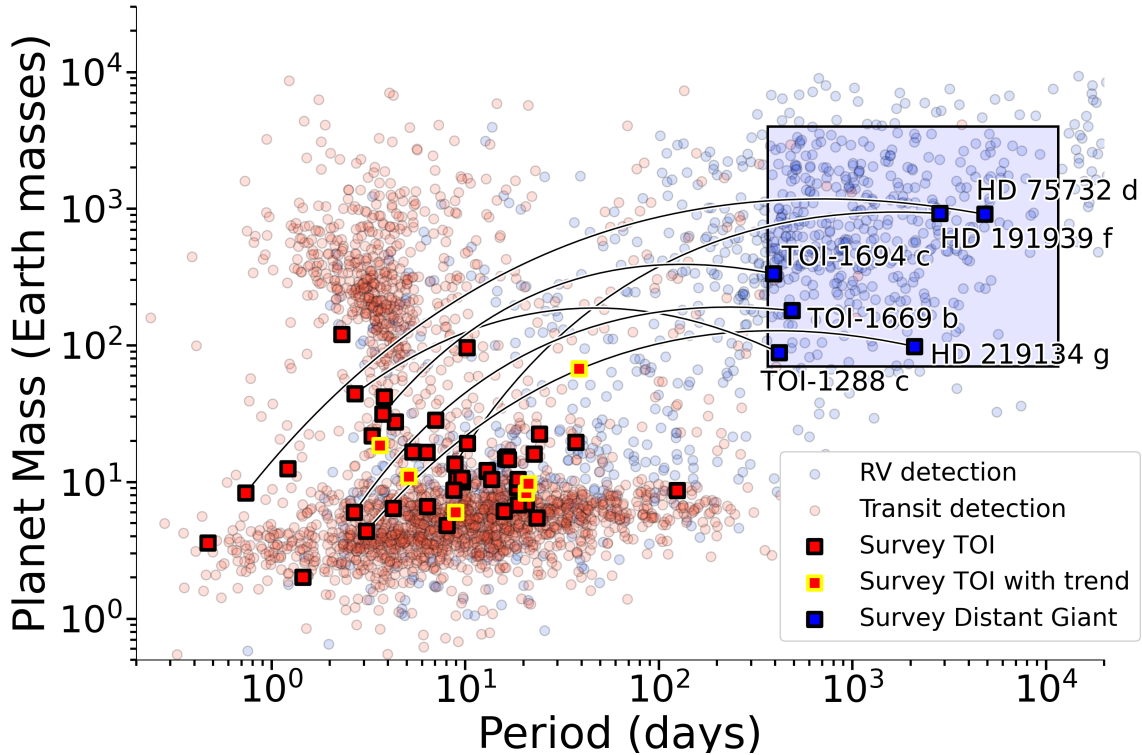


Figure 5.4: **Close-in small planets and their distant giant companions.** Masses and periods of exoplanets from our survey (bold squares) and the NASA Exoplanet Archive (faded circles) for context. Red/blue points indicate planets discovered using the transit/RV method. Red squares show true masses of transiting planets in the Distant Giants Survey measured by RVs (Polanski et al., 2024), while blue squares show minimum mass measurements ($M \sin i$). For systems with multiple transiting planets, we show the parameters of the transiting planet with the lowest TOI designation that passed our filters. Red squares with yellow borders indicate systems in which we detected a linear/quadratic trend. Giant planets in our sample are connected to the inner planet in their system by a black line. The box corresponds to our nominal definition of a Distant Giant.

the relative probability of each scenario in Section 5.5, incorporating astrometric and imaging constraints where available. In Figure 5.5 we show the planet masses and separations for each system in our survey, and indicate the systems in which we detected a trend.

Table 5.4: Distant Giants trend data

TOI	TKS Name	$\dot{\gamma}$ (m/s/yr)	$\ddot{\gamma}$ (m/s/yr ²)	$\Delta\mu$ (mas/yr)	Direct Imaging?	P(planet)	P(BD)	P(star)
1174	T001174	-27.0 ± 3.7	14.3 ± 2.1	—	True	0.53	0.22	0.26

Continued on next page

Table 5.4 – continued from previous page

TOI	TKS Name	$\dot{\gamma}$ (m/s/yr)	$\ddot{\gamma}$ (m/s/yr ²)	$\Delta\mu$ (mas/yr)	Direct Imaging?	P(planet)	P(BD)	P(star)
1339	191939	26.9 ± 0.5	-9.9 ± 0.5	0.13 ± 0.03	True	0.98	0.02	0.00
1438	T001438	10.9 ± 1.4	-13.5 ± 1.7	—	True	0.79	0.08	0.12
1469	219134	-4.4 ± 0.3	0.0 ± 0.0	0.15 ± 0.06	True	1.00	0.00	0.00
1471	12572	-22.0 ± 0.4	-0.5 ± 0.5	0.07 ± 0.05	True	0.61	0.08	0.31
1742	156141	13.1 ± 0.5	-6.4 ± 0.5	—	True	0.78	0.15	0.08
1773	75732	-68.6 ± 12.5	6.8 ± 1.0	0.07 ± 0.06	False	0.91	0.03	0.07
1797	93963	-9.4 ± 1.8	-12.7 ± 1.8	—	True	0.81	0.07	0.12
1823	TIC142381532	-8.6 ± 2.1	0.5 ± 0.9	—	True	0.32	0.31	0.38
Total						6.73	0.96	1.34

Note: RV, astrometric, and imaging information for the nine trend systems in our sample. We include HD 191939, HD 219134, and HD 75732 in this table despite knowing that their trends are planetary in origin because we treated their signals as trends in our statistical analysis. The three columns at the right give the probability of the measured signal in each system originating from a planetary, brown dwarf, or stellar companion between 3–64 AU. We derived these probabilities by integrating the posterior distributions we calculated using `ethraid` over the appropriate mass interval. Summing the probabilities for each object type suggests that these nine systems host 5–6 planets, 2–3 brown dwarfs, and ~ 1 stellar companion.

5.4.3 Treatment of pre-survey data

A handful of our targets’ data sets significantly exceed our three-year, 30-observation criteria. For example, HD 219134 and HD 75732 each have >600 observations over ~ 30 years. For such data sets, it is possible to detect many planets. We found that our detection pipeline, which was tuned for $N \sim 30$ observations and $t_{\text{base}} \sim 3$ yr, struggled to identify the correct orbital parameters of the smaller planets in these systems. We opted for a simple scheme by setting a maximum observing baseline of four years, which truncated the data sets of four systems: HD 207897, HD 191939, HD 219134, and HD 75732. The last three of these each

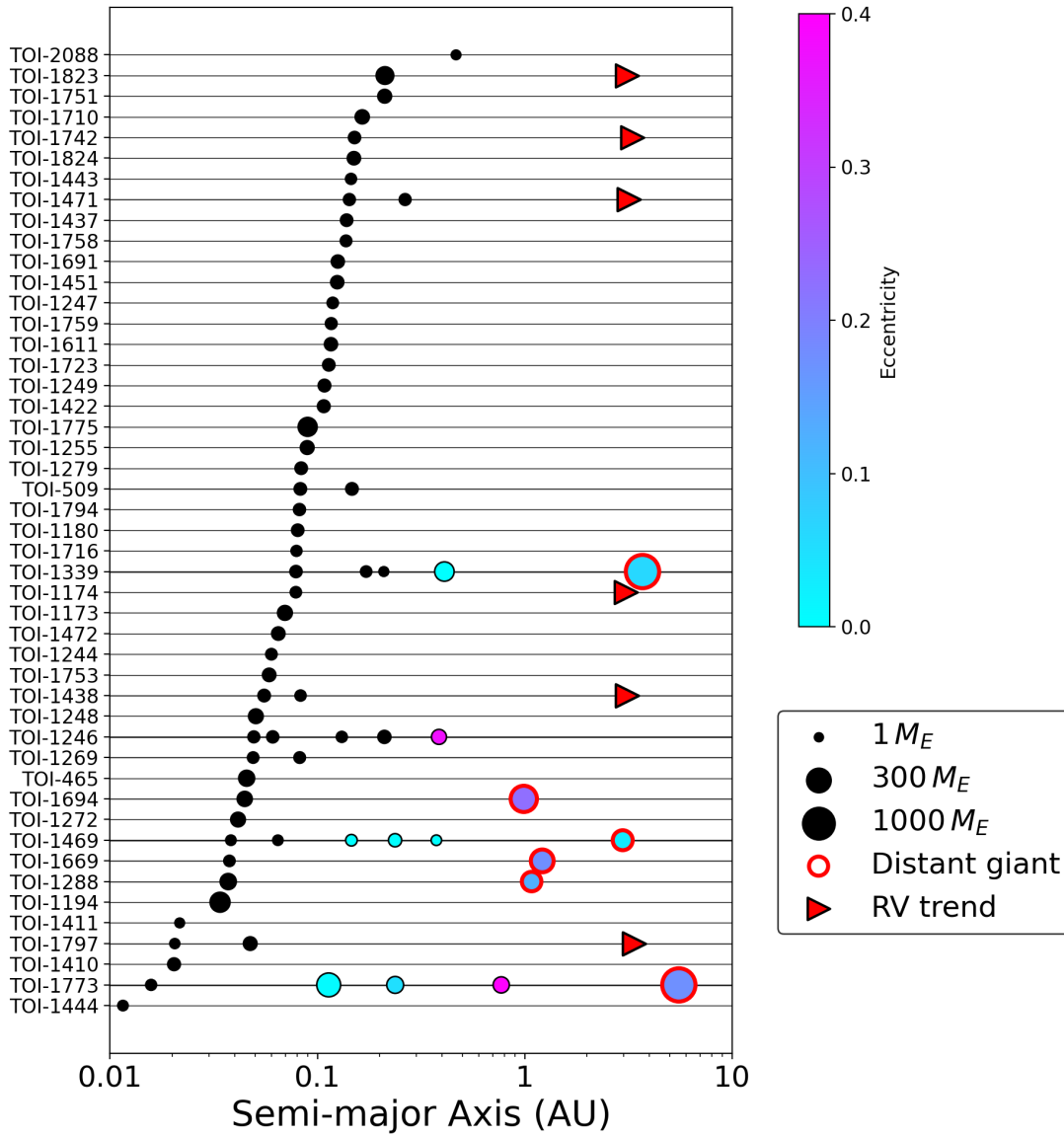


Figure 5.5: Masses and orbital spacings of the planets in each system in our survey. Systems are ordered according to the semi-major axis of the inner-most transiting planet. Transiting planets are shown with black markers and non-transiting planets are colored according to their eccentricity. Marker sizes are proportional to the square root of the planet true mass (for transiting planets) or minimum mass (for non-transiting planets). We use red borders to indicate planets which meet our definition of a distant giant. For systems with RV trends, we place a red triangle at a separation corresponding to six years, the approximate maximum period for which we could resolve a Keplerian orbit. Based on Figure 4 of [Weiss et al. \(2024\)](#).

host a distant giant with $P > 5$ years, which presented as trends in the truncated data. We treated these signals as trends for our trend analysis (Section 5.5) and occurrence calculations (Section 5.7), but recognized their planetary nature in our analysis of correlations between distant giants and inner small planet properties (Section 5.8). HD 219134 and HD 75732 each have many four-year windows which we could have selected for our analysis. We conducted our occurrence calculation multiple times using different observing windows, and therefore sampling different phases of the giant planet in each system, to verify that our results were not sensitive to our choice of observing window.

5.5 Trend Analysis

5.5.1 ethraid

We characterized companions detected as trends using `ethraid` (Van Zandt and Petigura, 2024a). This code determines the masses and orbital periods that are consistent with a measured RV trend, imaging constraints, and/or astrometric accelerations through importance sampling.

We assumed that the measured signal originated from a single object (as opposed to multiple bodies or stellar activity). We also assumed that its semi-major axis is between 3 and 64 AU; smaller orbits would be resolved as Keplerians and objects with larger orbits would have such high masses that they would be easily detected as stars. We considered companions between $0.1 - 1000 M_J$, covering planets, brown dwarfs, and low-mass stars. We adopted an informative M - a prior, which we expand upon in Section 5.5.2

We included astrometric constraints from the *Hipparcos* – *Gaia* Catalog of Accelerations (HGCA, Brandt 2021) and imaging constraints from Polanski et al. (2024). The joint M - a

constraints for these objects are shown in Appendix 5.12 along with notes on each system. For each system, we collected the posterior samples output by `ethraid` and integrated the distribution over three mass intervals: $M < 13 M_J$, $13 M_J < M < 80 M_J$, and $80 M_J < M$. We report these fractions in Table 5.4 as the probability that the companion is a planet, brown dwarf, or star, respectively.

5.5.2 Mass-Separation prior

We implemented a prior on mass and separation to reflect the intrinsic prevalence of companions with different properties. We derived this prior distribution based on the occurrence rates of sub-stellar (CLS; Rosenthal et al. 2021) and stellar (Raghavan et al., 2010) companions to Sun-like stars.

We chose to define this prior over the interval 0.03 – 64 AU, 0.05 – 1000 M_J , extending to smaller masses and separations than our trend analysis required both because the CLS has high sensitivity and many detections in this regime (see Figure 5.6), and to examine features of planet and brown dwarf occurrence as a function of separation (see Section 5.9.4). We calculated survey completeness in this domain using the ensemble of injection/recovery experiments published by Rosenthal et al. (2021).¹ Following previous occurrence studies (see Winn and Petigura 2024 for a review) we divided this region into two-dimensional intervals uniform in logarithmic space. We used five intervals in mass and five intervals in semi-major axis, giving 25 cells. Our mass bins approximately correspond to sub-Jupiters (0.05–0.3 M_J), Jupiter analogs (0.3–3 M_J), super-Jupiters (3–13 M_J), brown dwarfs (13–80 M_J), and stars (80–1000 M_J). We chose our semi-major axis bounds to approximate log-uniform spacing between 0.03–64 AU. We employed the Poisson occurrence method of Section 5.7.2 to calculate the occurrence rate in each cell.

¹Accessible at <https://github.com/leerosenthalj/CLSI/tree/master>

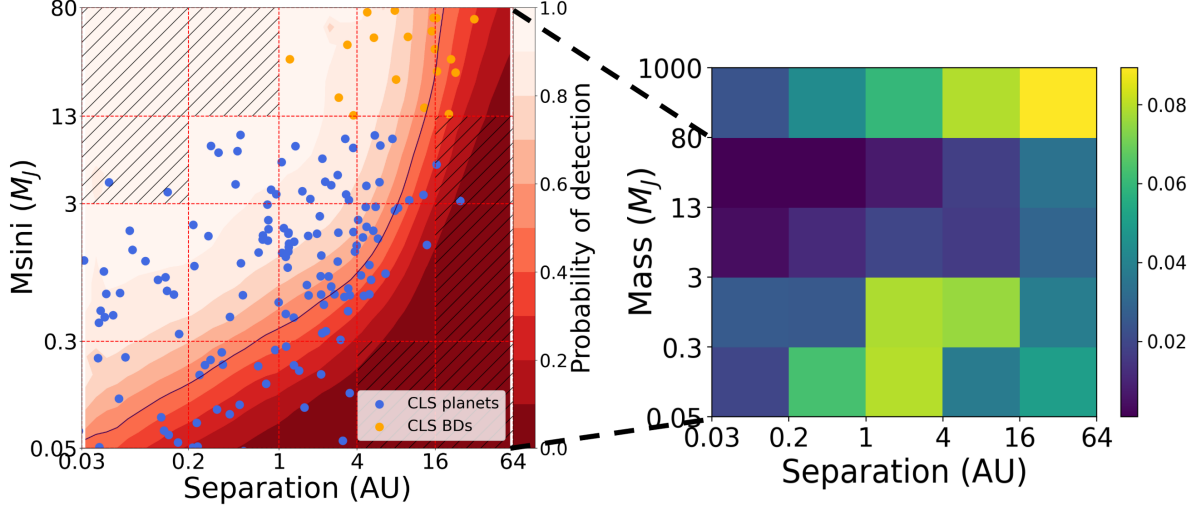


Figure 5.6: **Mass/separation prior informed by the Rosenthal et al. (2021) and Raghavan et al. (2010) surveys.** **Left:** Minimum masses and orbital separations of the CLS (Rosenthal et al., 2021) sample of planets (blue points) and brown dwarfs (orange points). We also show the survey-averaged completeness map (red contours) emphasizing the 50% contour with a black line. We compute companion occurrence in the cells defined by the red dashed lines. Hatch marks show cells containing fewer than three objects, giving rise to highly uncertain occurrence rates. However, inspection of the RV constraints in Appendix 5.12 shows negligible overlap with these regions, so they do not affect our overall results. **Right:** The domain of M and a we explore in our companion search. Each M - a sub-domain is colored with the number of objects per star and serves as our joint M - a prior described in Section 5.5.2. The highest mass bins are based on the Raghavan et al. (2010) rates.

For our stellar prior, we used the stellar period distribution of Raghavan et al. (2010). They fit a normal distribution to a log-period histogram of 259 stellar companions detected among a sample of 454 Sun-like stars, finding that $\log P \sim \mathcal{N}(5.03, 2.28)$. We integrated this distribution to estimate the number of companions in each of our five semi-major axis intervals. We then applied the same occurrence model to these cells, approximating 100% completeness. We illustrate our mass/separation prior in Figure 5.6.

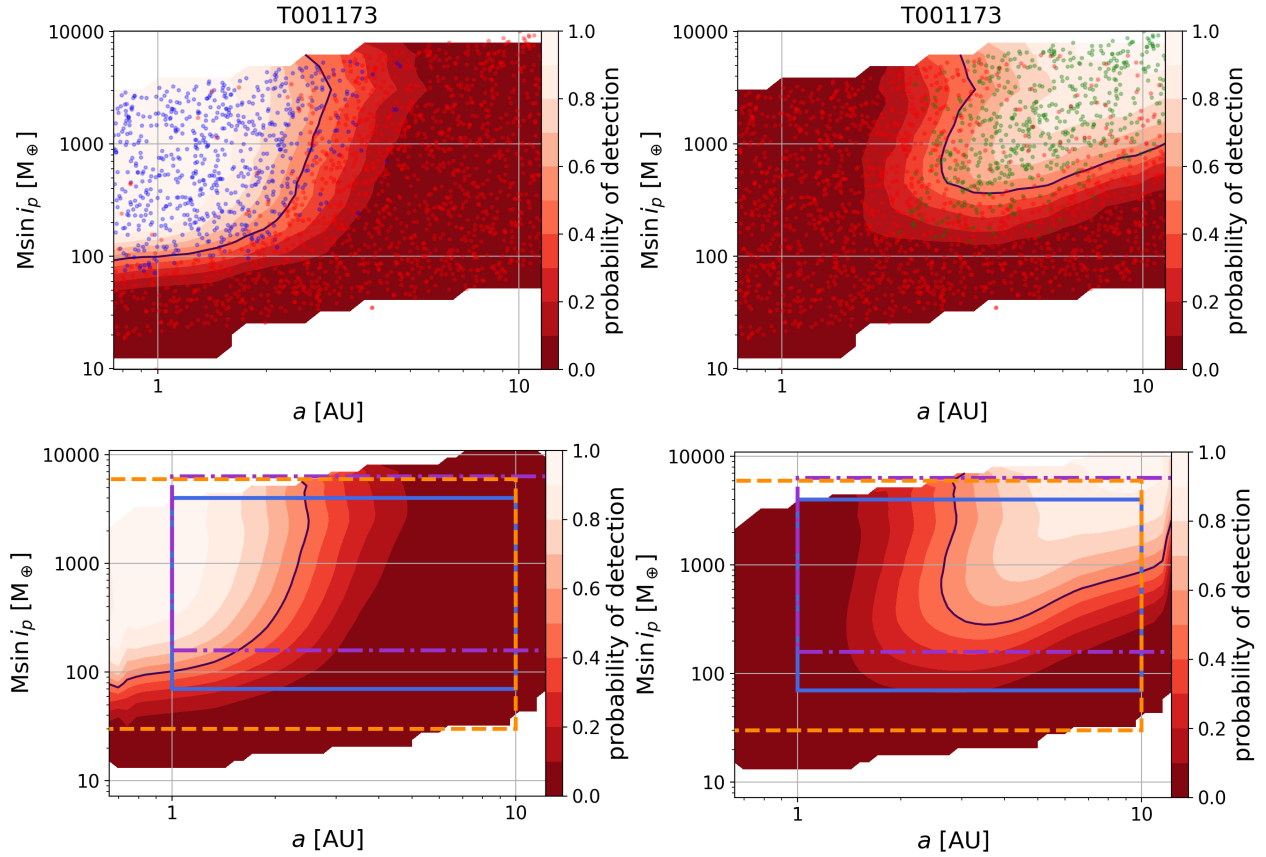


Figure 5.7: Side-by-side comparison of injection/recovery results and calculated completeness to resolved orbits (left) and trends (right). We tracked whether our automated search algorithm recovered injected RV signals successfully (blue/green points for resolved orbits/trends), or unsuccessfully (red points). From this collection of recoveries, we calculated a sensitivity map, with contour lines marking completeness deciles, and the black contour denoting the 50% completeness boundary. We injected 2000 signals for each system. **Top row:** Completeness for a typical system in our survey (TOI-1173: 3.9-year baseline, 27 observations). **Bottom row:** Average completeness of the 47 targets in our survey, with blue boxes indicating our nominal definition of a distant giant. Our average sensitivity in this interval is 30% for resolved orbits and 35% for trends. Orange and purple dashed boxes indicate the giant planet definitions used by Rosenthal et al. (2022) and Bryan et al. (2019), respectively. Our survey had 32% (27%) sensitivity to resolved orbits (trends) using the Rosenthal et al. (2022) definition, and 30% (43%) sensitivity using that of Bryan et al. (2019). Note that we treated resolved orbits and trends as distinct detection classes, meaning that an orbit recovered as a trend was considered an unsuccessful recovery in the resolved recovery map, and vice versa.

5.6 Survey Sensitivity

5.6.1 Distant Giants Survey

While we designed the Distant Giants survey to yield a high uniformity in sensitivity to distant giants, each star has differences in RV noise properties, observational sampling, and other properties. We evaluated our sensitivity to both resolved and partial orbits on a star-by-star basis using an injection/recovery scheme.

We began with the system’s preferred orbital model (see Section 5.3), subtracted any fitted trend/curvature from the data, and injected a synthetic planetary model. We generated these planets according to the following distributions: $\log P \sim \mathcal{U}(\log P_{\min}, \log P_{\max})$, $\log K \sim \mathcal{U}(\log K_{\min}, \log K_{\max})$, $e \sim \mathcal{B}(0.867, 3.03)$, $t_p \sim \mathcal{U}(0, P)$, $\omega \sim \mathcal{U}(0, 2\pi)$. Here, $P_{\min}, P_{\max} = (250 \text{ d}, 15000 \text{ d})$, $K_{\min}, K_{\max} = (2 \text{ m/s}, 300 \text{ m/s})$, and $\mathcal{B}(0.867, 3.03)$ is the beta distribution fit by [Kipping \(2013\)](#), which we chose to match [Rosenthal et al. \(2021\)](#) (see Section 5.6.2). Figure 5.7 shows the suite of experiments for TOI-1173 as an example. We permitted our algorithm to identify at most one additional planet via the same blind search described in Section 5.3 and in Figure 5.3, beginning by testing for a trend.

When the search terminated, we recorded any signals recovered during the search. We considered a planet *successfully* recovered if P , t_p , and K matched the injected values to 25% or better. We considered a recovered trend significant if the fitted value corresponded to $\geq 8 \text{ m/s}$ RV variation (i.e., three times the typical RV measurement error) over a three-year period. This threshold excluded low-significance trends in an analogous way to our 4σ trend threshold for our real catalog.

We computed completeness maps in $a\text{-}M \sin i$ space for each target by performing a moving average over the set of successful and unsuccessful detections (see Figure 5.7 for an example). The survey sensitivity is the average of all individual maps (see bottom row of Figure 5.7).

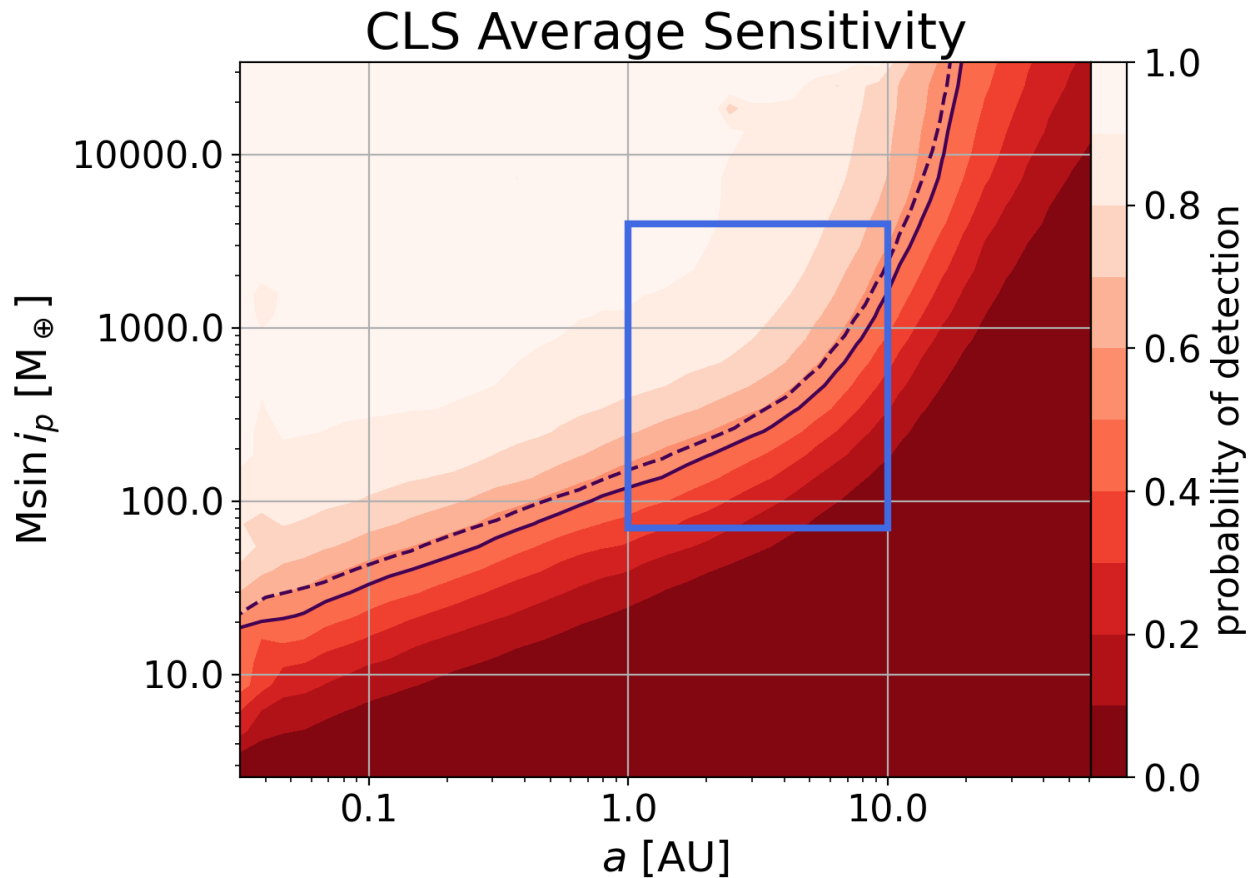


Figure 5.8: Average sensitivity to companions as a function of minimum mass and separation for the California Legacy Survey. Shaded regions show domains of constant detection probability, and the solid black contour shows the 50% detection probability boundary. We recalculated this map after adjusting for inclination effects to determine the CLS sensitivity to true mass (see Section 5.6.2). We show the 50% boundary of the adjusted map as a dashed black line. We use a blue rectangle to show our nominal definition of a distant giant ($a = 1 - 10$, $M = 70 - 4000 M_{\oplus}$). The average CLS sensitivity to minimum/true masses within this domain is 59%/52%.

As a point of reference, our sensitivity to Jupiter-mass planets as resolved orbits is nearly 100% at 1 AU and declines to 60% near 2 AU (roughly the average baseline). Planets three times the mass of Jupiter are recovered as trends with 60% completeness between 3–10 AU.

5.6.2 California Legacy Survey

To calculate the field occurrence rate of distant giants, $P(\text{DG})$, we averaged together the 719 target-by-target completeness maps computed by Rosenthal et al. (2021) for the CLS sample. Their sensitivity is superior to ours due to their larger RV data sets and longer target baselines. For example, they maintain $\geq 50\%$ sensitivity to $1 M_J$ objects out to 6 AU (see Figure 5.8), whereas our sensitivity to Jupiter analogs drops precipitously beyond 2 AU.

A direct comparison of Distant Giants conditional occurrence to CLS field occurrence makes the implicit assumption that the two samples have the same inclination distribution. However, if multi-planet systems inside/outside 1 AU are highly aligned, our selection of systems with transiting planets will favor distant giant planets with edge-on orbits. All else being equal, we would expect increased sensitivity at a given mass in the Distant Giants sample since edge-on planets are easier to detect.

In the limiting case where all CS+DG systems are perfectly aligned (i.e., $\sin i = 1$), the completeness maps shown in Figure 5.7 should be interpreted as $M-a$ (as opposed to $M \sin i-a$). On the other hand, if all systems have random orientations, then the maps are on equal footing with those of the CLS sample.

We modeled both extremes by recomputing the CLS completeness in the following manner: for each injected orbit, we drew 10 inclinations from a distribution uniform in $\cos i$. We then generated 10 realizations of the true mass of the injected companion by dividing $M \sin i$ by $\sin i$ for each of the inclination draws. We maintained each injection's status as a successful/unsuccessful recovery during this process. We then computed the survey-averaged completeness of the CLS in $M-a$ (as opposed to $M \sin i-a$). The difference between the corrected and uncorrected maps is minor: at 3 AU, the CLS sensitivity to $M \sin i=1 M_J$ is 60%, while the sensitivity to $M=1 M_J$ is 50%. We show both extremes in Figure 5.8.

The average completeness of the CLS survey to minimum masses within our nominal distant giant domain is 59%, while the sensitivity to true masses in the same interval is 52%. This change produces a 1σ (2%) difference in our inferred field occurrence rate $P(\text{DG})$.

5.7 Computing Planet Occurrence

5.7.1 Definitions

In this work, we define a ‘close-in’ planet to have $a < 1$ AU and a distant planet to have $a = 1 - 10$ AU. We define a ‘small’ planet to have $R_p = 1 - 4 R_\oplus$ for CS planets and a ‘giant’ planet to have $M = 70 - 4000 M_\oplus$ ($0.22 - 12.6 M_J$). We also consider modified boundaries when making direct comparisons to previous studies.

5.7.2 Occurrence Model

Our goal is to measure *both* the conditional occurrence of giant planets in systems with small planets $P(\text{DG}|\text{CS})$ *and* the field occurrence rate of giant planets $P(\text{DG})$ and compare the two rates. For both rates we are considering the number of planets per star.

Following the prescription in [Rosenthal et al. \(2022\)](#), we modeled our observed planet catalog as a realization of a censored Poisson process. The process is censored because some planets are missed in regions of imperfect survey completeness ($Q(a, M) < 1$). Our task is to infer the parameters, θ , of the occurrence rate density function $\lambda(a, M|\theta)$, where the latter is defined as the number of planets per star per $\log a$ - $\log M$ interval. We model λ as log-uniform over the DG domain; θ is thus a single number.

The appropriate likelihood has been described previously (e.g., [Rogers and Owen 2021](#)) and

is

$$P(\{\boldsymbol{\omega}\}, N_p | \boldsymbol{\theta}) = \frac{e^{-\Lambda} \Lambda^{N_p}}{N_p!} \prod_{k=1}^{N_p} \frac{Q(\boldsymbol{\omega}_k) \lambda(\boldsymbol{\omega}_k | \boldsymbol{\theta})}{\Lambda}. \quad (5.1)$$

Here, N_p is the number of observed planets, $\boldsymbol{\omega}_k$ is the (a, M) tuple for the k th planet, and Λ — the ‘intensity parameter’ — is

$$\Lambda = N_\star \int Q(\boldsymbol{\omega}_k) \lambda(\boldsymbol{\omega}_k | \boldsymbol{\theta}) d \log(a) d \log(M), \quad (5.2)$$

where N_\star is the number of host stars in our sample. Conceptually, the likelihood in Equation 5.1 can be understood as the product of two terms: the term before the product operator is the probability of observing N planets regardless of their parameters, and the second is the probability of observing those planets with their specific a and M values.

Since companions are either detected as trends or resolved orbits, we construct separate likelihoods for each and multiply their results.

$$P(\{\boldsymbol{\omega}_{\text{pl}}, \boldsymbol{\omega}_{\text{tr}}\}, N_{\text{pl}}, N_{\text{tr}} | \boldsymbol{\theta}) = P(\{\boldsymbol{\omega}_{\text{pl}}\}, N_{\text{pl}} | \boldsymbol{\theta}) \cdot P(\{\boldsymbol{\omega}_{\text{tr}}\}, N_{\text{tr}} | \boldsymbol{\theta}) \quad (5.3)$$

Here, the subscripts “pl” and “tr” refer to the resolved and trend sub-samples, respectively.

We capture catalog uncertainties by sampling many catalog realizations from our full set of posteriors, where each realization comprises one sample from each of the 12 posteriors (three resolved orbits and nine trends). We discard any of the samples that fall outside of our occurrence domain, and derive the posterior surface using Equation 5.3. We average together many such distributions to obtain a robust estimate of the occurrence rate density.

5.7.3 Occurrence Computation

We used this occurrence methodology to calculate $P(\text{DG}|\text{CS})$. We first collected the posterior distributions for all systems hosting a resolved distant giant or a trend. For the resolved planet posteriors, we used gaussian distributions defined by the planet parameters in Table 5.3. For the trends, we used posterior distributions produced by `ethraid` (see Appendix 5.12). We drew one sample from each posterior distribution, kept only the samples that satisfied our distant giant definition, and used Equation 5.3 to calculate planet occurrence with that realization of our catalog. We repeated this procedure 500 times and averaged the resulting planet occurrence estimates to account for our uncertainties.

5.8 Results

5.8.1 Distant giants may be enhanced in the presence of close-in small planets

Using the procedure described in Section 5.7, we found a conditional occurrence rate of $P(\text{DG}|\text{CS}) = 31_{-11}^{+12}\%$. We then calculated $P(\text{DG})$ to be between $16_{-2}^{+2}\%$ (not inclination-corrected) and $18_{-2}^{+2}\%$ (inclination-corrected) using the sample of [Rosenthal et al. \(2021\)](#). The true field rate is likely intermediate between these two extremes. Our results suggest with 1σ confidence that $P(\text{DG}|\text{CS})$ is enhanced over $P(\text{DG})$ by a factor of $\lesssim 2$.

To quantify the significance of the enhancement, we randomly drew 10^4 values from the $P(\text{DG}|\text{CS})$ and $P(\text{DG})$ posteriors and found $P(\text{DG}|\text{CS}) > P(\text{DG})$ among 92% of the draws. An analogous experiment with the inclination-corrected $P(\text{DG})$ returned 90%. We therefore conclude that $P(\text{DG}|\text{CS})$ is enhanced over $P(\text{DG})$ with $\geq 90\%$ confidence, and that inclination disparities caused by our transit-hosting sample do not significantly affect this result.

We summarize our results in Figure 5.9, and report our calculated occurrence rates under our nominal planet definitions in Table 5.5.

We repeated our analysis with planet definitions that more closely match those of Rosenthal et al. (2022) and Bryan et al. (2019), hereafter R22 and B19, respectively (see bottom row of Figure 5.7). R22 adopted the following definitions: DG — $a = 0.23\text{--}10$ AU, $M_p \sin i = 30\text{--}6000 M_\oplus$; CS — $a = 0.023\text{--}1$ AU, $M_p \sin i = 2\text{--}30 M_\oplus$. The $30 M_\oplus$ boundary corresponds to $R_p \sim 6 R_\oplus$ (Chen and Kipping, 2017). With this definition, we found $P(\text{DG}|\text{CS}) = 34_{-13}^{+17}\%$ and $P(\text{DG}) = 20_{-2}^{+2}\%$, as well as a 95% probability that $P(\text{DG}|\text{CS}) > P(\text{DG})$. Our conditional rate is also consistent with R22’s finding of $P(\text{DG}|\text{CS}) = 41_{-13}^{+15}\%$ using a different sample, though our field rate is 1σ higher than their value of $P(\text{DG}) = 17.6_{-1.9}^{+2.4}\%$, likely owing to our exclusion of M dwarfs from the CLS sample.

B19 required that $a = 1\text{--}20$ AU, $M_p \sin i = 0.5\text{--}20 M_J$ for DGs and $R_p = 1\text{--}4 R_\oplus$ for CS planets. Under this definition, we found $P(\text{DG}|\text{CS}) = 24_{-10}^{+13}\%$, lower than their quoted rate of $39 \pm 7\%$, and marginally enhanced over the field rate of $P(\text{DG}) = 16_{-2}^{+2}\%$. We expect that this disagreement is due to differences both in our stellar samples and completeness correction procedures. Using the R22 and B19 definitions, we found evidence for an enhancement of $P(\text{DG}|\text{CS})$ at 95% and 78% confidence, respectively (see Figure 5.9). We list the results of these tests in Table 5.5. We did not perform $\sin i$ corrections when replicating the field rate calculations of Rosenthal et al. (2022) and Bryan et al. (2019) because these studies did not select purely for transiting inner planets in their stellar samples.

Table 5.5: Distant Giants occurrence rates

DG mass limits (M_\oplus)	N_\star (CLS)	N_{DG}	P(DG)	CS radius limits (R_\oplus)	$N_{\text{transiting}}$	N_{resolved}	N_{trend}	P(DG CS)
70-4000	598	55	$16_{-2}^{+2}\%$	1-4	35	1.0	5.3	$31_{-11}^{+12}\%$
				1-6	42	2.3	6.0	$33_{-11}^{+13}\%$
30-6000	598	74	$20_{-2}^{+2}\%$	1-4	32	1.0	4.8	$34_{-13}^{+17}\%$
				1-6	39	3.0	5.5	$41_{-14}^{+17}\%$
158-6356	598	54	$16_{-2}^{+2}\%$	1-4	32	0.8	4.4	$24_{-10}^{+13}\%$

Continued on next page

Table 5.5 – continued from previous page

DG mass limits (M_{\oplus})	N_{\star} (CLS)	N_{DG}	P(DG)	CS radius limits (R_{\oplus})	$N_{\text{transiting}}$	N_{resolved}	N_{trend}	P(DG CS)
				1-6	39	1.2	5.1	$25^{+13}_{-10}\%$

Note: Field and conditional distant giant occurrence rates under different planet definitions. The first DG mass limit is our nominal definition. The second and third match Rosenthal et al. (2022) and Bryan et al. (2019), respectively. We require that CS and DG planets have $a < 1$ AU and $a = 1\text{--}10$ AU, respectively. For the other two cases, we adopt the CS and/or DG separation limits given in Rosenthal et al. (2022) ($a = 0.023\text{--}1$ AU for CS and $0.23\text{--}10$ AU for DG) and Bryan et al. (2019) ($a = 1\text{--}20$ AU for DG). We calculated field occurrence rates using the CLS sample (Rosenthal et al., 2021), to which we applied a mass cut ($M_{\star} \geq 0.6 M_{\odot}$) to exclude M dwarfs.

5.8.2 No strong evidence that high-metallicity systems exhibit a greater enhancement of distant giants

Zhu (2024) and Bryan and Lee (2024) reported an enhancement of DGs in the presence of CS planets specifically in metal-rich ($[\text{Fe}/\text{H}] > 0$) systems, beyond the enhancement expected from the established occurrence-metallicity relation (Fischer and Valenti, 2005a). Van Zandt and Petigura (2024b) tested this claim by repeating the analysis of Bryan and Lee (2024) but using a single sample to measure both the field and conditional occurrence in metal-rich systems. They did not find evidence that the enhancement was specific to metal-rich systems.

We tested the effect of metallicity on giant companion occurrence in the Distant Giants sample by repeating the analysis of Section 5.7 with only metal-rich systems. Of the 47 systems in our sample, 19 have super-solar metallicity and host a CS planet under $4 R_{\oplus}$. This subsample includes one of the three systems with a resolved giant with $P < 5$ yr (TOI-1669), two of the three systems with a resolved giant with $P > 5$ yr (HD 219134 and HD 75732),

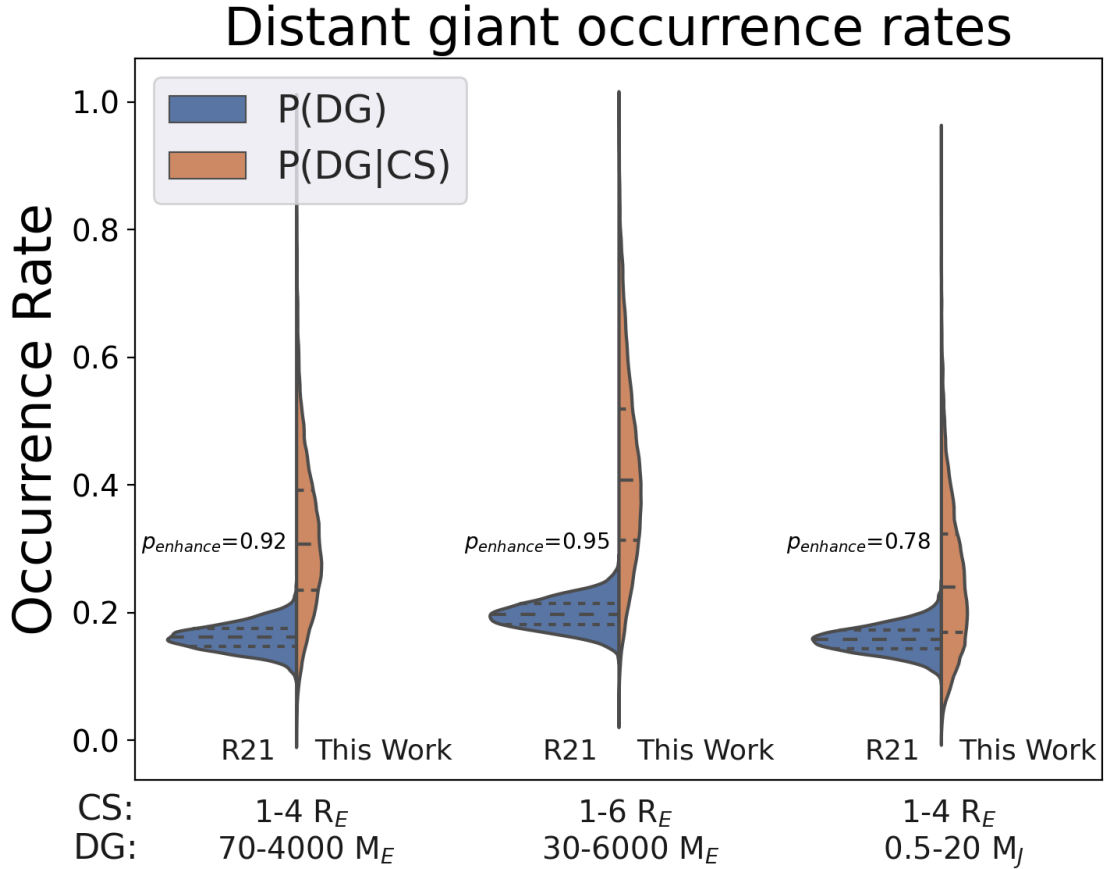


Figure 5.9: Measurements of the field (blue) and conditional (orange) occurrence of distant giants under different planet definitions. Black lines show distribution quartiles. The left set of distributions show occurrence rates for our nominal definitions: $a = 1-10$ AU, $M_p \sin i = 70-4000 M_\oplus$ for DGs and $a > 1$ AU, $R_p = 1-4 R_\oplus$ for CS planets. The distributions in the center and right show occurrence rates for planet definitions matching those of [Rosenthal et al. \(2022\)](#) and [Bryan et al. \(2019\)](#), respectively. We annotate each distribution with the probability that the conditional rate is enhanced over the field rate.

and three of the six trend systems (TOI-1438, HD 156141, and HD 93963). We calculated a metal-rich conditional occurrence rate of $P(\text{DG}|\text{CS}, [\text{Fe}/\text{H}]>0) = 44_{-18}^{+22}\%$. We applied the same filters to the CLS sample and found a metal-rich field rate of $P(\text{DG}||[\text{Fe}/\text{H}]>0) = 23_{-3}^{+3}\%$, yielding a probability of 89% that $P(\text{DG}|\text{CS}, [\text{Fe}/\text{H}]>0)$ is enhanced over $P(\text{DG}||[\text{Fe}/\text{H}]>0)$, similar to our results using the non-metal rich sample. We conclude that there is not strong evidence that metal-rich systems exhibit a greater enhancement of the conditional distant giant occurrence rate over the field rate than field stars do.

We also calculated occurrence using the 16 metal-poor systems in our sample that host a CS planet under $4 R_{\oplus}$. We found $P(\text{DG}|\text{CS}, [\text{Fe}/\text{H}]<0) = 20_{-12}^{+19}\%$, against a field rate of $P(\text{DG}||[\text{Fe}/\text{H}]<0) = 6 \pm 2\%$, giving an 89% probability of enhancement. Our conditional rate is based on two systems, HD 191939 ($[\text{Fe}/\text{H}]=-0.15$) and TOI-1174 ($[\text{Fe}/\text{H}]=-0.004$), making it highly uncertain. Additionally, TOI-1174’s metallicity is consistent with solar. Excluding this system from the calculation gives $P(\text{DG}||[\text{Fe}/\text{H}]<0) = 16_{-10}^{+15}\%$ (84% enhancement probability). Both of these cases show occurrence rates consistent with an enhancement, though we caution that they are derived using small samples. Despite large uncertainties, our results in analyzing the metal-rich, metal-poor, and full samples indicate that metallicity does not exert a strong influence on the relative enhancement of giants. Rather, both the conditional and field occurrence rates rise with metallicity, maintaining an approximately fixed ratio.

5.8.3 Inner companions to resolved giants may be preferentially closer-in

Inspection of Figures 5.1, 5.4, and 5.5 shows that close-in small planets with resolved distant giants have shorter periods on average than the parent sample. We conducted a two-sample Kolmogorov-Smirnov test (Massey, 1951) to determine whether the separations of close-in companions in the six systems hosting a resolved giant were drawn from the same distribution

as the separations of the close-in companions in the 35 systems with neither a resolved giant nor a trend. In systems with multiple transiting planets, we used the separation of the first TOI detected in the system. We found a p -value of 0.006, meaning that under the assumption that the two populations are drawn from the same distribution, we would expect discrepancies greater than or equal to those observed to occur with 0.6% probability. We repeated this test using only the subset of our targets with transiting planet radii $< 4 R_{\oplus}$, finding $p = 0.015$. Our findings suggest that outer giants tend to have lower-separation inner companions, and that this trend may be slightly weaker for inner companions with smaller radii. We note that the transiting companion with the shortest period, HD 75732 e, is also accompanied by a 14-day warm Jupiter, which likely had a more significant dynamical impact on it than the distant giant in this system. We did not find a significant difference between the period distributions of inner planets in trend systems and of single inner planets (i.e., those in systems with no resolved giant and no trend).

We note that using the first detected TOI in a system favors shorter separations in systems with multiple transiting planets. Thus, the pattern described above may be explained if outer giants are more likely to occur in systems with multiple inner planets (see Section 5.8.5).

5.8.4 Outer companions may have preferentially low eccentricities

To evaluate the eccentricity distribution of our detected giants compared with the broader giant planet population, we performed the following experiment. For each of the six resolved giants in our catalog, we drew one eccentricity value from a gaussian distribution centered on the planet’s median eccentricity and with standard deviation equal to the derived eccentricity uncertainty. We then recorded the mean of these six eccentricities. We repeated this process 1000 times to account for the eccentricity uncertainty of each planet. We fit a gaussian

distribution to the average eccentricity values, finding that $\langle e_{\text{sample}} \rangle = 0.11 \pm 0.03$.

We used a similar process to quantify the eccentricities of distant giants around field stars. We began with all planets in the NASA Exoplanet Archive (NEA²) that met our definition of a distant giant and had eccentricity uncertainty below 0.13, the maximum eccentricity uncertainty measured among the giants in our catalog. Note that we did not exclude giants with known inner planets; because there are few systems hosting a confirmed giant and in which an inner planet can be ruled out at high significance, we chose to compute the field eccentricity distribution using all giants, irrespective of inner planet presence. To match the six resolved giants in our catalog, we drew six random planets from this pool, with probability proportional to our measured completeness to each planet (see Figure 5.7). We then repeated the procedure we applied to our detected giants, obtaining a distribution of mean eccentricities for the six sampled giants. We again iterated this process by drawing 1000 such six-planet samples and calculating average eccentricity distributions for each of them. We found that the typical average eccentricity among a random sample of six planets from the NEA is $\langle e_{\text{field}} \rangle = 0.25 \pm 0.09$.

We repeated this analysis with only the four resolved giants whose close-in small planet had $R_p < 4 R_{\oplus}$, and found a similar result: $\langle e_{\text{sample}} \rangle = 0.09 \pm 0.03$. Our findings show a discrepancy of $\sim 1.5 - 2\sigma$, indicating that the giants in our sample may have lower eccentricities than field giants. We show the distributions of giant planet eccentricities in Figure 5.10.

5.8.5 Systems with multiple transiting planets may be more likely to host an outer companion

Eight of the systems in our sample host more than one transiting planet. Four of these systems exhibit either a trend or a resolved orbit. We conducted a simple experiment

²<https://exoplanetarchive.ipac.caltech.edu/>

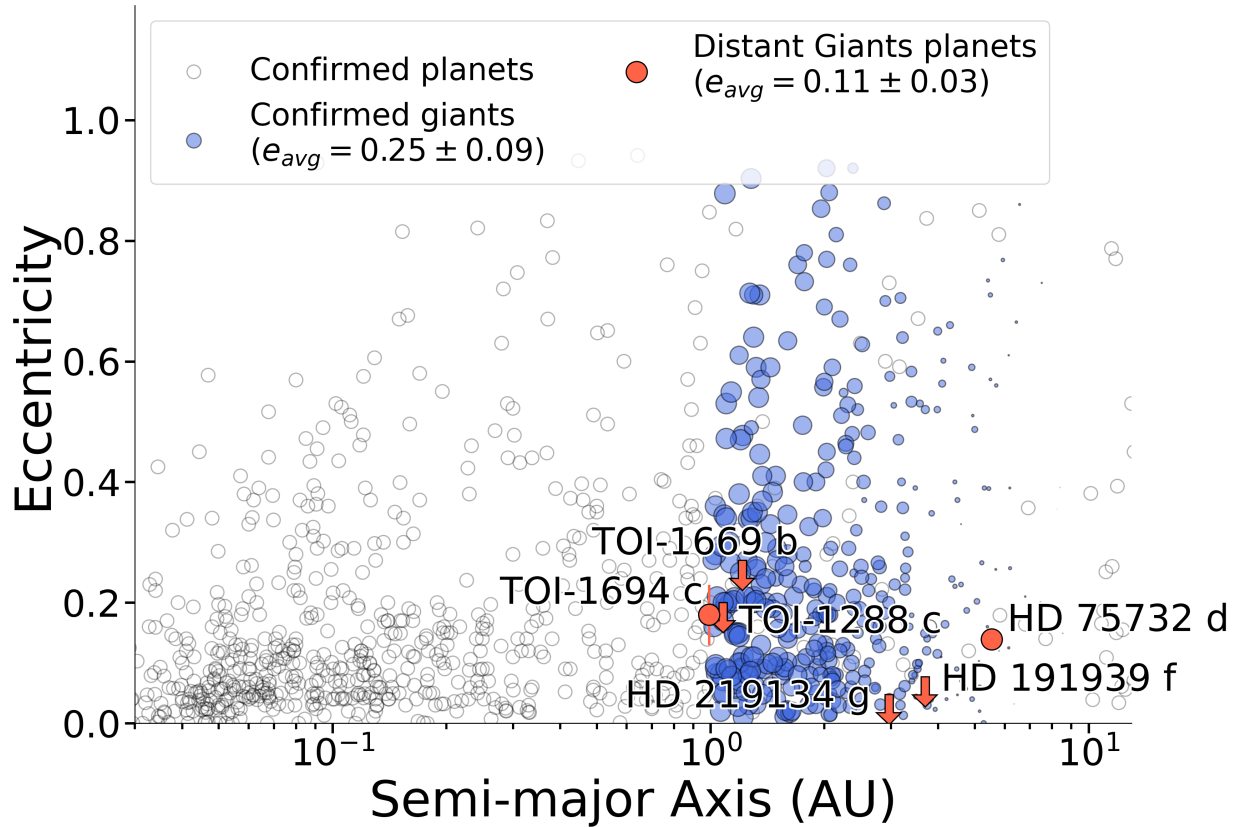


Figure 5.10: Distribution of eccentricity versus orbital separation for confirmed exoplanets in the NEA with $\sigma_e \leq 0.13$. Confirmed planets are shown as unfilled circles and confirmed distant giants (1–10 AU and 70–4000 M_\oplus) as blue circles. For confirmed giants, marker size is proportional to our survey-averaged completeness at the planet’s mass and separation. We show giants in our survey in orange and indicate measurements with less than 3σ eccentricity precision with an arrow, placing the bottom of the arrow at the 1σ upper limit. The giant companions in our survey may have lower eccentricities than the average distant giant, but a larger sample is needed to draw a strong conclusion.

to evaluate the statistical significance of the relationship of between inner planet multiplicity and outer companion occurrence. We randomly drew 12 of the systems from our survey, corresponding to the number of companions detected in our catalog either as resolved orbits or as trends, and counted how many of them belonged to the subset of systems with multiple transiting planets. In 10% of our 10^4 experiments, four or more of the sampled systems had multiple inner planets. This finding corresponds to a p -value of 0.1, providing a tentative indication that the systems exhibiting resolved orbits or trends have multiple transiting planets more often than average.

Because the nature of the trend systems is uncertain, we repeated the above experiment using only the resolved systems, two of which host multiple inner planets. We drew six systems from our target list, and calculated the fraction of times that two or more of them had multiple inner planets. In this case, there was no evidence of a correlation between inner planet multiplicity and outer giant presence ($p=0.27$). We found similar results when considering only systems hosting inner planets with $R_p < 4 R_\oplus$.

5.8.6 Outer companion occurrence does not correlate with stellar parameters

We conducted KS tests for a variety of stellar parameters to see they correlated with distant giant occurrence. We found no significant correlations between the resolved giants in our sample and T_{eff} ($p=0.57$), $\log R'_{\text{HK}}$ ($p=0.95$), or radius ($p=0.94$). We found tentative evidence that stars hosting resolved giants have lower-than-average $v \sin i$ ($p=0.06$) and higher-than-average stellar metallicity ($p=0.09$), in agreement with the the established occurrence-metallicity relation (Fischer and Valenti, 2005a). We found similar results when restricting our analysis to the systems with transiting planets smaller than $4 R_\oplus$.

5.9 Discussion

5.9.1 Distant giant occurrence

Our finding of a possible positive correlation between CS and DG planets is consistent with most previous studies of this relationship (Rosenthal et al., 2022; Bryan et al., 2019; Zhu and Wu, 2018). Each of these studies used different — though overlapping — target samples compiled according to distinct criteria and analyzed by different methods, and although none was large enough to conclusively measure $P(\text{DG}|\text{CS})$, the overarching agreement between them points to a linked formation history between these classes.

We derived a lower enhancement factor of $P(\text{DG}|\text{CS})$ over $P(\text{DG})$ than prior works, which may be due to differences between our stellar sample and theirs. We constructed the Distant Giants sample using a uniform selection function, and we built up the RV baselines for most of our targets from scratch. Further, our requirement of transiting inner planets necessitated a more involved completeness correction to account for potential inclination biases. We expect that these choices resulted in higher accuracy in our inferred occurrence rates, but they also reduced statistical power by restricting our sample size. Another possible explanation for our lower enhancement factor is our use of the CLS sample to calculate the distant giant field rate. Zhu (2022) found that the CLS sample has a hot Jupiter abundance three times the commonly accepted value of $\sim 1\%$ (Cumming et al., 2008; Mayor et al., 2011; Wittenmyer et al., 2020). Given that hot Jupiters are frequently accompanied by a distant giant companion (Zink and Howard, 2023), the overabundance of hot Jupiters in the CLS may have also led to an overabundance of distant giants. Correcting for this effect could lower our calculated field occurrence, broadening the gap between $P(\text{DG})$ and $P(\text{DG}|\text{CS})$.

The recently-completed Keck Giant Planet Search (KGPS; Weiss et al. 2024) is the largest survey (63 stars) yet used to address conditional giant planet occurrence, and also targeted

transiting planet hosts with a uniform selection function and consistent observing strategy. Due to its similarity to the Distant Giants Survey, the KGPS will serve as a useful point of comparison for the results presented here.

We calculated our conditional and field occurrence rates using two different stellar samples, resulting in potential offsets stemming from different stellar parameter distributions (e.g. mass, metallicity, temperature). The sample sizes of current long-baseline RV surveys ($\lesssim 1000$ stars) limits the possibility of measuring both $P(\text{DG}|\text{CS})$ and $P(\text{DG})$ in a single sample. Large future surveys of statistically identical stellar samples will alleviate this problem, in addition to providing more accurate and precise occurrence measurements.

5.9.2 Distant giants and metallicity

The occurrence-metallicity relation has been known for two decades: gas giant planets are more prevalent around metal-rich stars (Fischer and Valenti, 2005a). This pattern implies that the high densities of solid material in the protoplanetary disks of metal-rich stars facilitate the formation of giant planets. Our study and others before it suggest that giants are also more prevalent in systems hosting an inner small planet.

A natural question is what the interplay between these two effects is. For example, do systems with a metal-rich host star *and* a close-in companion show the same relative enhancement over metal-rich field stars as non-metal-rich stars with close-in planets show over non-metal-rich field stars? Recently, Bryan and Lee (2024) reported an increased relative enhancement in metal-rich systems, suggesting that high-metallicity environments are especially well-suited to producing DG-CS systems. In contrast, our findings suggest that metallicity does not strongly influence the relative enhancement; rather, our full sample exhibits a similar enhancement of distant giants in the presence of close-in small planets as the metal-rich sample.

5.9.3 Distant giants and inner planet properties

A positive correlation between DG and CS planets could indicate that DGs help inner planets form, or that both planets develop independently in similar environments. Whether the DG-CS relation is causative may be encoded in the dynamical characteristics of the systems that host them.

In Section 5.8, we found preliminary evidence that, in systems with both an inner transiting planet and a distant giant, the inner planet(s) have shorter-than-average periods, and the giants have lower-than-average eccentricities. If real, these patterns could shed light on the formation history of this class of systems. For example, these giants may have excited the eccentricities of their inner companions, initiating high-eccentricity migration to shorter periods through the eccentric von Zeipel-Lidov-Kozai mechanism (Li et al., 2014; Naoz, 2016). On the other hand, this picture requires a high mutual inclination between the inner and outer planets, in tension with the possible overrepresentation of giants in multi-transiting systems. Another explanation is that the giants underwent early Type II disk migration (Lin and Papaloizou, 1986), entraining gas and planetesimals in the inner disk and driving them to shorter separations (Batygin and Laughlin, 2015).

We also found that outer giants may be more common in systems with multiple inner transiting planets. This is somewhat unexpected, given that a misaligned outer giant could dynamically perturb the multi-transiting geometry (Naoz, 2016). The fact that the system configurations endured suggests that their giants have low mutual inclinations. This feature, coupled with the observed tendency for giant companions to have lower eccentricities, points to a preference for CS/DG systems to either maintain or settle into dynamically cool final configurations, much like the Solar System.

Obliquity offers another indication of dynamical evolution. Of the six systems hosting resolved outer giants, four have measurements of the sky-projected spin-orbit angle between

the host star and the inner transiting planet: HD 191939 ($\lambda = 3.7 \pm 5$ deg; [Lubin et al. 2024b](#)), HD 219134 ($\lambda = 0 - 20$ deg; [Folsom et al. 2018](#)), TOI-1694 ($\lambda = 9_{-18}^{+22}$ deg; [Handley et al. 2024](#)), and HD 75732 ($\lambda = 10_{-20}^{+17}$ deg; [Zhao et al. 2023](#)). The high degree of alignment in these systems comports with a picture involving low mutual inclinations and gentle planetary migration mechanisms. Obliquity measurements in the remaining two giant-hosting systems will test this pattern.

Many of the findings presented in this work are suggestive at the $2-3\sigma$ level, but not statistically unassailable. To confirm or refute them, similar studies must be performed using larger stellar samples. For example, the number of *TESS* candidate hosts recently surpassed 7000, enabling the construction of a quadrupled (200-star) sample under our target selection criteria. Meanwhile, next-generation RV spectrographs such as the Keck Planet Finder ([Gibson et al., 2016](#)), NEID ([Schwab et al., 2016](#)), and the Habitable Zone Planet Finder ([Mahadevan et al., 2012](#)) in the north, as well as ESPRESSO ([Pepe et al., 2021](#)) in the south, offer vastly improved throughput over their predecessors, and more than enough precision to detect long-period giants. Their enhanced efficiency would permit a survey of an additional 150 systems using the same amount of telescope time needed to observe our original 47-star sample. Such a survey would open the door to conditional occurrence measurements at the $3-5\sigma$ level, providing dispositive evidence for or against a correlation.

Additionally, the fourth data release of the *Gaia* mission ([Gaia Collaboration et al., 2016](#)) is expected to yield tens of thousands of giant companion detections (e.g., [Feng 2024](#); [Wallace et al. 2024](#)). These detections will enable precise estimates of the field rate of super-Jupiter planets and, combined with small planet detections from RV and/or transit missions, may help constrain their conditional occurrence as well.

5.9.4 Brown dwarf occurrence

The mass/separation prior we derived in Section 5.5.2 sheds light on the occurrence rate of brown dwarfs as a function of orbital separation. Our work takes advantage of the CLS’s sensitivity to brown dwarfs at wide separations ($\lesssim 64$ AU), which extends into the discovery space of high-contrast imaging surveys at ~ 5 –1000 AU (e.g. [Bowler et al. 2020](#); [Bowler and Nielsen 2018](#); [Chauvin 2018](#)). [Nielsen et al. \(2019\)](#) measured the prevalence of brown dwarfs from 10–100 AU, finding that $0.8_{-0.5}^{+0.8}\%$ of stars host such a companion. They also found that brown dwarfs and giant planets (5 – $13 M_J$) exhibit different semi-major axis distributions, with planets peaking in occurrence between 1–10 AU and brown dwarfs favoring wider separations.

We integrated our mass-separation prior between 13 – $80 M_J$ and 10 – 30 AU, finding that brown dwarfs occur at a rate of 1.6 per 100 stars in this interval. Using the simplifying assumption that the occurrence rate is log-uniform out to 100 AU, we estimate that 3.2% of stars host a brown dwarf between 10–100 AU, significantly greater than the finding of [Nielsen et al. \(2019\)](#) over the same interval. On the other hand, we observed a distinction between giant planet and brown dwarf occurrence, in agreement with [Nielsen et al. \(2019\)](#). We found that giant planets, which we define as having $M = 3 - 13 M_J$, peak in occurrence in the interval 1–4 AU, and decline at greater separations. By contrast, brown dwarf occurrence may increase at greater separations, reaching its maximum in the interval 16–64 AU. Like the distinct eccentricity distributions between brown dwarfs and giant planets fit by [Bowler et al. \(2020\)](#), our finding of disparate separation distributions supports the idea that these objects follow different formation pathways. We note that our brown dwarf occurrence rate value of 3.2% is based on a significant extrapolation of the RV-derived occurrence rates in order to produce a consistent comparison with [Nielsen et al. \(2019\)](#). More work is needed to perform a comparison without extrapolation.

It is important to note that a number of effects may have influenced our calculated occurrence rates. First, stellar companions on inclined orbits may masquerade as lower-mass objects in RV surveys. We simulated this effect by applying random orbital orientations to a set of stars following the distribution of [Raghavan et al. \(2010\)](#). We found that on average, one of the nine brown dwarfs we used in our calculation are likely to be stars, insufficient to explain the disagreement with [Nielsen et al. \(2019\)](#). Nevertheless, the small number of brown dwarfs means that significant contamination remains a possibility. Second, despite its multi-decade baseline, the CLS has limited sensitivity to companions at tens of AU. Many of the detections are partial orbits with large mass and separation uncertainties, and may therefore not fall within the bin in which we counted them. For example, the mass of HD 28185 c was recently revised from $40_{-28}^{+43} M_J$ to $6 \pm 0.6 M_J$ through the incorporation of HGCA astrometry ([Venner et al., 2024](#)). We reserve a more detailed analysis and a firmer conclusion for future work.

5.10 Conclusion

We presented the results of a three-year RV survey to search for outer giant planets around 47 Sun-like stars with known inner planets. Our final catalog includes six RV trends and six well-characterized giants. We incorporated all of these detections into a Poisson likelihood model to calculate the conditional occurrence of distant giants in the presence of close-in small planets, $P(\text{DG}|\text{CS})$. We corrected for missed planets by characterizing our detection sensitivity in each system. We found that $31_{-11}^{+12}\%$ of stars that host a CS planet ($a < 1$ AU, $R_p \leq 4 R_\oplus$) also host a DG ($a = 1 - 10$ AU, $M_p \sin i = 70 - 4000 M_\oplus$). Meanwhile, using the larger CLS sample of [Rosenthal et al. \(2021\)](#), we determined that between $16_{-2}^{+2}\%$ and $18_{-2}^{+2}\%$ of stars host a DG planet irrespective of the presence of CS planets. Our findings give tentative evidence for a 1.5 – 2x enhancement of giants in CS-hosting systems, suggesting

that outer giants and inner small planets may be positively correlated, with giants even promoting the formation of inner planets.

Sample size and homogeneity are vital components of a precise and accurate measurement of conditional giant occurrence. Studies of this topic to date, including this one, have had to prioritize one of these components at the expense of the other. However, advancements over the last few years have made possible a dramatic increase in sample size without compromising sample purity. Making use of this progress will bring the nuances of planetary formation into sharper focus.

5.11 Acknowledgments

We thank the reviewer for providing helpful comments which improved this study. J.V.Z. acknowledges support from NASA FINESST Fellowship 80NSSC22K1606. J.V.Z. and E.A.P. acknowledge support from NASA XRP award 80NSSC21K0598. J.M.A.M. is supported by the National Science Foundation (NSF) Graduate Research Fellowship Program (GRFP) under Grant No. DGE-1842400. J.M.A.M. and N.M.B. acknowledge support from NASA'S Interdisciplinary Consortia for Astrobiology Research (NNH19ZDA001N-ICAR) under award number 19-ICAR19_2-0041. E. V. T. acknowledges support from a David & Lucile Packard Foundation grant. T.F. acknowledges support from an appointment through the NASA Postdoctoral Program at the NASA Astrobiology Center, administered by Oak Ridge Associated Universities under contract with NASA. M.L.H. would like to acknowledge NASA support via the FINESST Planetary Science Division, NASA award number 80NSSC21K1536.

This work was supported by NASA Keck PI Data Awards, and NASA Key Project Mission Support proposals administered by the NASA Exoplanet Science Institute. Data presented herein was obtained at the W. M. Keck Observatory from telescope time allocated to the

National Aeronautics and Space Administration through the agency’s scientific partnership with the California Institute of Technology and the University of California. The Observatory was made possible by the generous financial support of the W. M. Keck Foundation.

The authors wish to recognize and acknowledge the very significant cultural role and reverence that the summit of Maunakea has always had within the indigenous Hawaiian community. We are most fortunate to have the opportunity to conduct observations from this mountain.

5.12 Appendix 5A: Companions Detected as Trends

5.12.1 TOI-1174

TOI-1174 is a K2 dwarf at a distance of 95 pc hosting a transiting $2.3 R_{\oplus}$ sub-Neptune with a 9.0-day period. We measured RV trend and curvature of -27.48 ± 5.97 m/s/yr and 14.48 ± 2.89 m/s/yr² in this system, indicating the presence of an outer companion (Figure 5.11). Although we were unable to precisely constrain a and M_p in this system due to the lack of astrometry data, 832 nm speckle imaging observations from the 'Alopeke imager coupled to the 8-m Gemini North telescope (Scott et al., 2021) and reduced according to Howell et al. (2011) ruled out luminous companions beyond ~ 40 AU and more massive than $\sim 200 M_J$. We depict the direct imaging constraints by converting the measured contrast curves to mass/separation space, assuming circular face-on orbits for simplicity as explained in Van Zandt and Petigura (2024a). We found that the source of the measured RV variability is most likely planetary: $P(\text{planet}) = 53\%$.

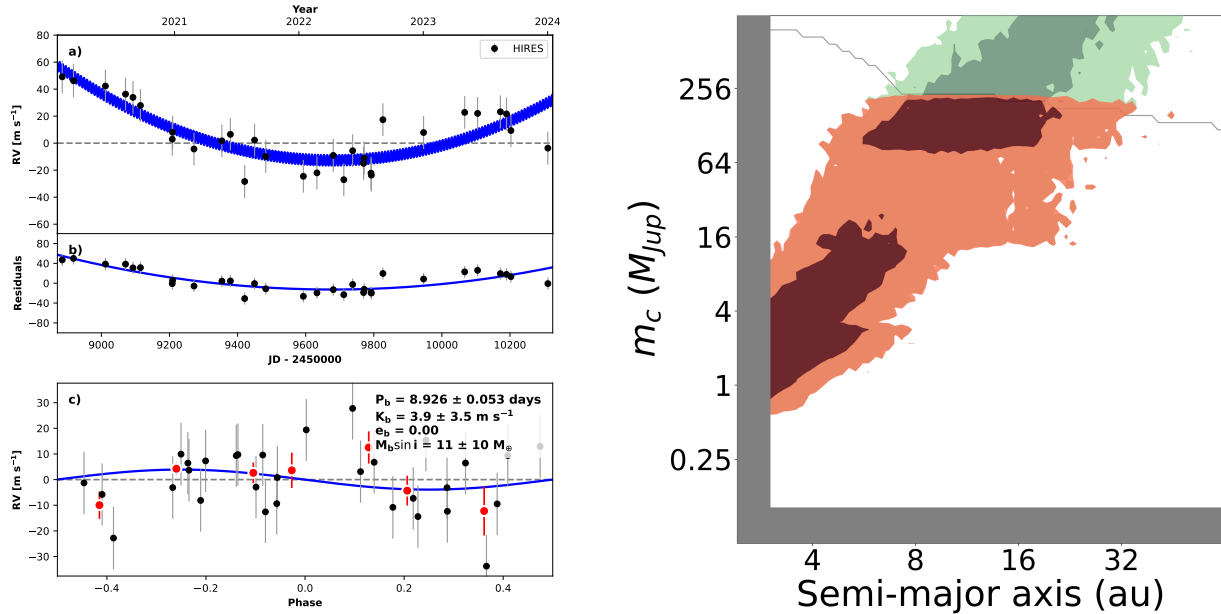


Figure 5.11: **Left:** Our orbital fit to the TOI-1174 system using `radvel`. Panel a) shows the full RV time series and errors with black circles, with our preferred model as a blue line. Panel b) shows the residuals to the planetary model, isolating the fitted trend/curvature. Panel c) shows the RV time series phase-folded to the period of the inner planet in this system. Red points give binned RV values. We did not recover the inner transiting planet signal in the RVs. **Right:** Our `ethraid` posterior surface derived using the measured trend. Green regions show models consistent with the RV trend, and red regions show models consistent with both the RVs and the direct imaging for this system, which revealed no luminous companions. Dark (light) regions indicate 68% (95%) confidence intervals. The gray line approximates the contrast limits imposed by imaging for a circular, face-on companion. Gray panels at low mass and short separations show companion parameters incompatible with the observed trend due to our observing baseline.

5.12.2 HD 191939

HD 191939 is a G0 dwarf 54 pc away hosting three transiting sub-Neptunes with periods of 8.9, 28.6, and 38.4 days. Multiple studies have probed this system with RVs (Badenas-Agusti et al., 2020; Lubin et al., 2022b, 2024b), resulting in mass measurements of the transiting planets, a determination that the system is aligned, and the discovery of a 100-day super-Saturn (e) and an eight-year super-Jupiter (f). We truncated this system’s time series to four years, causing HD 191939 f to present as a trend. We combined this trend with an HGCA astrometric acceleration of 0.13 ± 0.03 mas/yr, which resulted in a 98% probability that the trend’s origin is planetary. We included adaptive optics imaging from Gemini/NIRI in our analysis, though it does not rule out any companion models. Figure 5.12 shows our orbital fit and trend analysis for this system. Our automated search algorithm recovered planet e, as well as a spurious 900-day planet. This planet demonstrates a shortcoming of our automated algorithm, which is not designed to be sensitive to multiple signals. Nevertheless, with an RV semi-amplitude of 3.2 m/s, it did not detract significantly from the signal of planet f, which has $K = 47$ m/s.

5.12.3 TOI-1438

TOI-1438 is a K1 dwarf at 111 pc hosting two transiting sub-Neptunes, the inner of which has a radius of $3.0 R_{\oplus}$ and a period of 5.1 days (Persson et al. in prep.). TOI-1438 showed the largest RV trend in our sample: $\dot{\gamma} = 41.41 \pm 3.41$ m/s/yr, $\ddot{\gamma} = -13.65 \pm 1.40$ m/s/yr² (Figure 5.13). Our trend analysis, along with 832 nm speckle imaging from ‘Alopeke, indicated that these signals may originate from a planet (79%), brown dwarf (8%) or stellar companion (12%).

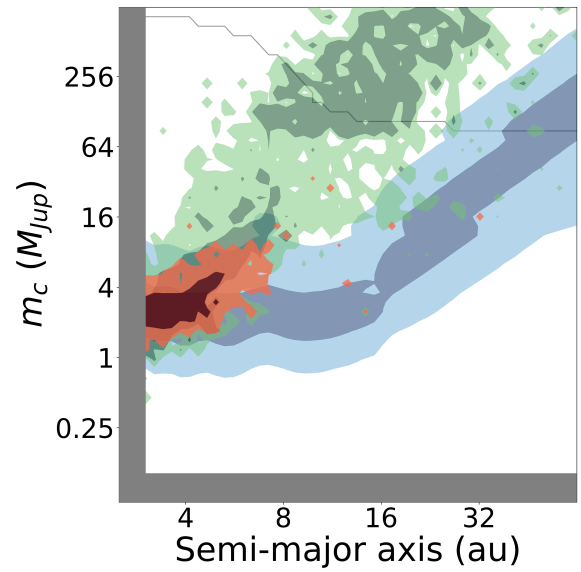
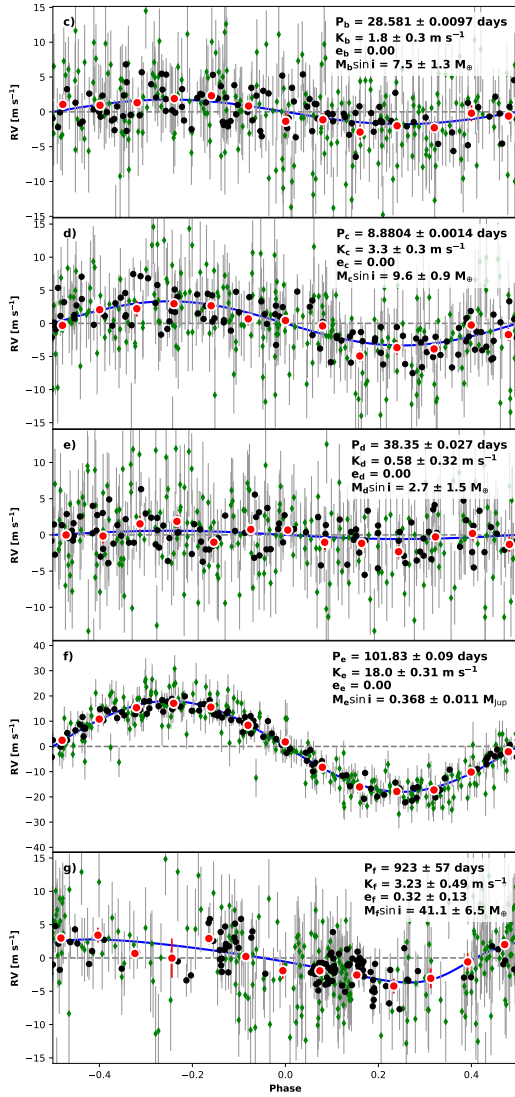
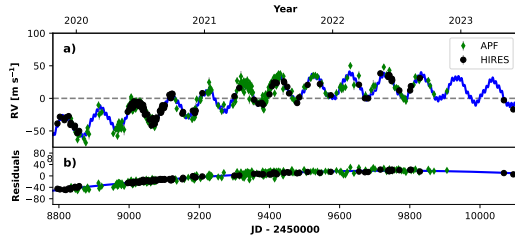


Figure 5.12: Same as Figure 5.11 for HD 191939. We included the three transiting planets in our model, and our blind search algorithm detected the known 100-day super-Saturn as well as a spurious long-period planet. The blue posterior surface shows constraints imposed by the astrometric acceleration measured in this system. The trend and curvature in our truncated RV time series along with the astrometric acceleration, yield a high planetary odds ratio.

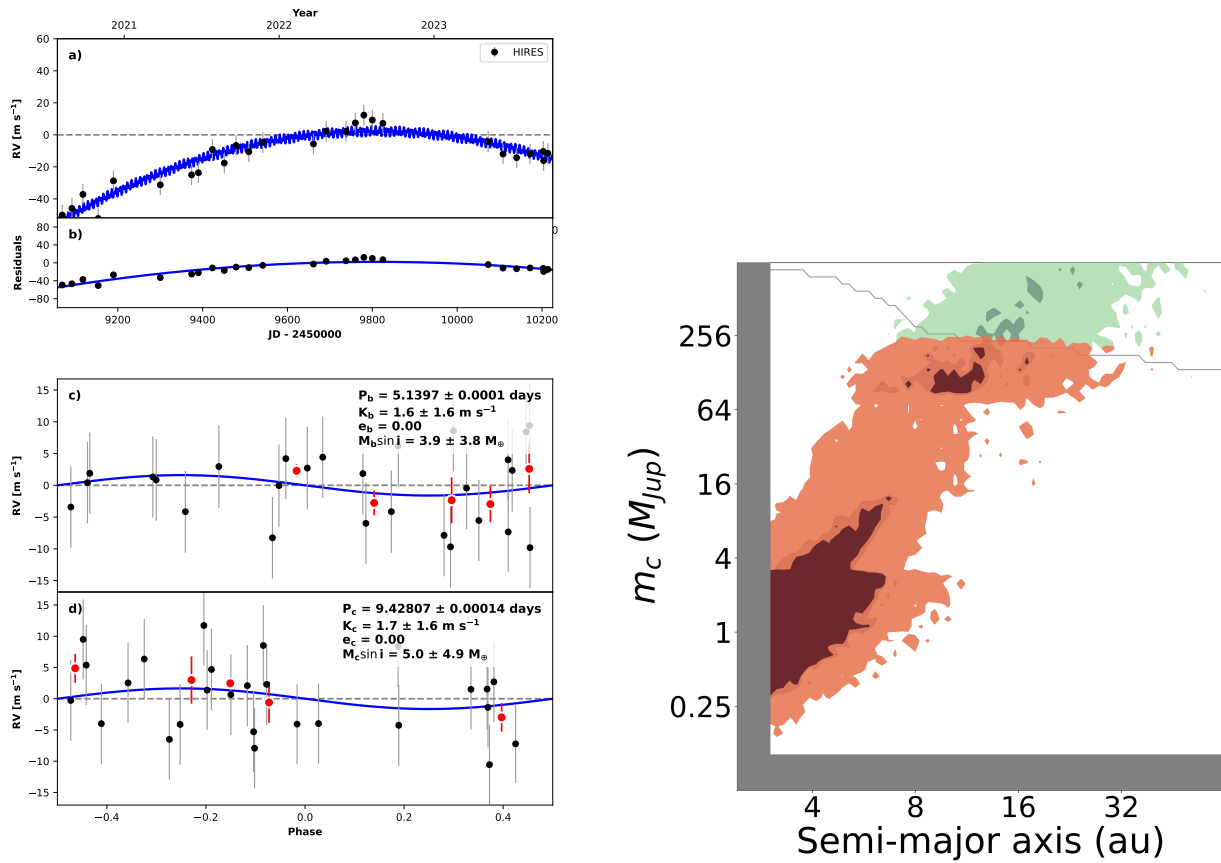


Figure 5.13: Same as Figure 5.11 for TOI-1438. We were unable to detect the transiting planets in this system, but we measured strong trend and curvature, consistent with planetary, brown dwarf, or stellar companion models.

5.12.4 HD 219134

HD 219134 is a nearby (6.5 pc) K3 dwarf hosting two transiting super-Earths with periods of 3.1 and 6.8 days. This system has been observed for multiple decades, providing detections of four additional planets, including a six-year super-Saturn meeting our distant giant definition (Vogt et al., 2015). As with HD 191939, we truncated this system’s baseline to four years and performed our blind search. We tested the dependence of our results on our choice of truncation window, and found that it had a negligible effect. Our automated algorithm detected the 47-day Neptune analog (e), but missed a known super-Earth with a 23-day period (d) and a 94-day super-Earth (f). It also found a strong trend due to HD 219134 g, which we analyzed together with an HGCA acceleration to find a high planetary odds ratio of $P(\text{planet}) \sim 100\%$. Figure 5.14 shows the results of our full and partial orbit fits.

5.12.5 HD 12572

HD 12572 is a G9 dwarf at a distance of 73 pc hosting two transiting sub-Neptunes. The inner planet, HD 12572 b, has a radius of $3.9 R_{\oplus}$ and a 20.8-day period (Osborn et al., 2023). This star’s high brightness ($V = 9.2$) allowed us to obtain contemporaneous APF RVs alongside our HIRES observations. We measured RV trend and curvature of -22.09 ± 2.11 m/s/yr and -0.05 ± 0.73 m/s/yr² in this system, as well as a marginally significant astrometric acceleration of $\Delta\mu = 0.07 \pm 0.05$ mas/yr (Figure 5.15). Coupled with Br γ direct imaging from NIRC2, we calculated a 61% probability that the outer companion in this system is a planet. Our results are in tension with Osborn et al. (2023), who concluded that the outer companion is a brown dwarf between 15-50 AU. This disagreement may be due in part to our informative mass prior, which disfavors brown dwarf companions.

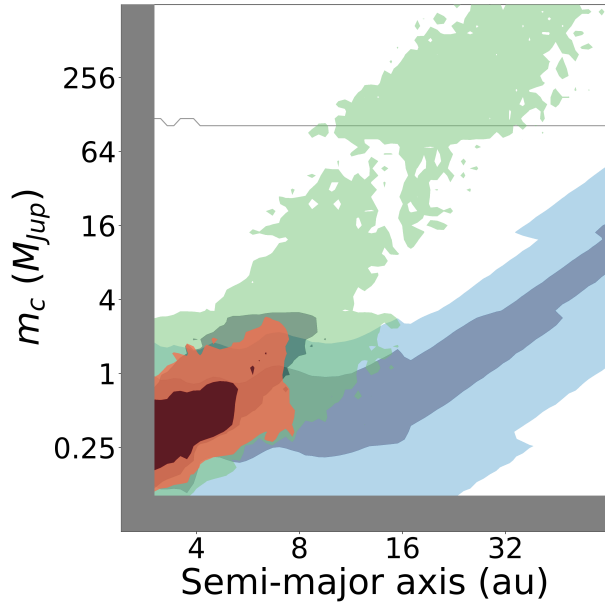
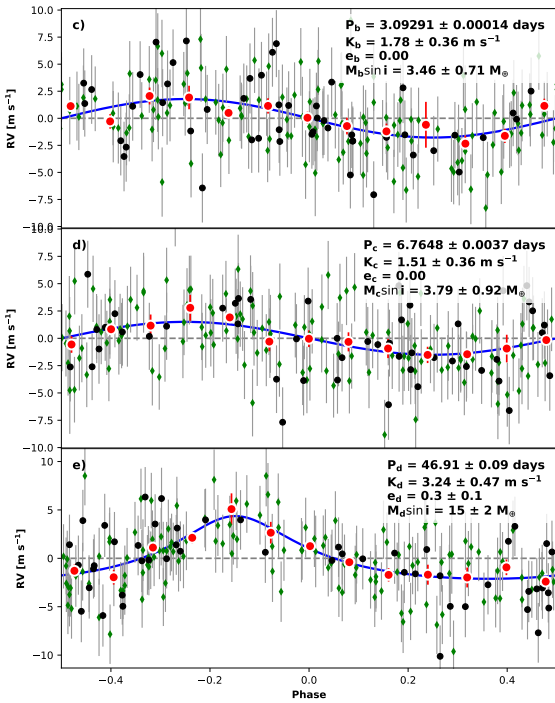
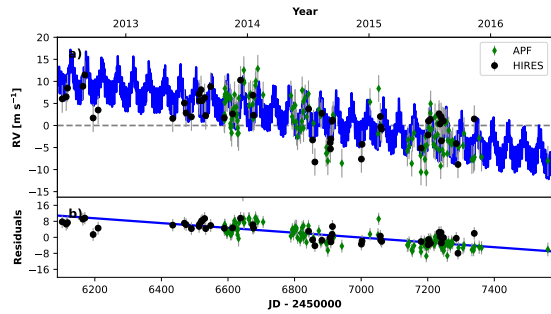


Figure 5.14: Same as Figure 5.11 for HD 219134. We chose RV measurements from an arbitrary four-year span of this system’s full data set. We recovered one of the non-transiting planets using a blind search, but missed two others. We analyzed the measured trend and HGCA astrometry to calculate a probability near 1 of this signal originating from a planet. We also tested other four-year spans and verified that our choice did not strongly influence our final odds ratio.

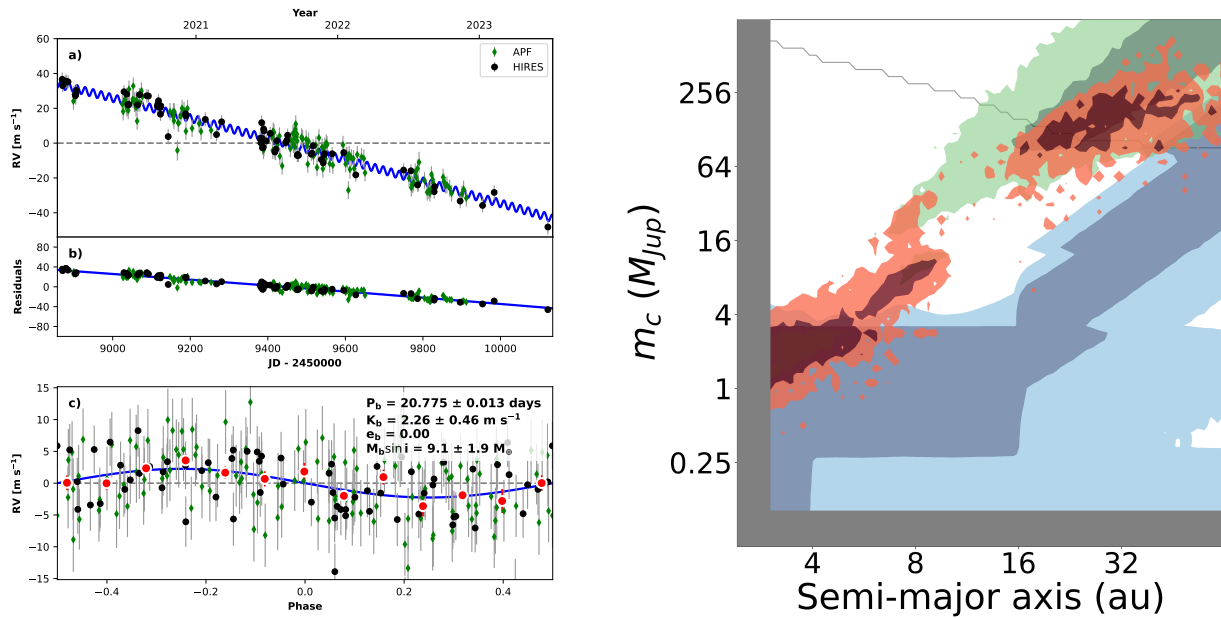


Figure 5.15: Same as Figure 5.11 for HD 12572. We measured the mass of the 20-day sub-Neptune in this system and also found a strong linear trend with no significant curvature. We also measured a marginal astrometric acceleration, which imposed added constraints (blue contours). Note that the gray line marks orbital models which are ruled out by direct imaging under the assumption of a circular, face-on orbit. Companions with non-zero inclinations and eccentricities may lie beyond the line without being ruled out.

5.12.6 HD 156141

HD 156141 is a solar analog (G2) at a distance of 73 pc hosting a transiting $2.2 R_{\oplus}$ sub-Neptune with a 21.3-day period. We measured RV trend and curvature of 30.20 ± 1.87 m/s/yr and -7.22 ± 0.72 m/s/yr², and ruled out high-mass stellar models using NIRC2 Br γ imaging (Fig 5.16). We found that the outer companion in this system has a 78% probability of being a planet.

5.12.7 HD 75732

HD 75732 is a nearby (12.5 pc) K0 dwarf hosting a transiting ultra-short period (0.74-day) super-Earth. Like HD 219134, this system is well-characterized from decades of RV observation (e.g., [Fischer et al. 2008](#)). We chose an arbitrary four-year window over which to fit these RVs, and verified that our choice did not significantly impact our characterization of the outer planet. We detected the hot Jupiter HD 75732 b, but did not detect the four other non-transiting planets. The outermost of these, a super-Jupiter with a period of nearly 14 years, manifested as a trend in our truncated RV time series. We combined this trend with a marginal detection of HGCA acceleration to constrain the companion’s mass and separation. Our analysis indicates that the trend is almost certainly planetary, with $P(\text{planet}) \sim 91\%$. We show our orbital fit and partial orbit analysis in Figure 5.17.

5.12.8 HD 93963

HD 93963 A is a G2 dwarf at a distance of 83 pc hosting a transiting $3.2 R_{\oplus}$ sub-Neptune with a 3.6-day period ([Serrano et al., 2022](#)). Our measured RV trend and curvature of -10.51 ± 2.66 m/s/yr and -7.50 ± 3.55 m/s/yr², together with 832 nm speckle imaging from ‘Alopeke, indicate an 81% probability of a planetary outer companion (Figure 5.18). [Serrano](#)

et al. (2022) estimated that the stellar companion to this star, HD 93963 B, has a separation of ≥ 484 AU and a spectral type of M5 V ($\approx 170 M_J$; Pecaut and Mamajek 2013b). We show in Figure 5.19 that a companion of that mass and separation is incompatible with the measured RV signature.

5.12.9 TIC 142381532

TIC 142381532 is a K0 dwarf 72 pc away hosting a transiting $8.1 R_{\oplus}$ sub-Saturn with a 38.8-day period (Polanski et al., 2024). We measured RV trend and curvature of -13.99 ± 4.60 m/s/yr and 1.79 ± 1.27 m/s/yr², and used 832 nm speckle imaging from 'Alopeke to rule out high-mass stellar companions (Figure 5.20). We calculated a 32% probability that the measured signals originate from a planet. Despite passing our original radius filter of $R_p < 10 R_{\oplus}$, the transiting planet in this system does not fit most definitions of a “small” planet. We include it for completeness, but exclude it from our conditional occurrence calculations.

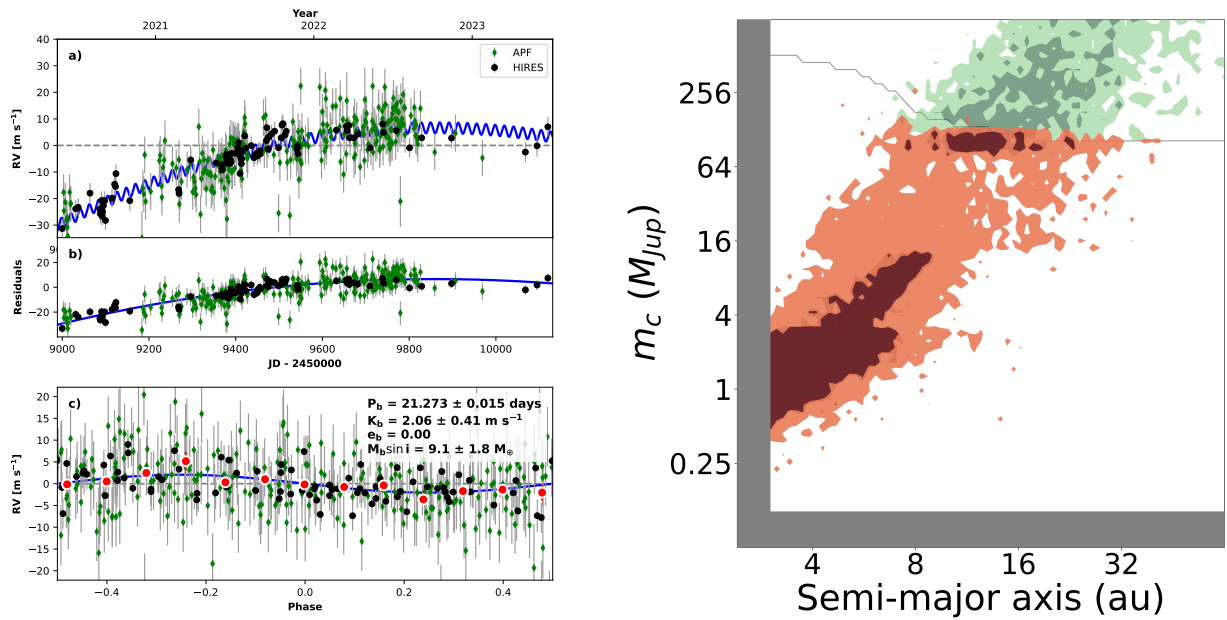


Figure 5.16: Same as Figure 5.11 for HD 156141. We obtained a marginally significant measurement of the inner transiting planet’s mass, and high-significance trend and curvature measurements. The long-term signals in this system are consistent with planets and brown dwarfs, whereas stellar models are nearly ruled out with the aid of direct imaging.

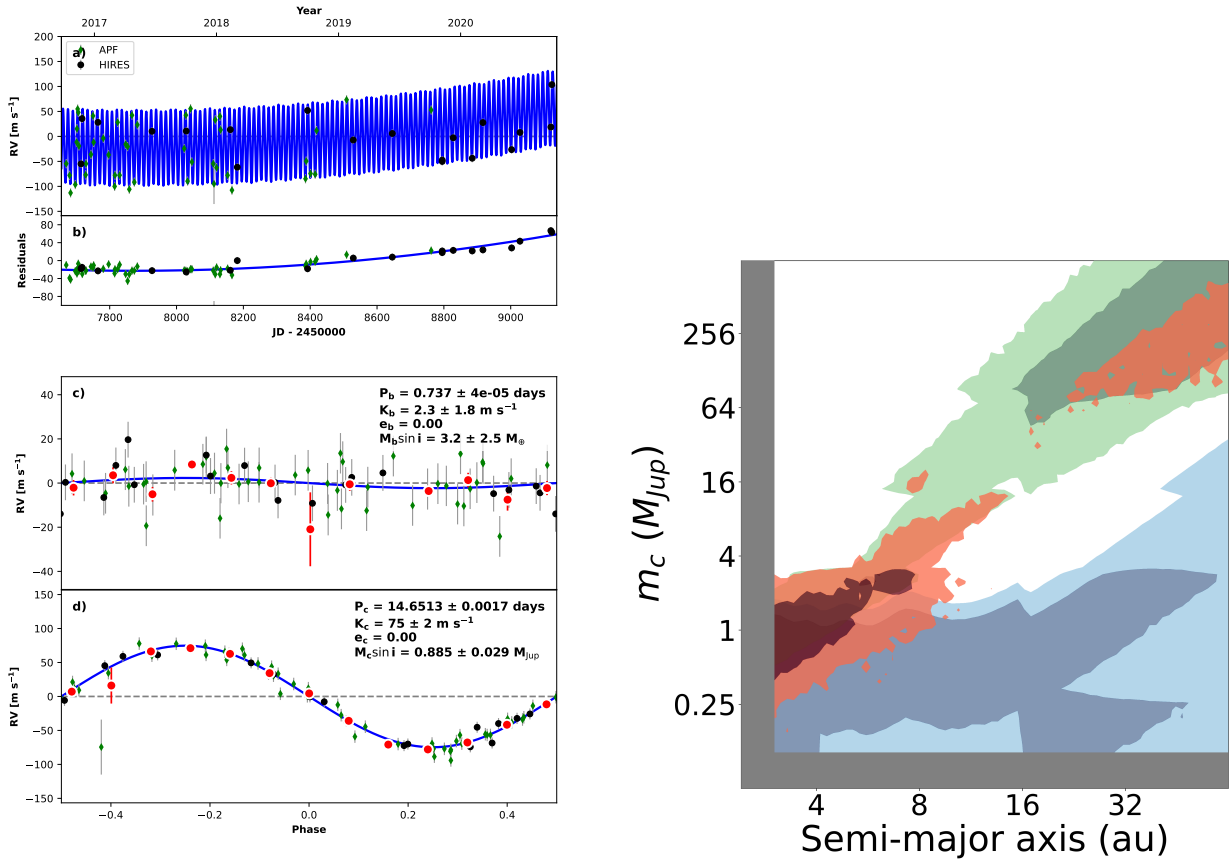


Figure 5.17: Same as Figure 5.11 for HD 75732. We detected only one of the four non-transiting planets in this system using our blind search algorithm. The residual trend, together with a low-significance astrometric acceleration, constrains the mass-separation posterior primarily to the planetary regime.

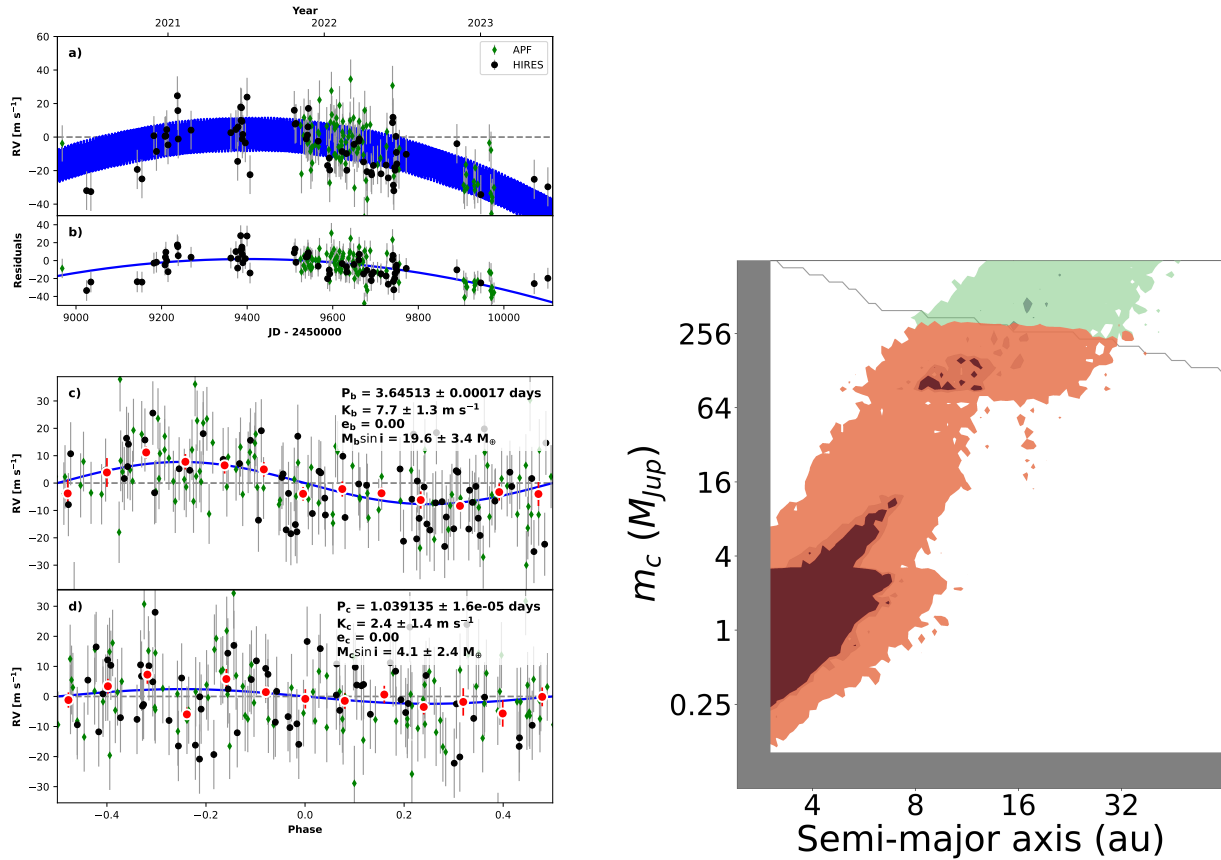


Figure 5.18: Same as Figure 5.11 for HD 93963. We did not recover either of this system’s two transiting planets at high significance. We measured a significant trend and marginal curvature in this system. Our analysis showed that the source of this RV variability is most likely a planet.

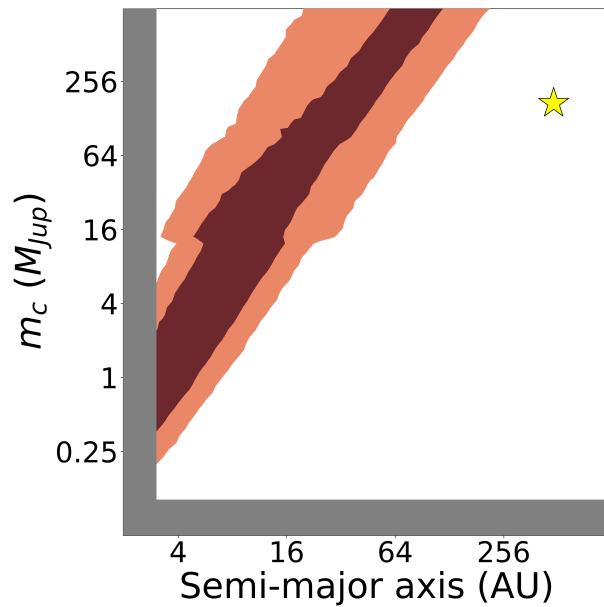


Figure 5.19: Our second analysis of the trend in the HD 93963 system. We expanded the semi-major axis range over which we tested companion models and therefore did not use the informative mass/separation prior described in Section 5.5.2, which is defined for separations ≤ 64 AU. We indicate the position of the stellar companion, HD 93963 B, with a yellow star. Our analysis suggests that an M5 dwarf at a separation of 484 AU is too small/too distant to have caused the observed trend.

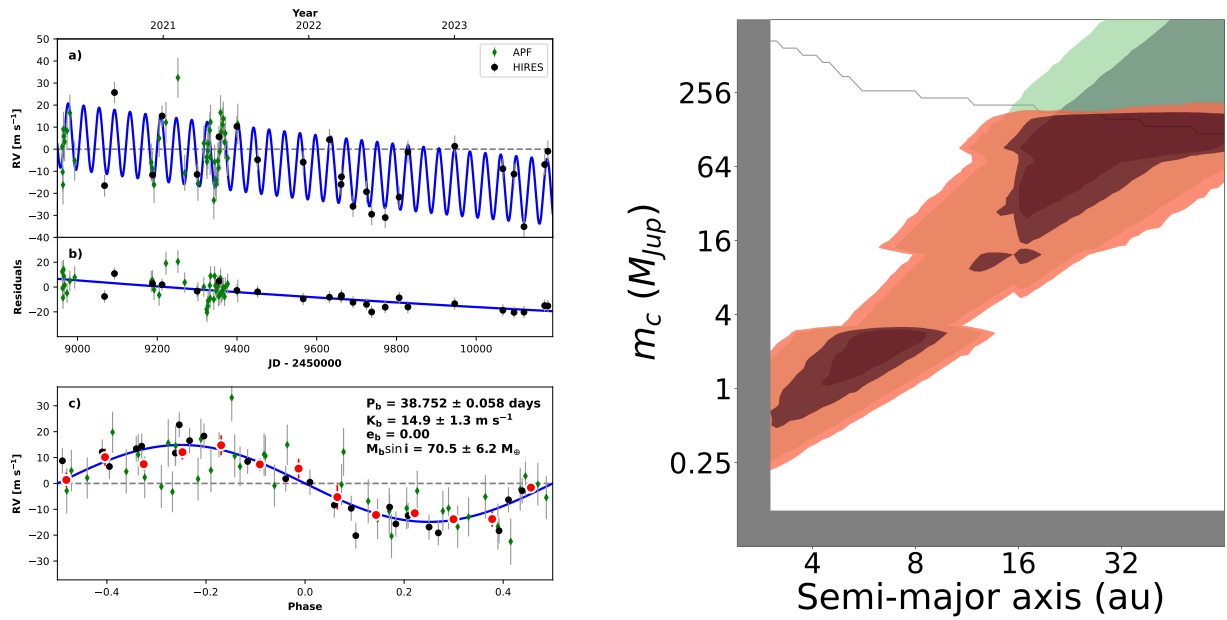


Figure 5.20: Same as Figure 5.11 for TIC 142381532. The inner transiting planet in this system is a sub-Saturn, which we characterized at high significance. Although this planet passed our $R_p < 10 R_{\oplus}$, it is likely a gas giant, so we exclude this system from our occurrence calculations. Our trend measurement is marginal, and evinces planetary and brown dwarf models with roughly equal probability.

Bibliography

- (1997). *The HIPPARCOS and TYCHO catalogues. Astrometric and photometric star catalogues derived from the ESA HIPPARCOS Space Astrometry Mission*, volume 1200 of *ESA Special Publication*.
- Akaike, H. (1974). A new look at the statistical model identification. *IEEE Transactions on Automatic Control*, 19(6):716–723.
- Badenas-Agusti, M., Günther, M. N., Daylan, T., Mikal-Evans, T., Vanderburg, A., Huang, C. X., Matthews, E., Rackham, B. V., Bieryla, A., Stassun, K. G., Kane, S. R., Shporer, A., Fulton, B. J., Hill, M. L., Nowak, G., Ribas, I., Pallé, E., Jenkins, J. M., Latham, D. W., Seager, S., Ricker, G. R., Vanderspek, R. K., Winn, J. N., Abril-Pla, O., Collins, K. A., Serra, P. G., Niraula, P., Rustamkulov, Z., Barclay, T., Crossfield, I. J. M., Howell, S. B., Ciardi, D. R., Gonzales, E. J., Schlieder, J. E., Caldwell, D. A., Fausnaugh, M., McDermott, S., Paegert, M., Pepper, J., Rose, M. E., and Twicken, J. D. (2020). HD 191939: Three Sub-Neptunes Transiting a Sun-like Star Only 54 pc Away. *Astrophysical Journal*, 160(3):113.
- Baraffe, I., Chabrier, G., Allard, F., and Hauschildt, P. H. (1998). Evolutionary models for solar metallicity low-mass stars: mass-magnitude relationships and color-magnitude diagrams. *Astronomy and Astrophysics*, 337:403–412.

- Baraffe, I., Chabrier, G., Barman, T. S., Allard, F., and Hauschildt, P. H. (2003). Evolutionary models for cool brown dwarfs and extrasolar giant planets. The case of HD 209458. *Astronomy and Astrophysics*, 402:701–712.
- Batygin, K. and Laughlin, G. (2015). Jupiter’s decisive role in the inner Solar System’s early evolution. *Proceedings of the National Academy of Science*, 112(14):4214–4217.
- Belorizky, D. (1938). Le Soleil, Etoile Variable. *L’Astronomie*, 52:359–361.
- Blunt, S., Nielsen, E. L., De Rosa, R. J., Konopacky, Q. M., Ryan, D., Wang, J. J., Pueyo, L., Rameau, J., Marois, C., Marchis, F., Macintosh, B., Graham, J. R., Duchêne, G., and Schneider, A. C. (2017). Orbits for the Impatient: A Bayesian Rejection-sampling Method for Quickly Fitting the Orbits of Long-period Exoplanets. *Astrophysical Journal*, 153(5):229.
- Blunt, S., Wang, J. J., Angelo, I., Ngo, H., Cody, D., De Rosa, R. J., Graham, J. R., Hirsch, L., Nagpal, V., Nielsen, E. L., Pearce, L., Rice, M., and Tejada, R. (2020). orbitize!: A Comprehensive Orbit-fitting Software Package for the High-contrast Imaging Community. *Astrophysical Journal*, 159(3):89.
- Bond, I. A., Udalski, A., Jaroszyński, M., Rattenbury, N. J., Paczyński, B., Soszyński, I., Wyrzykowski, L., Szymański, M. K., Kubiak, M., Szewczyk, O., Żebruń, K., Pietrzyński, G., Abe, F., Bennett, D. P., Eguchi, S., Furuta, Y., Hearnshaw, J. B., Kamiya, K., Kilmartin, P. M., Kurata, Y., Masuda, K., Matsubara, Y., Muraki, Y., Noda, S., Okajima, K., Sako, T., Sekiguchi, T., Sullivan, D. J., Sumi, T., Tristram, P. J., Yanagisawa, T., Yock, P. C. M., and OGLE Collaboration (2004). OGLE 2003-BLG-235/MOA 2003-BLG-53: A Planetary Microlensing Event. *Astrophysical Journal Letters*, 606(2):L155–L158.
- Bonomo, A. S., Dumusque, X., Massa, A., Mortier, A., Bongiolatti, R., Malavolta, L., Sozzetti, A., Buchhave, L. A., Damasso, M., Haywood, R. D., Morbidelli, A., Latham, D. W., Molinari, E., Pepe, F., Poretti, E., Udry, S., Affer, L., Boschin, W., Charbonneau,

- D., Cosentino, R., Cretignier, M., Ghedina, A., Lega, E., López-Morales, M., Margini, M., Martínez Fiorenzano, A. F., Mayor, M., Micela, G., Pedani, M., Pinamonti, M., Rice, K., Sasselov, D., Tronsgaard, R., and Vanderburg, A. (2023). Cold Jupiters and improved masses in 38 Kepler and K2 small planet systems from 3661 HARPS-N radial velocities. No excess of cold Jupiters in small planet systems. *Astronomy and Astrophysics*, 677:A33.
- Borucki, W. J., Koch, D., Basri, G., Batalha, N., Brown, T., Caldwell, D., Caldwell, J., Christensen-Dalsgaard, J., Cochran, W. D., DeVore, E., Dunham, E. W., Dupree, A. K., Gautier, T. N., Geary, J. C., Gilliland, R., Gould, A., Howell, S. B., Jenkins, J. M., Kondo, Y., Latham, D. W., Marcy, G. W., Meibom, S., Kjeldsen, H., Lissauer, J. J., Monet, D. G., Morrison, D., Sasselov, D., Tarter, J., Boss, A., Brownlee, D., Owen, T., Buzasi, D., Charbonneau, D., Doyle, L., Fortney, J., Ford, E. B., Holman, M. J., Seager, S., Steffen, J. H., Welsh, W. F., Rowe, J., Anderson, H., Buchhave, L., Ciardi, D., Walkowicz, L., Sherry, W., Horch, E., Isaacson, H., Everett, M. E., Fischer, D., Torres, G., Johnson, J. A., Endl, M., MacQueen, P., Bryson, S. T., Dotson, J., Haas, M., Kolodziejczak, J., Van Cleve, J., Chandrasekaran, H., Twicken, J. D., Quintana, E. V., Clarke, B. D., Allen, C., Li, J., Wu, H., Tenenbaum, P., Verner, E., Bruhweiler, F., Barnes, J., and Prsa, A. (2010). Kepler Planet-Detection Mission: Introduction and First Results. *Science*, 327(5968):977.
- Bowler, B. P., Blunt, S. C., and Nielsen, E. L. (2020). Population-level Eccentricity Distributions of Imaged Exoplanets and Brown Dwarf Companions: Dynamical Evidence for Distinct Formation Channels. *Astrophysical Journal*, 159(2):63.
- Bowler, B. P. and Nielsen, E. L. (2018). Occurrence Rates from Direct Imaging Surveys. In Deeg, H. J. and Belmonte, J. A., editors, *Handbook of Exoplanets*, page 155.
- Brandt, T. D. (2018). The Hipparcos-Gaia Catalog of Accelerations. *Astrophysical Journal Supplemental*, 239(2):31.

- Brandt, T. D. (2021). The Hipparcos-Gaia Catalog of Accelerations: Gaia EDR3 Edition. *arXiv e-prints*, page arXiv:2105.11662.
- Brandt, T. D., Dupuy, T. J., Li, Y., Brandt, G. M., Zeng, Y., Michalik, D., Bardalez Gagliuffi, D. C., and Raposo-Pulido, V. (2021). orvara: An Efficient Code to Fit Orbits Using Radial Velocity, Absolute, and/or Relative Astrometry. *Astrophysical Journal*, 162(5):186.
- Bryan, M. L., Knutson, H. A., Lee, E. J., Fulton, B. J., Batygin, K., Ngo, H., and Meshkat, T. (2019). An Excess of Jupiter Analogs in Super-Earth Systems. *Astrophysical Journal*, 157(2):52.
- Bryan, M. L. and Lee, E. J. (2024). Friends Not Foes: Strong Correlation between Inner Super-Earths and Outer Gas Giants. *Astrophysical Journal Letters*, 968(2):L25.
- Bryson, S., Coughlin, J., Batalha, N. M., Berger, T., Huber, D., Burke, C., Dotson, J., and Mullally, S. E. (2020). A Probabilistic Approach to Kepler Completeness and Reliability for Exoplanet Occurrence Rates. *Astrophysical Journal*, 159(6):279.
- Butler, R. P., Marcy, G. W., Fischer, D. A., Brown, T. M., Contos, A. R., Korzennik, S. G., Nisenson, P., and Noyes, R. W. (1999). Evidence for Multiple Companions to ν Andromedae. , 526(2):916–927.
- Butler, R. P., Marcy, G. W., Vogt, S. S., Fischer, D. A., Henry, G. W., Laughlin, G., and Wright, J. T. (2003). Seven New Keck Planets Orbiting G and K Dwarfs. *Astrophysical Journal*, 582(1):455–466.
- Butler, R. P., Marcy, G. W., Williams, E., Hauser, H., and Shirts, P. (1997). Three New “51 Pegasi-Type” Planets. *Astrophysical Journal Letters*, 474(2):L115–L118.
- Butler, R. P., Marcy, G. W., Williams, E., McCarthy, C., Dosanjh, P., and Vogt, S. S. (1996). Attaining Doppler Precision of 3 M s⁻¹. , 108:500.

- Campbell, B., Walker, G. A. H., and Yang, S. (1988). A Search for Substellar Companions to Solar-type Stars. , 331:902.
- Charbonneau, D., Brown, T. M., Latham, D. W., and Mayor, M. (2000). Detection of Planetary Transits Across a Sun-like Star. *Astrophysical Journal Letters*, 529(1):L45–L48.
- Chauvin, G. (2018). Two decades of exoplanetary science with adaptive optics. In Close, L. M., Schreiber, L., and Schmidt, D., editors, *Adaptive Optics Systems VI*, volume 10703 of *Society of Photo-Optical Instrumentation Engineers (SPIE) Conference Series*, page 1070305.
- Chauvin, G., Lagrange, A. M., Dumas, C., Zuckerman, B., Mouillet, D., Song, I., Beuzit, J. L., and Lowrance, P. (2004). A giant planet candidate near a young brown dwarf. Direct VLT/NACO observations using IR wavefront sensing. *AAP*, 425:L29–L32.
- Chen, J. and Kipping, D. (2017). Probabilistic Forecasting of the Masses and Radii of Other Worlds. *Astrophysical Journal*, 834(1):17.
- Chiang, E. and Laughlin, G. (2013). The minimum-mass extrasolar nebula: in situ formation of close-in super-Earths. , 431(4):3444–3455.
- Chontos, A., Akana Murphy, J. M., MacDougall, M. G., Fetherolf, T., **Judah Van Zandt**, and 26 colleagues (2022a). The TESS-Keck Survey: Science Goals and Target Selection. *The Astronomical Journal*, 163(6):297. [\[ADS\]](#).
- Chontos, A., Murphy, J. M. A., MacDougall, M. G., Fetherolf, T., Van Zandt, J., Rubenzahl, R. A., Beard, C., Huber, D., Batalha, N. M., Crossfield, I. J. M., Dressing, C. D., Fulton, B., Howard, A. W., Isaacson, H., Kane, S. R., Petigura, E. A., Robertson, P., Roy, A., Weiss, L. M., Behrard, A., Dai, F., Dalba, P. A., Giacalone, S., Hill, M. L., Lubin, J., Mayo, A., Močnik, T., Polanski, A. S., Rosenthal, L. J., Scarsdale, N., Turtelboom, E. V., Ricker, G. R., Vanderspek, R., Latham, D. W., Seager, S., Winn, J. N., Jenkins, J. M.,

- Quinn, S. N., Guerrero, N. M., Collins, K. A., Ciardi, D. R., Shporer, A., Goeke, R. F., Levine, A. M., Ting, E. B., Bieryla, A., Collins, K. I., Kielkopf, J. F., Barkaoui, K., Benni, P., Esparza-Borges, E., Conti, D. M., Hooton, M. J., Kagetani, T., Laloum, D., Marino, G., Massey, B., Murgas, F., Papini, R., Schwarz, R. P., Srdoc, G., Stockdale, C., Wang, G., Wittrock, J. M., and Zou, Y. (2022b). The TESS-Keck Survey: Science Goals and Target Selection. *Astrophysical Journal*, 163(6):297.
- Cochran, W. D., Hatzes, A. P., Butler, R. P., and Marcy, G. W. (1997). The Discovery of a Planetary Companion to 16 Cygni B. , 483(1):457–463.
- Cumming, A., Butler, R. P., Marcy, G. W., Vogt, S. S., Wright, J. T., and Fischer, D. A. (2008). The Keck Planet Search: Detectability and the Minimum Mass and Orbital Period Distribution of Extrasolar Planets. , 120(867):531.
- Dalba, P. A., Gupta, A. F., Rodriguez, J. E., Dragomir, D., Huang, C. X., Kane, S. R., Quinn, S. N., Bieryla, A., Esquerdo, G. A., Fulton, B. J., Scarsdale, N., Batalha, N. M., Beard, C., Behmard, A., Chontos, A., Crossfield, I. J. M., Dressing, C. D., Giacalone, S., Hill, M. L., Hirsch, L. A., Howard, A. W., Huber, D., Isaacson, H., Kosiarek, M., Lubin, J., Mayo, A. W., Mocnik, T., Akana Murphy, J. M., Petigura, E. A., Robertson, P., Rosenthal, L. J., Roy, A., Rubenzahl, R. A., Van Zandt, J., Weiss, L. M., Knudstrup, E., Andersen, M. F., Grundahl, F., Yao, X., Pepper, J., Villanueva, Steven, J., Ciardi, D. R., Cloutier, R., Jacobs, T. L., Kristiansen, M. H., LaCourse, D. M., Lendl, M., Osborn, H. P., Palle, E., Stassun, K. G., Stevens, D. J., Ricker, G. R., Vanderspek, R., Latham, D. W., Seager, S., Winn, J. N., Jenkins, J. M., Caldwell, D. A., Daylan, T., Fong, W., Goeke, R. F., Rose, M. E., Rowden, P., Schlieder, J. E., Smith, J. C., and Vanderburg, A. (2020). The TESS-Keck Survey. I. A Warm Sub-Saturn-mass Planet and a Caution about Stray Light in TESS Cameras. *Astrophysical Journal*, 159(5):241.
- Dawson, R. I. and Fabrycky, D. C. (2010). Radial Velocity Planets De-aliased: A New, Short Period for Super-Earth 55 Cnc e. *Astrophysical Journal*, 722(1):937–953.

- Feng, F. (2024). Astrometric detection of exoplanets. *arXiv e-prints*, page arXiv:2403.08226.
- Fischer, D. A., Marcy, G. W., Butler, R. P., Vogt, S. S., Frink, S., and Apps, K. (2001). Planetary Companions to HD 12661, HD 92788, and HD 38529 and Variations in Keplerian Residuals of Extrasolar Planets. *Astrophysical Journal*, 551(2):1107–1118.
- Fischer, D. A., Marcy, G. W., Butler, R. P., Vogt, S. S., Henry, G. W., Pourbaix, D., Walp, B., Misch, A. A., and Wright, J. T. (2003). A Planetary Companion to HD 40979 and Additional Planets Orbiting HD 12661 and HD 38529. *Astrophysical Journal*, 586(2):1394–1408.
- Fischer, D. A., Marcy, G. W., Butler, R. P., Vogt, S. S., Laughlin, G., Henry, G. W., Abouav, D., Peek, K. M. G., Wright, J. T., Johnson, J. A., McCarthy, C., and Isaacson, H. (2008). Five Planets Orbiting 55 Cancri. *Astrophysical Journal*, 675(1):790–801.
- Fischer, D. A., Marcy, G. W., and Spronck, J. F. P. (2014). The Twenty-five Year Lick Planet Search. *Astrophysical Journal Supplemental*, 210(1):5.
- Fischer, D. A. and Valenti, J. (2005a). The Planet-Metallicity Correlation. *Astrophysical Journal*, 622(2):1102–1117.
- Fischer, D. A. and Valenti, J. (2005b). The Planet-Metallicity Correlation. *Astrophysical Journal*, 622(2):1102–1117.
- Folsom, C. P., Fossati, L., Wood, B. E., Sreejith, A. G., Cubillos, P. E., Vidotto, A. A., Alecian, E., Girish, V., Lichtenegger, H., Murthy, J., Petit, P., and Valyavin, G. (2018). Characterization of the HD 219134 multiplanet system I. Observations of stellar magnetism, wind, and high-energy flux. , 481(4):5286–5295.
- Foreman-Mackey, D., Hogg, D. W., Lang, D., and Goodman, J. (2013). emcee: The MCMC Hammer. , 125(925):306.

- Fulton, B. J. (2017a). *APF-50: A robotic search for Earth's nearest neighbors*. PhD thesis, University of Hawaii, Manoa.
- Fulton, B. J. (2017b). *APF-50: A robotic search for Earth's nearest neighbors*. PhD thesis, University of Hawaii, Manoa.
- Fulton, B. J. and Petigura, E. A. (2018). The California-Kepler Survey. VII. Precise Planet Radii Leveraging Gaia DR2 Reveal the Stellar Mass Dependence of the Planet Radius Gap. *Astrophysical Journal*, 156(6):264.
- Fulton, B. J., Petigura, E. A., Blunt, S., and Sinukoff, E. (2018). RadVel: The Radial Velocity Modeling Toolkit. , 130(986):044504.
- Fulton, B. J., Petigura, E. A., Howard, A. W., Isaacson, H., Marcy, G. W., Cargile, P. A., Hebb, L., Weiss, L. M., Johnson, J. A., Morton, T. D., Sinukoff, E., Crossfield, I. J. M., and Hirsch, L. A. (2017). The California-Kepler Survey. III. A Gap in the Radius Distribution of Small Planets. *Astrophysical Journal*, 154(3):109.
- Fulton, B. J., Rosenthal, L. J., Hirsch, L. A., Isaacson, H., Howard, A. W., Dedrick, C. M., Sherstyuk, I. A., Blunt, S. C., Petigura, E. A., Knutson, H. A., Behmard, A., Chontos, A., Crepp, J. R., Crossfield, I. J. M., Dalba, P. A., Fischer, D. A., Henry, G. W., Kane, S. R., Kosiarek, M., Marcy, G. W., Rubenzahl, R. A., Weiss, L. M., and Wright, J. T. (2021). The California Legacy Survey II. Occurrence of Giant Planets Beyond the Ice line. *arXiv e-prints*, page arXiv:2105.11584.
- Gaia Collaboration, Prusti, T., de Bruijne, J. H. J., Brown, A. G. A., Vallenari, A., Babusiaux, C., Bailer-Jones, C. A. L., Bastian, U., Biermann, M., Evans, D. W., Eyer, L., Jansen, F., Jordi, C., Klioner, S. A., Lammers, U., Lindegren, L., Luri, X., Mignard, F., Milligan, D. J., Panem, C., Poinson, V., Pourbaix, D., Randich, S., Sarri, G., Sartoretti, P., Siddiqui, H. I., Soubiran, C., Valette, V., van Leeuwen, F., Walton, N. A., Aerts, C., Arenou, F., Cropper, M., Drimmel, R., Høg, E., Katz, D., Lattanzi, M. G., O'Mullane,

W., Grebel, E. K., Holland, A. D., Huc, C., Passot, X., Bramante, L., Cacciari, C., Castañeda, J., Chaoul, L., Cheek, N., De Angeli, F., Fabricius, C., Guerra, R., Hernández, J., Jean-Antoine-Piccolo, A., Masana, E., Messineo, R., Mowlavi, N., Nienartowicz, K., Ordóñez-Blanco, D., Panuzzo, P., Portell, J., Richards, P. J., Riello, M., Seabroke, G. M., Tanga, P., Thévenin, F., Torra, J., Els, S. G., Gracia-Abril, G., Comoretto, G., Garcia-Reinaldos, M., Lock, T., Mercier, E., Altmann, M., Andrae, R., Astraatmadja, T. L., Bellas-Velidis, I., Benson, K., Berthier, J., Blomme, R., Busso, G., Carry, B., Cellino, A., Clementini, G., Cowell, S., Creevey, O., Cuypers, J., Davidson, M., De Ridder, J., de Torres, A., Delchambre, L., Dell’Oro, A., Ducourant, C., Frémat, Y., García-Torres, M., Gosset, E., Halbwachs, J. L., Hambly, N. C., Harrison, D. L., Hauser, M., Hestroffer, D., Hodgkin, S. T., Huckle, H. E., Hutton, A., Jasniewicz, G., Jordan, S., Kontizas, M., Korn, A. J., Lanzafame, A. C., Manteiga, M., Moitinho, A., Muinonen, K., Osinde, J., Pancino, E., Pauwels, T., Petit, J. M., Recio-Blanco, A., Robin, A. C., Sarro, L. M., Siopis, C., Smith, M., Smith, K. W., Sozzetti, A., Thuillot, W., van Reeven, W., Viala, Y., Abbas, U., Abreu Aramburu, A., Accart, S., Aguado, J. J., Allan, P. M., Allasia, W., Altavilla, G., Álvarez, M. A., Alves, J., Anderson, R. I., Andrei, A. H., Anglada Varela, E., Antiche, E., Antoja, T., Antón, S., Arcay, B., Atzei, A., Ayache, L., Bach, N., Baker, S. G., Balaguer-Núñez, L., Barache, C., Barata, C., Barbier, A., Barblan, F., Baroni, M., Barrado y Navascués, D., Barros, M., Barstow, M. A., Becciani, U., Bellazzini, M., Bellei, G., Bello García, A., Belokurov, V., Bendjoya, P., Berihuete, A., Bianchi, L., Bienaymé, O., Billebaud, F., Blagorodnova, N., Blanco-Cuaresma, S., Boch, T., Bombrun, A., Borrachero, R., Bouquillon, S., Bourda, G., Bouy, H., Bragaglia, A., Breddels, M. A., Brouillet, N., Brüsemeister, T., Bucciarelli, B., Budnik, F., Burgess, P., Burgon, R., Burlacu, A., Busonero, D., Buzzì, R., Caffau, E., Cambras, J., Campbell, H., Cancelliere, R., Cantat-Gaudin, T., Carlucci, T., Carrasco, J. M., Castellani, M., Charlot, P., Charnas, J., Charvet, P., Chassat, F., Chiavassa, A., Clotet, M., Coccozza, G., Collins, R. S., Collins, P., Costigan, G., Crifo, F., Cross, N. J. G., Crosta, M., Crowley, C., Dafonte, C.,

Damerdj, Y., Dapergolas, A., David, P., David, M., De Cat, P., de Felice, F., de Laverny, P., De Luise, F., De March, R., de Martino, D., de Souza, R., Debosscher, J., del Pozo, E., Delbo, M., Delgado, A., Delgado, H. E., di Marco, F., Di Matteo, P., Diakite, S., Distefano, E., Dolding, C., Dos Anjos, S., Drazinos, P., Durán, J., Dzigan, Y., Ecale, E., Edvardsson, B., Enke, H., Erdmann, M., Escolar, D., Espina, M., Evans, N. W., Eynard Bontemps, G., Fabre, C., Fabrizio, M., Faigler, S., Falcão, A. J., Farràs Casas, M., Faye, F., Federici, L., Fedorets, G., Fernández-Hernández, J., Fernique, P., Fienga, A., Figueras, F., Filippi, F., Findeisen, K., Fonti, A., Fouesneau, M., Fraile, E., Fraser, M., Fuchs, J., Furnell, R., Gai, M., Galleti, S., Galluccio, L., Garabato, D., García-Sedano, F., Garé, P., Garofalo, A., Garralda, N., Gavras, P., Gerssen, J., Geyer, R., Gilmore, G., Girona, S., Giuffrida, G., Gomes, M., González-Marcos, A., González-Núñez, J., González-Vidal, J. J., Granvik, M., Guerrier, A., Guillout, P., Guiraud, J., Gúrpide, A., Gutiérrez-Sánchez, R., Guy, L. P., Haignon, R., Hatzidimitriou, D., Haywood, M., Heiter, U., Helmi, A., Hobbs, D., Hofmann, W., Holl, B., Holland, G., Hunt, J. A. S., Hypki, A., Icardi, V., Irwin, M., Jevardat de Fombelle, G., Jofré, P., Jonker, P. G., Jorissen, A., Julbe, F., Karampelas, A., Kochoska, A., Kohley, R., Kolenberg, K., Kontizas, E., Kopusov, S. E., Kordopatis, G., Koubsky, P., Kowalczyk, A., Krone-Martins, A., Kudryashova, M., Kull, I., Bachchan, R. K., Lacoste-Seris, F., Lanza, A. F., Lavigne, J. B., Le Poncin-Lafitte, C., Lebreton, Y., Lebzelter, T., Leccia, S., Leclerc, N., Lecoeur-Taibi, I., Lemaitre, V., Lenhardt, H., Leroux, F., Liao, S., Licata, E., Lindstrøm, H. E. P., Lister, T. A., Livanou, E., Lobel, A., Löffler, W., López, M., Lopez-Lozano, A., Lorenz, D., Loureiro, T., MacDonald, I., Magalhães Fernandes, T., Managau, S., Mann, R. G., Mantelet, G., Marchal, O., Marchant, J. M., Marconi, M., Marie, J., Marinoni, S., Marrese, P. M., Marschalkó, G., Marshall, D. J., Martín-Fleitas, J. M., Martino, M., Mary, N., Matijević, G., Mazeh, T., McMillan, P. J., Messina, S., Mestre, A., Michalik, D., Millar, N. R., Miranda, B. M. H., Molina, D., Molinaro, R., Molinaro, M., Molnár, L., Moniez, M., Montegriffo, P., Monteiro, D., Mor, R., Mora, A., Morbidelli, R., Morel, T., Morgenthaler, S., Morley, T., Morris, D.,

Mulone, A. F., Muraveva, T., Musella, I., Narbonne, J., Nelemans, G., Nicastro, L., Noval, L., Ordénovic, C., Ordieres-Meré, J., Osborne, P., Pagani, C., Pagano, I., Pailler, F., Palacin, H., Palaversa, L., Parsons, P., Paulsen, T., Pecoraro, M., Pedrosa, R., Pentikäinen, H., Pereira, J., Pichon, B., Piersimoni, A. M., Pineau, F. X., Plachy, E., Plum, G., Poujoulet, E., Prša, A., Pulone, L., Ragaini, S., Rago, S., Rambaux, N., Ramos-Lerate, M., Ranalli, P., Rauw, G., Read, A., Regibo, S., Renk, F., Reylé, C., Ribeiro, R. A., Rimoldini, L., Ripepi, V., Riva, A., Rixon, G., Roelens, M., Romero-Gómez, M., Rowell, N., Royer, F., Rudolph, A., Ruiz-Dern, L., Sadowski, G., Sagristà Sellés, T., Sahlmann, J., Salgado, J., Salguero, E., Sarasso, M., Savietto, H., Schnorhk, A., Schultheis, M., Sciacca, E., Segol, M., Segovia, J. C., Segransan, D., Serpell, E., Shih, I. C., Smareglia, R., Smart, R. L., Smith, C., Solano, E., Solitro, F., Sordo, R., Soria Nieto, S., Souchay, J., Spagna, A., Spoto, F., Stampa, U., Steele, I. A., Steidelmüller, H., Stephenson, C. A., Stoev, H., Suess, F. F., Süveges, M., Surdej, J., Szabados, L., Szegedi-Elek, E., Tapiador, D., Taris, F., Tauran, G., Taylor, M. B., Teixeira, R., Terrett, D., Tingley, B., Trager, S. C., Turon, C., Ulla, A., Utrilla, E., Valentini, G., van Elteren, A., Van Hemelryck, E., van Leeuwen, M., Varadi, M., Vecchiato, A., Veljanoski, J., Via, T., Vicente, D., Vogt, S., Voss, H., Votruba, V., Voutsinas, S., Walmsley, G., Weiler, M., Weingrill, K., Werner, D., Wevers, T., Whitehead, G., Wyrzykowski, Ł., Yoldas, A., Žerjal, M., Zucker, S., Zurbach, C., Zwitter, T., Alecu, A., Allen, M., Allende Prieto, C., Amorim, A., Anglada-Escudé, G., Arsenijevic, V., Azaz, S., Balm, P., Beck, M., Bernstein, H. H., Bigot, L., Bijaoui, A., Blasco, C., Bonfigli, M., Bono, G., Boudreault, S., Bressan, A., Brown, S., Brunet, P. M., Bunclark, P., Buonanno, R., Butkevich, A. G., Carret, C., Carrion, C., Chemin, L., Chéreau, F., Corcione, L., Darmigny, E., de Boer, K. S., de Teodoro, P., de Zeeuw, P. T., Delle Luche, C., Domingues, C. D., Dubath, P., Fodor, F., Frézouls, B., Fries, A., Fustes, D., Fyfe, D., Gallardo, E., Gallegos, J., Gardiol, D., Gebran, M., Gomboc, A., Gómez, A., Grux, E., Gueguen, A., Heyrovsky, A., Hoar, J., Iannicola, G., Isasi Parache, Y., Janotto, A. M., Joliet, E., Jonckheere, A., Keil, R., Kim, D. W., Klagyivik, P., Klar, J., Knude,

J., Kochukhov, O., Kolka, I., Kos, J., Kutka, A., Lainey, V., LeBouquin, D., Liu, C., Loreggia, D., Makarov, V. V., Marseille, M. G., Martayan, C., Martinez-Rubi, O., Marsart, B., Meynadier, F., Mignot, S., Munari, U., Nguyen, A. T., Nordlander, T., Ocvirk, P., O’Flaherty, K. S., Olias Sanz, A., Ortiz, P., Osorio, J., Oszkiewicz, D., Ouzounis, A., Palmer, M., Park, P., Pasquato, E., Peltzer, C., Peralta, J., Péturaud, F., Pieniluoma, T., Pigozzi, E., Poels, J., Prat, G., Prod’homme, T., Raison, F., Rebordao, J. M., Risquez, D., Rocca-Volmerange, B., Rosen, S., Ruiz-Fuertes, M. I., Russo, F., Sembay, S., Serraller Vizcaino, I., Short, A., Siebert, A., Silva, H., Sinachopoulos, D., Slezak, E., Soffel, M., Sosnowska, D., Straižys, V., ter Linden, M., Terrell, D., Theil, S., Tiede, C., Troisi, L., Tsalmantza, P., Tur, D., Vaccari, M., Vachier, F., Valles, P., Van Hamme, W., Veltz, L., Virtanen, J., Wallut, J. M., Wichmann, R., Wilkinson, M. I., Ziaepour, H., and Zschocke, S. (2016). The Gaia mission. *Astronomy and Astrophysics*, 595:A1.

Gibson, S. R., Howard, A. W., Marcy, G. W., Edelstein, J., Wishnow, E. H., and Poppett, C. L. (2016). KPF: Keck Planet Finder. In Evans, C. J., Simard, L., and Takami, H., editors, *Ground-based and Airborne Instrumentation for Astronomy VI*, volume 9908 of *Society of Photo-Optical Instrumentation Engineers (SPIE) Conference Series*, page 990870.

Grunblatt, S. K., Saunders, N., Huber, D., Thorngren, D., Vissapragada, S., Yoshida, S., Schlaufman, K. C., Giacalone, S., Macdougall, M., Chontos, A., Turtelboom, E., Beard, C., Murphy, J. M. A., Rice, M., Isaacson, H., Angus, R., and Howard, A. W. (2024). TESS Giants Transiting Giants. IV. A Low-density Hot Neptune Orbiting a Red Giant Star. *Astrophysical Journal*, 168(1):1.

Guerrero, N. M., Seager, S., Huang, C. X., Vanderburg, A., Garcia Soto, A., Mireles, I., Hesse, K., Fong, W., Glidden, A., Shporer, A., Latham, D. W., Collins, K. A., Quinn, S. N., Burt, J., Dragomir, D., Crossfield, I., Vanderspek, R., Fausnaugh, M., Burke, C. J., Ricker, G., Daylan, T., Essack, Z., Günther, M. N., Osborn, H. P., Pepper, J., Rowden,

P., Sha, L., Villanueva, Steven, J., Yahalomi, D. A., Yu, L., Ballard, S., Batalha, N. M., Berardo, D., Chontos, A., Dittmann, J. A., Esquerdo, G. A., Mikal-Evans, T., Jayaraman, R., Krishnamurthy, A., Louie, D. R., Mehrle, N., Niraula, P., Rackham, B. V., Rodriguez, J. E., Rowden, S. J. L., Sousa-Silva, C., Watanabe, D., Wong, I., Zhan, Z., Zivanovic, G., Christiansen, J. L., Ciardi, D. R., Swain, M. A., Lund, M. B., Mullally, S. E., Fleming, S. W., Rodriguez, D. R., Boyd, P. T., Quintana, E. V., Barclay, T., Colón, K. D., Rinehart, S. A., Schlieder, J. E., Clampin, M., Jenkins, J. M., Twicken, J. D., Caldwell, D. A., Coughlin, J. L., Henze, C., Lissauer, J. J., Morris, R. L., Rose, M. E., Smith, J. C., Tenenbaum, P., Ting, E. B., Wohler, B., Bakos, G. Á., Bean, J. L., Berta-Thompson, Z. K., Bieryla, A., Bouma, L. G., Buchhave, L. A., Butler, N., Charbonneau, D., Doty, J. P., Ge, J., Holman, M. J., Howard, A. W., Kaltenegger, L., Kane, S. R., Kjeldsen, H., Kreidberg, L., Lin, D. N. C., Minsky, C., Narita, N., Paegert, M., Pál, A., Palle, E., Sasselov, D. D., Spencer, A., Sozzetti, A., Stassun, K. G., Torres, G., Udry, S., and Winn, J. N. (2021). The TESS Objects of Interest Catalog from the TESS Prime Mission. *Astrophysical Journal Supplemental*, 254(2):39.

Handley, L. B., Howard, A. W., Rubenzahl, R. A., Dai, F., Tyler, D., Lee, R. A., Giccalone, S., Isaacson, H., Householder, A., Halverson, S., Roy, A., and Walawender, J. (2024). An Obliquity Measurement of the Hot Neptune TOI-1694b. *arXiv e-prints*, page arXiv:2412.07950.

Hansen, B. M. S. and Murray, N. (2012). Migration Then Assembly: Formation of Neptune-mass Planets inside 1 AU. *Astrophysical Journal*, 751(2):158.

Henry, G. W., Marcy, G. W., Butler, R. P., and Vogt, S. S. (2000). A Transiting “51 Peg-like” Planet. , 529(1):L41–L44.

Henry, T. J., Soderblom, D. R., Donahue, R. A., and Baliunas, S. L. (1996). A Survey of Ca II H and K Chromospheric Emission in Southern Solar-Type Stars. *Astrophysical Journal*, 111:439.

- Householder, A. and Weiss, L. (2022). The Inconsistent use of ω in the RV Equation. *arXiv e-prints*, page arXiv:2212.06966.
- Howard, A. W., Johnson, J. A., Marcy, G. W., Fischer, D. A., Wright, J. T., Bernat, D., Henry, G. W., Peek, K. M. G., Isaacson, H., Apps, K., Endl, M., Cochran, W. D., Valenti, J. A., Anderson, J., and Piskunov, N. E. (2010a). The California Planet Survey. I. Four New Giant Exoplanets. *Astrophysical Journal*, 721:1467–1481.
- Howard, A. W., Marcy, G. W., Johnson, J. A., Fischer, D. A., Wright, J. T., Isaacson, H., Valenti, J. A., Anderson, J., Lin, D. N. C., and Ida, S. (2010b). The Occurrence and Mass Distribution of Close-in Super-Earths, Neptunes, and Jupiters. *Science*, 330(6004):653.
- Howell, S. B., Everett, M. E., Sherry, W., Horch, E., and Ciardi, D. R. (2011). Speckle Camera Observations for the NASA Kepler Mission Follow-up Program. *Astrophysical Journal*, 142(1):19.
- Huang, C. X., Vanderburg, A., Pál, A., Sha, L., Yu, L., Fong, W., Fausnaugh, M., Shporer, A., Guerrero, N., Vanderspek, R., and Ricker, G. (2020a). Photometry of 10 Million Stars from the First Two Years of TESS Full Frame Images: Part I. *Research Notes of the American Astronomical Society*, 4(11):204.
- Huang, C. X., Vanderburg, A., Pál, A., Sha, L., Yu, L., Fong, W., Fausnaugh, M., Shporer, A., Guerrero, N., Vanderspek, R., and Ricker, G. (2020b). Photometry of 10 Million Stars from the First Two Years of TESS Full Frame Images: Part II. *Research Notes of the American Astronomical Society*, 4(11):206.
- Isaacson, H. and Fischer, D. (2010). Chromospheric Activity and Jitter Measurements for 2630 Stars on the California Planet Search. *Astrophysical Journal*, 725(1):875–885.
- Izidoro, A. and Raymond, S. N. (2018). Formation of Terrestrial Planets. In Deeg, H. J. and Belmonte, J. A., editors, *Handbook of Exoplanets*, page 142.

- Izidoro, A., Raymond, S. N., Morbidelli, A., Hersant, F., and Pierens, A. (2015). Gas Giant Planets as Dynamical Barriers to Inward-Migrating Super-Earths. *Astrophysical Journal Letters*, 800(2):L22.
- Jenkins, J. M. (2002). The Impact of Solar-like Variability on the Detectability of Transiting Terrestrial Planets. *Astrophysical Journal*, 575(1):493–505.
- Jenkins, J. M., Chandrasekaran, H., McCauliff, S. D., Caldwell, D. A., Tenenbaum, P., Li, J., Klaus, T. C., Cote, M. T., and Middour, C. (2010). Transiting planet search in the Kepler pipeline. In Radziwill, N. M. and Bridger, A., editors, *Software and Cyberinfrastructure for Astronomy*, volume 7740 of *Society of Photo-Optical Instrumentation Engineers (SPIE) Conference Series*, page 77400D.
- Jenkins, J. M., Tenenbaum, P., Seader, S., Burke, C. J., McCauliff, S. D., Smith, J. C., Twicken, J. D., and Chandrasekaran, H. (2020). Kepler Data Processing Handbook: Transiting Planet Search. Kepler Science Document KSCI-19081-003, id. 9. Edited by Jon M. Jenkins.
- Jenkins, J. M., Twicken, J. D., McCauliff, S., Campbell, J., Sanderfer, D., Lung, D., Mansouri-Samani, M., Girouard, F., Tenenbaum, P., Klaus, T., Smith, J. C., Caldwell, D. A., Chacon, A. D., Henze, C., Heiges, C., Latham, D. W., Morgan, E., Swade, D., Rinehart, S., and Vanderspek, R. (2016). The TESS science processing operations center. In *Software and Cyberinfrastructure for Astronomy IV*, volume 9913 of , page 99133E.
- Johnson, J. A., Aller, K. M., Howard, A. W., and Crepp, J. R. (2010). Giant Planet Occurrence in the Stellar Mass-Metallicity Plane. , 122(894):905.
- Johnson, J. A., Gazak, J. Z., Apps, K., Muirhead, P. S., Crepp, J. R., Crossfield, I. J. M., Boyajian, T., von Braun, K., Rojas-Ayala, B., Howard, A. W., Covey, K. R., Schlawin, E., Hamren, K., Morton, T. D., Marcy, G. W., and Lloyd, J. P. (2012). Characterizing

- the Cool KOIs. II. The M Dwarf KOI-254 and Its Hot Jupiter. *Astronomical Journal*, 143(5):111.
- Judah Van Zandt** and 42 colleagues (2025). The TESS-Keck Distant Giants Survey XXIV: Outer Giants May be More Prevalent in the Presence of Inner Small Planets. *The Astronomical Journal*, 169(5):235.
- Judah Van Zandt** and 44 colleagues (2023). TESS-Keck Survey. XIV. Two Giant Exoplanets from the Distant Giants Survey. *The Astronomical Journal*, 165(2):60.
- Judah Van Zandt** and Petigura, E. A. (2024a). ethraid: A Simple Method for Characterizing Long-period Companions Using Doppler, Astrometric, and Imaging Constraints. *The Astronomical Journal*, 167(6):250.
- Judah Van Zandt** and Petigura, E. A. (2024b). No Evidence for a Metallicity-dependent Enhancement of Distant Giant Companions to Close-in Small Planets in the California Legacy Survey. *The Astronomical Journal*, 168(6):268.
- Kervella, P., Arenou, F., Mignard, F., and Thévenin, F. (2019). Stellar and substellar companions of nearby stars from Gaia DR2. Binarity from proper motion anomaly. *Astronomy and Astrophysics*, 623:A72.
- Kiefer, F. (2019). Determining the mass of the planetary candidate HD 114762 b using Gaia. *AAP*, 632:L9.
- Kipping, D. M. (2013). Parametrizing the exoplanet eccentricity distribution with the beta distribution. , 434:L51–L55.
- Kloek, T., Kloek, T., and Van Dijk, H. (1978). Bayesian estimates of equation system parameters: An application of integration by monte carlo. *Econometrica*, 46:1–19.
- Knudstrup, E., Gandolfi, D., Nowak, G., Persson, C. M., Furlan, E., Livingston, J., Matthews, E., Lundkvist, M. S., Winther, M. L., Rørsted, J. L., Albrecht, S. H., Goffo,

E., Carleo, I., Deeg, H. J., Collins, K. A., Narita, N., Isaacson, H., Redfield, S., Dai, F., Hirano, T., Akana Murphy, J. M., Beard, C., Buchhave, L. A., Cary, S., Chontos, A., Crossfield, I., Cochran, W. D., Conti, D., Dalba, P. A., Esposito, M., Fajardo-Acosta, S., Giacalone, S., Grunblatt, S. K., Guerra, P., Hatzes, A. P., Holcomb, R., Horta, F. G., Howard, A. W., Huber, D., Jenkins, J. M., Kabáth, P., Kane, S., Korth, J., Lam, K. W. F., Lester, K. V., Matson, R., McLeod, K. K., Orell-Miquel, J., Murgas, F., Palles, E., Polanski, A. S., Ricker, G., Robertson, P., Rubenzahl, R., Schlieder, J. E., Seager, S., Smith, A. M. S., Tenenbaum, P., Turtelboom, E., Vanderspek, R., Weiss, L., and Winn, J. (2023). Radial velocity confirmation of a hot super-Neptune discovered by TESS with a warm Saturn-mass companion. , 519(4):5637–5655.

Kraft, R. P. (1967). Studies of Stellar Rotation. V. The Dependence of Rotation on Age among Solar-Type Stars. *Astrophysical Journal*, 150:551.

Laliois, K., Burt, J. A., Mamajek, E. E., Li, Z., Perdelwitz, V., Zhao, J., Butler, R. P., Holden, B., Rosenthal, L., Fulton, B. J., Feng, F., Kane, S. R., Bailey, J., Carter, B., Crane, J. D., Furlan, E., Gnilka, C. L., Howell, S. B., Laughlin, G., Shectman, S. A., Teske, J. K., Tinney, C. G., Vogt, S. S., Wang, S. X., and Wittenmyer, R. A. (2023). Doppler Constraints on Planetary Companions to Nearby Sun-like Stars: An Archival Radial Velocity Survey of Southern Targets for Proposed NASA Direct Imaging Missions. *Astrophysical Journal*, 165(4):176.

Latham, D. W., Mazeh, T., Stefanik, R. P., Mayor, M., and Burki, G. (1989). The unseen companion of HD114762: a probable brown dwarf. *Nature*, 339(6219):38–40.

Latham, D. W., Tonry, J., Bahcall, J. N., Soneira, R. M., and Schechter, P. (1984). Detection of binaries with projected separations as large as 0.1 parsec. *Astrophysical Journal Letters*, 281:L41–L45.

- Li, G., Naoz, S., Kocsis, B., and Loeb, A. (2014). Eccentricity Growth and Orbit Flip in Near-coplanar Hierarchical Three-body Systems. *Astrophysical Journal*, 785(2):116.
- Li, J., Tenenbaum, P., Twicken, J. D., Burke, C. J., Jenkins, J. M., Quintana, E. V., Rowe, J. F., and Seader, S. E. (2019). Kepler Data Validation II-Transit Model Fitting and Multiple-planet Search. , 131(996):024506.
- Lin, D. N. C. and Papaloizou, J. (1986). On the Tidal Interaction between Protoplanets and the Protoplanetary Disk. III. Orbital Migration of Protoplanets. *Astrophysical Journal*, 309:846.
- Lindegren, L., Hernández, J., Bombrun, A., Klioner, S., Bastian, U., Ramos-Lerate, M., de Torres, A., Steidelmüller, H., Stephenson, C., Hobbs, D., Lammers, U., Biermann, M., Geyer, R., Hilger, T., Michalik, D., Stampa, U., McMillan, P. J., Castañeda, J., Clotet, M., Comoretto, G., Davidson, M., Fabricius, C., Gracia, G., Hambly, N. C., Hutton, A., Mora, A., Portell, J., van Leeuwen, F., Abbas, U., Abreu, A., Altmann, M., Andrei, A., Anglada, E., Balaguer-Núñez, L., Barache, C., Becciani, U., Bertone, S., Bianchi, L., Bouquillon, S., Bourda, G., Brüsemeister, T., Bucciarelli, B., Busonero, D., Buzzzi, R., Cancelliere, R., Carlucci, T., Charlot, P., Cheek, N., Crosta, M., Crowley, C., de Bruijne, J., de Felice, F., Drimmel, R., Esquej, P., Fienga, A., Fraile, E., Gai, M., Garralda, N., González-Vidal, J. J., Guerra, R., Hauser, M., Hofmann, W., Holl, B., Jordan, S., Lattanzi, M. G., Lenhardt, H., Liao, S., Licata, E., Lister, T., Löffler, W., Marchant, J., Martin-Fleitas, J. M., Messineo, R., Mignard, F., Morbidelli, R., Poggio, E., Riva, A., Rowell, N., Salguero, E., Sarasso, M., Sciacca, E., Siddiqui, H., Smart, R. L., Spagna, A., Steele, I., Taris, F., Torra, J., van Elteren, A., van Reeve, W., and Vecchiato, A. (2018). Gaia Data Release 2. The astrometric solution. *Astronomy and Astrophysics*, 616:A2.
- Lindegren, L., Klioner, S. A., Hernández, J., Bombrun, A., Ramos-Lerate, M., Steidelmüller, H., Bastian, U., Biermann, M., de Torres, A., Gerlach, E., Geyer, R., Hilger, T., Hobbs, D., Lammers, U., McMillan, P. J., Stephenson, C. A., Castañeda, J., Davidson, M., Fabricius,

C., Gracia-Abril, G., Portell, J., Rowell, N., Teyssier, D., Torra, F., Bartolomé, S., Clotet, M., Garralda, N., González-Vidal, J. J., Torra, J., Abbas, U., Altmann, M., Anglada Varela, E., Balaguer-Núñez, L., Balog, Z., Barache, C., Becciani, U., Bernet, M., Bertone, S., Bianchi, L., Bouquillon, S., Brown, A. G. A., Bucciarelli, B., Busonero, D., Butkevich, A. G., Buzzi, R., Cancelliere, R., Carlucci, T., Charlot, P., Cioni, M. R. L., Crosta, M., Crowley, C., del Peloso, E. F., del Pozo, E., Drimmel, R., Esquej, P., Fienga, A., Fraile, E., Gai, M., Garcia-Reinaldos, M., Guerra, R., Hambly, N. C., Hauser, M., Janßen, K., Jordan, S., Kostrzewa-Rutkowska, Z., Lattanzi, M. G., Liao, S., Licata, E., Lister, T. A., Löffler, W., Marchant, J. M., Masip, A., Mignard, F., Mints, A., Molina, D., Mora, A., Morbidelli, R., Murphy, C. P., Pagani, C., Panuzzo, P., Peñalosa Esteller, X., Poggio, E., Re Fiorentin, P., Riva, A., Sagristà Sellés, A., Sanchez Gimenez, V., Sarasso, M., Sciacca, E., Siddiqui, H. I., Smart, R. L., Souami, D., Spagna, A., Steele, I. A., Taris, F., Utrilla, E., van Reeve, W., and Vecchiato, A. (2021). Gaia Early Data Release 3. The astrometric solution. *Astronomy and Astrophysics*, 649:A2.

Lubin, J., **Judah Van Zandt**, and 34 colleagues (2022a). TESS-Keck Survey. IX. Masses of Three Sub-Neptunes Orbiting HD 191939 and the Discovery of a Warm Jovian plus a Distant Substellar Companion. *The Astronomical Journal*, 163(2):101. [\[ADS\]](#).

Lubin, J., Petigura, E. A., **Judah Van Zandt**, and 25 colleagues (2024a). The HD 191939 Exoplanet System is Well Aligned and Flat. *The Astronomical Journal*, 168(5):196.

Lubin, J., Petigura, E. A., Van Zandt, J., Beard, C., Dai, F., Halverson, S., Holcomb, R., Howard, A. W., Isaacson, H., Luhn, J., Robertson, P., Rubenzahl, R. A., Stefánsson, G., Winn, J. N., Brodheim, M., Deich, W., Hill, G. M., Gibson, S. R., Holden, B., Householder, A., Laher, R. R., Lanclos, K., Payne, J., Roy, A., Smith, R., Shaum, A. P., Schwab, C., and Walawender, J. (2024b). The HD 191939 Exoplanet System is Well Aligned and Flat. *Astrophysical Journal*, 168(5):196.

Lubin, J., Van Zandt, J., Holcomb, R., Weiss, L. M., Petigura, E. A., Robertson, P., Akana

Murphy, J. M., Scarsdale, N., Batygin, K., Polanski, A. S., Batalha, N. M., Crossfield, I. J. M., Dressing, C., Fulton, B., Howard, A. W., Huber, D., Isaacson, H., Kane, S. R., Roy, A., Beard, C., Blunt, S., Chontos, A., Dai, F., Dalba, P. A., Gary, K., Giacalone, S., Hill, M. L., Mayo, A., Močnik, T., Kosiarek, M. R., Rice, M., Rubenzahl, R. A., Latham, D. W., Seager, S., Winn, J. N., and Gary, K. (2022b). TESS-Keck Survey. IX. Masses of Three Sub-Neptunes Orbiting HD 191939 and the Discovery of a Warm Jovian plus a Distant Substellar Companion. *Astrophysical Journal*, 163(2):101.

Luque, R., Pallé, E., Kossakowski, D., Dreizler, S., Kemmer, J., Espinoza, N., Burt, J., Anglada-Escudé, G., Béjar, V. J. S., Caballero, J. A., Collins, K. A., Collins, K. I., Cortés-Contreras, M., Díez-Alonso, E., Feng, F., Hatzes, A., Hellier, C., Henning, T., Jeffers, S. V., Kaltenegger, L., Kürster, M., Madden, J., Molaverdikhani, K., Montes, D., Narita, N., Nowak, G., Ofir, A., Oshagh, M., Parviainen, H., Quirrenbach, A., Reffert, S., Reiners, A., Rodríguez-López, C., Schlecker, M., Stock, S., Trifonov, T., Winn, J. N., Zapatero Osorio, M. R., Zechmeister, M., Amado, P. J., Anderson, D. R., Batalha, N. E., Bauer, F. F., Bluhm, P., Burke, C. J., Butler, R. P., Caldwell, D. A., Chen, G., Crane, J. D., Dragomir, D., Dressing, C. D., Dynes, S., Jenkins, J. M., Kaminski, A., Klahr, H., Kotani, T., Lafarga, M., Latham, D. W., Lewin, P., McDermott, S., Montañés-Rodríguez, P., Morales, J. C., Murgas, F., Nagel, E., Pedraz, S., Ribas, I., Ricker, G. R., Rowden, P., Seager, S., Shectman, S. A., Tamura, M., Teske, J., Twicken, J. D., Vanderspeck, R., Wang, S. X., and Wohler, B. (2019). Planetary system around the nearby M dwarf GJ 357 including a transiting, hot, Earth-sized planet optimal for atmospheric characterization. *Astronomy and Astrophysics*, 628:A39.

Ma, B., Ge, J., Muterspaugh, M., Singer, M. A., Henry, G. W., González Hernández, J. I., Sithajan, S., Jeram, S., Williamson, M., Stassun, K., Kimock, B., Varosi, F., Schofield, S., Liu, J., Powell, S., Cassette, A., Jakeman, H., Avner, L., Grieves, N., Barnes, R., Zhao, B., Gilda, S., Grantham, J., Stafford, G., Savage, D., Bland, S., and Ealey, B. (2018).

The first super-Earth detection from the high cadence and high radial velocity precision Dharma Planet Survey. , 480(2):2411–2422.

Mahadevan, S., Ramsey, L., Bender, C., Terrien, R., Wright, J. T., Halverson, S., Hearty, F., Nelson, M., Burton, A., Redman, S., Osterman, S., Diddams, S., Kasting, J., Endl, M., and Deshpande, R. (2012). The habitable-zone planet finder: a stabilized fiber-fed NIR spectrograph for the Hobby-Eberly Telescope. In McLean, I. S., Ramsay, S. K., and Takami, H., editors, *Ground-based and Airborne Instrumentation for Astronomy IV*, volume 8446 of *Society of Photo-Optical Instrumentation Engineers (SPIE) Conference Series*, page 84461S.

Marcy, G., Butler, R. P., Fischer, D., Vogt, S., Wright, J. T., Tinney, C. G., and Jones, H. R. A. (2005a). Observed Properties of Exoplanets: Masses, Orbits, and Metallicities. *Progress of Theoretical Physics Supplement*, 158:24–42.

Marcy, G. W. and Butler, R. P. (1996). A Planetary Companion to 70 Virginis. , 464:L147.

Marcy, G. W., Butler, R. P., Vogt, S. S., Fischer, D. A., Henry, G. W., Laughlin, G., Wright, J. T., and Johnson, J. A. (2005b). Five New Extrasolar Planets. *Astrophysical Journal*, 619(1):570–584.

Massey, F. J. (1951). The kolmogorov-smirnov test for goodness of fit. *Journal of the American Statistical Association*, 46(253):68–78.

Mayor, M., Imbert, M., Andersen, J., Ardeberg, A., Benz, W., Lindgren, H., Martin, N., Maurice, E., Nordstrom, B., and Prevot, L. (1984). Studies of dynamical properties of globular clusters. I. Kinematic parameters and binary frequency in 47 Tucanae. *AAP*, 134:118–122.

Mayor, M., Marmier, M., Lovis, C., Udry, S., Ségransan, D., Pepe, F., Benz, W., Bertaux, J. L., Bouchy, F., Dumusque, X., Lo Curto, G., Mordasini, C., Queloz, D., and Santos,

- N. C. (2011). The HARPS search for southern extra-solar planets XXXIV. Occurrence, mass distribution and orbital properties of super-Earths and Neptune-mass planets. *arXiv e-prints*, page arXiv:1109.2497.
- Mayor, M. and Queloz, D. (1995). A Jupiter-mass companion to a solar-type star. *Nature*, 378(6555):355–359.
- Mazeh, T., Holczer, T., and Faigler, S. (2016). Dearth of short-period Neptunian exoplanets: A desert in period-mass and period-radius planes. *Astronomy and Astrophysics*, 589:A75.
- Millholland, S. C. and Winn, J. N. (2021). Split Peas in a Pod: Intra-system Uniformity of Super-Earths and Sub-Neptunes. , 920(2):L34.
- Mistry, P., Pathak, K., Prasad, A., Lekkas, G., Bhattarai, S., Gharat, S., Maity, M., Kumar, D., Collins, K. A., Schwarz, R. P., Mann, C. R., Furlan, E., Howell, S. B., Ciardi, D., Bieryla, A., Matthews, E. C., Gonzales, E., Ziegler, C., Crossfield, I., Giacalone, S., Tan, T.-G., Evans, P., Helminiak, K. G., Collins, K. I., Narita, N., Fukui, A., Pozuelos, F. J., Dressing, C., Soubkiou, A., Benkhaldoun, Z., Schlieder, J. E., Suarez, O., Barkaoui, K., Palle, E., Murgas, F., Srdoc, G., Goliguzova, M. V., Strakhov, I. A., Gnilka, C., Lester, K., Littlefield, C., Scott, N., Matson, R., Gillon, M., Jehin, E., Timmermans, M., Ghachoui, M., Abe, L., Bendjoya, P., Guillot, T., and Triaud, A. H. M. J. (2023). VaTEST. II. Statistical Validation of 11 TESS-detected Exoplanets Orbiting K-type Stars. *Astrophysical Journal*, 166(1):9.
- Mordasini, C., Alibert, Y., Benz, W., and Naef, D. (2009). Extrasolar planet population synthesis. II. Statistical comparison with observations. *Astronomy and Astrophysics*, 501(3):1161–1184.
- Mugrauer, M., Neuhäuser, R., Seifahrt, A., Mazeh, T., and Guenther, E. (2005). Four new wide binaries among exoplanet host stars. *Astronomy and Astrophysics*, 440(3):1051–1060.
- Murray, C. D. and Dermott, S. F. (2010). *Solar system dynamics*. Cambridge Univ. Press.

- Naoz, S. (2016). The Eccentric Kozai-Lidov Effect and Its Applications. , 54:441–489.
- Nielsen, E., De Rosa, R., Macintosh, B., Wang, J., Ruffio, J.-B., Chiang, E., Marley, M., Saumon, D., Savransky, D., Fabrycky, D., Konopacky, Q., Patience, J., and Bailey, V. (2019). The Gemini Planet Imager Exoplanet Survey: Giant Planet and Brown Dwarf Demographics from 10-100 AU. In *AAS/Division for Extreme Solar Systems Abstracts*, volume 51 of *AAS/Division for Extreme Solar Systems Abstracts*, page 100.02.
- Noyes, R. W., Hartmann, L. W., Baliunas, S. L., Duncan, D. K., and Vaughan, A. H. (1984). Rotation, convection, and magnetic activity in lower main-sequence stars. *Astrophysical Journal*, 279:763–777.
- Osborn, H. P., Nowak, G., Hébrard, G., Masseron, T., Lillo-Box, J., Pallé, E., Bekkelien, A., Florén, H. G., Guterman, P., Simon, A. E., Adibekyan, V., Bieryla, A., Borsato, L., Brandeker, A., Ciardi, D. R., Collier Cameron, A., Collins, K. A., Egger, J. A., Gandolfi, D., Hooton, M. J., Latham, D. W., Lendl, M., Matthews, E. C., Tuson, A., Ulmer-Moll, S., Vanderburg, A., Wilson, T. G., Ziegler, C., Alibert, Y., Alonso, R., Anglada, G., Arnold, L., Asquier, J., Barrado y Navascues, D., Baumjohann, W., Beck, T., Belinski, A. A., Benz, W., Biondi, F., Boisse, I., Bonfils, X., Broeg, C., Buchhave, L. A., Bérczy, T., Barros, S. C. C., Cabrera, J., Cardona Guillen, C., Carleo, I., Castro-González, A., Charnoz, S., Christiansen, J., Cortes-Zuleta, P., Csizmadia, S., Dalal, S., Davies, M. B., Deleuil, M., Delfosse, X., Delrez, L., Demory, B. O., Dunlavey, A. B., Ehrenreich, D., Erikson, A., Fernandes, R. B., Fortier, A., Forveille, T., Fossati, L., Fridlund, M., Gillon, M., Goeke, R. F., Goliguzova, M. V., Gonzales, E. J., Günther, M. N., Güdel, M., Heidari, N., Henze, C. E., Howell, S., Hoyer, S., Frey, J. I., Isaak, K. G., Jenkins, J. M., Kiefer, F., Kiss, L., Korth, J., Maxted, P. F. L., Laskar, J., Lecavelier des Etangs, A., Lovis, C., Lund, M. B., Luque, R., Magrin, D., Almenara, J. M., Martioli, E., Mecina, M., Medina, J. V., Moldovan, D., Morales-Calderón, M., Morello, G., Moutou, C., Murgas, F., Jensen, E. L. N., Nascimbeni, V., Olofsson, G., Ottensamer, R., Pagano, I., Peter, G., Piotto,

- G., Pollacco, D., Queloz, D., Ragazzoni, R., Rando, N., Rauer, H., Ribas, I., Ricker, G., Demangeon, O. D. S., Smith, A. M. S., Santos, N., Scandariato, G., Seager, S., Sousa, S. G., Steller, M., Szabó, G. M., Ségransan, D., Thomas, N., Udry, S., Ulmer, B., Van Grootel, V., Vanderspek, R., Walton, N., and Winn, J. N. (2023). Two warm Neptunes transiting HIP 9618 revealed by TESS and Cheops. , 523(2):3069–3089.
- Pecaut, M. J. and Mamajek, E. E. (2013a). Intrinsic Colors, Temperatures, and Bolometric Corrections of Pre-main-sequence Stars. *Astrophysical Journal Supplemental*, 208(1):9.
- Pecaut, M. J. and Mamajek, E. E. (2013b). Intrinsic Colors, Temperatures, and Bolometric Corrections of Pre-main-sequence Stars. *Astrophysical Journal Supplemental*, 208(1):9.
- Pepe, F., Cristiani, S., Rebolo, R., Santos, N. C., Dekker, H., Cabral, A., Di Marcantonio, P., Figueira, P., Lo Curto, G., Lovis, C., Mayor, M., Mégevand, D., Molaro, P., Riva, M., Zapatero Osorio, M. R., Amate, M., Manescau, A., Pasquini, L., Zerbi, F. M., Adibekyan, V., Abreu, M., Affolter, M., Alibert, Y., Aliverti, M., Allart, R., Allende Prieto, C., Álvarez, D., Alves, D., Avila, G., Baldini, V., Bandy, T., Barros, S. C. C., Benz, W., Bianco, A., Borsa, F., Bourrier, V., Bouchy, F., Broeg, C., Calderone, G., Cirami, R., Coelho, J., Conconi, P., Coretti, I., Cumani, C., Cupani, G., D’Odorico, V., Damasso, M., Deiries, S., Delabre, B., Demangeon, O. D. S., Dumusque, X., Ehrenreich, D., Faria, J. P., Fragoso, A., Genolet, L., Genoni, M., Génova Santos, R., González Hernández, J. I., Hughes, I., Iwert, O., Kerber, F., Knudstrup, J., Landoni, M., Lavie, B., Lillo-Box, J., Lizon, J. L., Maire, C., Martins, C. J. A. P., Mehner, A., Micela, G., Modigliani, A., Monteiro, M. A., Monteiro, M. J. P. F. G., Moschetti, M., Murphy, M. T., Nunes, N., Oggioni, L., Oliveira, A., Oshagh, M., Pallé, E., Pariani, G., Poretti, E., Rasilla, J. L., Rebordão, J., Redaelli, E. M., Santana Tschudi, S., Santin, P., Santos, P., Ségransan, D., Schmidt, T. M., Segovia, A., Sosnowska, D., Sozzetti, A., Sousa, S. G., Spanò, P., Suárez Mascareño, A., Taberner, H., Tenegi, F., Udry, S., and Zanutta, A. (2021). ESPRESSO at VLT. On-sky performance and first results. *Astronomy and Astrophysics*, 645:A96.

- Petigura, E. A. (2015). *Prevalence of Earth-size Planets Orbiting Sun-like Stars*. PhD thesis, University of California, Berkeley.
- Petigura, E. A., Howard, A. W., Marcy, G. W., Johnson, J. A., Isaacson, H., Cargile, P. A., Hebb, L., Fulton, B. J., Weiss, L. M., Morton, T. D., Winn, J. N., Rogers, L. A., Sinukoff, E., Hirsch, L. A., and Crossfield, I. J. M. (2017). The California-Kepler Survey. I. High-resolution Spectroscopy of 1305 Stars Hosting Kepler Transiting Planets. *Astrophysical Journal*, 154(3):107.
- Petigura, E. A., Marcy, G. W., and Howard, A. W. (2013). A Plateau in the Planet Population below Twice the Size of Earth. *Astrophysical Journal*, 770(1):69.
- Petigura, E. A., Marcy, G. W., Winn, J. N., Weiss, L. M., Fulton, B. J., Howard, A. W., Sinukoff, E., Isaacson, H., Morton, T. D., and Johnson, J. A. (2018). The California-Kepler Survey. IV. Metal-rich Stars Host a Greater Diversity of Planets. *Astrophysical Journal*, 155(2):89.
- Pinamonti, M., Damasso, M., Marzari, F., Sozzetti, A., Desidera, S., Maldonado, J., Scandariato, G., Affer, L., Lanza, A. F., Bignamini, A., Bonomo, A. S., Borsa, F., Claudi, R., Cosentino, R., Giacobbe, P., González-Álvarez, E., González Hernández, J. I., Gratton, R., Leto, G., Malavolta, L., Martinez Fiorenzano, A., Micela, G., Molinari, E., Pagano, I., Pedani, M., Perger, M., Piotto, G., Rebolo, R., Ribas, I., Suárez Mascareño, A., and Toledo- Padrón, B. (2018). The HADES RV Programme with HARPS-N at TNG. VIII. GJ15A: a multiple wide planetary system sculpted by binary interaction. *Astronomy and Astrophysics*, 617:A104.
- Polanski, A. S. and 72 colleagues, including **Judah Van Zandt** (2024). The TESS-Keck Survey. XX. 15 New TESS Planets and a Uniform RV Analysis of All Survey Targets. , 272(2):32.
- Polanski, A. S., Lubin, J., Beard, C., Akana Murphy, J. M., Rubenzahl, R., Hill, M. L.,

- Crossfield, I. J. M., Chontos, A., Robertson, P., Isaacson, H., Kane, S. R., Ciardi, D. R., Batalha, N. M., Dressing, C., Fulton, B., Howard, A. W., Huber, D., Petigura, E. A., Weiss, L. M., Angelo, I., Behrard, A., Blunt, S., Brinkman, C. L., Dai, F., Dalba, P. A., Fetherolf, T., Giacalone, S., Hirsch, L. A., Holcomb, R., Kosiarek, M. R., Mayo, A. W., MacDougall, M. G., Močnik, T., Pidhorodetska, D., Rice, M., Rosenthal, L. J., Scarsdale, N., Turtelboom, E. V., Tyler, D., Van Zandt, J., Yee, S. W., Coria, D. R., Dulz, S. D., Hartman, J. D., Householder, A., Lange, S., Langford, A., Louden, E. M., Siegel, J. C., Gilbert, E. A., Gonzales, E. J., Schlieder, J. E., Boyle, A. W., Christiansen, J. L., Clark, C. A., Fernandes, R. B., Lund, M. B., Savel, A. B., Gill, H., Beichman, C., Matson, R., Matthews, E. C., Furlan, E., Howell, S. B., Scott, N. J., Everett, M. E., Livingston, J. H., Ershova, I. O., Cheryasov, D. V., Safonov, B., Lillo-Box, J., Barrado, D., and Morales-Calderón, M. (2024). The TESS-Keck Survey. XX. 15 New TESS Planets and a Uniform RV Analysis of All Survey Targets. *Astrophysical Journal Supplemental*, 272(2):32.
- Powell, M. J. D. (1964). An efficient method for finding the minimum of a function of several variables without calculating derivatives. *The Computer Journal*, 7(2):155.
- Price-Whelan, A. M., Hogg, D. W., Foreman-Mackey, D., and Rix, H.-W. (2017). The Joker: A Custom Monte Carlo Sampler for Binary-star and Exoplanet Radial Velocity Data. *Astrophysical Journal*, 837(1):20.
- Raghavan, D., McAlister, H. A., Henry, T. J., Latham, D. W., Marcy, G. W., Mason, B. D., Gies, D. R., White, R. J., and ten Brummelaar, T. A. (2010). A Survey of Stellar Families: Multiplicity of Solar-type Stars. *Astrophysical Journal Supplemental*, 190(1):1–42.
- Ricker, G. R., Winn, J. N., Vanderspek, R., Latham, D. W., Bakos, G. Á., Bean, J. L., Berta-Thompson, Z. K., Brown, T. M., Buchhave, L., Butler, N. R., Butler, R. P., Chaplin, W. J., Charbonneau, D., Christensen-Dalsgaard, J., Clampin, M., Deming, D., Doty, J., De Lee, N., Dressing, C., Dunham, E. W., Endl, M., Fressin, F., Ge, J., Henning, T., Holman, M. J., Howard, A. W., Ida, S., Jenkins, J. M., Jernigan, G., Johnson, J. A.,

- Kaltenegger, L., Kawai, N., Kjeldsen, H., Laughlin, G., Levine, A. M., Lin, D., Lissauer, J. J., MacQueen, P., Marcy, G., McCullough, P. R., Morton, T. D., Narita, N., Paegert, M., Palle, E., Pepe, F., Pepper, J., Quirrenbach, A., Rinehart, S. A., Sasselov, D., Sato, B., Seager, S., Sozzetti, A., Stassun, K. G., Sullivan, P., Szentgyorgyi, A., Torres, G., Udry, S., and Villaseñor, J. (2015). Transiting Exoplanet Survey Satellite (TESS). *Journal of Astronomical Telescopes, Instruments, and Systems*, 1:014003.
- Rogers, J. G. and Owen, J. E. (2021). Unveiling the planet population at birth. , 503(1):1526–1542.
- Rogers, L. A. (2015). Most 1.6 Earth-radius Planets are Not Rocky. *Astrophysical Journal*, 801(1):41.
- Rosenthal, L. J., Fulton, B. J., Hirsch, L. A., Isaacson, H. T., Howard, A. W., Dedrick, C. M., Sherstyuk, I. A., Blunt, S. C., Petigura, E. A., Knutson, H. A., Behmard, A., Chontos, A., Crepp, J. R., Crossfield, I. J. M., Dalba, P. A., Fischer, D. A., Henry, G. W., Kane, S. R., Kosiarek, M., Marcy, G. W., Rubenzahl, R. A., Weiss, L. M., and Wright, J. T. (2021). The California Legacy Survey. I. A Catalog of 178 Planets from Precision Radial Velocity Monitoring of 719 Nearby Stars over Three Decades. *Astrophysical Journal Supplemental*, 255(1):8.
- Rosenthal, L. J., Knutson, H. A., Chachan, Y., Dai, F., Howard, A. W., Fulton, B. J., Chontos, A., Crepp, J. R., Dalba, P. A., Henry, G. W., Kane, S. R., Petigura, E. A., Weiss, L. M., and Wright, J. T. (2022). The California Legacy Survey. III. On the Shoulders of (Some) Giants: The Relationship between Inner Small Planets and Outer Massive Planets. *Astrophysical Journal Supplemental*, 262(1):1.
- Rubenzahl, R. A., Dai, F., Howard, A. W., Chontos, A., Giacalone, S., Lubin, J., Rosenthal, L. J., Isaacson, H., Batalha, N. M., Crossfield, I. J. M., Dressing, C., Fulton, B., Huber, D., Kane, S. R., Petigura, E. A., Robertson, P., Roy, A., Weiss, L. M., Beard, C., Hill,

- M. L., Mayo, A., Močnik, T., Akana Murphy, J. M., and Scarsdale, N. (2021). The TESS-Keck Survey IV: A Retrograde, Polar Orbit for the Ultra-Low-Density, Hot Super-Neptune WASP-107b. *arXiv e-prints*, page arXiv:2101.09371.
- Santos, N. C., Israelian, G., and Mayor, M. (2004). Spectroscopic [Fe/H] for 98 extra-solar planet-host stars. Exploring the probability of planet formation. *Astronomy and Astrophysics*, 415:1153–1166.
- Schwab, C., Rakich, A., Gong, Q., Mahadevan, S., Halverson, S. P., Roy, A., Terrien, R. C., Robertson, P. M., Hearty, F. R., Levi, E. I., Monson, A. J., Wright, J. T., McElwain, M. W., Bender, C. F., Blake, C. H., Stürmer, J., Gurevich, Y. V., Chakraborty, A., and Ramsey, L. W. (2016). Design of NEID, an extreme precision Doppler spectrograph for WIYN. In Evans, C. J., Simard, L., and Takami, H., editors, *Ground-based and Airborne Instrumentation for Astronomy VI*, volume 9908 of *Society of Photo-Optical Instrumentation Engineers (SPIE) Conference Series*, page 99087H.
- Schwarz, G. (1978). Estimating the Dimension of a Model. *The Annals of Statistics*, 6(2):461 – 464.
- Scott, N. J., Howell, S. B., Gnilka, C. L., Stephens, A. W., Salinas, R., Matson, R. A., Furlan, E., Horch, E. P., Everett, M. E., Ciardi, D. R., Mills, D., and Quigley, E. A. (2021). Twin High-resolution, High-speed Imagers for the Gemini Telescopes: Instrument description and science verification results. *Frontiers in Astronomy and Space Sciences*, 8:138.
- Serrano, L. M., Gandolfi, D., Hoyer, S., Brandeker, A., Hooton, M. J., Sousa, S., Murgas, F., Ciardi, D. R., Howell, S. B., Benz, W., Billot, N., Florén, H. G., Bekkelien, A., Bonfanti, A., Krenn, A., Mustill, A. J., Wilson, T. G., Osborn, H., Parviainen, H., Heidari, N., Pallé, E., Fridlund, M., Adibekyan, V., Fossati, L., Deleuil, M., Knudstrup, E., Collins, K. A., Lam, K. W. F., Grziwa, S., Salmon, S., Albrecht, S. H., Alibert, Y., Alonso, R.,

Anglada-Escudé, G., Bárczy, T., Barrado y Navascues, D., Barros, S. C. C., Baumjohann, W., Beck, M., Beck, T., Bieryla, A., Bonfils, X., Boyd, P. T., Broeg, C., Cabrera, J., Charnoz, S., Chazelas, B., Christiansen, J. L., Collier Cameron, A., Cortés-Zuleta, P., Csizmadia, S., Davies, M. B., Deline, A., Delrez, L., Demangeon, O. D. S., Demory, B. O., Dunlavey, A., Ehrenreich, D., Erikson, A., Fortier, A., Fukui, A., Garai, Z., Gillon, M., Güdel, M., Hébrard, G., Heng, K., Huang, C. X., Isaak, K. G., Jenkins, J. M., Kiss, L. L., Laskar, J., Latham, D. W., Lecavelier des Etangs, A., Lendl, M., Levine, A. M., Lovis, C., Lund, M. B., Magrin, D., Maxted, P. F. L., Narita, N., Nascimbeni, V., Olofsson, G., Ottensamer, R., Pagano, I., Pessanha, A. C. S. V., Peter, G., Piotto, G., Pollacco, D., Queloz, D., Ragazzoni, R., Rando, N., Ratti, F., Rauer, H., Ribas, I., Ricker, G., Rowden, P., Santos, N. C., Scandariato, G., Seager, S., Ségransan, D., Simon, A. E., Smith, A. M. S., Steller, M., Szabó, G. M., Thomas, N., Twicken, J. D., Udry, S., Ulmer, B., Van Grootel, V., Vanderspek, R., Viotto, V., and Walton, N. (2022). The HD 93963 A transiting system: A 1.04 d super-Earth and a 3.65 d sub-Neptune discovered by TESS and CHEOPS. *Astronomy and Astrophysics*, 667:A1.

Soderblom, D. R., Duncan, D. K., and Johnson, D. R. H. (1991). The Chromospheric Emission–Age Relation for Stars of the Lower Main Sequence and Its Implications for the Star Formation Rate. *Astrophysical Journal*, 375:722.

Struve, O. (1952). Proposal for a project of high-precision stellar radial velocity work. *The Observatory*, 72:199–200.

Twicken, J. D., Catanzarite, J. H., Clarke, B. D., Girouard, F., Jenkins, J. M., Klaus, T. C., Li, J., McCauliff, S. D., Seader, S. E., Tenenbaum, P., Wohler, B., Bryson, S. T., Burke, C. J., Caldwell, D. A., Haas, M. R., Henze, C. E., and Sanderfer, D. T. (2018). Kepler Data Validation I—Architecture, Diagnostic Tests, and Data Products for Vetting Transiting Planet Candidates. , 130(988):064502.

Van Eylen, V., Agentoft, C., Lundkvist, M. S., Kjeldsen, H., Owen, J. E., Fulton, B. J.,

- Petigura, E., and Snellen, I. (2018). An asteroseismic view of the radius valley: stripped cores, not born rocky. , 479(4):4786–4795.
- Van Zandt, J. and Petigura, E. (2024a). ethraid: A simple method for characterizing long-period companions using Doppler, astrometric, and imaging constraints. *arXiv e-prints*, page arXiv:2403.16340.
- Van Zandt, J. and Petigura, E. A. (2024b). No Evidence for a Metallicity-dependent Enhancement of Distant Giant Companions to Close-in Small Planets in the California Legacy Survey. *Astrophysical Journal*, 168(6):268.
- Van Zandt, J., Petigura, E. A., Lubin, J., Weiss, L. M., Turtelboom, E. V., Fetherolf, T., Murphy, J. M. A., Crossfield, I. J. M., Gilbert, G. J., Močnik, T., Batalha, N. M., Dressing, C., Fulton, B., Howard, A. W., Huber, D., Isaacson, H., Kane, S. R., Robertson, P., Roy, A., Angelo, I., Behmard, A., Beard, C., Chontos, A., Dai, F., Giacalone, S., Hill, M. L., Holcomb, R., Howell, S. B., Mayo, A. W., Pidhorodetska, D., Polanski, A. S., Rogers, J., Rosenthal, L. J., Rubenzahl, R. A., Scarsdale, N., Tyler, D., Yee, S. W., and Zink, J. (2025). The TESS–Keck Survey. XXIV. Outer Giants May Be More Prevalent in the Presence of Inner Small Planets. , 169(5):235.
- Van Zandt, J., Petigura, E. A., MacDougall, M., Gilbert, G. J., Lubin, J., Barclay, T., Batalha, N. M., Crossfield, I. J. M., Dressing, C., Fulton, B., Howard, A. W., Huber, D., Isaacson, H., Kane, S. R., Robertson, P., Roy, A., Weiss, L. M., Behmard, A., Beard, C., Chontos, A., Dai, F., Dalba, P. A., Fetherolf, T., Giacalone, S., Henze, C. E., Hill, M. L., Hirsch, L. A., Holcomb, R., Howell, S. B., Jenkins, J. M., Latham, D. W., Mayo, A., Mireles, I., Močnik, T., Murphy, J. M. A., Pidhorodetska, D., Polanski, A. S., Ricker, G. R., Rosenthal, L. J., Rubenzahl, R. A., Seager, S., Scarsdale, N., Turtelboom, E. V., Vanderspek, R., and Winn, J. N. (2023). TESS-Keck Survey. XIV. Two Giant Exoplanets from the Distant Giants Survey. *Astrophysical Journal*, 165(2):60.

- Van Zandt, J. E. and Petigura, E. (2024c). ethraid v2.4.3: Characterize long-period companions with partial orbits.
- Venner, A., An, Q., Huang, C. X., Brandt, T. D., Wittenmyer, R. A., and Vanderburg, A. (2024). HD 28185 revisited: an outer planet, instead of a brown dwarf, on a Saturn-like orbit. , 535(1):90–106.
- Villaver, E., Livio, M., Mustill, A. J., and Siess, L. (2014). Hot Jupiters and Cool Stars. *Astrophysical Journal*, 794(1):3.
- Vogt, S. S., Allen, S. L., Bigelow, B. C., Bresee, L., Brown, B., Cantrall, T., Conrad, A., Couture, M., Delaney, C., Epps, H. W., Hilyard, D., Hilyard, D. F., Horn, E., Jern, N., Kanto, D., Keane, M. J., Kibrick, R. I., Lewis, J. W., Osborne, J., Pardeilhan, G. H., Pfister, T., Ricketts, T., Robinson, L. B., Stover, R. J., Tucker, D., Ward, J., and Wei, M. Z. (1994). HIRES: the high-resolution echelle spectrometer on the Keck 10-m Telescope. In Crawford, D. L. and Craine, E. R., editors, *Instrumentation in Astronomy VIII*, volume 2198 of *Society of Photo-Optical Instrumentation Engineers (SPIE) Conference Series*, page 362.
- Vogt, S. S., Burt, J., Meschiari, S., Butler, R. P., Henry, G. W., Wang, S., Holden, B., Gapp, C., Hanson, R., Arriagada, P., Keiser, S., Teske, J., and Laughlin, G. (2015). Six Planets Orbiting HD 219134. *Astrophysical Journal*, 814(1):12.
- Vogt, S. S., Radovan, M., Kibrick, R., Butler, R. P., Alcott, B., Allen, S., Arriagada, P., Bolte, M., Burt, J., Cabak, J., Chloros, K., Cowley, D., Deich, W., Dupraw, B., Earthman, W., Epps, H., Faber, S., Fischer, D., Gates, E., Hilyard, D., Holden, B., Johnston, K., Keiser, S., Kanto, D., Katsuki, M., Laiterman, L., Lanclos, K., Laughlin, G., Lewis, J., Lockwood, C., Lynam, P., Marcy, G., McLean, M., Miller, J., Misch, T., Peck, M., Pfister, T., Phillips, A., Rivera, E., Sandford, D., Saylor, M., Stover, R., Thompson, M., Walp,

- B., Ward, J., Wareham, J., Wei, M., and Wright, C. (2014). APF—The Lick Observatory Automated Planet Finder. , 126(938):359.
- Wallace, A. L., Casey, A. R., Brown, A. G. A., and Castro-Ginard, A. (2024). Detection and Characterisation of Giant Planets with Gaia Astrometry. *arXiv e-prints*, page arXiv:2411.06705.
- Wang, S., Jones, M., Shporer, A., Fulton, B. J., Paredes, L. A., Trifonov, T., Kossakowski, D., Eastman, J., Redfield, S., Günther, M. N., Kreidberg, L., Huang, C. X., Millholland, S., Seligman, D., Fischer, D., Brahm, R., Wang, X.-Y., Cruz, B., Henry, T., James, H.-S., Addison, B., Liang, E.-S., Davis, A. B., Tronsgaard, R., Worku, K., Brewer, J. M., Kürster, M., Zhang, H., Beichman, C. A., Bieryla, A., Brown, T. M., Christiansen, J. L., Ciardi, D. R., Collins, K. A., Esquerdo, G. A., Howard, A. W., Isaacson, H., Latham, D. W., Mazeh, T., Petigura, E. A., Quinn, S. N., Shahaf, S., Siverd, R. J., Rodler, F., Reffert, S., Zakhozhay, O., Ricker, G. R., Vanderspek, R., Seager, S., Winn, J. N., Jenkins, J. M., Boyd, P. T., Fűrész, G., Henze, C., Levine, A. M., Morris, R., Paegert, M., Stassun, K. G., Ting, E. B., Vezie, M., and Laughlin, G. (2019). HD 202772A b: A Transiting Hot Jupiter around a Bright, Mildly Evolved Star in a Visual Binary Discovered by TESS. *Astrophysical Journal*, 157(2):51.
- Weiss, L. M., Dai, F., Huber, D., Brewer, J. M., Collins, K. A., Ciardi, D. R., Matthews, E. C., Ziegler, C., Howell, S. B., Batalha, N. M., Crossfield, I. J. M., Dressing, C., Fulton, B., Howard, A. W., Isaacson, H., Kane, S. R., Petigura, E. A., Robertson, P., Roy, A., Rubenzahl, R. A., Twicken, J. D., Claytor, Z. R., Stassun, K. G., MacDougall, M. G., Chontos, A., Giacalone, S., Dalba, P. A., Mocnik, T., Hill, M. L., Beard, C., Akana Murphy, J. M., Rosenthal, L. J., Behrard, A., Van Zandt, J., Lubin, J., Kosiarek, M. R., Lund, M. B., Christiansen, J. L., Matson, R. A., Beichman, C. A., Schlieder, J. E., Gonzales, E. J., Briceño, C., Law, N., Mann, A. W., Collins, K. I., Evans, P., Fukui, A., Jensen, E. L. N., Murgas, F., Narita, N., Palle, E., Parviainen, H., Schwarz, R. P., Tan, T.-

- G., Acton, J. S., Bryant, E. M., Chaushev, A., Gill, S., Eigmüller, P., Jenkins, J., Ricker, G., Seager, S., and Winn, J. N. (2021). The TESS-Keck Survey. II. An Ultra-short-period Rocky Planet and Its Siblings Transiting the Galactic Thick-disk Star TOI-561. *Astrophysical Journal*, 161(2):56.
- Weiss, L. M., Isaacson, H., Howard, A. W., Fulton, B. J., Petigura, E. A., Fabrycky, D., Jontof-Hutter, D., Steffen, J. H., Schlichting, H. E., Wright, J. T., Beard, C., Brinkman, C. L., Chontos, A., Giacalone, S., Hill, M. L., Kosiarek, M. R., MacDougall, M. G., Močnik, T., Polanski, A. S., Turtelboom, E. V., Tyler, D., and Van Zandt, J. (2024). The Kepler Giant Planet Search. I. A Decade of Kepler Planet-host Radial Velocities from W. M. Keck Observatory. *Astrophysical Journal Supplemental*, 270(1):8.
- Weiss, L. M. and Marcy, G. W. (2014). The Mass-Radius Relation for 65 Exoplanets Smaller than 4 Earth Radii. *Astrophysical Journal Letters*, 783(1):L6.
- Weiss, L. M., Marcy, G. W., Petigura, E. A., Fulton, B. J., Howard, A. W., Winn, J. N., Isaacson, H. T., Morton, T. D., Hirsch, L. A., Sinukoff, E. J., Cumming, A., Hebb, L., and Cargile, P. A. (2018). The California-Kepler Survey. V. Peas in a Pod: Planets in a Kepler Multi-planet System Are Similar in Size and Regularly Spaced. *Astrophysical Journal*, 155(1):48.
- Winn, J. N. and Fabrycky, D. C. (2015). The Occurrence and Architecture of Exoplanetary Systems. , 53:409–447.
- Winn, J. N. and Petigura, E. (2024). Planet Occurrence from Doppler and transit surveys, 2nd ed. *arXiv e-prints*, page arXiv:2401.16451.
- Wittenmyer, R. A., Butler, R. P., Tinney, C. G., Horner, J., Carter, B. D., Wright, D. J., Jones, H. R. A., Bailey, J., and O’Toole, S. J. (2016). The Anglo-Australian Planet Search XXIV: The Frequency of Jupiter Analogs. *Astrophysical Journal*, 819(1):28.

- Wittenmyer, R. A., Clark, J. T., Trifonov, T., Addison, B. C., Wright, D. J., Stassun, K. G., Horner, J., Lowson, N., Kielkopf, J., Kane, S. R., Plavchan, P., Shporer, A., Zhang, H., Bowler, B. P., Mengel, M. W., Okumura, J., Rabus, M., Johnson, M. C., Harbeck, D., Tronsgaard, R., Buchhave, L. A., Collins, K. A., Collins, K. I., Gan, T., Jensen, E. L. N., Howell, S. B., Furlan, E., Gnilka, C. L., Lester, K. V., Matson, R. A., Scott, N. J., Ricker, G. R., Vanderspek, R., Latham, D. W., Seager, S., Winn, J. N., Jenkins, J. M., Rudat, A., Quintana, E. V., Rodriguez, D. R., Caldwell, D. A., Quinn, S. N., Essack, Z., and Bouma, L. G. (2022). TOI-1842b: A Transiting Warm Saturn Undergoing Reinflation around an Evolving Subgiant. *Astrophysical Journal*, 163(2):82.
- Wittenmyer, R. A., Wang, S., Horner, J., Butler, R. P., Tinney, C. G., Carter, B. D., Wright, D. J., Jones, H. R. A., Bailey, J., O’Toole, S. J., and Johns, D. (2020). Cool Jupiters greatly outnumber their toasty siblings: occurrence rates from the Anglo-Australian Planet Search. , 492(1):377–383.
- Wolszczan, A. and Frail, D. A. (1992). A planetary system around the millisecond pulsar PSR1257 + 12. *Nature*, 355(6356):145–147.
- Wright, J. T., Marcy, G. W., Howard, A. W., Johnson, J. A., Morton, T. D., and Fischer, D. A. (2012). The Frequency of Hot Jupiters Orbiting nearby Solar-type Stars. *Astrophysical Journal*, 753(2):160.
- Yee, S. W., Petigura, E. A., and von Braun, K. (2017). Precision Stellar Characterization of FGKM Stars using an Empirical Spectral Library. *Astrophysical Journal*, 836(1):77.
- Zhao, L. L., Kunovac, V., Brewer, J. M., Llama, J., Millholland, S. C., Hedges, C., Szymkowiak, A. E., Roettenbacher, R. M., Cabot, S. H. C., Weiss, S. A., and Fischer, D. A. (2023). Measured spin-orbit alignment of ultra-short-period super-Earth 55 Cancri e. *Nature Astronomy*, 7:198–205.

- Zhu, W. (2022). The Intrinsic Multiplicity Distribution of Exoplanets Revealed from the Radial Velocity Method. *Astrophysical Journal*, 164(1):5.
- Zhu, W. (2024). The Metallicity Dimension of the Super Earth-cold Jupiter Correlation. *Research in Astronomy and Astrophysics*, 24(4):045013.
- Zhu, W. and Wu, Y. (2018). The Super Earth-Cold Jupiter Relations. *Astrophysical Journal*, 156(3):92.
- Zink, J. K. and Howard, A. W. (2023). Hot Jupiters Have Giant Companions: Evidence for Coplanar High-eccentricity Migration. *Astrophysical Journal Letters*, 956(1):L29.